ABSTRACT

NUCLEAR SPECTROSCOPIC STUDIES OF SHORT-LIVED NEUTRON-DEFICIENT SPECIES IN THE $f_{7/2}$-SHELL REGION

By

Jerry Nelson Black

The decay schemes of ^{53g}Fe and ^{53m}Fe were studied by the use of standard techniques for β- and γ-ray spectroscopy. The γ-decay of ^{40}Sc also was investigated by means of on-line, pulsed-beam techniques. An extensive search was conducted for γ-ray evidence to support the existence of high-spin metastable states in ^{53}Co, ^{43}Ti and ^{43}Sc.

Although normal spectroscopic methods using high-resolution Ge(Li) and Si(Li) detectors were employed in most of these studies, the development of cyclotron pulsing, data routing and other on-line techniques for the investigation of short-lived species was a significant part of this work. A pneumatic rabbit system and a helium-jet thermalizer also were utilized in many of the experiments.

At least two new γ-rays were observed in the decay of 8.5 m ^{53g}Fe. These γ-rays allowed the establishment of a decay scheme with levels at 0, 377.9, 1288.0 and 1619.0 keV. The β^+ decay was found to have end-point energies of 2.8, 2.4 and 1.7 MeV. Subsequent β^+-γ coincidence experiments demonstrated that the 2.8- and 2.4-MeV groups feed the ground state and first excited

state, respectively.

The decay of 2.5 m ^{53m}Fe was found to have six γ rays which could be placed in a consistent decay scheme with levels at 0, 1328.1, 2339.6 and 3040.6 keV. Careful examination of the γ rays de-exciting this 19/2- metastable state resulted in the direct observation of transitions of multipolarities of $M5$ and $E6$ -- the highest ever observed experimentally.

The Oak Ridge Shell Model Code of French, et al., was utilized to predict the level schemes of ^{53}Mn and ^{53}Fe. The results were compared with other calculations and with the experimentally determined values. Partial half-lives for the γ rays de-exciting ^{53m}Fe also were calculated and compared with experimental results.

Using on-line, pulsed-beam techniques, seven γ rays were observed in the decay of 0.183 s ^{40}Sc, and subsequently placed in a consistent decay scheme with levels at 0, 3736.9, 4491.3, 5612.7 and 7656.3 keV. Based on the γ-ray intensities observed, β^+ feeding values and log ft values were deduced.

Various γ-ray techniques were used to conduct an exhaustive search for three-particle metastable states analogous to that observed in ^{53m}Fe. The nuclei ^{53}Co, ^{43}Ti and ^{43}Sc were studied carefully in order to determine if γ rays were present which could be attributed to the decay of metastable states. The results of this study failed to establish the existence of γ rays which could be attributed to such states in these nuclei. If these states exist, then either the γ-branch of their decay is very small or the cross section for their formation by the reactions used is very low.

NUCLEAR SPECTROSCOPIC STUDIES OF SHORT-LIVED NEUTRON-DEFICIENT SPECIES IN THE $f_{7/2}$-SHELL REGION

By

Jerry Nelson Black

A THESIS

Submitted to
Michigan State University
in partial fulfillment of the requirements
for the degree of

ACKNOWLEDGMENTS

I wish to thank Dr. Wm. C. McHarris not only for suggesting this region of study but also for his guidance, support and enthusiasm throughout the various facets of the investigation. His encouragement and constant interest during the experimental work and the thesis preparation are greatly appreciated.

I also wish to thank Dr. W. H. Kelly of the Physics Department for his advice and assistance. His cooperation and discussions during this project were invaluable.

Dr. F. M. Bernthal has provided many useful discussions and advice during the latter part of this study.

I wish to acknowledge Dr. B. H. Wildenthal for his advice and help with the Oak Ridge Shell Model Codes. His calculation of the ^{53m}Fe transition probabilities required considerable effort and I am grateful for the results which he provided.

Dr. H. G. Blosser, Mr. H. Hilbert and Dr. W. P. Johnson assisted with the operation and maintenance of the Michigan State University Sector-Focused Cyclotron, which was used for the various irradiations required in this investigation. Dr. P. Miller and Mr. P. Sigg assisted in the development of beam pulsing techniques for the cyclotron.

The members of our research group have all helped in some way in the course of this study. Dr. D. Beery, Mr. W. Chaffee, Dr. J. Cross, Dr. R. Doebler, Dr. R. Eppley, Mr. R. Firestone, Dr. G. Giesler, Dr. R. Goles, Mr. K. Kosanke, Mr. C. Morgan, Mr. L. Samuelson, Dr. R. Todd and Dr. R. Warner have provided assistance and advice during various phases of experimentation and analysis. Dr. D. Beery and Dr. R. Warner

deserve special mention for their assistance with experimental problems. Mr. K. Kosanke has provided valuable help with the pneumatic rabbit and Helium-jet thermalizer systems.

Mr. R. Au, Mr. and Mrs. W. Merritt, and the cyclotron computer staff have aided greatly in the data acquisition and evaluation through the use of the laboratory's XDS Sigma-7 computer. Their assistance in various programming problems is greatly appreciated.

Help also has been received from Mr. R. Mercer and his staff in the cyclotron machine shop, and from Mr. W. Harder and the cyclotron electronics shop.

The cyclotron drafting staff, especially Mr. A. Daudi, have been very helpful in preparing the drawings for this thesis.

Our secretary Mrs. P. Warstler typed much of this thesis. Her efficiency, expertise, and patience have greatly facilitated its preparation.

I acknowledge the financial assistance of the National Aeronautics and Space Administration, National Science Foundation, U.S. Atomic Energy Commission, and Michigan State University.

TABLE OF CONTENTS

Chapter

Page

Chapter

Page

Chapter

Page

Chapter

Page

LIST OF TABLES

Table

Page

LIST OF FIGURES

Figure

Page

Figure

Page

CHAPTER I

INTRODUCTION

". . . . There are two ways in which physics tries to obtain a consistent picture of the structure of the atomic nucleus. One of these is the study of the elementary particles, their properties and mutual interactions. Thus one hopes to obtain a fundamental knowledge of the nuclear forces, from which one can then deductively understand the complicated nuclear structures. The other way consists in gaining, by direct experimentation, as many different data as possible for individual nuclei, and examining the relations among these data. One expects to obtain a network of correlations and connections which indicate some elementary laws of nuclear structure. These two ways have not yet met to establish a complete understanding of the nucleus, although many connections have been found . . . ." (May55).

Even though these words were written some sixteen years ago, they remain a very basic description of the motivation for modern research in nuclear physics and chemistry. In spite of the tremendous advances in experimental technology and theoretical methods, the long awaited meeting of experimental fact and theoretical prediction has not yet been realized in the nuclear problem. Notwithstanding the success of various specialized semi-empirical models, the goal of developing a complete comprehensive nuclear theory has not been attained. Although a large number of correlations have been established, no "fundamental" laws have been discovered which simplify or completely resolve the problem of predicting nuclear structure and properties. As Blatt and

Weisskopf state in their preface: "Nuclear physics is by no means a finished edifice" (Bla52).

Thus, one finds that the basic impetus for performing nuclear spectroscopy is not the acquisition of knowledge for its own sake, but instead represents another step towards understanding the entire nuclear problem. Each small contribution to the ever growing body of knowledge both experimental and theoretical relating to nuclear structure, brings one closer to the realization of a complete solution. The many correlations and systematics may eventually reveal the true nature of the nuclear force, and consequently the ability to predict nuclear properties from first principles.

Since an overall understanding of nuclear structure has not been achieved, current descriptions must rely on various semi-empirical models developed for specific types of nuclei. While these models cannot predict accurately all of the properties of various nuclei, each has been reasonably successful in its particular region of application. Since these models are semi-empirical, that is they utilize experimentally determined results to establish required parameters, the availability and quality of experimental results may limit the extent to which the model is capable of accurately predicting nuclear properties. In addition, the model itself may need to be modified and improved as the quality and quantity of available data increase. Thus, the acquisition of nuclear data is justified not only as a contribution to the general body of knowledge concerning nuclei, but also as a stimulant for testing and modifying present nuclear models.

One of the most successful and popular of the present nuclear

models is the so-called shell model. This description of the nucleus, detailed in Chapter V, envisions the nuclear protons and neutrons as circulating about in orbits analogous to the atomic electron shell structure. Closed shells are found to occur at proton or neutron "magic" numbers of 2, 8, 20, 28, 50, 82, and 126. The model has achieved its greatest success in treating nuclei near these closed shells. As the model has developed, interest has increased in extending its application to nuclei containing particles outside closed shells. This thesis encompasses a number of such nuclei in the $f_{7/2}$ - shell region, particularly ^{53}Mn and ^{53}Fe.

A portion of the Chart of the Nuclides covering the region studied here is shown in Figure 1-1. The original objective of this investigation was simply to elucidate the levels in ^{53}Mn populated by the β^+/ε decay of ^{53}Fe. However, the discovery of a high-spin, three-quasiparticle metastable state in ^{53}Fe by Eskola (Esk66,67) motivated a comprehensive study of the $^{53m+g}$Fe decay. A brief investigation of the decay of ^{40}Sc to levels in ^{40}Ca was performed both to ascertain the levels so populated and to learn something about the structure of ^{40}Sc. This investigation was also used to develop cyclotron pulsing and data routing techniques for studying short-lived species. Next, an extensive search was carried out to look for high-spin, three-quasiparticle states analogous to ^{53m}Fe in ^{53}Co, ^{43}Ti and ^{43}Sc. These nuclei were examined carefully to determine if γ rays were present which could be attributed to the decay of possible three-quasiparticle metastable states.

The experimental equipment and techniques employed during this

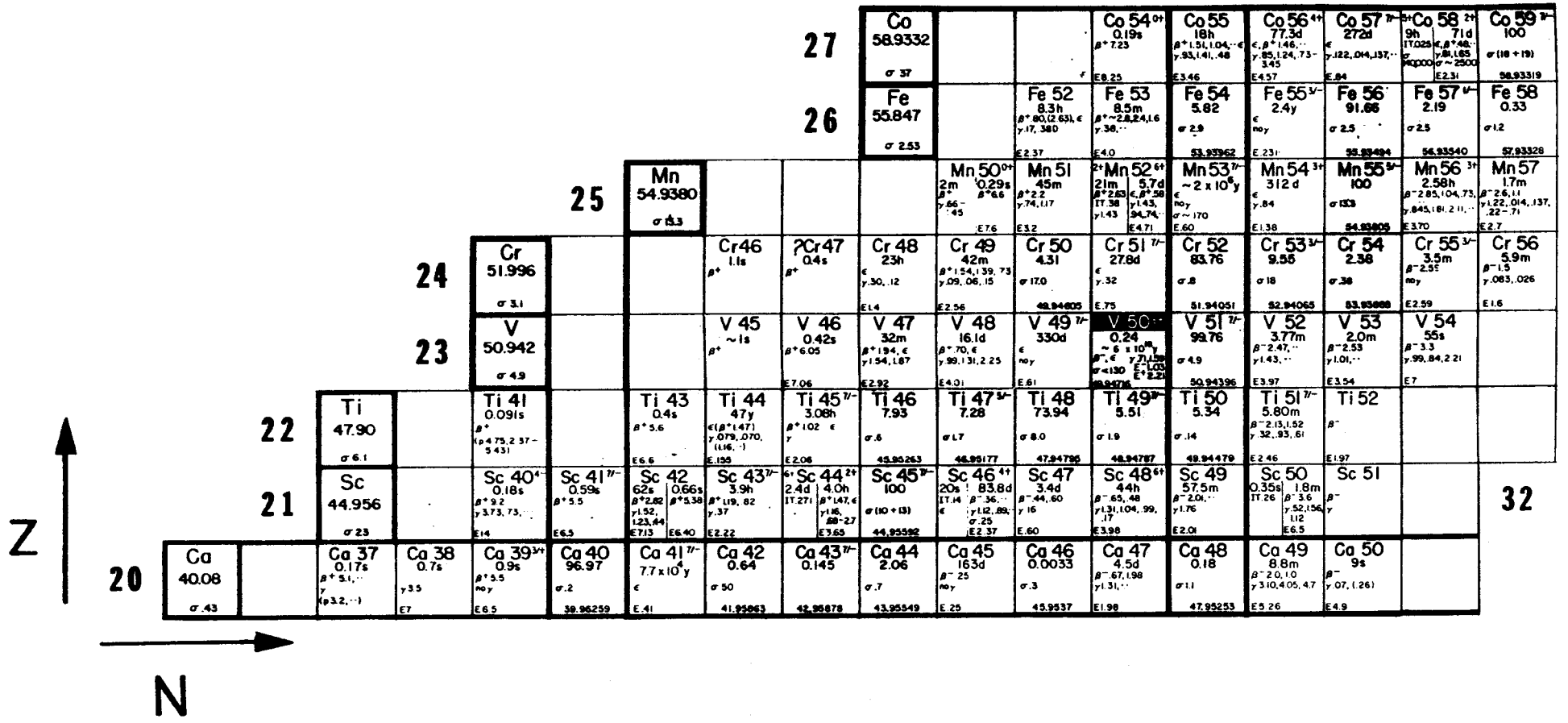

Figure 1-1. Portion of the Chart of the Nuclides, showing the calcium through cobalt region involved in this study. This section was taken from the Chart of the Nuclides, compiled by the Knolls Atomic Power Laboratory, Ninth Edition.

investigation are discussed in Chapter II. A number of methods which were developed for the pulsed in-beam study of short-lived species are covered, as well as conventional techniques for β- and γ-ray spectroscopy. The use of the pneumatic target (rabbit) and helium-jet transport systems for studying moderately short-lived isotopes also is described.

Since the analysis of acquired data is often quite complex, a complete chapter has been devoted to the methods of data analysis. Chapter III describes the various procedures used for analyzing β- and γ-ray spectra -- including various computer programs written for or adapted to the XDS Sigma 7 computer at the Michigan State University Cyclotron Laboratory.

The rather extensive γ- and β- spectroscopic studies of the decays of ^{53g}Fe and ^{53m}Fe are presented in Chapter IV. Level schemes for both species are deduced. The study is highlighted by the elucidation of the metastable state ^{53m}Fe and the discovery of transitions having multipolarities of $M5$ and $E6$ -- the highest ever observed experimentally.

In Chapter V the nuclear Shell Model is described and utilized to predict the structure of ^{53}Fe and ^{53}Mn. Level schemes are predicted for both isotopes and compared with other calculations and with the experimental results contained in Chapter IV. In addition, partial half-lives for those γ rays de-exciting ^{53m}Fe are predicted both from the simple Moszkowski single particle estimates and from the more elaborate Shell Model theory. These results are then compared with the experimental values obtained earlier.

A brief study of the decay of ^{40}Sc comprises Chapter VI. Pulsed-beam routing techniques were used to study the γ-decay of ^{40}Sc to obtain

the levels populated in ^{40}Ca with a relatively high degree of accuracy.

Chapters VII and VIII are concerned with the search for high-spin, three-quasiparticle metastable states in nuclei analogous to ^{53}Fe. Chapter VII presents the known facts about the existence of ^{53m}Co, together with the results of this study. The search for γ rays de-exciting possible $19/2^-$ states in ^{43}Ti and ^{43}Sc is discussed in Chapter VIII.

A short summary and discussion of the above investigations is presented in Chapter IX.

CHAPTER II

EXPERIMENTAL APPARATUS AND METHODS

2.1 The Cyclotron and Beam Transport System

2.1.1 The Cyclotron

The performance of pulsed-beam experiments and the production of short activations require a reliable, high-quality cyclotron. At Michigan State University we are fortunate to have such a machine, in the form of a variable-energy, sector-focused cyclotron (Blo61). The principle and design details of this accelerator together with its operation have been reported previously (Blo66, Gor68). A diagram of particle energy vs orbital frequency for the MSU cyclotron is shown in Figure 2-1. This figure illustrates the possible energies of various particles and the harmonic (N) on which they are accelerated. At the present time, protons, deuterons, helium-3 and alpha particles are routinely accelerated using the first and second harmonics. The development of heavy-ion beams is underway. The bulk of the material reported here was obtained using 24-45 MeV proton beams.

In the operation of the cyclotron the most important objective is to produce a well-tuned beam with a high extraction efficiency. This condition can be established by: (1) precise setting of the main magnetic field, (2) careful centering of the beam in order to reduce the effect of *RF* ripple and (3) good selection of a narrow phase group in order to produce an optimum single turn extraction.

The proton (H^+) beam is extracted at a radius of approximately

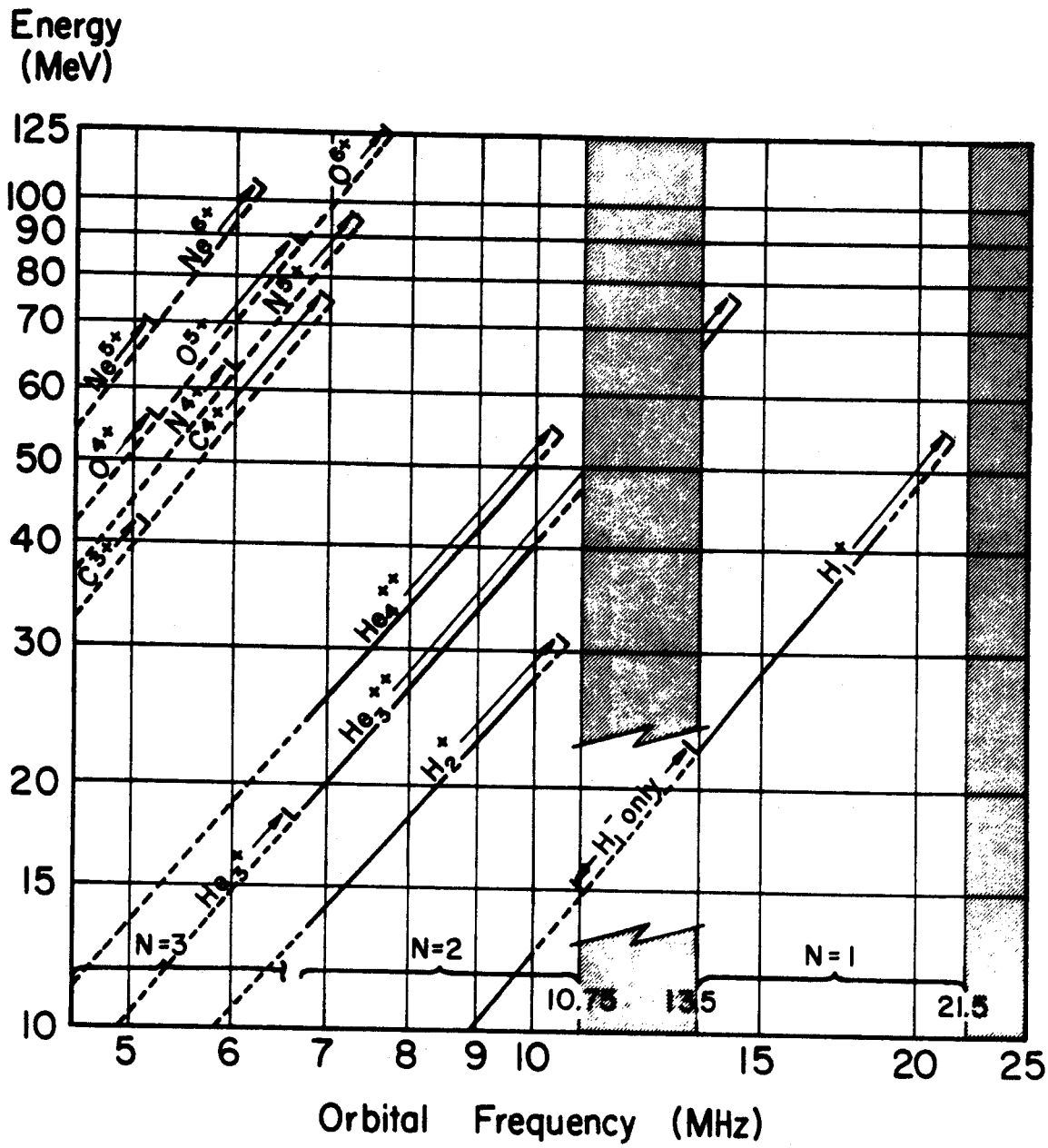

Figure 2-1. Diagram of Particle Energy vs Orbital Frequency for the MSU Cyclotron.

29 inches (212 turns), using a first harmonic bump field to induce a coherent radial oscillation. An electrostatic deflector and a focusing air-core magnetic channel are used to guide the beam from the machine. After extraction, the beam is balanced on the exit slits S1, illustrated in Figure 2-2. For our activation experiments, internal beam currents were typically 2 to 6 microamperes with almost 100% extraction efficiencies.

2.1.2 The Beam Transport System

The portion of the external beam transport system used in these experiments is shown in Figure 2-2. The details of the optical properties of the beam and of the energy analysis system have been discussed in previous publications (Mac67, Sne67, Ben68). M1 and M2 are horizontal bending magnets for alignment of the beam through the object slit S3. S2 is a vertical slit which was not used in most experiments. The beam is focused on S3 by means of two quadrupole doublets Q_1, Q_2 and Q_3, Q_4. The distance between S3 and S4 is about four feet. The divergence of the beam is determined by the openings of S3 and S4. M3 and M4 are two 45° analyzing magnets, whose fields are adjusted in such a manner as to direct the beam on the image slit, S5. The magnetic fields in M3 and M4, which determine the beam energy, are measured by nuclear magnetic resonance fluxmeters (Scanditronix, NMR-656C). Q5 and Q6 are quadrupole magnets used for refocusing. The beam must be balanced simultaneously on S3, S4 and S5. This balance can be achieved by equalizing the current on the sides of each individual slit. The shape (focus) of the beam can be examined directly with scintillators in front of S3 and S5. After the beam is properly aligned through S5, it is bent into the 45° goniometer line by the distributing magnet

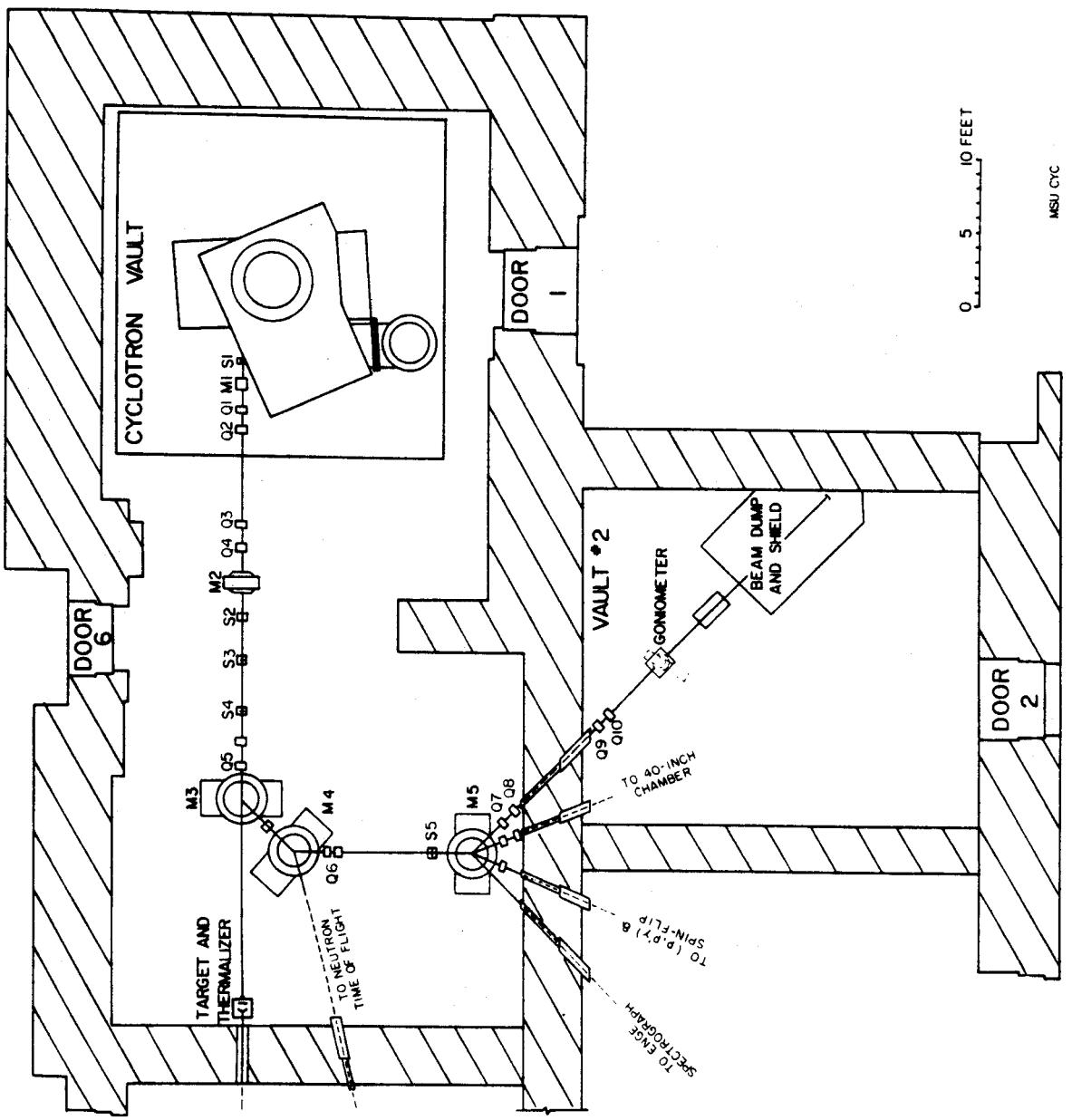

Figure 2-2. Diagram of the external beam transport system used in this study.

M5. Two more quadrupole doublets Q7, Q8 and Q9, Q10 are used to focus the beam on the target.

When using the various target chambers in the Goniometer line, the final beam focusing and alignment was performed by inserting a plastic scintillator in the target position and viewing the beam spot directly with a TV camera. With the enlarged image of the scintillator the beam could be focused and centered quite easily. The beam current on the rear Faraday Cup was monitored to assure that none of the beam was being lost on the beamline and chamber. Two additional methods were used in aligning and maintaining the beam during the course of the experiment. First, the neutron background was carefully monitored in the vicinity of the target chamber, so that if the beam wandered and struck the target frame or the chamber, an immediate increase in the neutron counting rate would be observed. Second, when possible, the front collimator and/or rear exit pipe of the chamber was isolated and the current from it monitored. For optimum conditions, both the neutron background and the collimator current were minimized with respect to the beam current measured at the Faraday Cup. For most on-line, pulsed-beam experiments a very low beam current (0.3-30.0 nanoamperes) was adequate. These currents were achieved by circulating a minimum current within the machine and then closing the water-cooled slits (S1 and S4) as necessary.

The Faraday Cup consisted of a half-inch aluminum beam stop, isolated from the target chamber and shielded by concrete blocks stacked 6 feet wide and 7 feet high. Additional shielding was provided by a cylinder of paraffin surrounding the beam pipe about 3 feet from the target chamber. These shielding measures reduced the neutron background

by a factor of ten. This resulted not only in cleaner data, but also in significantly extended detector lifetimes.

2.2 Cyclotron Beam Pulsing and Timing

Conventional methods of target handling are not suitable for the study of short-lived radioactive species (i.e., those with half-lives in the nanosecond to millisecond region). With such short half-lives, these targets cannot be moved, and therefore must be counted in the same position as they occupied during the irradiation. (A few "plunger" and "rotating-wheel" devices have been tried, but were found to be relatively slow and unreliable.) Since only the γ rays from the radioactive decay of these isotopes were of interest to us (as opposed to direct excitation γ rays from $(p,n\gamma)$ type reactions), it was imperative that the beam was turned off during the counting intervals. The only method that can satisfy all of the above conditions is that of pulsing the cyclotron beam. Although pulsed-beam experiments present a number of difficulties, they are a very powerful tool for studying short-lived isotopes. A number of different techniques are used, depending on the experimental requirements and the half-life one wishes to investigate.

2.2.1 *RF* Modulation Techniques

For many of the on-line γ-ray spectroscopy experiments reported here, the so-called "slow-pulsing" mode was utilized. This pulsing is accomplished by modulation of the *RF* accelerating voltage with a rectangular wave form, effectively turning the beam off and on. The minimum pulsing period is limited to a few hundred milliseconds, however, because of the time constant associated with the dees. Two variations of this technique have been employed, each using a different pulsing device together with a suitable data-taking program.

2.2.1A The Clock Module

The basis of the simplest and most popular method for slow pulsing is a routing-timer module designed by Dr. Peter Miller of the MSU Cyclotron Laboratory. The front and rear controls and outputs for this unit are shown in Figure 2-3. Within certain time limits, this module is ideally suited for pulsed-beam γ-ray work. It can provide beam-on (or beam-off) times ranging from 0.4 to 4.0 sec. Both positive and negative outputs are available on the rear of the module for beam pulsing. We have found it desirable to select the *RF* amplitude that maximizes beam current while there is no output from the timer module, and then use the module output (added algebraically to the amplitude so selected) to *detune* the beam. This is in contrast to the alternate condition where the *RF* is tuned while the module voltage is on. This choice was dictated by the fact that the timer output voltage is less stable than its zero level. Understandably, the cyclotron operator must exercise some care when optimizing the *RF* during an experiment, since it is possible to change from one to the other of the above conditions simply by a coarse adjustment of the cyclotron *RF* voltage control. In practice, such a coarse *RF* adjustment can result in routing the data taken with the beam on, into locations previously reserved for counts accumulated with the beam off — an undesirable condition wherein one sees his data gradually sink into a sea of meaningless background.

An inhibit feature of the clock module may be used to delay the counting for any interval desired after the beam is turned off. This provision is useful for eliminating very hot, short-lived background contaminants, and in the event of very high beam-on counting

Figure 2-3. Front and rear views of the routing timer (clock) module, showing the various controls and outputs available on the unit.

rates, provides a period for the electronics to recover. In addition, logic signals are output from connectors on the front of the module and may be used to route the data into as many as seven beam-off spectra, plus an additional spectrum of the total beam-on data. Each routed spectrum contains only the counts for a specific time interval after the counting begins. For example, one might wish to route seven 0.1 sec intervals following a beam pulse and a preset inhibition period. The durations of all routed spectra are set simultaneously, there being no provision for routing different spectra for different lengths of time in the same beam-off period. One can, however fill the beam-off period with any number of routed spectra from only one to a total of seven. A timing staircase made up of the routing pulses is available for computer programs which require this type of input. A target position switch generates either manual or automatic signals for use with plunger-type devices where the target is moved out of the immediate beam area for counting. Some of the logic pulses available from this module are illustrated in Figure 2-4. The range of the routing pulses is 0.04 to 2.0 sec per pulse. A routing frequency range switch located on the rear of the unit must be set to designate the appropriate range (high or low). The limits on the routing range are determined by the frequency of the routing clock. If one wished to extend the range, the installation of a different multivibrator clock would be necessary.

Oscilloscope tracings of the outputs from this timer module during a typical experiment are pictured in Figures 2-5, 2-6 and 2-7. In Figure 2-5, the top trace shows the beam-on, beam-off signals generated by the master clock. (The beam-off period is in the center of the picture, i.e., the lower portion of the trace.) The bottom

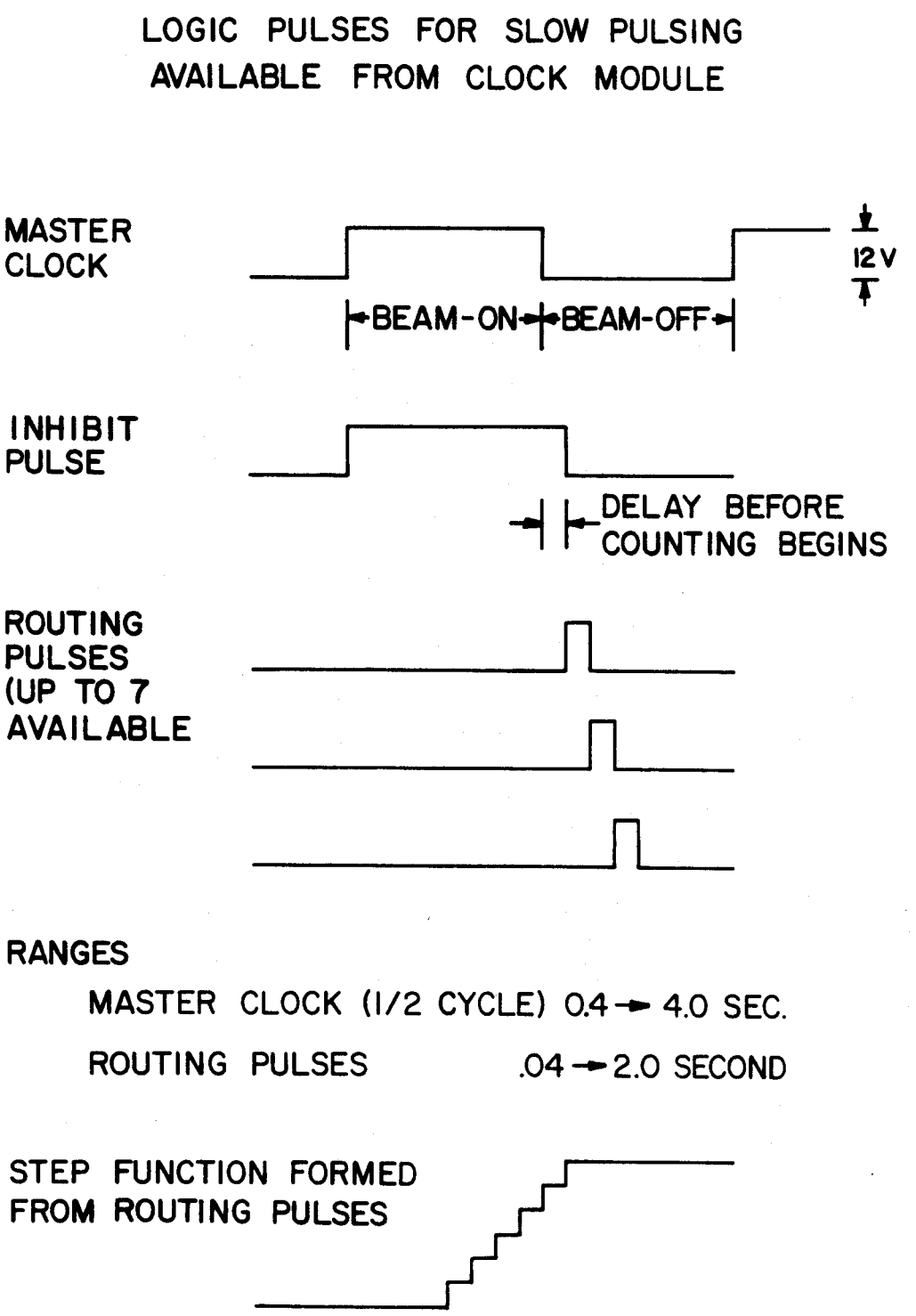

Figure 2-4. Diagram of the logic pulses available from the routing timer module.

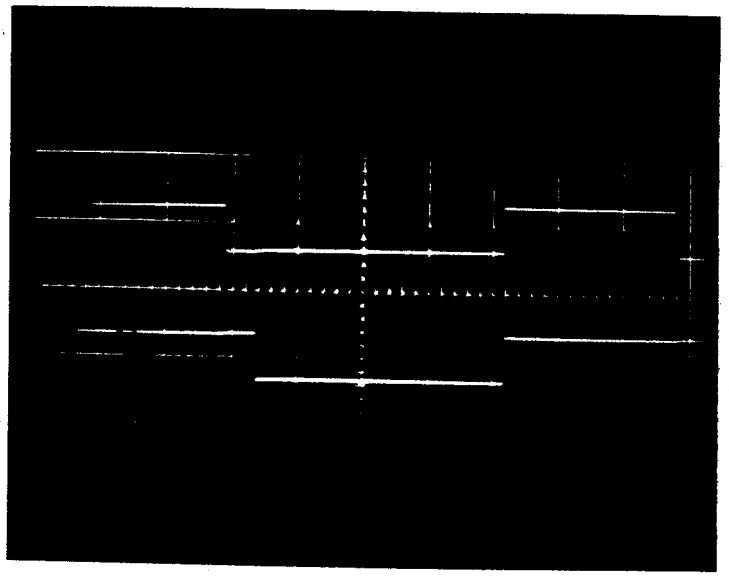

Figure 2-5. Oscilloscope tracings of the outputs from the routing timer module, illustrating the beam-on, beam-off signals of the master clock (top) and the inhibition period before routing begins (bottom).

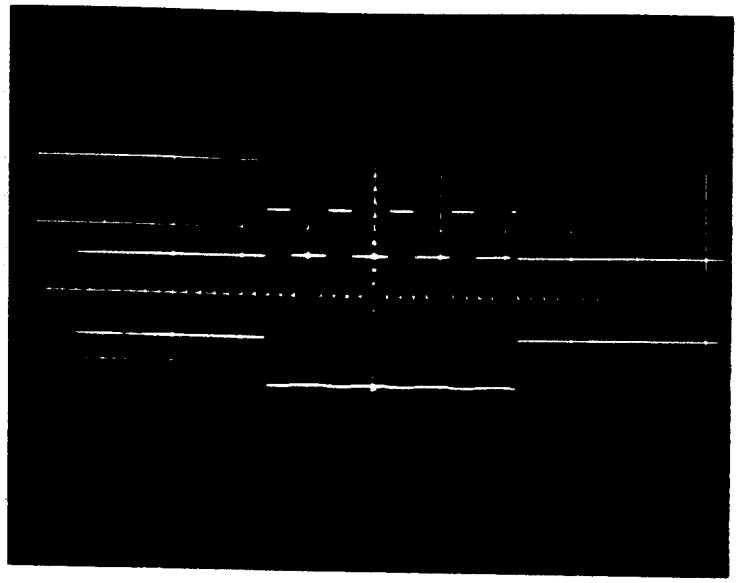

Figure 2-6. Oscilloscope tracings illustrating the routing signals (top), generated within the beam-off period (bottom).

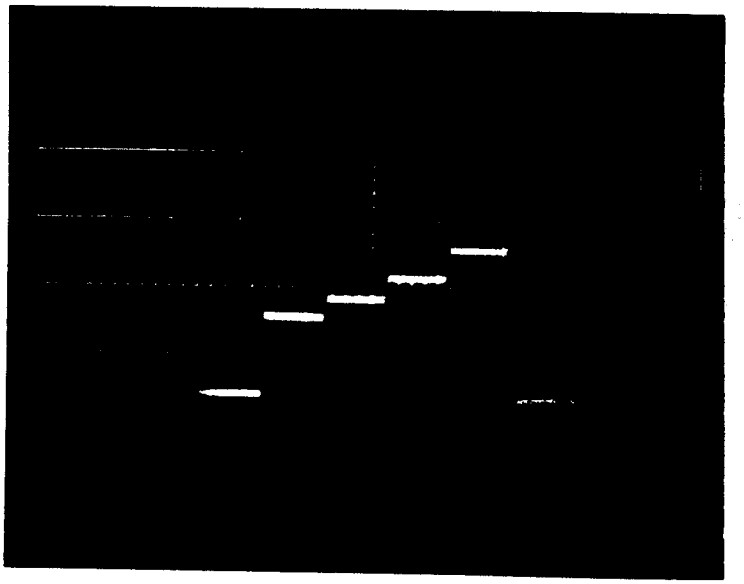

Figure 2-7. Staircase generated by the routing pulses.

trace shows the inhibition period within the beam-off time before routing begins. This time is shown by the difference in drop off between the top and bottom traces — in this case ≈0.05 sec. (horizontal scale approximately 1 cm = 0.1 sec). In Figure 2-6 the bottom trace is the same as in the bottom pulse of Figure 2-5, i.e., it is the beam-off time after the inhibition period. This part of the cycle represents the time available for counting, ≈0.38 sec in this example. The top trace in Figure 2-6 shows the routing pulses that were chosen to fill the counting interval. Note that the first routing interval begins when the inhibition period is over and lasts for ≈0.09 sec before the next routing pulse appears. In most experiments, four of these routing periods were used, plus a fifth which was just allowed to start within the beam-off interval. This fifth pulse was started to assure that no beam-on spillover into the fourth routed spectrum could occur. Figure 2-7 shows the staircase generated by the routing pulses for use as required in some computer programs.

The XDS Σ-7 computer and the data acquisition program HYDRA were used with the above clock module. This program, written by Richard Au of the MSU Cyclotron Laboratory, is a time-shared task which can handle four 13-bit ADC's independently with an eight-way fanout for each. For a typical experiment only one ADC is used, with five-4096 channel spectra being routed — one for beam-on data and four for the beam-off data. As many as three ADC's, each with a five-way fanout, have been used with the clock module routing outputs. (Since the routing box inputs for our ADC's cannot be connected internally, this requires teeing all the inputs together — see Figure 2-8.) Each ADC is controlled independently by the program. During an experiment, the contents of any ADC, or portion thereof, can be analyzed, printed, plotted or punched. The processing time per count

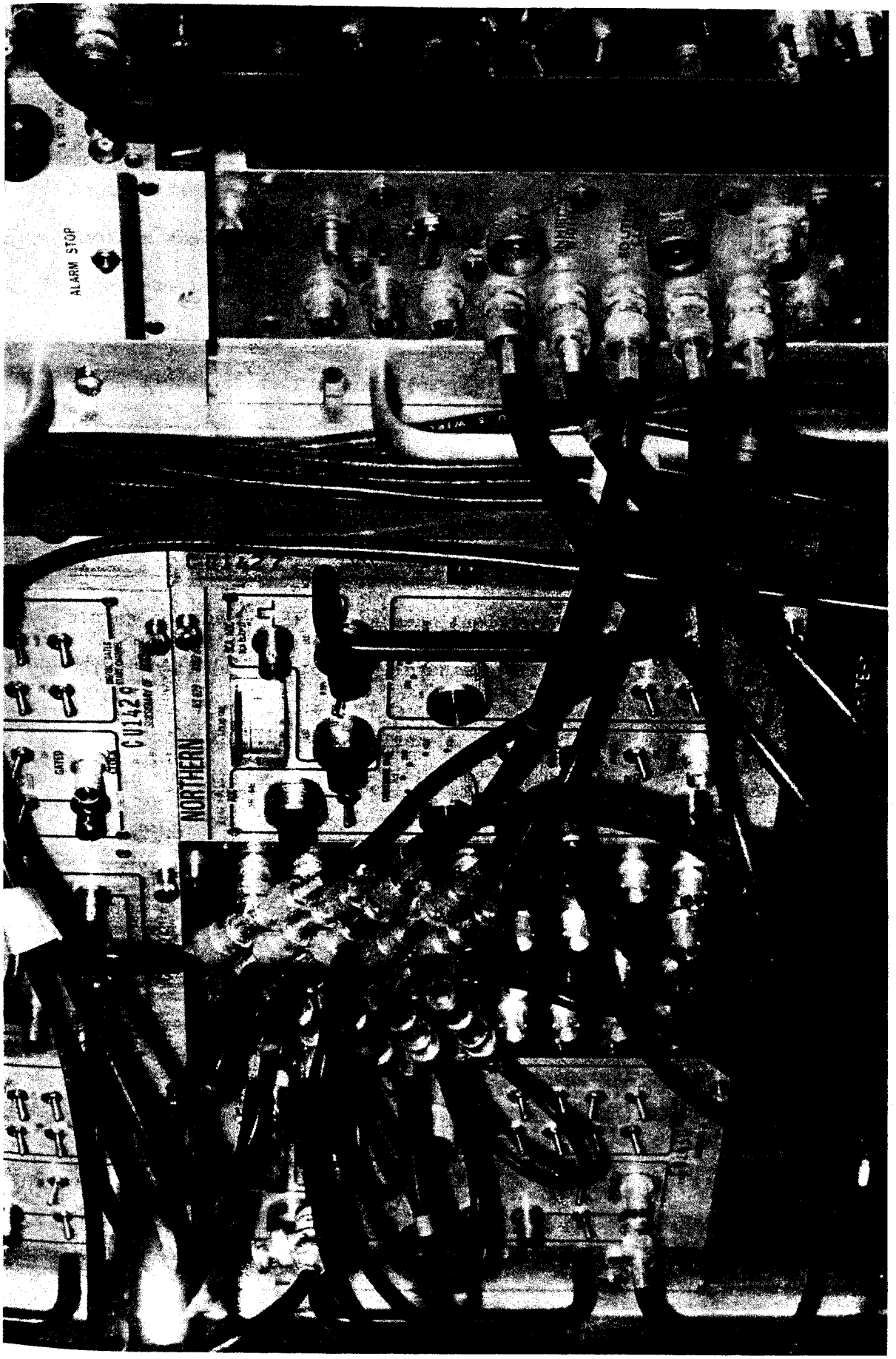

Figure 2-8. Wiring setup for using the routing timer module with three ADC's each having a five-way fanout.

for this system is the ADC conversion time plus 8 μsec, or 30 μsec, whichever is longer. The ADC's employed were Northern Scientific 629's, which have a digitizing rate of 50 MHz. Under HYDRA each channel of data is stored in a half-word of the Σ-7, so that overflow occurs at 64,000 counts -- the maximum number that can be contained in a half-word. (Since this number is sometimes insufficient, a full-word option soon may be added to the program.)

The combination of the clock module and HYDRA has been found to be a very effective means for performing pulsed-beam experiments. This system has the advantage of simplicity and reliability. For many experiments it is ideal, for others, less so. The principal disadvantages of the routing clock module are: (1) the time limits of both the master and routing clocks may be too narrow for the half-life one wishes to study, (2) the beam-on and beam-off times are not independently adjustable, (3) the routing intervals are all of the same duration.

2.2.1B The Beam Pulser

When the pulsing periods available from the clock module are not suitable for a particular experiment or when unequal counting intervals are desired, a second method is available. This method makes use of another beam pulser, which modulates the *RF* as described above, but which can provide a wider range of pulse times -- with adjustable beam-on times from 0.01 to 24.0 sec and beam-off times from 0.01 to 100 sec. These on and off times are independently adjustable for this pulser. (The pulser and its controls are shown in Figure 2-9.) Since this device does not provide routing outputs or do internal timing other than pulsing the beam, the following method is used for obtaining the desired time intervals for counting.

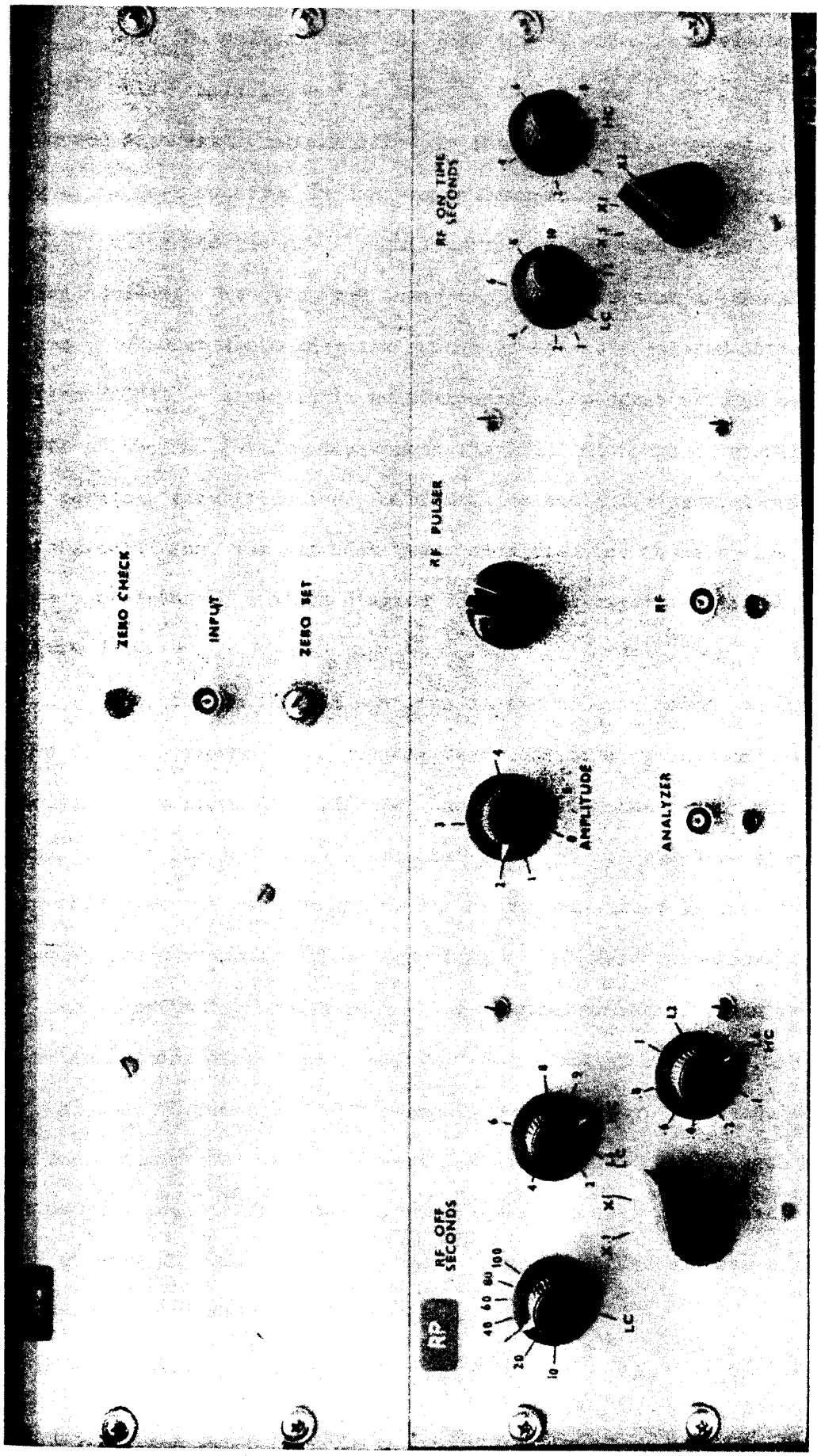

Figure 2-9. Front view of the beam pulser, showing various controls and outlets.

When the pulser turns the beam on, it simultaneously outputs a logic pulse that is used to reset a timing ramp -- usually created by using an operational amplifier to integrate a +12-V signal. Two ADC's are then operated in the synchronous mode, with one receiving the Ge(Li) pulses and the other receiving the timing ramp as gated by the Ge(Li) pulses. The data from these two ADC's are sent to the XDS Sigma 7 computer where they are processed by a time-shared software called TOOTSIE — a versatile multidimensional program written by D. L. Bayer of the MSU Physics Department (Bay71). Although originally written for particle identification, TOOTSIE is suitable for general multiparameter data acquisition, and has been used unmodified for these energy vs time experiments. A block diagram for such an experiment is shown in Figure 2-10.

The program TOOTSIE operates in two modes — *Setup* and *Run*. When in the *Setup* mode the program functions as a two-dimensional analyzer of maximum size 128×128 channels, using the seven most significant bits of the ADC's. A horizontal slice of the two-dimensional array (in this case the two dimensions are energy and time) is then chosen for display and appropriate bands are drawn — each band corresponding to a time spectrum in the *Run* mode. The maximum number of bands is a function of the size of the spectra. For example, only five bands are allowed if one needs 4096 channels per spectrum. After selection of the appropriate number and width of bands (the width of each band is proportional to the time interval viewed by that particular spectrum), the program is switched to *Run* mode. Each band then becomes a normal, one-dimensional spectrum of the designated size.

A display generated by TOOTSIE while in the *Setup* mode is

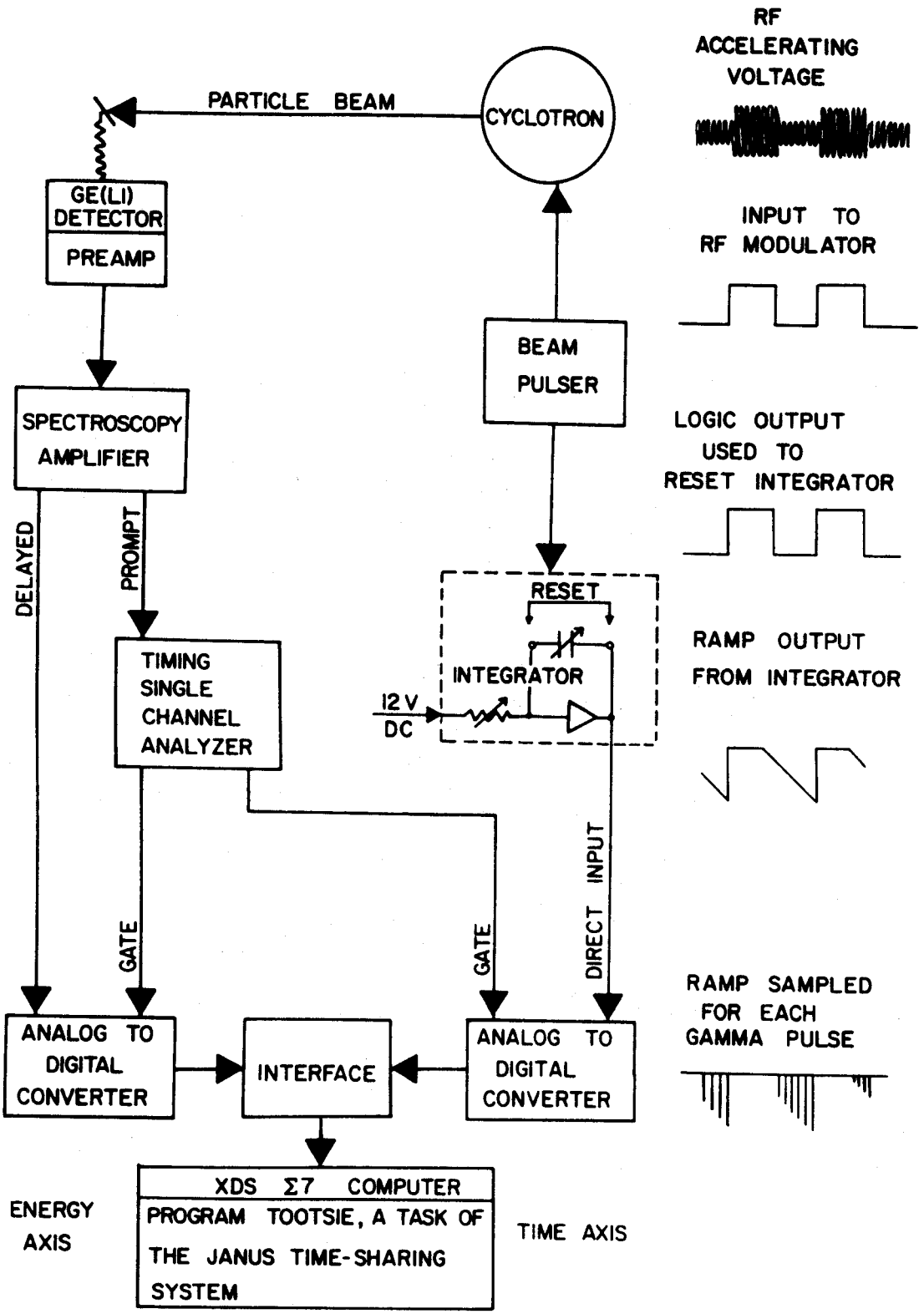

Figure 2-10. Block diagram of electronics used for energy *vs* time experiments under TOOTSIE.

shown in Figure 2-11. This display represents a horizontal slice parallel to the energy-time plane, showing all the locations containing counts between two specified limits. The vertical axis is the time axis and the horizontal axis is the energy axis. Arrows and numbers showing the channel numbers as well as the horizontal slice limits can be displayed but were suppressed in this picture. The data shown are from a ^{43m}Ti search, using the microstructure of the beam to set half-life limits. The display represents γ rays from one complete beam burst, the beam-off period, and another beam burst. The horizontal lines represent the lower and upper limits of the five bands. The same line that forms the upper limit of one band may be defined as the lower limit of the next band. These bands can be of any desired size (i.e., time). If desired, the limits need not be straight lines, but can be curves of any order polynomial up to 10.

Figure 2-12 shows a three-dimensional display of the ^{43m}Ti data. This is a 64×64 section of the two-dimensional display, shown as an approximate isometric display. Figure 2-11 is a horizontal slice of such a contour.

A scope display of TOOTSIE in the *Run* mode is shown in Figure 2-13. The top spectrum is the first band (i.e. the beam-on spectrum), and the bottom spectrum is the fifth band (i.e. the fourth beam-off time interval) from a ^{43m}Ti experiment. The arrows and numbers at each end of a spectrum indicate the limits of the expanded region. The intermediate arrow and number show the marker, which can be moved back and forth for further expansion or channel number determination. In the upper left corner of each spectrum, the number of counts in the highest channel of the spectrum is shown. The number of the band

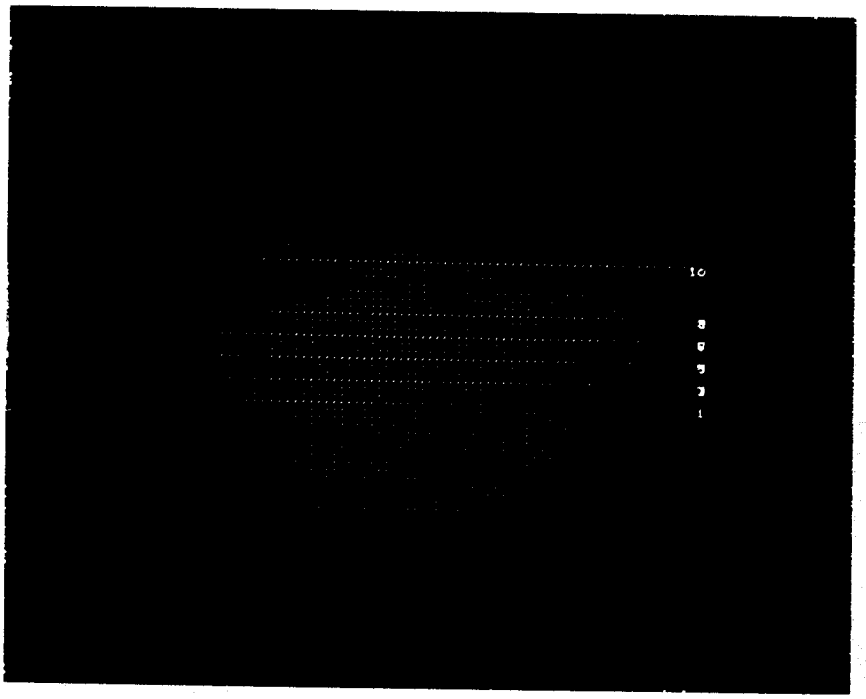

Figure 2-11. Two-dimensional oscilloscope display produced by TOOTSIE in the *Setup* mode.

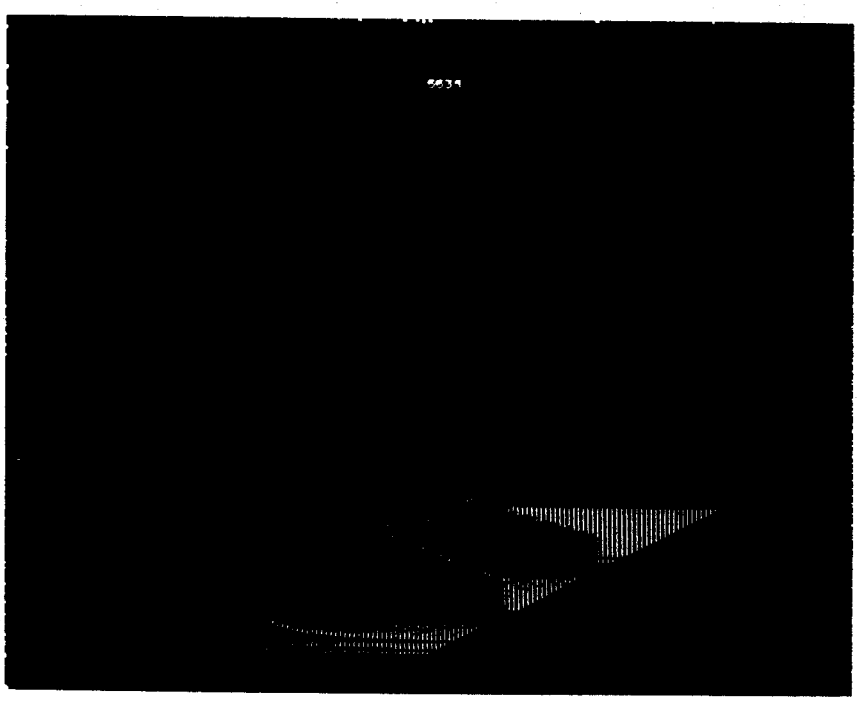

Figure 2-12. Three-dimensional display available from TOOTSIE in the *Setup* mode.

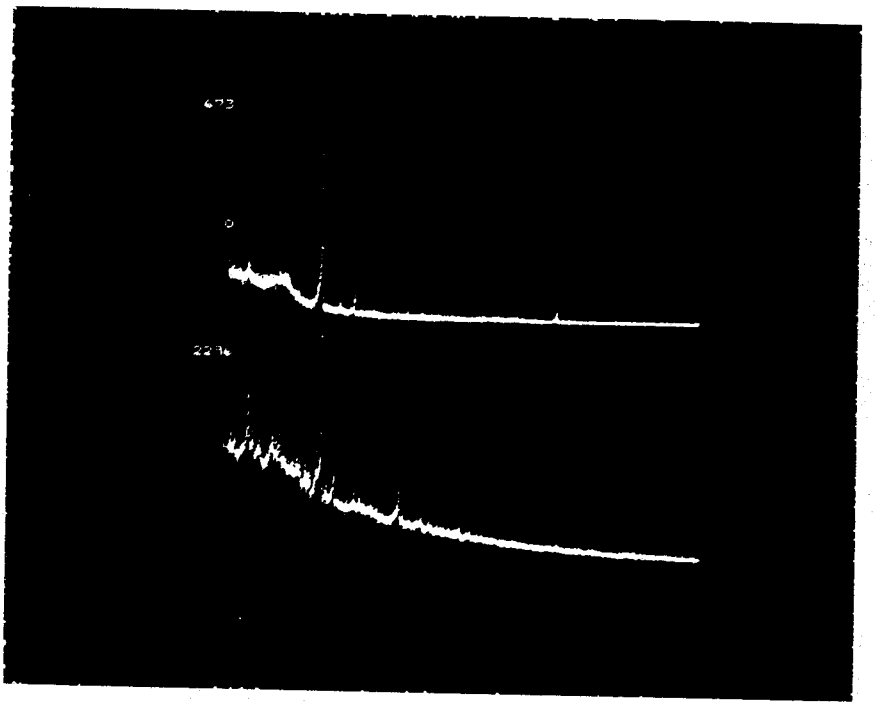

Figure 2-13. Oscilloscope display produced by TOOTSIE in the *Run* mode.

being displayed is shown below this maximum-count channel number. (The bands are numbered from 0 to n-1.) Any two spectra from the selected bands may be displayed simultaneously. The program and displays are controlled by sense switches together with a teletype.

The use of the slow beam pulser combined with program TOOTSIE has provided an extremely versatile system for pulsed-beam studies of short-lived species. Half-lives from a few milliseconds to tens of seconds can be examined without difficulty. The experimenter is free to choose any time intervals he desires for optimum half-life discrimination. This method provides for successive spectra taken for independently selected time intervals out of a total period limited only by the pulser time ranges and the duration of the timing ramp. (Use of the operational amplifier for integration gives a ramp time range from about 10^{-4} sec to 10^{4} sec. However, since linearity of the ramp is quite essential, long time periods should be avoided.)

This method has all the advantages of that using the routing timer module, with the additional features of individually adjustable counting periods for the "routed" spectra; individually adjustable beam-on, beam-off times; and a larger range of beam on-off times. The only disadvantages of the TOOTSIE approach are that it requires two ADC's and is initially more complex to set up and calibrate.

2.2.2 Deflection Plate Method

An alternate method to the *RF* modulation type of pulsing is that of using the pulser output to drive electrostatic deflection plates located so as to be able to deflect the cyclotron beam in its first turn. Thus, shortly after leaving the ion source, the beam is periodically diverted from the path

traversing a set of slits near the center of the machine. This technique is very adaptable and can be used for pulsing over wide range of times from nanoseconds to seconds. "Fast" pulsing (in the nanosecond region) is available by using these plates to eliminate, for example, nine of every ten bunches from the *RF* microstructure of the beam. Likewise, both beam pulsers discussed in Section 2.2.1 can be used to power the same plates for slow pulsing. Since the plates physically intercept the beam when it is pulsed, they must be located near the center of the machine before the particles are accelerated.

Although this method is potentially a very useful technique for beam pulsing, it has not been utilized fully. Operation of the *RF* modulation pulsing has been so successful that other means of achieving the same goal have not been tried. Recent attempts to use the plates for microsecond range pulsing have been thwarted by thermally-induced geometry changes within the center region of the cyclotron, and consequent misalignment of the plates. Redesign of the center region in order to prevent this difficulty is currently underway. The method itself is a proven technique, having been used routinely in the past for fast pulsing.

2.2.3 Utilization of the Microscopic Beam Structure

By virtue of having a cyclotron, one always possesses a "pulsed" beam — albeit rather fast. At a typical proton energy of 36.0 MeV, one pulse occurs every 56.68 nsec with a duration of about 0.5 nsec, depending on the phase width. This pulse rate is very convenient for measuring the life-times of certain states or setting limits on very short-lived species. A block diagram of a typical electronics setup for utilization of this beam

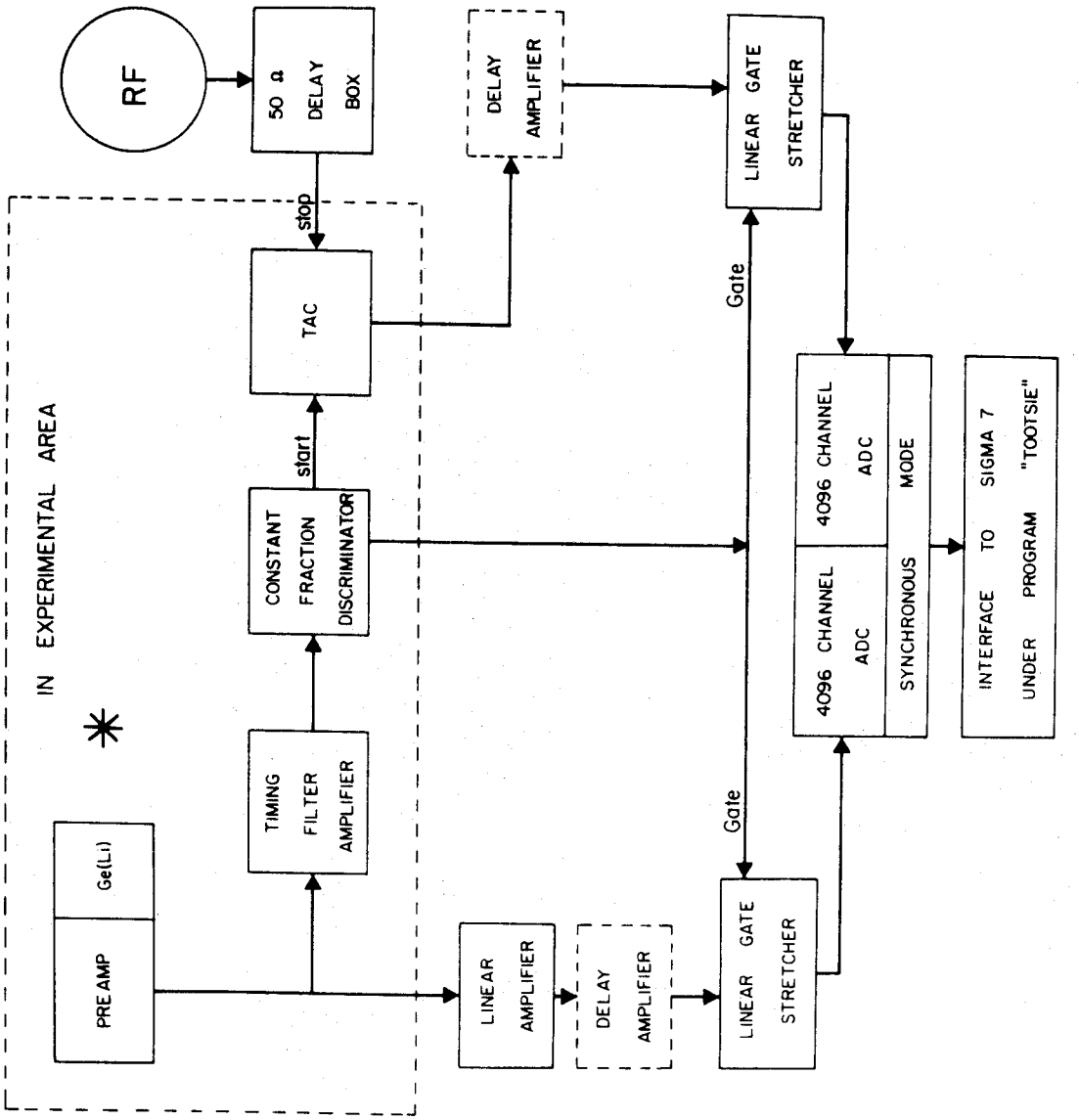

Figure 2-14. Block diagram of the electronics setup for utilization of the cyclotron beam microstructure for pulsing.

microstructure is shown in Figure 2-14. The program TOOTSIE is used in the same manner as described in Section 2.2.1B, with the setting of time bands and the resulting spectra for intervals chosen. Calibration of the time is achieved by introducing a delay into the *RF* side and observing the shift in the two-dimensional display under the *Setup* mode. The bands drawn in Figure 2-11 are from an experiment of this type. The small bands for the "routed" spectra represent a period of about 4.2 nsec each. A set of time spectra from this experiment are shown in Figure 8-2 . Since beam pulsing in the microsecond range has not been available, employment of the microscopic beam structure together with slow (milliseconds) pulsing has allowed the "bracketing" of half-lives in this time range.

2.3 Activation Chambers for On-Line γ-Ray Spectroscopy

2.3.1 The Goniometer Chamber

When this project was begun there had been little previous effort toward performing on-line γ-ray spectroscopy at our facility. As a result, no specific equipment was available for this type of experiment. However, an elaborate goniometer had been constructed for charged particle scattering experiments (Tho68, Tho69),and its adaptation to on-line, γ-ray work was a natural first step. A portion of the goniometer in one of its many experimental configurations is shown in Figure 2-15. The 8-inch diameter chamber shown in the picture was used almost exclusively, in preference to a larger 16-inch one. The top of the chamber contains a 4-inch Marman flange, which is the type of standard coupling used in the beam line. The square box located on top of the chamber is part of the vacuum manifold, which leads to a diffusion pump on the left. The top of this box is also fitted with a 4-inch Marman flange,which is used with a target transfer system to allow installation of targets under vacuum. The beam enters the chamber from the beampipe on the left. The beam input port consists of a coupling that fastens to the standard beam pipe and tapers down to slip into a 1-inch diameter hole in the target chamber through a double O-ring seal. To aid in alignment of the beam into the chamber, there is an insulated, 9/16 inch inside diameter, annular, tantalum slit located just before the restricted section. An exit port similar to this entrance port is provided for use with the 16-inch chamber. However, the smaller 8-inch chamber does not have a primary beam exit port, but instead has a slot in its side extending from -15° to +177°.

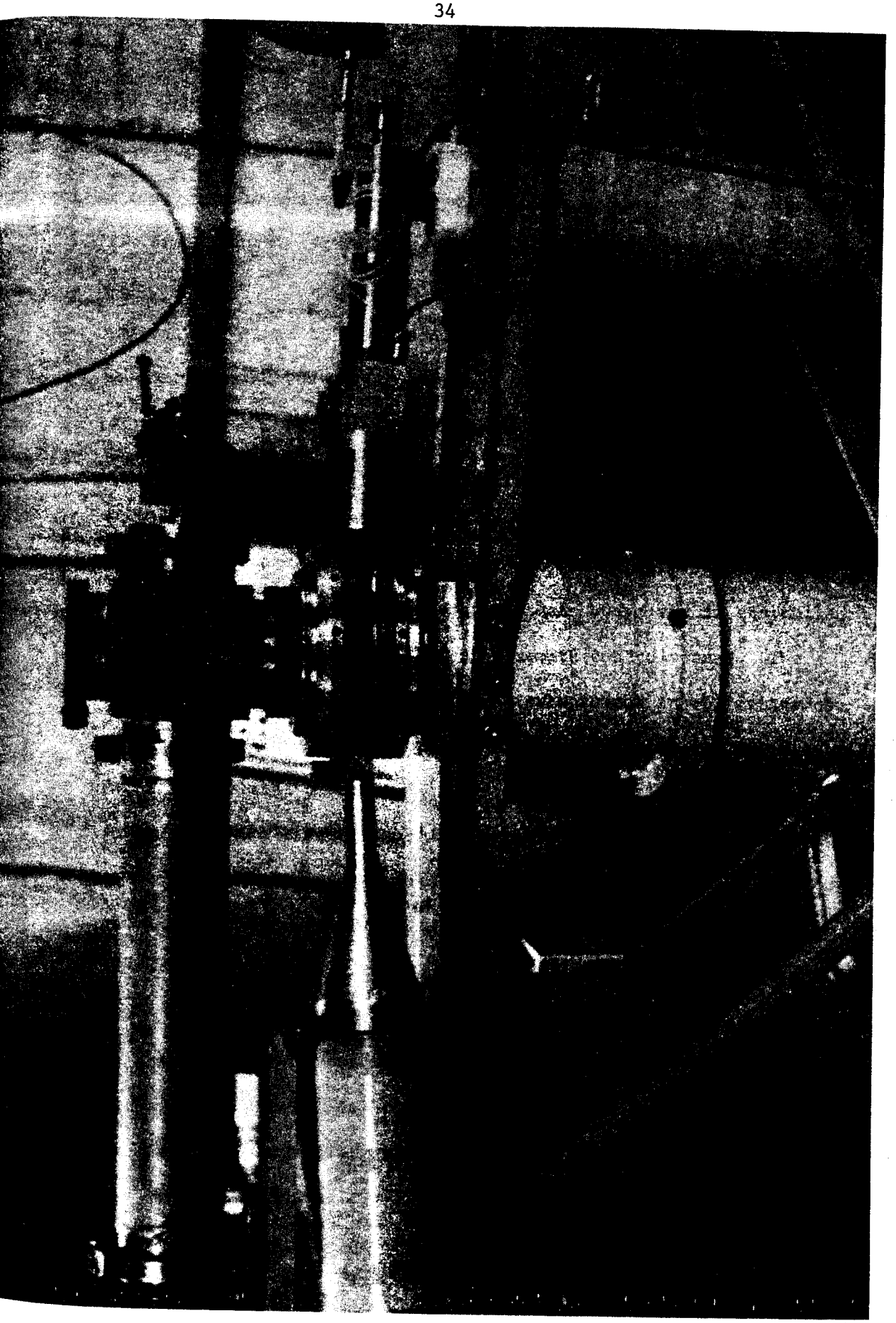

Figure 2-15. The goniometer facility, showing the 8-inch activation chamber and detector mounting.

An O-ring groove is located 1/16 inch outside of this slot on the outside surface of the chamber. This slot port can be used in two different configurations. One configuration utilizes a foil window for the beam to pass through, while the other employs a sliding vacuum seal for precise scattering work. For on-line γ-ray experiments the foil window was used, as shown in Figure 2-15. This window consisted of a 1/2 mil Kapton foil glued to an aluminum frame, which was bolted to the target chamber through the O-ring seal.

The goniometer facility provides a number of other conveniences that are useful for γ-ray spectroscopy experiments. A large arm extends to both sides of the unit and provides a mounting for one or more detector packages (cryostat, dewar, preamp, etc.). This arm rotates about the vertical axis of the main body and is controlled either by the local control box or a remote control panel. The targets are held in a vertical ladder arrangement in the center of the chamber. Three 1×2-in. target frames may be mounted in this holder. Vertical movement of the ladder for target selection, as well as rotation of the target plane with respect to the beam, can be controlled remotely or locally. A small manually positioned arm is located under the chamber and is quite convenient for mounting counters, accessories, and the like.

The remote control panel, located in the data room, is shown in Figure 2-16. The various controls are in three vertical groups. The controls and digital counter for the target angle are located on the right hand side. In the center are the target height controls and counter. Automatic positioning of any one of the three targets is achieved merely by pushing the corresponding numbered buttons.

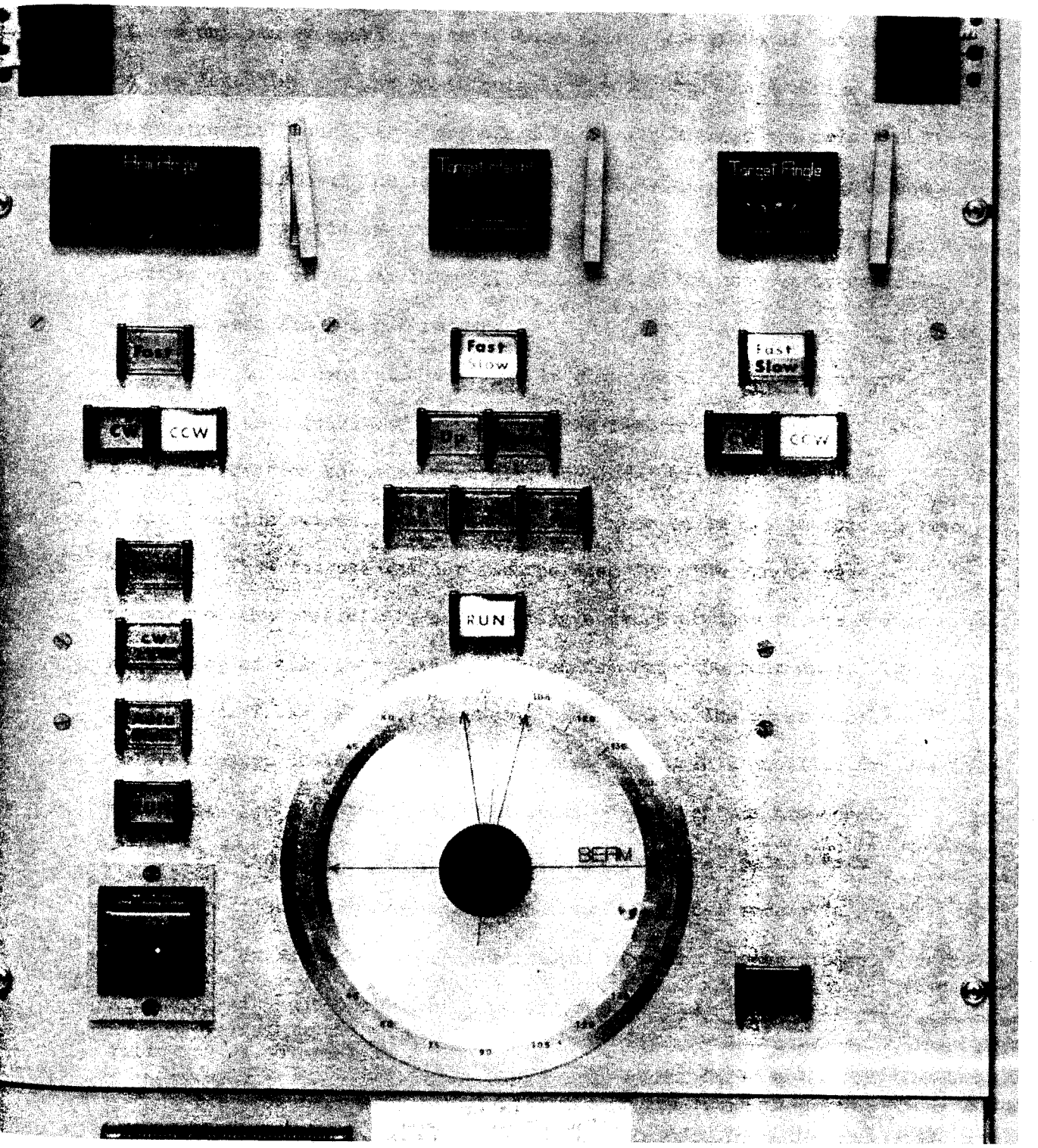

Figure 2-16. Remote control panel for the goniometer.

A manual mode allows further vertical positioning of a target in case of non-uniform or poorly centered materials. The group of controls on the left side are for positioning the main arm. In addition, this remote control panel has a graphic display which shows the relative angular positions of the incident beam, the main arm, the target, and the manually positioned arm. This display is located in the lower portion of the panel and is coupled to the digital readout system for both the main arm and the target.

The local control box, shown in Figure 2-17, contains essentially the same functions as found on the remote control panel. However, in addition to these controls, the local box has a main arm limit override switch, permitting the detector to be driven through zero degrees. This feature was not incorporated into the remote panel because of the possibility of crunching a detector into the beam-pipe when using an exit port with pipe extending into the beam dump. The local control box is portable, being connected to the power supply and relays through 30 feet of multiconductor cable. This mobility feature is very handy for alignment and positioning of the various components.

The goniometer has been used in many on-line, pulsed-beam γ-ray experiments with reasonable success. The most successful configuration has been the 8-inch chamber with the Kapton window. Although this system provides several conveniences, it suffers the following disadvantages:

(1) The narrow (1/2-inch) section of the front (and rear) collimators as well as the Kapton foil and surrounding air, produce large amounts of unwanted γ-ray activities when struck by the primary and scattered beam. This

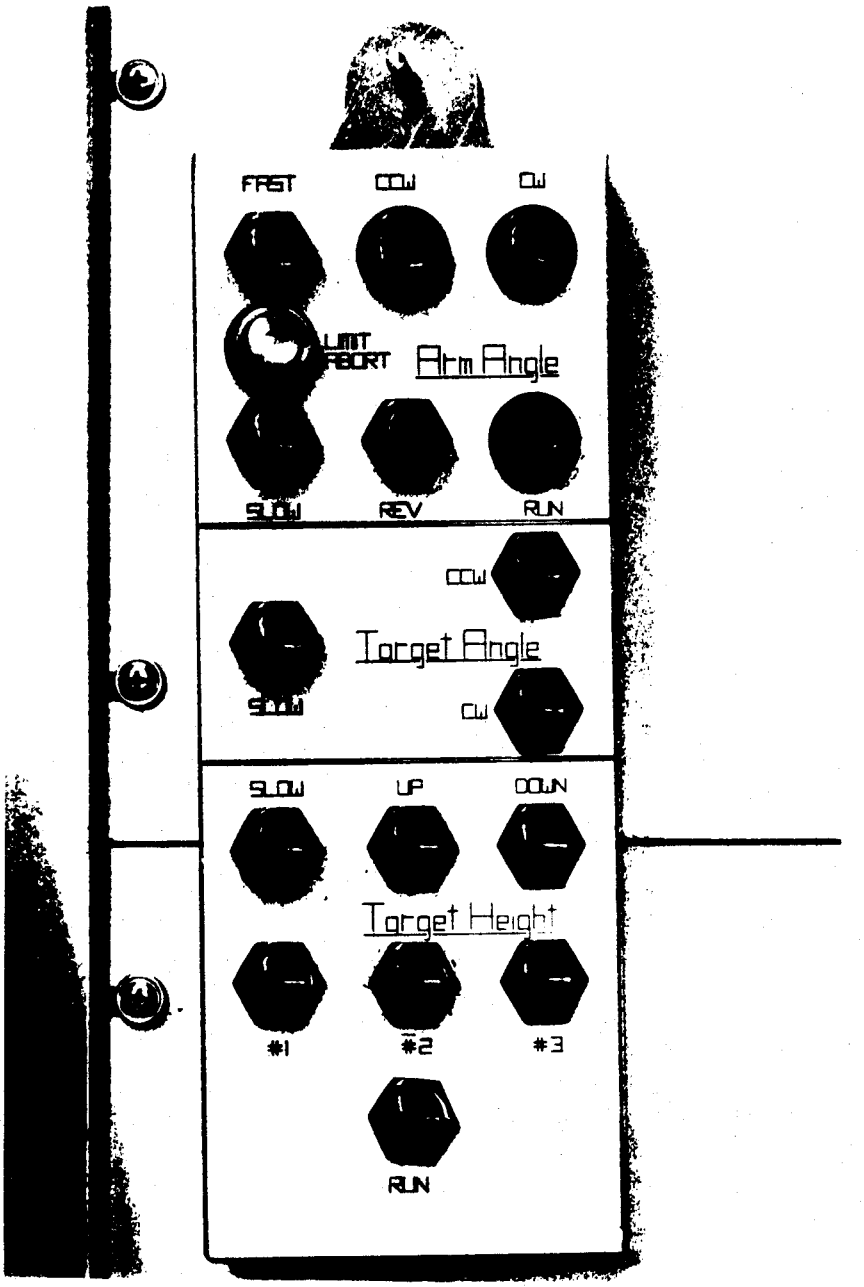

Figure 2-17. Local control box for the goniometer.

problem can be severe to the point of sometimes masking the target activity.

(2) The distance from the target to the detector is quite large (>4 inches). As a result the relatively inefficient Ge(Li) detector subtends only a small solid angle with respect to the target. For γ-ray singles experiments this can mean a higher unwanted-to-wanted γ-ray ratio due to beam-pipe activation. For coincidence experiments, the counting rate becomes prohibitively low.

2.3.2 The Coincidence Chamber

In order to overcome the disadvantages of the conventional goniometer chambers, a new chamber was designed for γ-ray singles and coincidence studies. This rather simple unit is shown in Figure 2-18. Although the chamber can be fitted any place in the beamline, it is used primarily in the goniometer line — where the necessary focusing magnets and beam dump already exist. The chamber is a rectangular box, 1-1/2 inches in width, 3 inches long, and 7-1/2 inches high. The sides are 1/2-inch plexiglass and are removable. Different sides of various materials, thickness, and windows can be made up to suit a particular experiment. The present setup uses 1/4-inch plexiglass sides with 1x2 1/2-inch windows covered with 1/2-mil Kapton. The beam enters and emerges from the chamber through 45° aluminum conical adaptors having a minimum inside diameter of one inch. These adapters slip into holes in the chamber through O-ring seals and attach to the beampipe with a standard 4-inch Marman flange. A brass rod with a split end and set screw holds the aluminum target frame in position. This rod passes through a sliding seal at

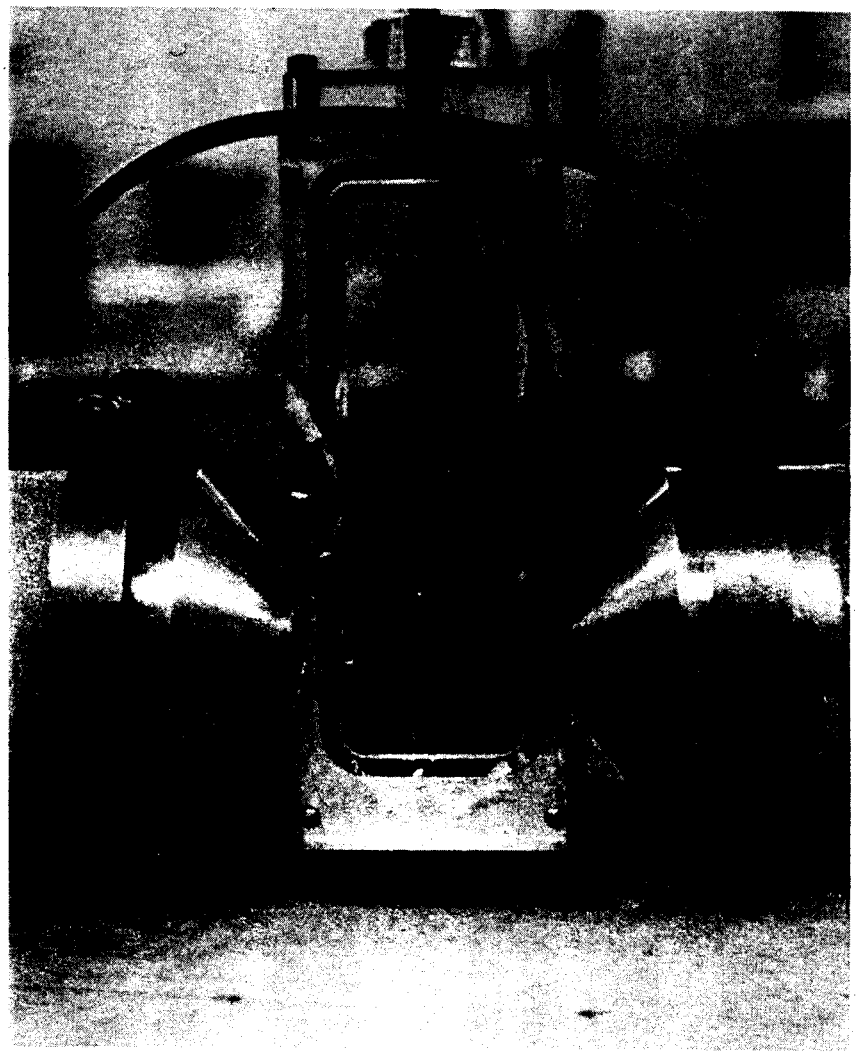

Figure 2-18. The coincidence chamber

the top of the chamber, allowing the removal of fragile targets from the direct air stream while the beam line is being pumped down or let up to atmospheric pressure. The large scattering tolerance allowed by this design has resulted in a significant decrease in the γ-ray background spectrum. In addition, the target-to-detector cryostat distance has been reduced to only one inch, with the provision for a detector on each side of the chamber for performing two-dimensional gamma-gamma coincidence experiments on line.

2.3.3 The Vacuum Transfer Chamber

The design of the coincidence chamber did not include a provision for the mounting of targets which, because of their chemical reactivity, had to be maintained in a vacuum. When the use of such targets became necessary, a suitable chamber was assembled from various components with little modification. The chamber configuration that was used is shown in Figure 2-19. The body of the chamber is part of the vacuum manifold assembly from the goniometer. This box is merely a 5-inch cube of aluminum, with two 3-1/2-inch holes milled completely through from two sides and a third such hole milled through a remaining side to within about 1/4 inch of the final side. The four holes opposite each other were each fitted with a standard 4-inch Marman flange. An O-ring groove was milled around the fifth opening and a 1/2-inch plexiglass window bolted into place. (For γ-ray experiments this plexiglass plate has been fitted with a thin Kapton window.) The box is placed in the beamline with the window on one side, as shown in Figure 2-19. A round aluminum plate with a ladder-type target holder attached is fitted to the bottom flange. The angle of the target plane with respect to the

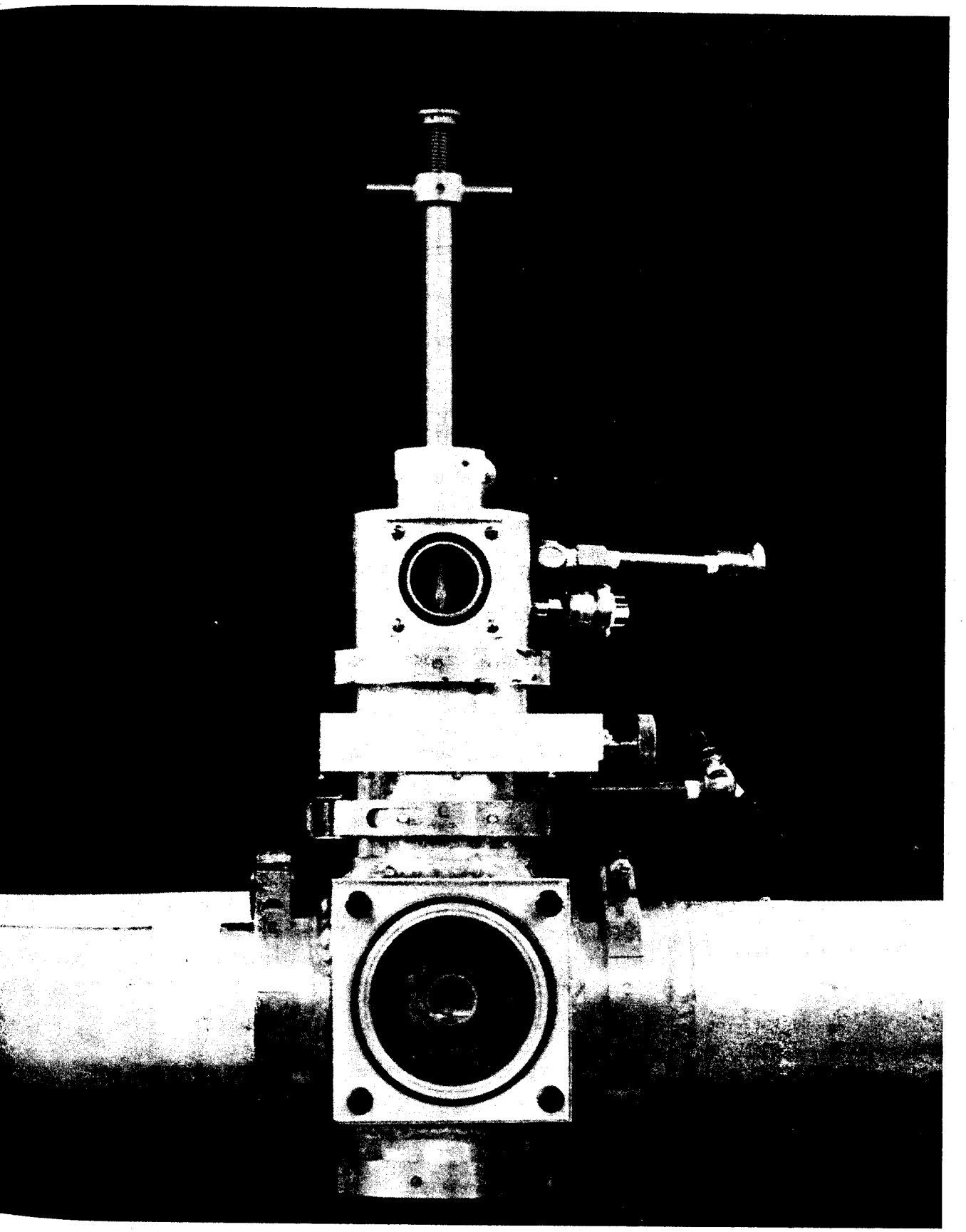

Figure 2-19. Vacuum transfer chamber, valve, and transfer lock assembly.

beam may be determined by rotation of the bottom plate before tightening its clamp. The vacuum transfer lock then attaches to the top flange.

As shown, the transfer lock consists of two parts — a valve, and a small, cylindrical vacuum chamber. The valve can be opened to an aperture of 3/4×2-1/2 inches, and will close vacuum tight. In the top and on the axis of the vacuum chamber there is a target transfer mechanism. This mechanism consists of a 3/16-inch steel rod inside of a 5/8-inch steel shaft. The larger shaft enters the top vacuum chamber through a double O-ring seal, while the smaller one enters the vacuum chamber through a double O-ring seal in the top of the larger shaft. The part which grasps the target frame is a split, conical, phosphor-bronze jaw. This fits into a conical hole in the lower end of the 5/8-inch shaft. The smaller shaft is screwed into the top of the jaw and is spring loaded to keep an upward pressure on the jaw mechanism.

Each target storage chamber is equipped with a valve like the one shown under the vacuum chamber. In order to transfer a target, one first removes the storage chamber and valve from the cryogenic pump system used for storage. The vacuum chamber is then attached to the other side of the valve and pumped down to a pressure similar to that in the storage chamber. The valve is opened, the inner shaft of the transfer mechanism is depressed to open the jaws, and the rod assembly is pushed in until the jaws are over the target frame on the storage ladder. The shaft is then released, allowing the spring to tighten the jaws on the target frame. The frame is withdrawn into the vacuum chamber, the valve is closed, and the storage chamber is removed. The storage chamber and valve unit is then fastened to the top flange of

the activation chamber. The beamline and chamber are evacuated. The valve is opened, and, while being sure that the frame is aligned properly, the target is lowered through the hole in the valve and into the target ladder. A clamp around the shaft is provided on the top of the vacuum chamber and prevents the transfer shaft from being drawn unexpectedly into the evacuated chamber. The removal of the target and return to storage is just the reverse of the above procedure.

In practice, this system has been used almost exclusively for the transfer and irradiation of ^{40}Ca and ^{48}Ca targets. Since γ-ray singles experiments were the primary objective of most of these studies, the current configuration of the chamber has proven very satisfactory.

Since the narrowest constriction in the chamber is 3-1/2 inches in diameter, activation of material other than the target has not been a problem. The rather large target-to-detector distance (3 inches) has not caused any difficulty in singles experiments. However, this dimension, together with the need for a second thin window, seriously limits the use of the chamber for γ-γ coincidence experiments.

2.3.4 Discussion and Improvements

All of the on-line activation chambers discussed above were designed or adapted to solve a particular set of problems. No one of these combines all of the desirable features into one unit, although these features are not mutually exclusive. A relatively easy and very useful improvement could be achieved by designing a standard, 4-inch flange assembly to fit on the top of the coincidence chamber. This would allow coincidence experiments to be performed on targets which are maintained under vacuum, with all the inherent advantages offered by

the coincidence chamber.

In order to take advantage of the existing features of the goniometer the construction of a completely new chamber would be necessary. Such a chamber would combine the various aspects of the above chambers with those of one which was compatible with the basic goniometer mountings, thereby retaining the remote control arm and ladder arrangement. Since the goniometer facility is of modular design, compatibility is only a matter of providing the correct size flanges. The beam entrance and exit ports should be made as large as possible (the 3-1/2-inch size on the vacuum transfer chamber seems to be quite adequate). A standard 4-inch flange on top of the chamber would insure fitting of the target lock and transfer mechanism. Shallow detector wells should be included in the sides of the chamber to allow the detectors as close to the target as possible. Interchangeable windows on the inside of these wells would allow flexibility in the thickness and type of materials used as windows. Construction of a target chamber incorporating these features would provide a versatile unit capable of handling many kinds of on-line γ-ray experiments.

2.4 Rabbit - Pneumatic Target System

The β- and γ-spectroscopic study of moderately short-lived species ($t_{1/2} \gtrsim 10$ sec) is best performed in off-line facilities where the background radiation is low and the highest-quality detectors can be used without fear of neutron damage. In order to accomplish this, the irradiated target must be transferred first to a low-background area for preparation. Early irradiations were carried out near the cyclotron, through a thin Havar window, which was part of a Faraday cup-beampipe cap assembly. Each target was carried into the vault by the experimenter and subsequently retrieved by him. For shorter-lived isotopes, this required a mad dashing over top of the lowering vault door, seizing the sample and sprinting to the preparation room. As more experiments were performed and the half-lives of interest grew even shorter, the need for a better target transfer system became quite obvious. After consideration of the various possibilities, a very successful pneumatic target system or "rabbit" was developed (Kos69).

One of the standard rabbits, i.e. the moving target holders, is shown in Figure 2-20. These units are 1-13/16 inches in diameter and 3 inches long, with teflon ends and a central frame of aluminum. A 1-1/8-inch square opening in the middle of the frame provides a place for carrying the target material and any needed absorbers. The rabbit shown in Figure 2-20 is equipped with a fast-transfer, disposable, aluminum foil target packet of the type used for irradiation of manganese powder in the ^{53m}Fe study. The interior and exterior terminals of the system are shown in Figures 2-21A and 2-21B, respectively. The interior terminal is located in the cyclotron vault, just beyond

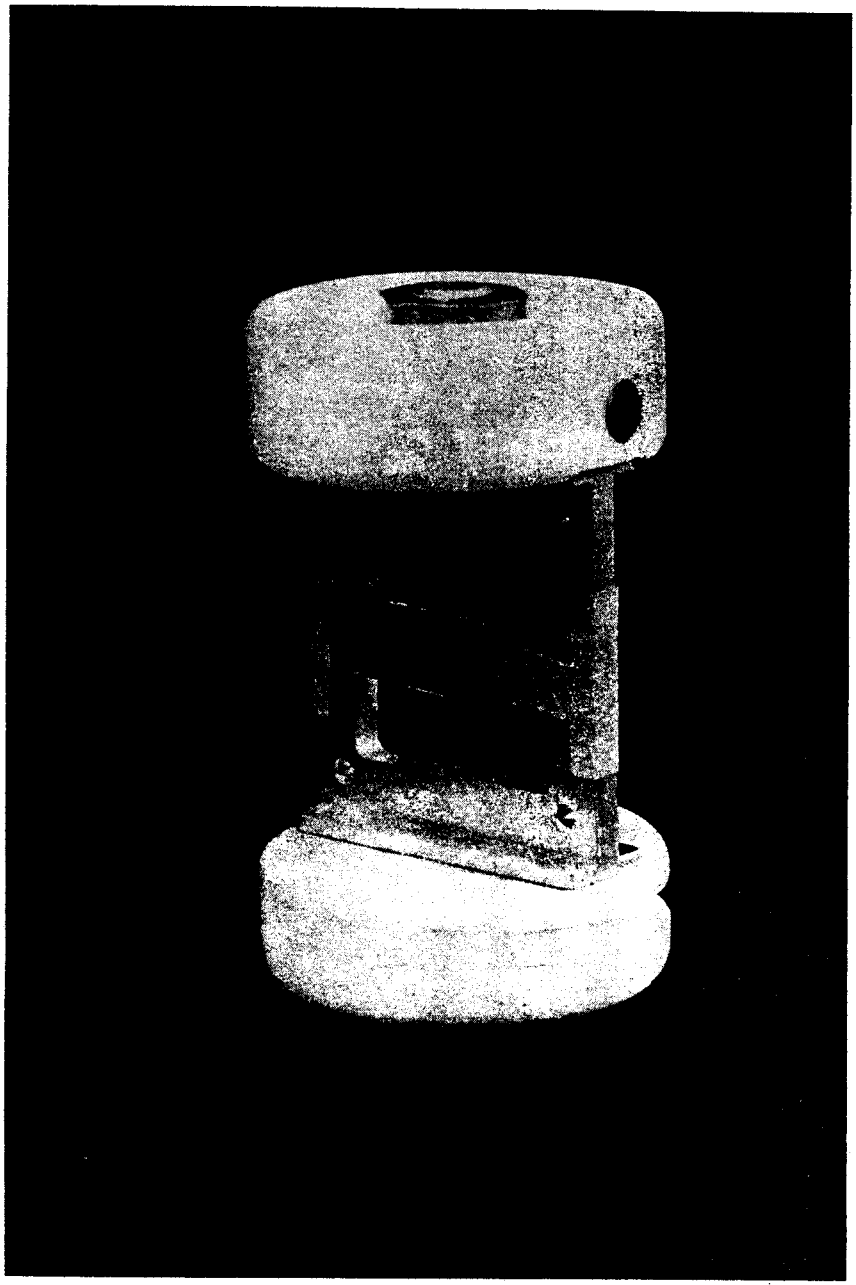

Figure 2-20. Typical "rabbit" used in the pneumatic target system, with foil target packet in place.

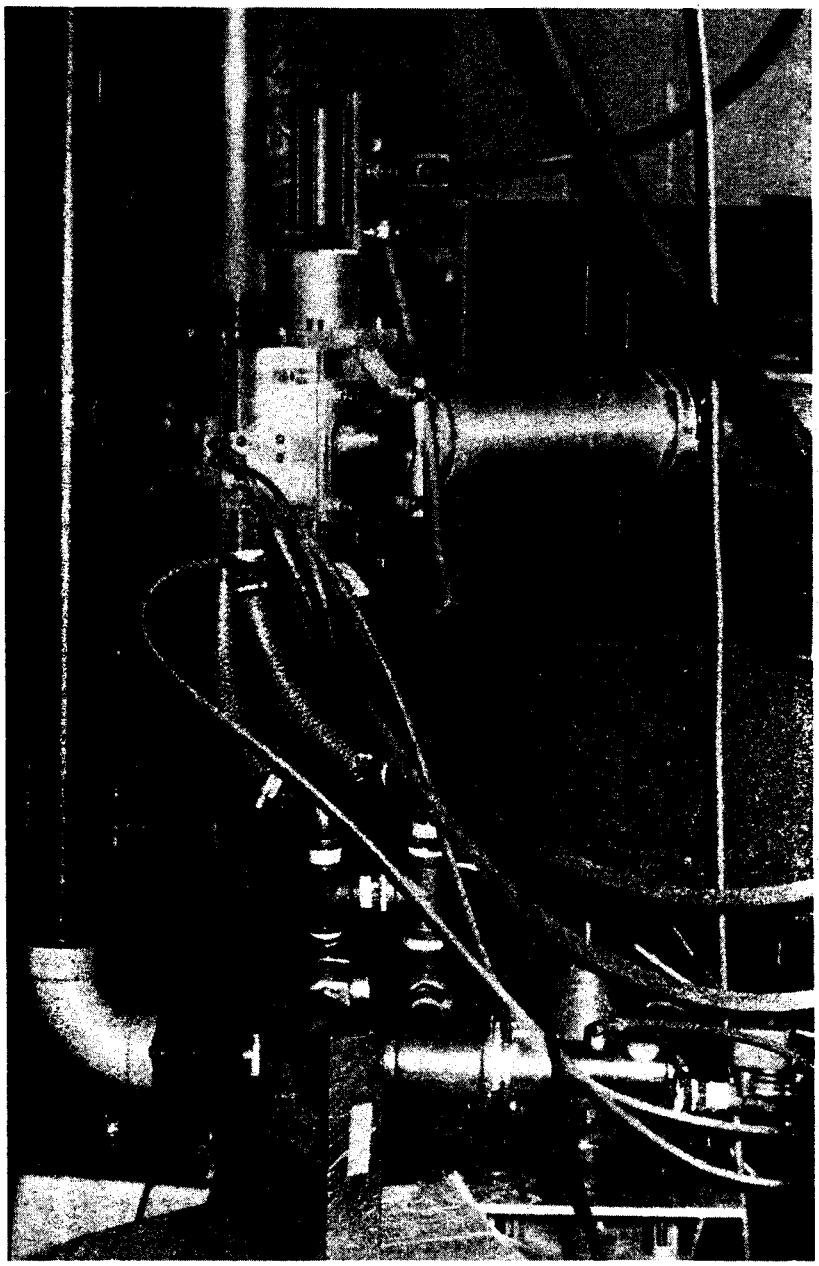

Figure 2-21A. Interior terminal of the rabbit system.

Figure 2-21B. Exterior terminal of the rabbit system.

the first large bending magnet (M3), which is used to divert the beam from the 0° line into the terminal. A plunging scintillator and viewing port as well as a water-cooled Faraday cup are provided for alignment of the beam. The exterior terminal is located in the target preparation room and is mounted on a cabinet containing the local control electronics. The rabbit is propelled between these terminals through a 2-inch clear cellulose acetate pipe (with bends made of the more easily bent polyvinyl-chloride pipe) by creating a pressure differential across the rabbit. A large commercial vacuum cleaner is used to create a partial vacuum on one side, while air pressure (≈3 psi) is applied to the other side. To prevent the rabbit from crashing into the terminals, an air cushion is used for braking. A small sensor attached to the rabbit pipe detects the passage of the orientation magnet in the rabbit and turns on the braking air. The transit time for the target is about 4-8 sec, although this can be shortened to 2-4 sec by increasing the working pressures. The length of the rabbit tubing between terminals is now ≈150 ft.

Upon reaching the interior terminal, the rabbit can be oriented with respect to the cyclotron beam. This orientation is achieved by first rotating the rabbit with a jet of air directed on a set of fins near its base. The rotation is stopped in the correct orientation by the attraction between a small permanent magnet in the top portion of the rabbit (Figure 2-20) and an electromagnet in the terminal. The target is air cooled directly and water cooled by conduction through the aluminum frame.

A block diagram of the rabbit system is shown in Figure 2-22. Several new features such as a remote control panel for the cyclotron console and an automatic retrieval and ADC control device are being added to the system.

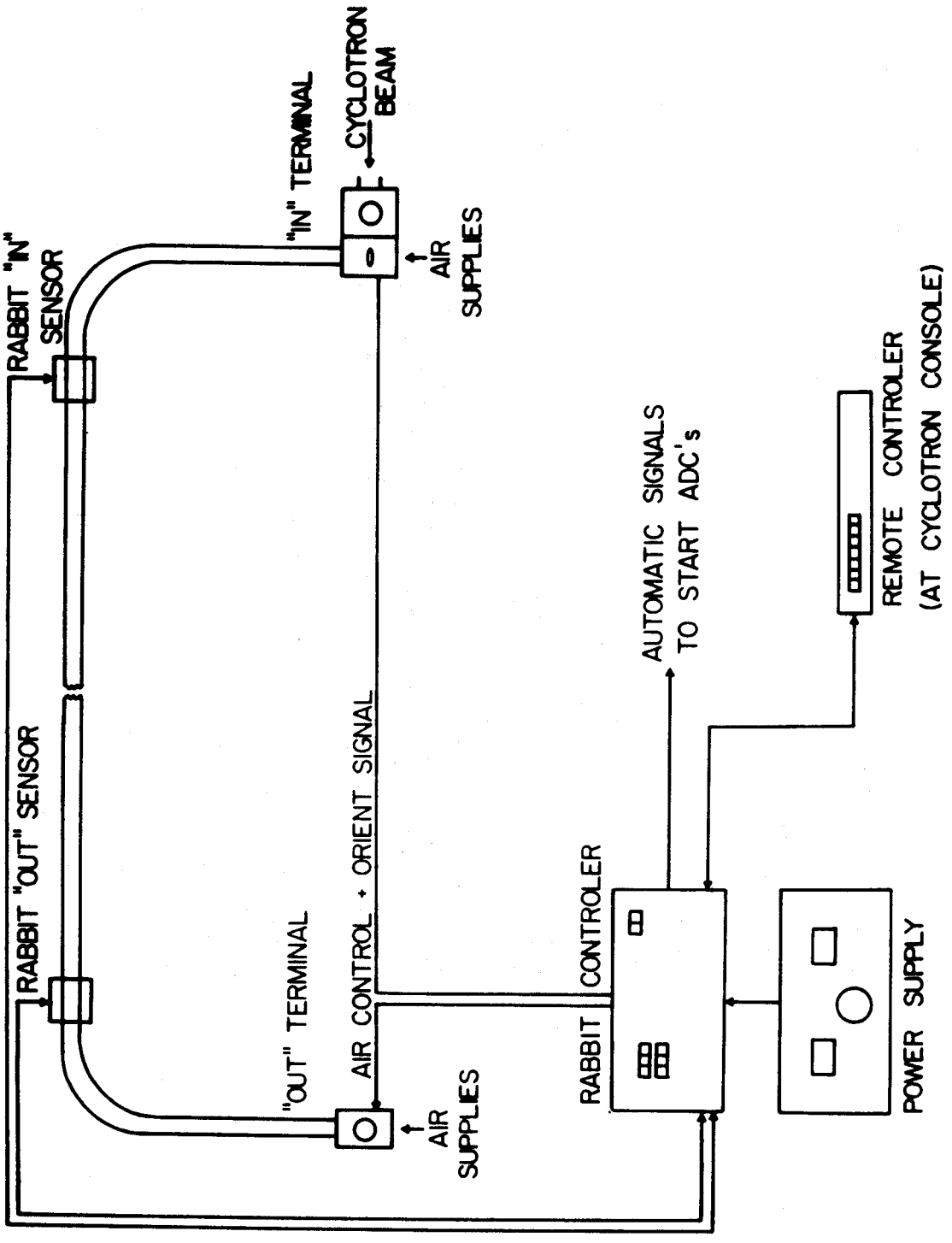

Figure 2-22. Block diagram of the rabbit system.

The rabbit has proven quite successful for irradiation of targets for off-line study. Because of its convenience, long-lived species as well as short-lived ones are routinely prepared using it. The system has been invaluable for experiments like the ^{53m}Fe *E*6 search, in which over 300 individual targets were irradiated and counted within a 24-h period. Without the rabbit such experiments would not be feasible.

2.5 Helium Thermalizer and Jet Transport

When half-lives in the 10.0 to 0.010-sec. time range are to be investigated, the simplest method is to utilize a helium thermalizer jet transport system. The system at the MSU Cyclotron Laboratory was constructed by K. Kosanke (Kos70) and patterned after that developed by R. D. MacFarlane (Mac63). The thermalizer box configuration as used in the experiments reported here is shown in Figure 2-23. The beam enters the box from the top through a thin Havar window. The target (usually a foil) is mounted in the water-cooled block directly behind the beam entrance. Recoils from the target are thermalized in helium (the box is maintained under 1-3 atmospheres of helium) and swept into the chromed-aluminum collecting hemisphere. This hemisphere is water-cooled and also serves as a Faraday Cup. The recoils, together with the helium, flow through a small hole in the rear of the hemisphere into a polyethylene capillary (ID ≈0.034 in.) where they are transported at sonic velocities over a distance of ≈50 ft, to a counting chamber on the roof of the cyclotron vault. This chamber is evacuated to $\approx 10^{-2}$ torr by means of a vacuum pump-Rootes blower system. A fixed collector consisting of a thin layer of vacuum grease on masking tape is used for most experiments. This collector is fixed to a thin plexiglass window directly opposite a Ge(Li) γ-ray detector. The tip of the capillary is placed perpendicular to the plane of the collector and about 1 cm from the surface. As the helium-recoil mixture flows from the capillary, the helium diverges rapidly, allowing the heavy recoils to continue more or less straight onto the collecting surface. The decay of the recoils is then detected in a relatively low-background area.

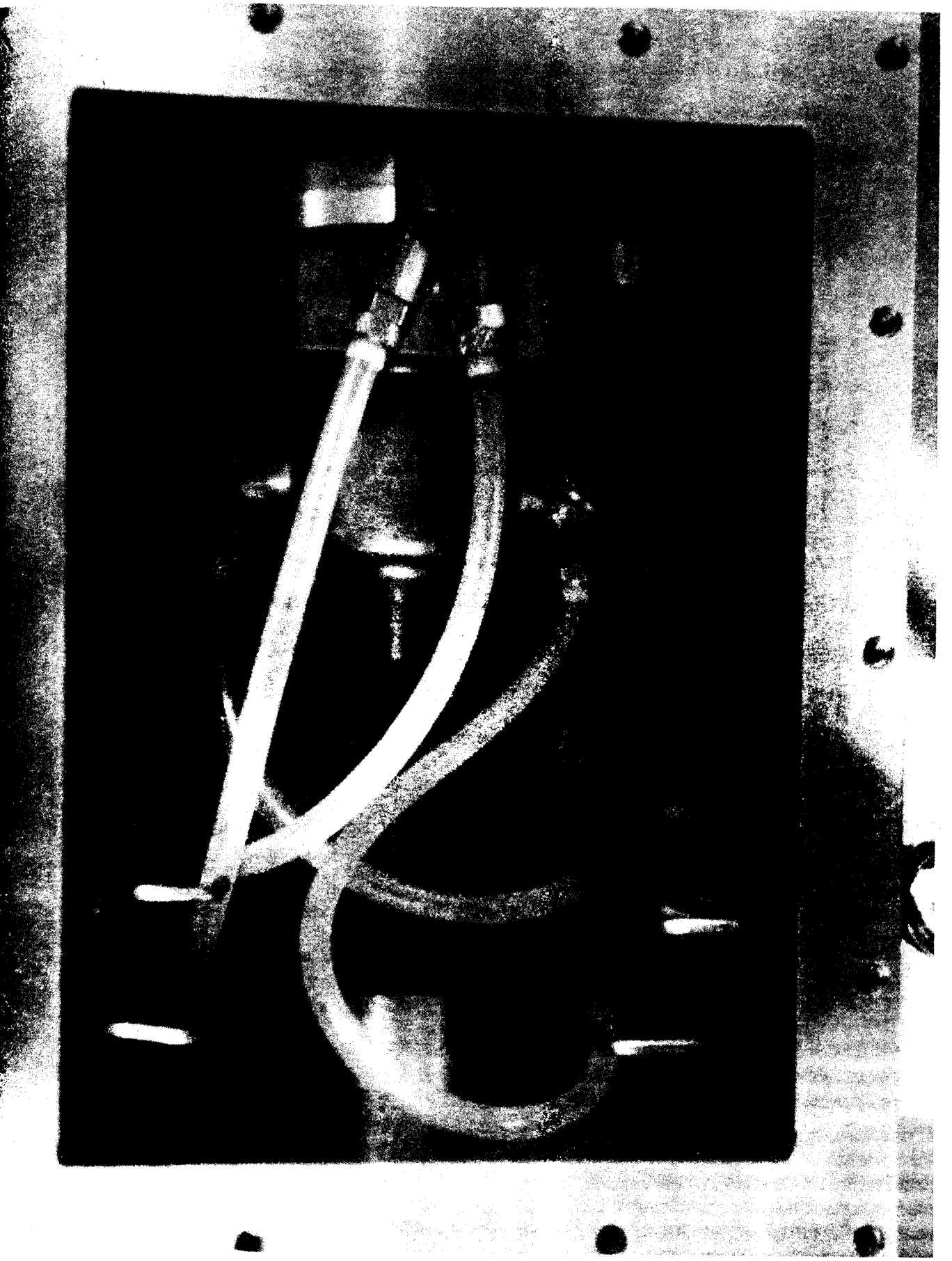

Figure 2-23. Interior of the thermalizer box, showing the aluminum

One problem with this system has been the buildup of long-lived contaminants on the fixed collector. A tape transport unit has been designed to provide a moving collecting surface that will alleviate this problem (Kos71). Two additional improvements need to be made on the system. The target holder and top plate of the thermalizer box need to be modified so that targets normally stored under vacuum can be inserted into the helium filled chamber without exposure to the atmosphere. This step would prevent some target oxidation, although the impurities in the helium would eventually damage thin targets of high chemical reactivity. The thermalizer-transport system will not function with highly purified helium. The slight impurities in the helium are thought to interact with the beam plasma to form very high molecular weight conglomerates, which serve as carriers for the recoils (Mac71). The second modification needed is the installation of a seal between the Havar window and the target holder in the thermalizer box. This would prevent unwanted recoils from the window being transported to the counting chamber. With the present apparatus significant amounts of γ-ray background from the window are observed. More efficient devices incorporating multiple targets and recoil collection at 90° to the beam have been developed (Kos71). These offer increased recoil intensity and lower window background but require a significantly longer collection time. For investigation of short-lived species, the hemisphere collector has proven quite adequate.

In the work reported here, the helium-jet thermalizer system has been used mostly for the three-particle isomer searches (see Chapters VII and VIII). Although the system allows relatively clean spectra to be taken with the best detectors, it has the disadvantage of not providing any

type of fast time discrimination. When looking for unknown species, the ability to route successive spectra in time becomes very important, since it permits elimination of many γ rays on the basis of half-life. Because the collection time within the thermalizer is stretched over a relatively long period, the system is not adaptable to pulsed-beam type experiments. However, for obtaining clean singles and coincidence spectra of short-lived species the helium-jet system is indispensable.

2.6 γ-Ray Spectrometer Systems

The development of Ge(Li) detectors in the early 1960's did much to revitalize the field of γ-ray spectroscopy. Complex nuclear structures having numerous γ-ray de-excitations, which were impossible to resolve previously, could now be studied with ease. This motivated the study of new decay schemes as well as the reinvestigation of earlier ones. As Ge(Li) detectors have grown in popularity and usage, their relative efficiencies and resolution have improved constantly. Early detectors were of the "homemade" variety, i.e.,fabricated entirely within each laboratory. As detector technology has increased, demanding better materials and facilities, this "black art" has been relegated to commercial vendors. During the relatively short period of this study (three and one-half years), the improvement in the quality of our detectors has been quite dramatic. Early experiments were performed with a "homemade" detector having a resolution of $\approx$5.6 keV FWHM (for the 1333-keV γ of ^{60}Co) and an efficiency of (0.4%) (as compared to a 3-in$\times$3-in NaI(Tl) detector 25 cm from a ^{60}Co source). Our latest detector was purchased from Nuclear Diodes and has a resolution of 2.1 keV and an efficiency of 10.4%.

The quality of other components of our spectrometer systems has kept pace with the detector improvements. The preamplifiers, once mounted in external units with room-temperature FET's, are now an integral part of the detector cryostat, sometimes utilizing cooled FET's for maximum noise reduction. Better protection circuits allow the detectors to be biased rapidly without damage to the FET's. Modern spectroscopy amplifiers have undergone many improvements, including such features as adjustable base-line restoration and pole-zero cancellation.

The multichannel analyzers (MCA's) have increased in number, capacity, speed and versatility. Early experiments utilized a hardwired MCA with 1024 channels and a digitizing rate of 4 MHz. Current experiments use up to four computer-interfaced, analog-to-digital converters (ADC's) with 8192 channels each and a digitizing rate of 50MHz. Minor changes in cryostat design and dewar capacity have added convenience to the systems.

2.6.1 Ge(Li) Singles Spectrometer

The Ge(Li) γ-ray singles spectrometer system contains several components, each of which contributes to the overall quality of the final spectrum. A typical singles spectrometer includes a Ge(Li) detector and its bias supply, a charge sensitive FET preamplifier, a "spectroscopy" amplifier, an analog-to-digital converter (ADC), and a memory storage unit together with a readout mechanism (usually for "hard" copy, such as cards or paper tape). With the exception of some preamplifiers, the majority of the electronics equipment is modular and more or less mutually compatible. Thus, different modules from various manufacturers can be combined to achieve the best results for a given type of experiment. A brief description of each of these components is helpful in understanding the system.

The Ge(Li) detectors have already been previewed above. Several different detectors have been used for the experiments reported in this study. The specifications of some of these detectors are listed in Table 2-1. This table presents the detectors in chronological order, clearly indicating the trend toward greater efficiency and better resolution. The choice of detectors for a given experiment will vary with the desired goal and conditions under which the experiment

Table 2-1

Ge(Li) Detector Specifications

Efficiency[a]	Resolution[b]	Peak to Compton Ratio	Shape	Preamp FET	Manufacturer
0.42%	5.6 keV	4.5 to 1	Trapezoidal	room temperature	MSU Cyclotron Lab.
~1.0%	3.2 keV	6 to 1	Trapezoidal	room temperature	MSU Cyclotron Lab.
2.0%	3.4 keV	8 to 1	Trapezoidal	room temperature	Nuclear Diodes
2.5%	2.2 keV	16.5 to 1	Trapezoidal	cooled	Nuclear Diodes
3.6%	2.0 keV	22 to 1	True Coaxial	room temperature	ORTEC
4.6%	1.9 keV	24 to 1	True Coaxial	room temperature	ORTEC
10.4%	2.1 keV	38 to 1	True Coaxial	cooled	Nuclear Diodes

[a] With respect to the 1332 keV peak of ^{60}Co at 25 cm from a 3×3-in NaI(Tl) detector.

[b] FWHM for the 1332 keV peak of ^{60}Co.

is to be carried out. Generally speaking, the detector with the best resolution and the highest efficiency is most desirable -- all other factors being the same. However, facts like the precision with which the efficiency curve is known at a certain distance, the amount of jitter associated with a given detector, or whether the detector should be exposed to in-beam conditions, may govern the choice of a detector. Simple matters like experimental priority and the availability of a given detector on a given date can dictate the final choice. The bias voltage for these detectors varies from a few hundred volts to a few thousand volts. Choice of a power supply is determined both by the capacity of the supply and the noise it may add to the system (thus, reducing the resolution). Large, well-regulated high-voltage supplies such as Fluke and Northeast seem to be much less noisy than the small, module types.

Taken in logical sequence, the next component is the charge-sensitive, field-effect transistor (FET) preamplifier. This preamplifier integrates and shapes the charge output from the detector and sends a tail pulse to the main amplifier. Typically, this pulse has a rise time of ≈25 nsec and a decay time of ≈50 μsec. These preamplifiers come both as separate, independent modules or as an integral part attached to a particular detector. The attached units may be of the usual room-temperature FET variety or the cooled FET type.

Today's spectroscopy amplifiers offer great versatility, with many features to improve the resolution, particularly at high count rates. Both unipolar and bipolar output pulses shaped with shaping constants ranging from 0.25 μsec to 4 μsec can be obtained with various maximum amplitudes of either polarity for use as an input to an ADC

or for timing purposes. These amplifiers have highly linear amplification responses and include such features as adjustable pole-zero cancellation, base-line restoration, and DC offset. The pole-zero cancellation feature permits precise elimination of undershoots on the amplifier pulse after the first differentiation. This becomes important at high counting rates, where if the undershoot saturates, the amplifier will be blocked not only for the time of the primary pulse, but also for the duration of the undershoot. In addition, the following pulses which fall into the undershoot will have an apparent area smaller than the actual area, therefore causing deterioration of the resolution. High count-rate resolution is also improved by the base-line restoration feature. This device restores the undershoot of the amplifier signals to a *DC* baseline after all other shaping has been performed. The improved resolution is brought about by the reduction of pile-up distortion caused by undershoot. The *DC* level adjustment matches the *DC* level of the amplifier unipolar output to the *DC* level of the direct input to the ADC. Additional features incorporated into some amplifiers are very convenient. The so-called "common mode" found on some amplifiers sometimes provides a solution for noise pickup in long cables. Almost all amplifiers now provide a convenient plug on the rear of the module for powering preamplifiers. Likewise 93Ω outputs are also found on most units for proper termination.

The last component in the spectrometer system is the multichannel analyzer. During the course of this study a variety of analyzers has been used. As one might expect, the size, versatility and sophistication of these devices has improved concurrently with other components of the system. The pertinent characteristics of several multichannel

analyzers used in this investigation are given in Table 2-2. As can be seen, the trend here has been toward increasing the number of channels and speeding up the digitizing rate. Tremendous versatility is achieved by interfacing the ADC's to a computer such as the Sigma 7. The on-line manipulation of the data, together with various acquisition modes such as routing, multi-dimensional storage, etc., are extremely powerful tools. These methods will be discussed in more detail in later sections.

2.6.2 Ge(Li)-NaI(Tl) Coincidence Spectrometer Systems

Although γ-ray singles experiments can provide very accurate energy and intensity measurements of γ rays associated with a decaying nucleus, they reveal nothing concerning the relationships of these γ rays to each other. In order to determine these relationships and establish a decay scheme, one must perform a number of coincidence experiments. Several different types of single parameter coincidence spectra are normally utilized. These include anticoincidence spectra, which reveal γ rays that are *not* in coincidence with any others, e.g. direct ground state (if not β^+-fed); any- or integral-coincidence spectra, which reveal γ rays that are in coincidence with any other event; gated-coincidence spectra, which show γ rays that are in coincidence with a particular transition or region; and, 511-511-γ coincidence spectra, which emphasize double escape peaks and β^+-fed levels. Each of these types will be discussed in the following sections.

2.6.2A Ge(Li) vs 3×3-in.NaI(Tl) Spectrometer

Prior to the fabrication of large, relatively efficient Ge(Li)

Table 2-2

Multichannel Analyzer Specifications

ADC	Maximum Number of Channels	Digitizing Rate	Memory
Nuclear Data 150	1024	4 MHz	Hard wired
Nuclear Data 160	1024	4 MHz	Hard wired
Nuclear Data 2200	4096	16 MHz	Hard wired
Northern Scientific 625	2x 4096	40 MHz	Interfaced to DEC PDP-9
Northern Scientific 629	4x 8192	50 MHz	Interfaced to XDS Sigma-7

detectors, which allowed Ge(Li) vs Ge(Li) coincidence experiments to be performed, the principal means of obtaining timing pulses for coincidence spectra were NaI(Tl) scintillators coupled to photomultiplier tubes. This system utilized the best advantages of the two types of detectors, with the poor-resolution, but highly efficient NaI(Tl) detector being used as a gate for the inefficient, high-resolution Ge(Li) detector. A block diagram of this type of set-up is shown in Figure 2-24. Besides the usual equipment required for a singles experiment, an additional detector and electronics are needed to provide timing information. A 3×3-in NaI(Tl) detector was used for this purpose. This detector had an efficiency approximately 10 times that of the best recent Ge(Li) detector (10.4%), and a resolution of ≈8% (for the 611-keV γ ray of ^{137}Cs). The pulses output from the photomultiplier were sent to a spectroscopy amplifier through a cathode follower, which serves as an impedance matching device between the tube type photomultiplier and transistor amplifier.

After amplification and shaping, the NaI(Tl) signals are input to a timing single channel analyzer (TSCA). The TSCA checks to see if the pulse falls within a predetermined gate (window), and, if it does, outputs a logic pulse to a fast coincidence unit. Likewise, a similar timing signal must be developed from the Ge(Li) linear signal. This is achieved by using a second TSCA which sends a logic signal to the same fast coincidence module. (Normally the gate on this second TSCA is opened completely, giving a timing pulse for each Ge(Li) pulse it receives.) The function of the fast coincidence unit is to output a logic signal only when a Ge(Li) and NaI(Tl) logic pulse arrive within

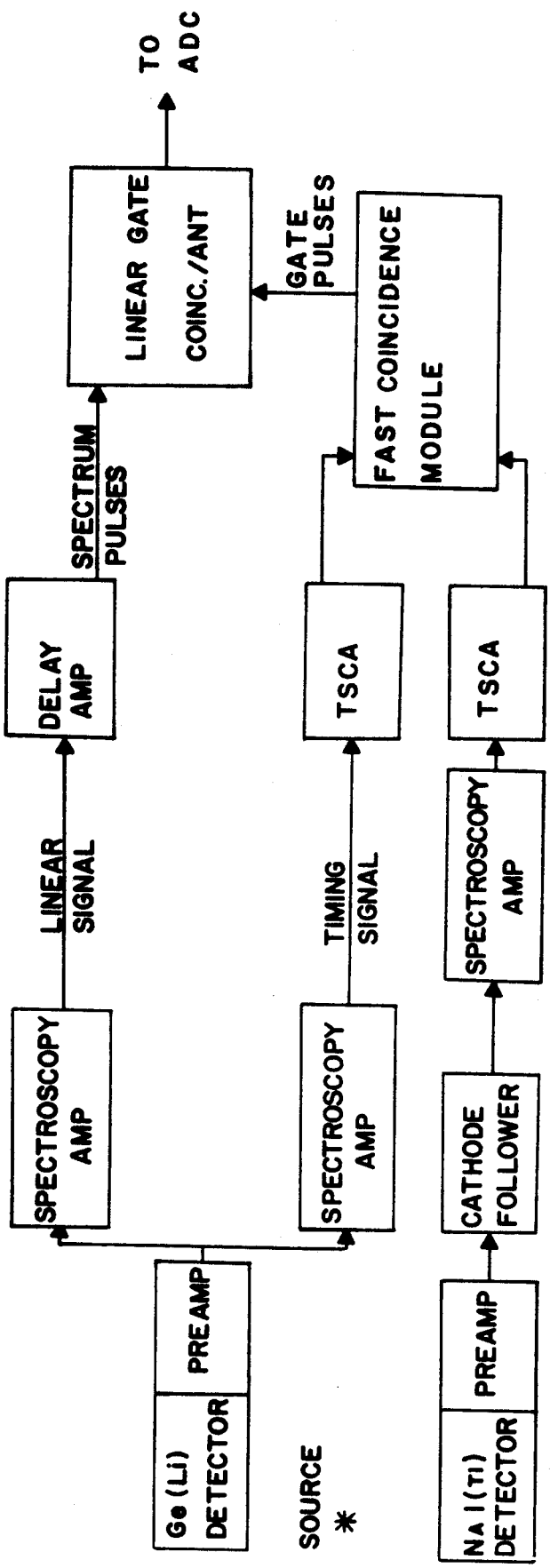

Figure 2-24. Block diagram of a typical Ge(Li)-NaI(Tl) coincidence experiment.

a specified time interval of each other. For most coincidence experiments, this resolving time (2τ) was set at ≈100 nsec. An external linear gate was used for almost all coincidence set-ups. A logic pulse from the fast coincidence module opens this gate for a predetermined length of time, allowing any linear signal present at the input during that time to pass through the open gate and on to the ADC. Thus, only pulses from γ-ray transitions occurring within the specified resolving time are allowed to pass through the linear gate and be processed by the ADC. The delay amplifier in the Ge(Li) linear circuit is merely to compensate for the delay incurred by the timing signals while they are traversing the coincidence units. The delay is adjusted so that the linear signals and the coincidence timing signals arrive simultaneously at the gate. This simple system has been used for several types of experiments. The normal geometry used has the Ge(Li) and NaI(Tl) detectors oriented at 90°, with the radioactive source at the apex. A graded lead absorber is used between the detectors to prevent scattering events in one from reaching the other. For integral coincidence experiments, the NaI(Tl) TSCA window is opened completely. Closing this window to a particular peak or region allows gated-coincidence experiments to be performed. If the window is opened but the linear gate is switched to anticoincidence mode, one obtains a very useful anticoincidence spectrum.

2.6.2B Ge(Li) vs 8×8-in. NaI(Tl) Split-Annulus Spectrometer

The 8×8-in. NaI(Tl) split annulus is the keystone in one of the most useful spectrometer systems available at this facility. The two optically-isolated halves of this detector can be combined with other detectors to perform a wide variety of experiments. Several configurations

using this annulus in conjunction with a Ge(Li) detector have been described by Auble et al. (Aub67). In the work reported here, the annulus has been used for the following types of experiments: anti-coincidence, integral coincidence, gated coincidence, 511-511-γ coincidence, and Compton suppression. An illustration of the various detector-source geometries for typical experiments is reproduced in Figure 2-25 (from Doe70).

A block diagram of the electronics set-up for using the annulus in an anticoincidence experiment is shown in Figure 2-26. As can be seen in Figure 2-25, a 3×3-in. NaI(Tl) detector is placed in one end of the annular tunnel in order to increase the solid angle subtended by the detectors. A Ge(Li) detector is then positioned in the other end of the tunnel, facing the 3×3-in. NaI(Tl) detector -- with the source in between, approximately in the middle of the tunnel. The electronics for each section is just like that described in the coincidence experiment in Section 2.6.2A above. Now, however, there are three NaI(Tl) timing signals instead of just one. These three timing signals are combined in two AND/OR gates that produce a timing signal whenever one or more of these signals is present. This is accomplished by using an ORTEC universal coincidence unit with the number of coincidence requirements set to one, as the AND/OR gate. In this mode, the resolving time control on the unit has no effect. The relevant time consideration is that of the fast coincidence module, which is normally set to 100 nsec in these experiments. The output from the fast coincidence unit is then used to trigger a linear gate operated in anticoincidence mode.

Such efficient anticoincidence experiments as this have been

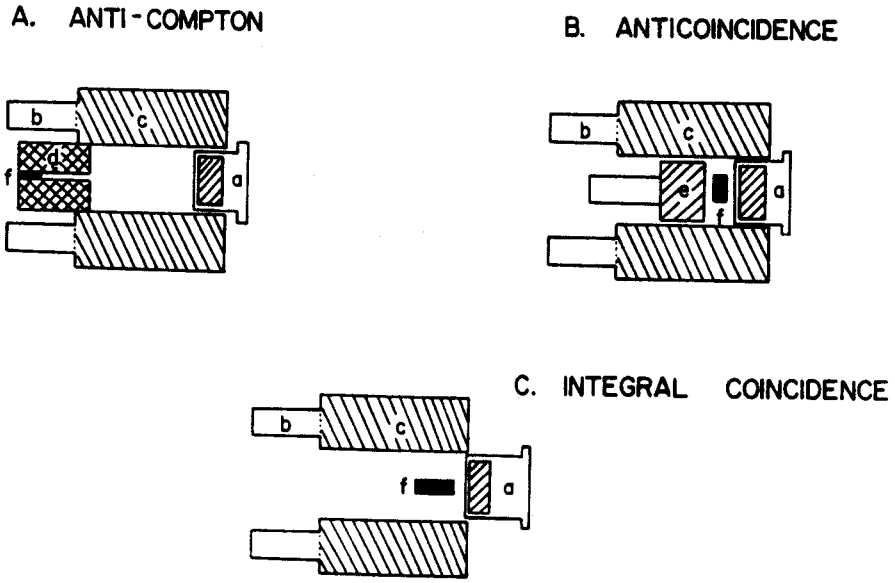

a. Ge(Li) Detector
b. Photomultiplier Tube
c. Half of Split Annulus
d. Graded Pb Collimator
e. 3×3-in. NaI(Tl) Detector
f. Radioactive Source

Figure 2-25. Detector-source geometries for several experiments utilizing the 8×8-in. NaI(Tl) split-annulus spectrometer.

helpful in identifying ground state transitions which were primarily electron-capture fed and also transitions from isomeric levels, i.e., transitions from levels having half-lives considerably longer than the resolving time of the apparatus. The anticoincidence spectra also show substantial reduction in the Compton background, since any γ-ray scattered in the Ge(Li) detector has a high probability of being detected by one of the surrounding NaI(Tl) detectors.

With only slight modification of the anticoincidence set-up, one achieves a "singles" spectrum having a drastically reduced Compton background. This Compton-suppression or "anti-Compton" experiment as it has come to be called, has been very valuable in extracting weak, lower energy peaks from the Compton background. In this type of experiment, the 3×3-in. NaI(Tl) detector is replaced by a graded lead collimator containing the source. As a result, the radiation from the source travels into the Ge(Li) detector, while being shielded from the NaI(Tl) annulus. Thus, the annulus sees only γ rays which are Compton scattered from the Ge(Li) detector. When such a γ ray is recorded by the annulus, the gate is closed and the Compton event observed by the Ge(Li) detector is rejected.

The equipment shown in Figure 2-26 can also be modified for use in obtaining integral and gated coincidence spectra. For integral coincidence experiments, the TSCA's in the NaI(Tl) timing circuits are each adjusted to accept all γ-ray energies above x-rays, and the linear gate is switched to "normal mode", i.e., closed until opened by a signal from the fast coincidence unit. With these changes, the resultant spectrum should contain only those γ rays involved in a cascade within the resolving time of the fast coincidence unit, normally about 100 nsec. (Improved resolving times of $2\tau \approx 20$ nsec are now possible).

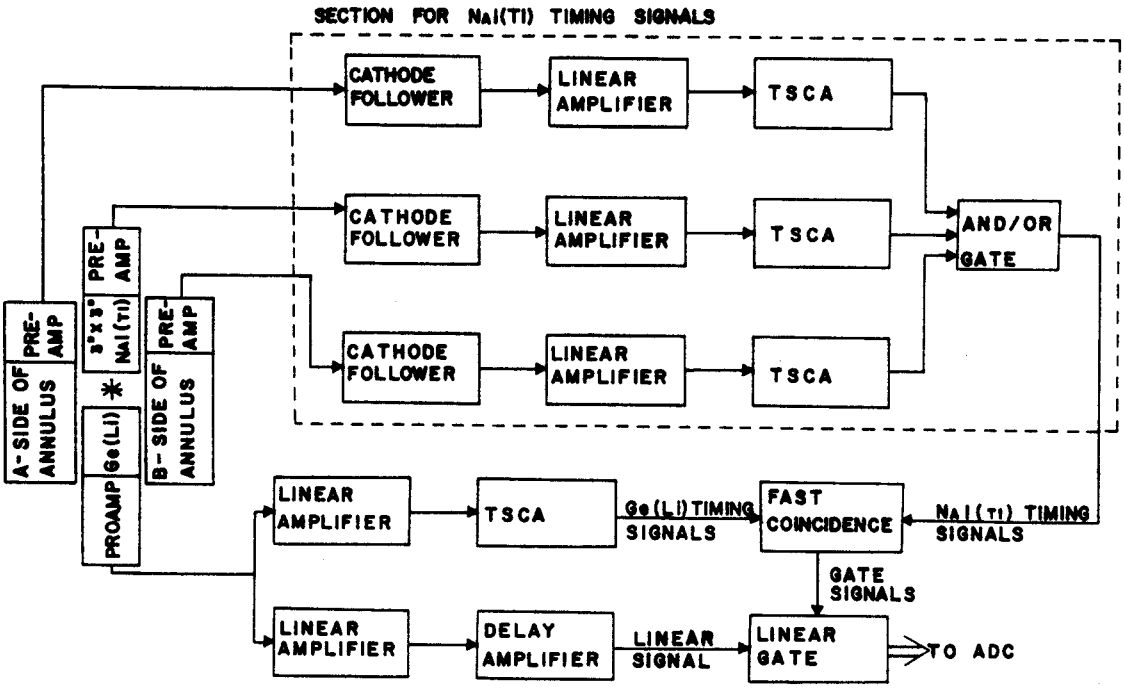

Figure 2-26. Block diagram of the electronics setup for an anti-coincidence experiment using the split annulus. The same equipment is used for obtaining pair spectra after elimination of the 3×3-in. NaI(Tl) detector and the AND/OR gate.

The equipment needed to perform a gated coincidence is the same as that used for the integral coincidence experiment just described. The only change needed is to set an energy window with the NaI(Tl) TSCA's so that only those γ rays falling within this window will cause the TSCA's to output a pulse to the fast coincidence unit. The gated spectrum then will contain only those γ rays that are in coincidence with this energy window, which is usually set on a particular transition or region of interest. This technique works quite well for simple spectra having only a few well-separated peaks. For complex spectra however, the poor resolution of the annulus ($\approx$10% for the 1332-keV γ ray of ^{60}Co) makes interpretation of gated spectra quite difficult, since each gate usually contains a number of γ rays. In addition, this technique is inefficient with respect to cyclotron time. In most cases the development of two-dimensional Ge(Li)-Ge(Li) coincidence systems has rendered this type of gated coincidence technique obsolete.

The annulus can also be used as a pair spectrometer (511-511-γ coincidence spectrometer) for examining the β^+ feeding to various levels. The apparatus needed for this type of experiment is similar to that shown in Figure 2-26, except that the 3×3-in. NaI(Tl) detector and its associated electronics are not required. Since a triple coincidence is required (that is, signals from *both* halves of the annulus and the Ge(Li) detector must arrive within the resolving time of the fast coincidence unit), the AND/OR gate is not necessary. The TSCA for each annulus half is set to gate on the 511-keV region. Thus, only γ rays occurring within the fast coincidence unit resolving time of two separate 511-keV γ rays are recorded. This results in spectra which show enhancement of those γ rays involved in prompt coincidence with levels which are fed by β^+ emission. As might be expected, double-escape

peaks also are enhanced in these spectra.

2.6.3 Ge(Li)-Ge(Li) Coincidence Spectrometers

The development of large volume Ge(Li) detectors having a relatively high efficiency has allowed their use not only as primary detectors but also as gate detectors for coincidence experiments. The superior resolution and peak-to-Compton ratios of these detectors now outweigh their characteristic inefficiencies and permit vastly improved coincidence experiments to be carried out. Although simple gated coincidence experiments of the type described above can be performed using two Ge(Li) detectors, this method has been superseded by the development of two-dimensional, "megachannel" coincidence techniques. Modifications of this very powerful method allow rather thorough investigation of short-lived isotopes.

2.6.3A Two-Dimensional Data Acquisition Using Routing

The technique for performing two-dimensional, "megachannel", γ-γ coincidence experiments has been refined and utilized extensively in this laboratory (Bee69, Epp70a, Doe70). However, application of this method to the investigation of short-lived isotopes ($t_{1/2}$ <1sec) has not been done previously.

The "classic" block diagram of the electronics used in a standard two-dimensional experiment is shown in Figure 2-27. The basic goal of such an experiment is to collect coincidence data for each and every peak (or region) of interest in a single run. This is done by a double coincidence set-up in which the linear signal from each detector is recorded when the fast coincidence unit senses two coincident events. The two linear signals are sent to two separate ADC's, operated in

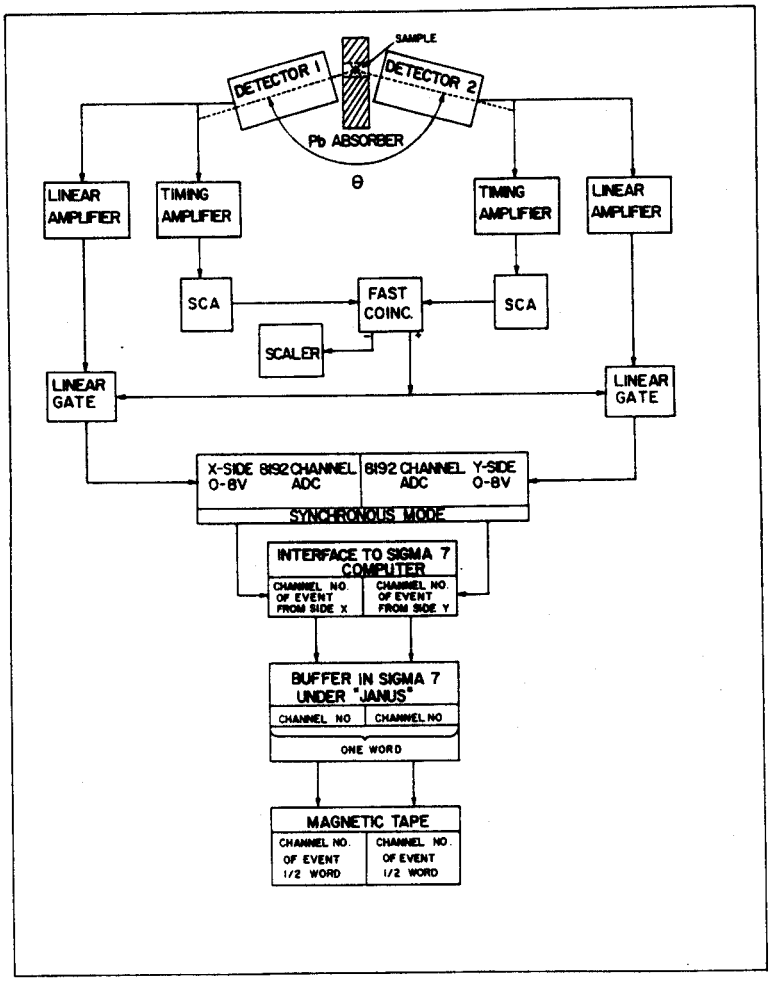

Figure 2-27. Block diagram of the electronics used in a typical two-dimensional γ–γ coincidence experiment.

synchronous mode and interfaced to the Sigma-7 computer. The addresses produced by these ADC's are then collected on magnetic tape under a program called EVENT (Bay71), which runs under the JANUS monitor system of our XDS Sigma-7 computer (Kop69). Each pair of correlated addresses is stored in two halves of a 32 bit computer word, each address being assigned the least significant 13 bits of each half word. The three most significant bits of each half word are then used to store the routing information which was present in each ADC at the time when the coincidence occurred. In practice, the routing signals (usually from the clock module) are teed into corresponding ADC inputs on the routing box so that these coincident pairs contain the same routing code. Each of these words, containing all the information for a single coincidence event, is stored first in a 240-word buffer. When this buffer is filled, it is written on magnetic tape, while a second buffer continues storage. The system is now limited to a count rate of ≈2000 events per second, due to the tape movement speed of the magnetic tape transport. However, this presents no problem, since the usual counting rate is ≈20-50 events per second. A normal 2400-foot, 9-track magnetic tape will hold almost two million events, written in 60-word records.

The data recorded on tape are recovered later, off-line, using a program called EVENT RECOVERY (Gie71). This program allows scanning of the data tape(s) with up to ten gates set for each single pass. Normally, one begins by displaying each spectrum as gated by the other entire spectrum, i.e.,he obtains the "integral" coincidence spectrum from each detector. Having done this, gates are chosen from one side and the various gated coincidence spectra are obtained for the other side, and vise versa. This program was modified recently for utilization of

the three bit routing code contained in each half word. Thus, integral and gated coincidence spectra may be obtained for any routed time interval. This technique, used with pulsed-beam methods, is a very powerful tool for studying and characterizing transitions in short-lived species. The greatest impediment to this approach for the in-beam experiments performed in this study was the need for very good statistics. For pulsed-beam experiments with only one-half of the total run time spent counting (the other half is beam-on time), one finds that dividing the acquired data by four or five leaves precious little for two-dimensional type analysis. Nevertheless, with sufficient time, valuable data can be extracted using the routed two-dimensional data. An early problem with the lack of on-line monitoring of total coincidence events was solved by modifying EVENT to run under program TOOTSIE (Bay71).

2.6.3B Multi-Dimensional Data Acquisition

Although the two-dimensional routed spectra described above provide a very much improved method for studying short-lived isotopes, a far more versatile and powerful technique is being developed. Since task EVENT (Bay71) is capable of taking n-dimensional coincidence data, a logical next step is to incorporate *time* as a third dimension and perform pulsed-beam, 3-dimensional γ-γ-time coincidence experiments. In such an experiment, each coincidence pair recorded would be accompanied by a signal proportional to the time elapsed since the end of a beam burst. This could be achieved easily by simultaneously sampling a voltage ramp which is restarted after each beam burst. Thus, gates could be set not only on gamma peaks, but also on any desired time intervals. Consequently, various half-lives could be determined and used most efficiently

in searching for unknown transitions or isomers. The ability to vary the time slices after the experiment is finished adds great versatility to this method. Problems with poor statistics in such an experiment would be no worse than in the routed case and most likely could be improved by the appropriate choice of time intervals. The program EVENT RECOVERY is now being modified to handle such three-dimensional experiments.

2.7 Beta Spectrometers

Prompted by the desire to re-investigate the positron end-point energies of ^{53}Fe, we have utilized several types of beta detectors in singles and coincidence experiments. Since the end-point energies were of primary interest, and some shape distortion could be tolerated, relatively simple techniques were employed.

2.7.1 Beta Singles Spectrometers

Preliminary investigation of the ^{53}Fe beta spectrum was performed with plastic (Pilot B and Naton 136) scintillators used in conjunction with photomultiplier tubes (e.g.,RCA 6342A). Since early experiments were carried out using previously prepared scintillator-photomultiplier tube packages sealed in foil and tape, the exact specifications of some detectors were unknown. All of our experiments were performed using sources external to the detector, with thin foil or aluminized mylar (1 mg/cm^2) windows for admission of the beta particles. Typical size of the scintillator material was 2.5 cm thick × 5 cm in diameter. All sources were chemically separated and dried on thin foil before being counted.

The availability of a Ge(Li) single crystal conversion-coefficient spectrometer manufactured in this laboratory by C. Maggiore, prompted an attempt to use it for the ^{53}Fe beta spectrum. This was a planar drift device, with a drift depth of ≈7mm and an active volume of ≈0.4 cm^3. The crystal was mounted in a conventional dipstick cryostat with a 0.25 mil Havar foil window. Since the conversion coefficients for the transitions being studied were very small, no peaks could be found in the beta spectrum corresponding to conversion electrons. As was expected, the γ-ray sensitivity of this device was so great that its contribution could not be subtracted from the total spectrum to

yield a reliable beta continuum. Therefore, the use of this detector for beta end-point energy determinations was abandoned.

The device used most often, and by far the most convenient and reliable, was a Si(Li) surface-barrier detector. The detector utilized had an area of 200 mm^2 with a thickness of 1000 μ. In order to reduce noise, this detector was mounted in a dipstick cryostat immersed in a methanol-dry ice bath ($\approx$-77°C). The detector itself was covered by an evacuated aluminum can with a 0.10-mil Havar window for admission of the beta particles. A 200-V bias was used for operation of the detector. A typical resolution of $\approx$5 keV was obtained for the ^{137}Cs K-conversion peak. In addition to the bias supply, an ORTEC 109A preamplifier and 451 spectroscopy amplifier were used in conjunction with a 1024-channel analyzer. Energy calibrations for the resulting spectra were obtained by using the conversion electrons of several well-known standards evaporated onto thin foil backings.

2.7.2 Si(Li) vs NaI(Tl) β^+-γ Coincidence Spectrometer

In order to elucidate the positron feeding to levels in the ^{53}Mn nucleus, a number of beta-gamma coincidence experiments were performed. For these experiments, a rather efficient 3×3-in. NaI(Tl) detector was used for the γ-ray gate, while the Si(Li) surface barrier detector described above was used to observe the positron spectra in coincidence with these γ rays. Both 90° and 180° source-detector geometries were used. By setting an appropriate window width on the NaI(Tl) TSCA, various transitions or regions may be used as the gate. This technique is very useful for determining which positron end-point energy feeds a given transition. Results obtained with this method are given in Chapter IV.

2.8 Fe-Mn Chemical Separation

Many of the experiments in which Mn was the target material required chemical separation in order to eliminate unwanted gamma and beta activity and to insure that only the Fe isotopes were being counted. The short half-lives of ^{53m}Fe (2.5 min) and ^{53m}Fe (8.5 min) prohibited the use of long, involved procedures. Of the various methods surveyed, the following was found to be simple, efficient, and most rapid.

The irradiated target weighing ≈0.3-0.5 g and consisting largely of powdered ^{55}Mn, plus Mn and Fe isotopes produced by the beam, was dissolved in 15 ml of 8.0N HCl. The resultant solution was then extracted twice with 5 ml of isopropyl ether, adding a small amount of ferric chloride carrier each time. The ether extract was then washed twice with 5 ml of 8.0 *N* HCl. The iron was then extracted from the ether with 2-4 ml of distilled water. For γ-ray counting, a portion of this iron solution was counted in a small glass vial. For beta counting, a drop of the solution was dried carefully on a thin foil holder. The total time required for this separation can be less than one minute. As many as 75 such separations have been performed during a single experiment.

Chapter III

DATA ANALYSIS

The increasing sophistication and complexity of nuclear spectroscopy experiments have been accompanied by a comparable increase in the rate of data acquisition. Whereas early experiments in this study allowed storage of one 1024-channel spectrum, present routing methods store five 4096-channel spectra plus two-dimensional megachannel data. A single multiparameter experiment now has the potential for yielding literally hundreds of coincidence spectra. Fortunately, the methods of data analysis have undergone similar increases in capability, so that the experimenter has not been completely inundated by this deluge of data. Nearly all of the current spectrum analysis routines are run on the MSU Cyclotron Laboratory XDS Sigma-7 computer, with programs either written for or adapted to it.

3.1 γ-Ray Energy and Intensity Analysis

The basic steps in the analysis of a γ-ray spectrum begin with the fitting of the background with some order polynomial, followed by subtraction of this background, determination of the photon peak areas and centroids, and finally relating these to intensities and energies through calibration curves. Such procedures are carried out with the aid of appropriate spectrum analysis codes. Three such codes were used in this study. These are called MOIRAE, MOD 7, and SAMPO.

3.1.1 Program MOIRAE

Until recently, the program MOIRAE was the primary method of spectrum analysis used by the nuclear spectroscopy group. This program, written in machine language and run under the JANUS monitor system, utilizes a Fairchild 737A live-display oscilloscope and sense switches for performing the analysis. The code was developed primarily by R. Au and G. Berzins, of the MSU Cyclotron Laboratory. Like all other programs currently in use at this facility, it is based on the analysis of photopeaks only.

Under MOIRAE, all analysis is performed by the operator, using interfaced sense switches located directly under the oscilloscope screen to send instructions to the computer. Data can be introduced either from the card reader or transferred directly from a data acquisition task. The oscilloscope and sense switches are shown in Figure 3-1. The oscilloscope furnishes a live display of the spectrum, a moveable pointer, channel markers, centroid position of an analyzed peak, and pertinent numerical values. The fitted background curve, as well as the net

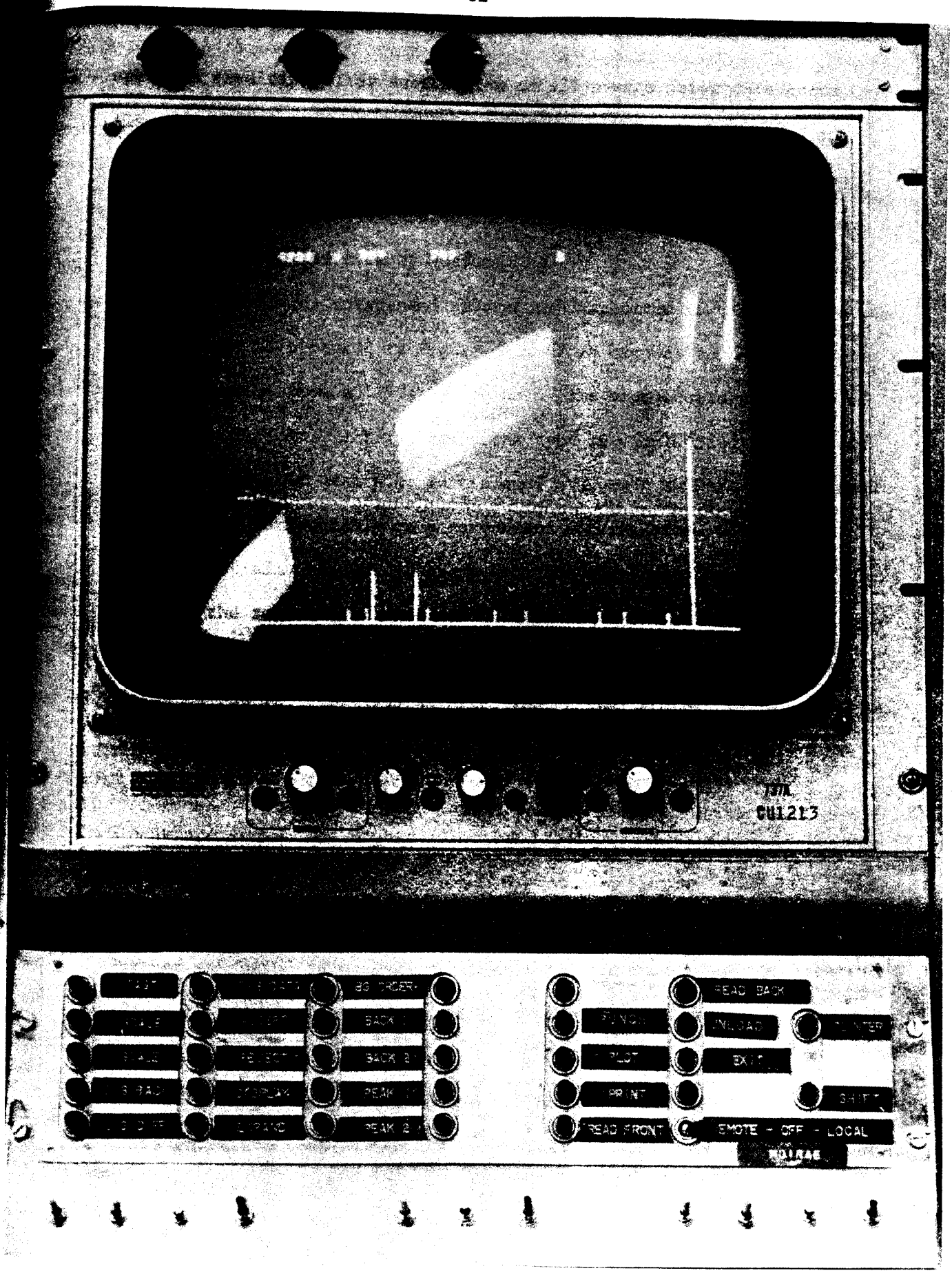

Figure 3-1. MOIRAE display oscilloscope and sense switches.

spectrum resulting after subtraction of all events below this curve also can be displayed. All display and calculational parameters are controlled by the sense switches, including the type of display (log or linear), the scale, expansion and shifting of the horizontal axis, background order and type of output.

A complete, unexpanded 4096-channel spectrum as displayed on the oscilloscope is pictured in Figure 3-2. (This happens to be the first routed spectrum from a ^{43m}Ti search using the microscopic structure of the cyclotron beam.) After chosing the type of display and background order desired, the next step in the analysis under MOIRAE, is to expand the spectrum horizontally to a convenient working size. Figure 3-3 shows a partially expanded segment from the spectrum shown in Figure 3-2, covering the region from channel 100 to channel 550. The numbers across the top indicate (from left to right) the number of counts in the location marked by the tall vertical pointer, the channel number of this location, the run number, the subroutine currently in use, and the order of the background fit being used. When a log display is chosen, instead of the linear one shown, the number of cycles is displayed to the left of the run number.

Since the peaks are not clearly discernable in Figure 3-3, a further expansion is necessary for easier determination of the background. As can be seen in Figure 3-3, the subroutine "*expand*" has been called, and the desired limits are designated on the left by a short channel marker and on the right by the tall pointer. The result of this expansion is shown in Figure 3-4 and covers approximately 100 channels. This expansion is sufficient to give good separation of the peaks and allow individual channels to be viewed for use in background selection. This same horizontal

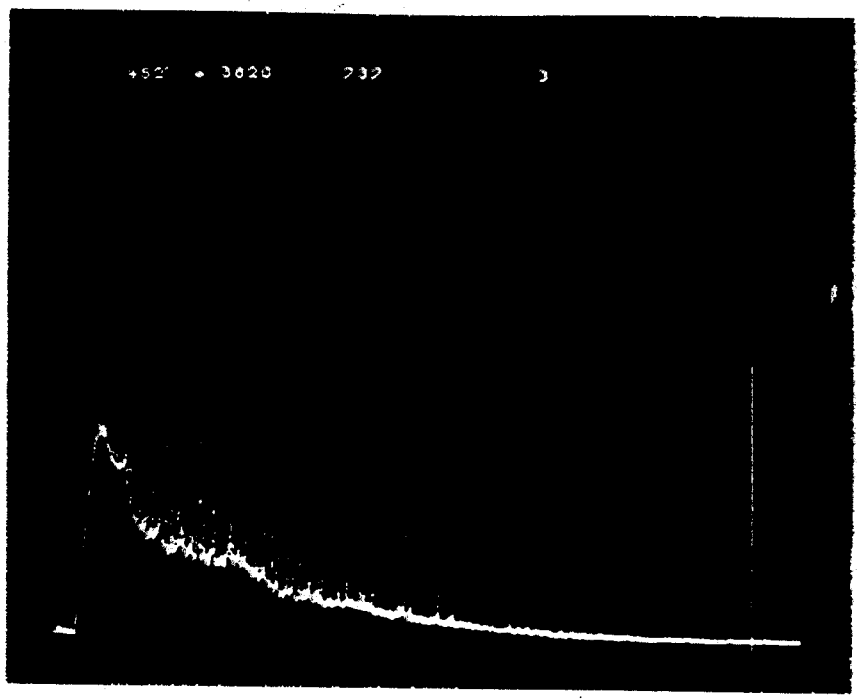

Figure 3-2. MOIRAE oscilloscope display of an unexpanded 4096-channel spectrum from the ^{43m}Ti search.

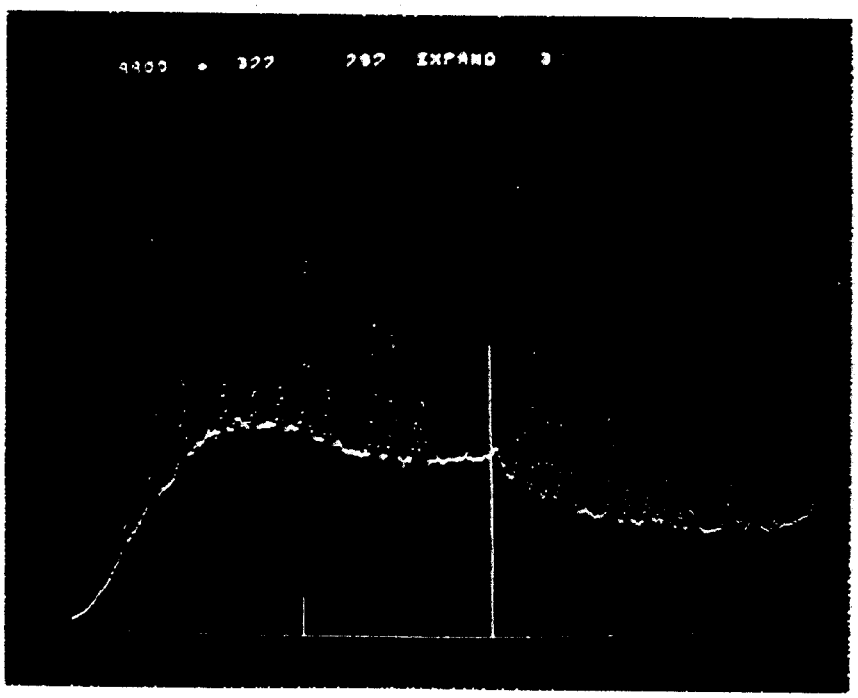

Figure 3-3. Partial expansion of the spectrum from Figure 3-2, showing the limits chosen for further expansion.

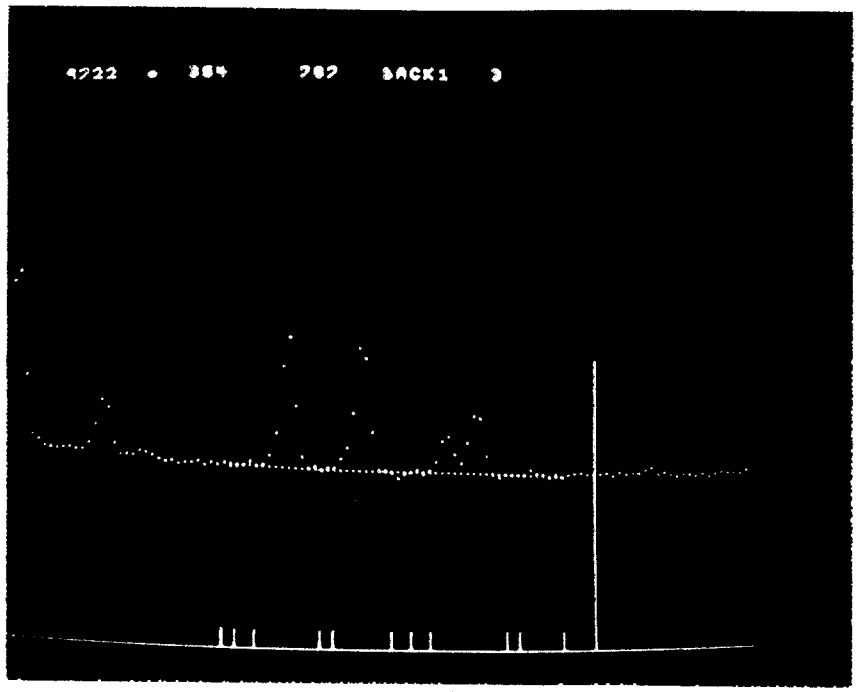

Figure 3-4. Display of the expanded segment from Figure 3-3. A third order background has been fitted using the BACK 1 routine.

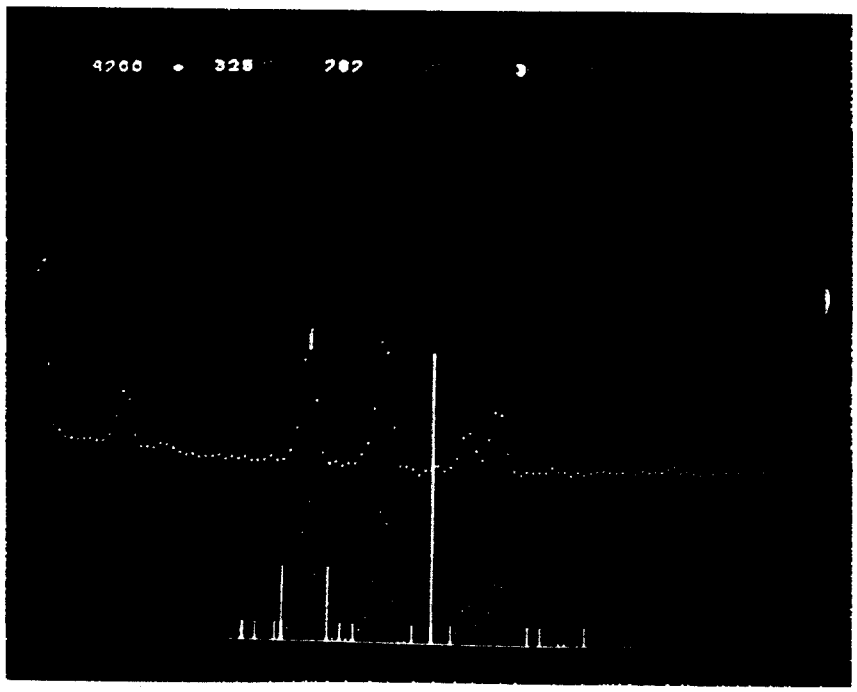

Figure 3-5. Display of the spectrum as shown in Figure 3-4, including the peaks after subtraction of the third order background. The selected peak limits and calculated centroid are shown for the 270-keV peak.

expansion is normally maintained throughout the entire analysis, with the spectrum being scanned across the scope by use of a sense switch. The vertical scale is readjusted to maintain a good view of the data as the number of counts varies.

A background is then fitted over all or any portion of the segment displayed. This background is comprised of channels chosen by the operator and included in a polynomial least-squares fit. The order of the polynomial can be varied from one to ten at the discretion of the operator. Figure 3-4 shows a background fit using a 3rd order polynomial. The tall vertical pointer on the right is the movable marker used for choosing channels to be used in the analysis. The short, vertical lines along the bottom of the display are markers, indicating which channels were accepted to be used in the least-squares background fit. Two routines are available for background selection: BACK 1 allows the selection of *individual* points to be used for the polynomial fit. BACK 2 permits the selection of regions or groups of points between two markers to be incorporated into the background fit. If the polynomial curve does not approximate the background (as judged by the operator), the fit can be rejected, and repeated or modified by accepting additional points.

Having achieved a satisfactory background fit under a given peak, the operator uses the vertical pointer to select the upper and lower channels to be considered as limits for that peak. A center of gravity calculation is then performed over the channels between the selected limits to determine the centroid of the peak. The scope display for this routine is shown in Figure 3-5. The two tall markers under the 270.5-keV peak (second from the left) indicate the limiting channels

used in the centroid calculation. The short vertical line near the top of the peak marks the location of the calculated centroid. Two routines are available for calculating the centroid. PEAK 1 calculates the centroid on the basis of the total raw peak, whereas PEAK 2 utilizes only that portion of the peak having counts greater than one-third the maximum. In either case the program calculates the peak centroid, area, sum of the raw data and background and the square root of that sum. These results for each peak are stored on a computer disk and are output either at the end of the analysis or when subroutine UNLOAD is called. The results are output on the line printer, punched on cards and/or plotted on a Calcomp plotter, as designated during the analysis. Figure 3-5 shows both the data and the difference spectrum after subtraction of the fitted background from the raw data. The shape of this difference spectrum provides another check on the accuracy of the background fit. The points near the top of the picture indicate the channels which have fewer counts than the fitted background. This process of background fitting and centroid determination is continued until all the resolvable peaks in the spectrum have been analyzed.

A sample of the line-printer output from MOIRAE is shown in Figure 3-6. The data are the same as shown in Figures 3-2 to 3-5. The top section gives the counts per channel of the fitted background. By examining the regularity of these numbers, one can determine whether the fitted background varies in a smooth manner. This is important, since the higher order polynomial fits can generate unwanted fluctuations, such as looping back on themselves. The center portion of the figure gives a channel-by-channel listing of the difference between the data and the fitted background. This listing is also helpful in determining the quality

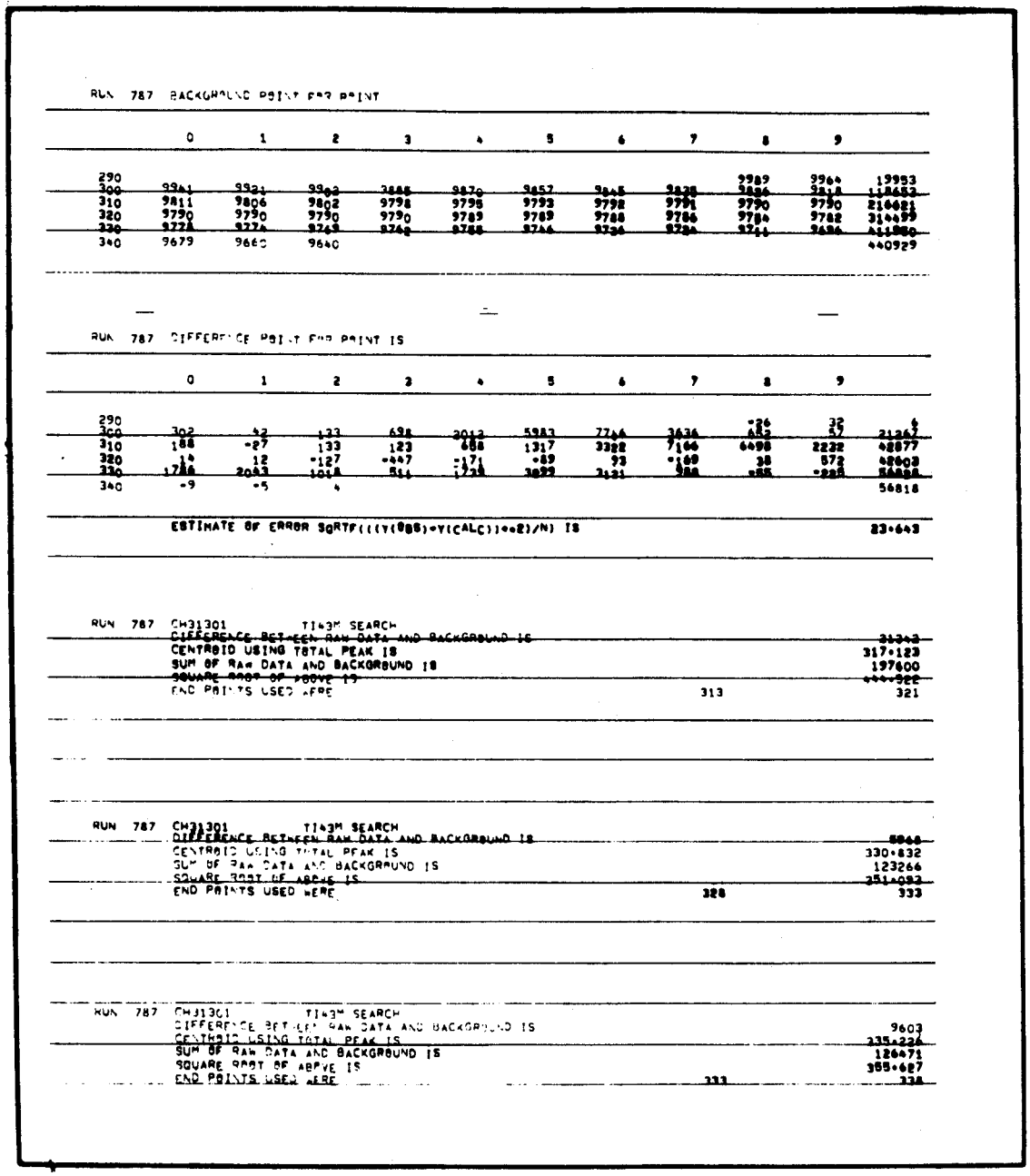

RUN 787 BACKGROUND POINT FOR POINT

	0	1	2	3	4	5	6	7	8	9	
290									9989	9944	19933
300	9941	9921	9903	9885	9870	9857	9845	9838	9836	9818	118683
310	9811	9806	9802	9798	9795	9793	9792	9791	9790	9790	216481
320	9790	9790	9790	9790	9789	9789	9788	9786	9784	9782	313459
330	9778	9774	9769	9762	9755	9746	9736	9724	9711	9696	411080
340	9679	9660	9640								440929

RUN 787 DIFFERENCE POINT FOR POINT IS

	0	1	2	3	4	5	6	7	8	9	
290									-26	32	6
300	302	42	133	698	2013	5983	7746	3636	1852	57	21367
310	188	-27	133	123	688	1317	3328	7144	6498	2232	48877
320	14	12	-127	-447	-171	-89	93	-169	38	572	42903
330	1788	2043	1618	811	1758	3899	3431	984	-885	-828	54888
340	-9	-5	4								56818

ESTIMATE OF ERROR SQRTF(((Y(OBS)-Y(CALC))**2)/N) IS 83.643

RUN 787 CH31301 TI43M SEARCH

DIFFERENCE BETWEEN RAW DATA AND BACKGROUND IS			31343
CENTROID USING TOTAL PEAK IS			317.123
SUM OF RAW DATA AND BACKGROUND IS			197600
SQUARE ROOT OF ABOVE IS			444.522
END POINTS USED WERE		313	321

RUN 787 CH31301 TI43M SEARCH

DIFFERENCE BETWEEN RAW DATA AND BACKGROUND IS			8948
CENTROID USING TOTAL PEAK IS			330.832
SUM OF RAW DATA AND BACKGROUND IS			123266
SQUARE ROOT OF ABOVE IS			351.093
END POINTS USED WERE		328	333

RUN 787 CH31301 TI43M SEARCH

DIFFERENCE BETWEEN RAW DATA AND BACKGROUND IS			9603
CENTROID USING TOTAL PEAK IS			335.224
SUM OF RAW DATA AND BACKGROUND IS			126471
SQUARE ROOT OF ABOVE IS			355.627
END POINTS USED WERE		333	338

Figure 3-6. Sample of the line-printer output from MOIRAE. The data are the same as shown in Figures 3-2 to 3-5.

of the background fit. The last three sections shown in the bottom half of Figure 3-6 are the listings of the analyzed parameters for three of the peaks for which the background was determined. (These are the last three peaks to the right in Figure 3-4.) The parameters listed are defined as follows: The "difference between raw data and background" is the net peak area to be used in the determination of the γ-ray intensity. The "centroid" likewise is used for the energy calculation (note that the program lists which routine, total (PEAK 1) or upper two-thirds of the peak (PEAK 2) was used). The "sum of raw data and background" is merely the raw data count of the peak. The "square root of the above" is the square root of the raw data count of the peak. The "end points used" are the lower and upper limit channels of the peak, as chosen for the centroid and net area determinations. Not shown in the figure, but printed out for each spectrum, is a listing of the raw data.

Conversion of the centroids and net areas determined by MOIRAE into energies and relative intensities is achieved by the program MOIRAE E(I). This FORTRAN program, written by D. Beery and G. Giesler, utilizes the card output from MOIRAE to read the results of the previous analysis. The centroids of several strong, well-known γ rays are used to perform a least-squares fit to a quadratic energy calibration curve. These "standard" centroids may be contained either within the same spectrum as the peaks of interest (internal standards) or in another spectrum taken under the same conditions (external standards). This energy calibration curve then is used to determine the energies of all the peaks in the spectrum. These energies and the corresponding net peak areas are used in conjunction with a predetermined detector

efficiency curve to produce the relative intensities. The resultant energies, relative intensities, input information, and calibration fit are output on the line-printer. A program listing of MOIRAE E(I) together with details of the efficiency curve preparations may be found in (Gie71).

The advantages and disadvantages of MOIRAE must be viewed in the perspective of time. When the program was first introduced it represented the most convenient and fastest method of data analysis. Previous programs required each individual peak interval and its background intervals to be specified on a control card. Obviously, MOIRAE with its live display and sense switch inputs, provided a much improved means of data analysis. Although faster, more sophisticated programs have since become available, MOIRAE retains some advantages. For example, the complete operator control of various subroutines used in the analysis is often very desirable. The background order, background points or intervals, and peak limits can be manipulated until a satisfactory result (in the judgment of the operator) is obtained. This can be important when dealing with complex spectra having irregular backgrounds. Another important feature of the program is its ability to scan through many spectra while maintaining the same expansion and channel location. This is very convenient when one is trying to determine transition half-lives by following a single peak or region in several spectra taken in sequence.

One of the principal disadvantages of MOIRAE can be a feature just cited as an advantage, i.e., complete operator control. The all important choice of "best" background fit is left up to the judgment of the operator. Such parameters as the interval to be fitted, selection

of points to be used, and order of the polynomial to be fitted to the background are all arbitrarily decided. For intense, well-shaped peaks situated on a smooth background, an accurate fit is easily possible. However, in the more realistic case, where one is dealing with many closely spaced peaks with poor statistics on an irregular background, the situation is quite difficult. One does not really know the shape of the underlying background. Normally, various backgrounds are tried, until the operator is satisfied that he has a reasonable approximation of the true background. The length of the interval fitted is usually a compromise between the speed gained in choosing a large interval, and the accuracy of fitting a smaller one. The key to good results lies in the degree of consistency with which operator selects the backgrounds and peak limits throughout the analysis. Since MOIRAE does not utilize a standard peak shape and the backgrounds are chosen at the whim of the operator, consistency is difficult to maintain. It should be noted that the area of the peak is much more sensitive to the background fit than is the centroid. Another disadvantage of MOIRAE is the fact that it cannot strip unresolved peak multiplets -- an important consideration in complex spectra. Compared to other methods of data analysis, MOIRAE is relatively slow, with analysis of a single complex spectrum requiring as much as three hours. Since MOIRAE utilizes a live display, it requires a large amount of computer time. Thus, when several programs are running simultaneously under the time-sharing monitor, all jobs are slowed and the display scope can become erratic. In spite of these difficulties, MOIRAE remains a useful and often convenient method of data analysis.

3.1.2 Program MOD 7

MOD 7 is actually an adaptation of MOIRAE, retaining most of the

subroutines found there. This task, developed by D. Bayer, utilizes a Tektronix 611 storage oscilloscope for the display and thus alleviates the problem of having to drive a live display from the computer, as with MOIRAE. The storage scope and sense switches used with MOD 7 are shown in Figure 3-7. There are two such terminals interfaced to the Sigma-7 computer, allowing two MOD 7 routines to be operated simultaneously. Being derived from MOIRAE, MOD 7 retains most of the advantages and disadvantages discussed earlier. A very useful modification has been the addition of a third subroutine for background fitting (BACK 3). With this feature, one is not restricted to existing data points, but may choose any number of locations and points, connected by straight lines, to form the desired background. Thus, a very complicated background can be approximated by a sufficient number of these points. Likewise, a simple linear fit can be obtained by selecting only two points. Since one is dealing with a storage scope, the spectrum cannot be continually scanned across the display screen but is shifted right or left by the number of channels between a moveable-cross marker and the corresponding side of the displayed expansion. Otherwise, MOD 7 is quite similar to MOIRAE. The smaller display screen together with smaller switches located in a less convenient arrangement, make data analysis with MOD 7 more difficult and lengthy. However, the increasing use of the computer has made the utilization of storage scopes almost imperative. Because of this restriction, MOD 7 is normally the program used for direct, operator-controlled data analysis.

3.1.3 Program SAMPO

SAMPO is a FORTRAN data analysis routine written by J. Routti

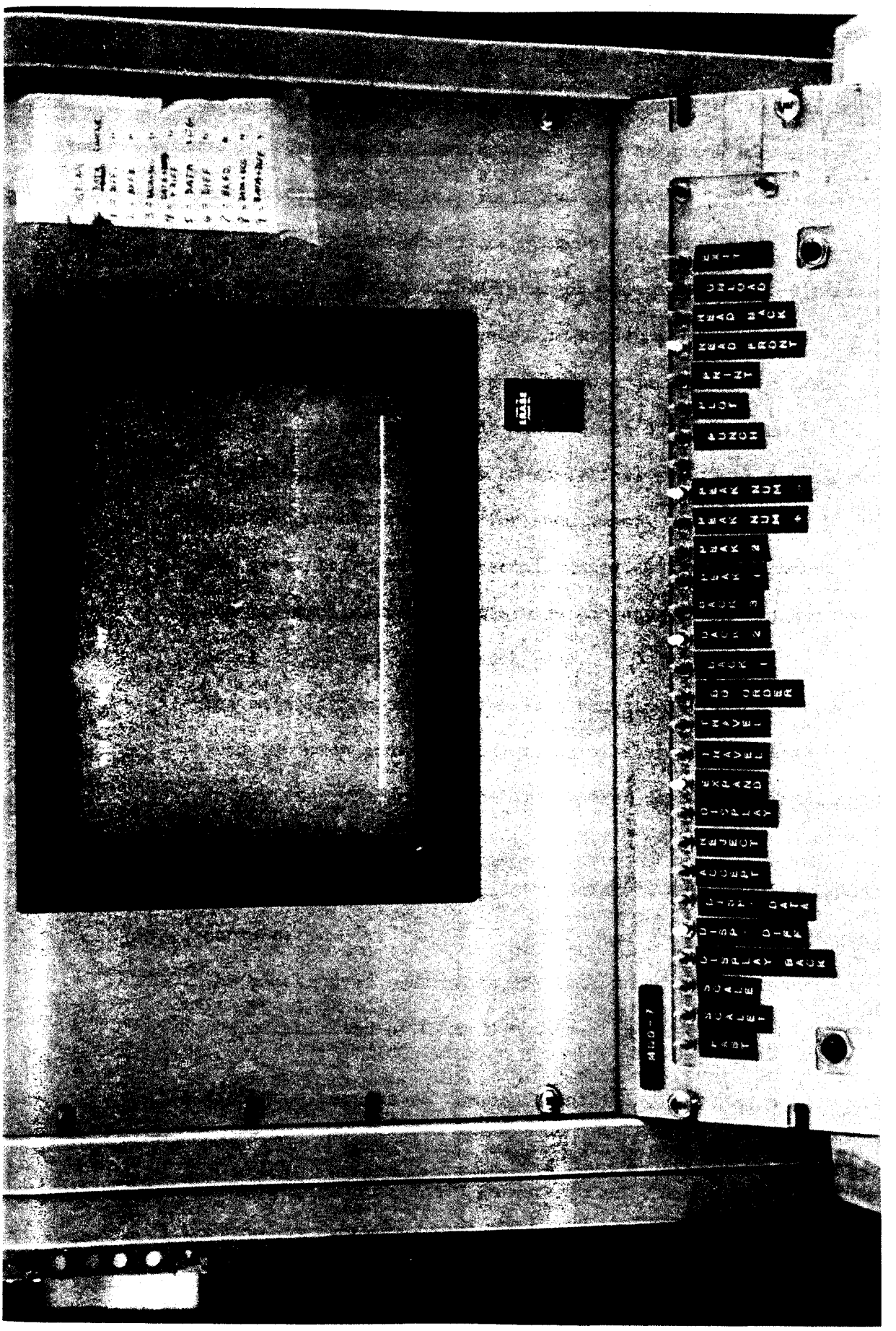

Figure 3-7. The storage scope and sense switches used with MOD 7.

(Rou69) and adapted for use on the Sigma-7 MSU cyclotron computer by T. Arnette, C. Merritt, and C. Morgan. Communication with the program can be maintained either by FORTRAN control cards or via a storage scope and sense switches. The task includes algorithms for line-shape, energy and efficiency calibrations, and peak-search and peak-fitting routines. The current version of SAMPO can provide most of the features found in previous programs, plus a number of important additions. Among the features used for nuclear spectroscopic data analysis are:

a) The fitting and subsequent subtraction of background.

b) The fitting of photopeaks to analytical functions and determination of the centroid for each peak.

c) The preparation of an internal energy calibration curve, and its application to determine the energy and the statistical error of the energy for each peak.

d) The calculation of net peak area and statistical error of the area for each peak and conversion of these to relative intensities via an internally prepared detector efficiency curve.

e) The resolving or stripping of multiplets using the peak-fitting parameters.

f) The plotting of spectra on the Calcomp or line-printer.

g) The calculation of half-life data.

The tabulated results of the SAMPO analysis, together with plots of the raw data, fitted background, and peak fits, are output on the line-printer. A section of a SAMPO output for a ^{43m}Ti spectrum is shown in Figure 3-8. These peaks are the same ones as used in the MOIRAE Figures and output example from Section 3.1.1.

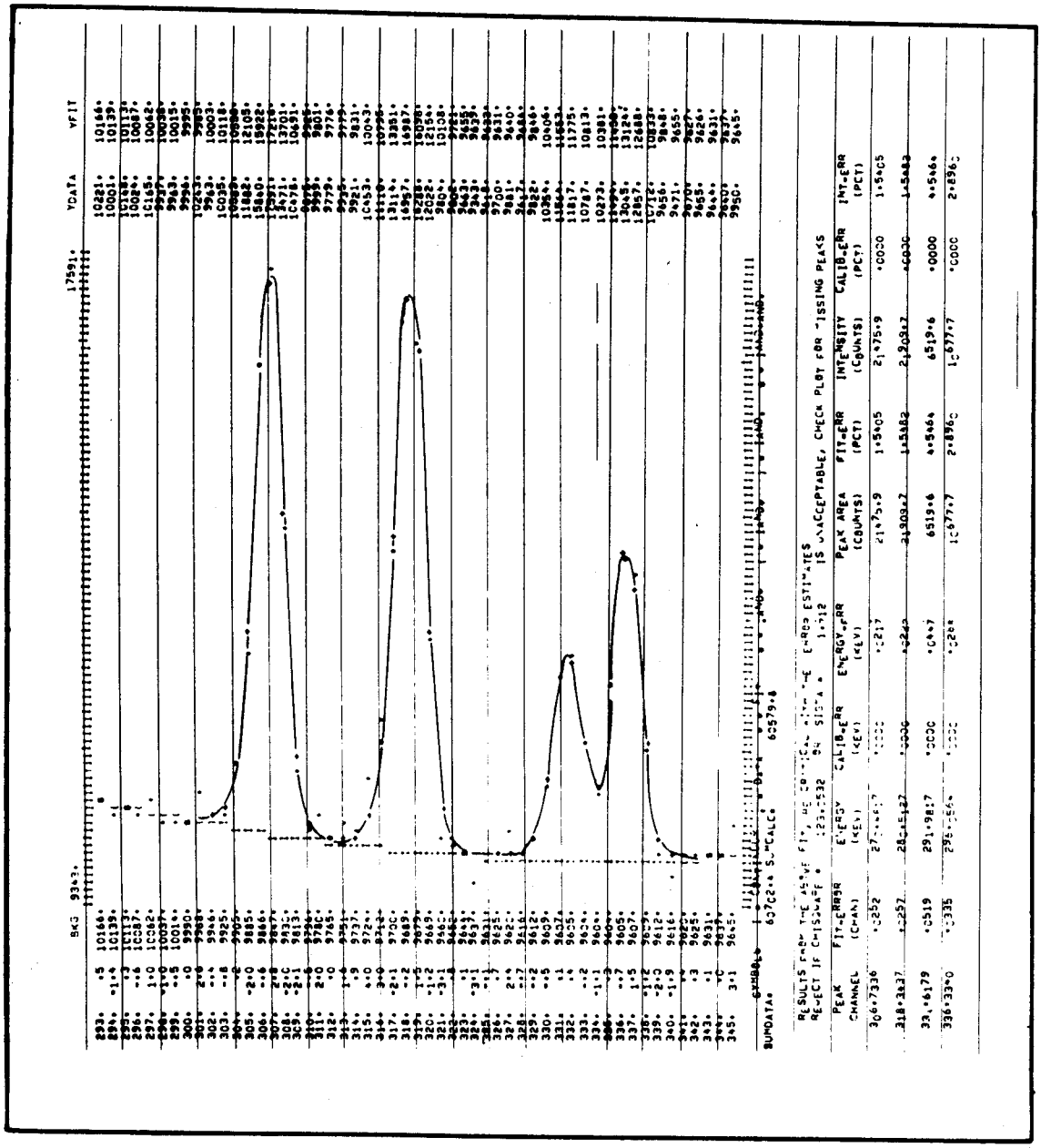

Figure 3-8. Photograph of a portion of the line-printer output from a SAMPO analysis. The peaks shown are the same as illustrated in section 3.1.1.

Each experimental peak is fitted to a Gaussian function having exponential tails. The shape parameters for the peak-fitting routine are obtained from an initial shape calibration using single, well-resolved γ peaks distributed over regular intervals throughout the entire spectrum under analysis. These shape parameters are stored and a linear interpolation is used to determine the parameters for fitting the remainder of the peaks in the spectrum. The shape parameters can be punched out and used in subsequent analysis of γ-ray spectra taken under the same experimental conditions, thereby providing a considerable savings in computer time.

The centroids determined for standard peaks, together with the energies for these standards, are then used to prepare an energy calibration curve. Although a higher-order polynomial can be used to form the calibration curve, the standard calibration method is to perform a piecewise linear fit between succeeding standard points. Likewise, an efficiency calibration curve can be prepared using a number of well-defined peaks and their relative intensities.

The data analysis performed under SAMPO can be done in two modes, automatic or manual. The complete analysis of all peaks in a spectrum normally requires utilization of both modes. In the automatic mode, SAMPO scans the spectrum and locates all statistically significant peaks based on the expected line shape. It then determines appropriate fitting intervals and fits the peaks using the shape, energy, and efficiency calibration data. The manual mode is then used for the analysis of peaks missed by the automatic scan. These include weak peaks which fall below the minimum statistical limit for automatic acceptance, multiplets that are not resolved, and other peaks having poor shape. In the manual

mode, only those peaks are analyzed for which approximate centroids and fitting intervals have been input. The entire spectrum can be analyzed manually, but in practice the automatic mode is almost always used for the first scan. Thus, a minimum of two passes of SAMPO through the computer is necessary to accomplish the complete analysis of a γ-ray spectrum.

As illustrated in Figure 3-8, the line-printer output from a SAMPO analysis lists the various parameters in considerable detail. A plot of each fitted interval is provided, showing the raw data, the calculated background, and the resultant fit for each peak. The columns on the right show the counts per channel for the raw data (YDATA) and the counts per channel for the background curve and fitted peak (YFIT). The three columns of numbers to the left of the plot give (from left to right): the channel number of each point contained in the interval shown; the difference between the raw data and the calculated fit at each point; and the calculated background at each location. The key to the symbols used in the plot is given directly under the plot itself. Near the bottom of the figure, the results of the analysis of the plotted section are presented in tabular form. This table includes, for each peak fit, the centroid and its error, the energy, the energy error due to the calibration curve, the overall energy error, the area of the fitted peak together with its error, the relative intensity of the fitted peak, the intensity error introduced by the efficiency calibration curve, and finally the total intensity error. When the intensity calibration data are not read in, only the net peak areas and relative peak areas are given in the output. The statistical error for each area determination is given as a percentage error and therefore reflects the difference

between the fitted analytical function and the raw data. Thus, this error indicates the degree to which a given peak shape matches the shapes of nearby standard peaks, as used in the shape-parameter determinations.

Although SAMPO offers many advantages over previous data analysis routines, its real forte is its ability to strip or resolve peaks in a multiplet. For complex spectra, containing many unresolved peaks, the amount of time saved by using SAMPO is phenomenal. Spectra which would normally require weeks to strip by hand can be analyzed in a matter of minutes.

The sheer speed of the program makes its use desirable for routine analysis. Even though several peaks may require the use of manual mode, SAMPO is considerably faster, more precise and more convenient than other methods. A relatively complex spectrum (50-75 peaks) can be analyzed in about 20 minutes, whereas the same spectrum analyzed with MOIRAE or MOD 7 would require 2-3 hours. In this study, SAMPO has been used extensively for the analysis of the many complex spectra obtained from pulsed-beam, routing experiments.

Although SAMPO has inherently fewer disadvantages than the other programs described here, it does have a number of difficulties. The relatively low order of the background fitted (2nd), together with the short fitting intervals used, result in a poorly approximated background in regions of low statistics and/or near Compton edges. (Higher background orders are now available.) Consequently, these regions must be fitted in the slower manual mode. The use of a standard peak shape sometimes results in many missed peaks. For example, beam-on spectra and high count-rate spectra having irregular peak shapes are often difficult to analyze under SAMPO.

An on-line, interactive version of SAMPO also has been adapted to the Sigma-7 system by C. Morgan. In this mode, the data are displayed on a storage oscilloscope and control is maintained through sense switches. Each fit may then be examined visually by the operator before being accepted. If a fit is not acceptable, the operator may change the length of the fitting interval or alter the number of peaks and/or their centroids. However, the background fit is restricted to a second order polynomial. Although the fits obtained using this technique are improved, the direct operator control adds two disadvantages common to other methods, i.e., longer analysis time and further injection of operator bias.

Generally speaking, SAMPO represents a significant advancement in the speed and versatility of data analysis. The results of analyses using all three programs are comparable. Intensity determinations show the greatest variation among methods, because of their sensitive dependence on background fit. This variation is especially pronounced for weak, poorly-shaped peaks on irregular backgrounds. The best method of analysis of any particular spectrum must be determined by weighing the character of that spectrum against the advantages and disadvantages of the various data analysis routines.

3.1.4 γ-Ray Energy and Intensity Calculation

Regardless of the analysis method used, the resultant centroids and areas of the unknown peaks must somehow be related to relative energies and intensities. This is accomplished by calibrating the detector system using well-known standard sources. The γ-ray energies are obtained by computing a least-squares quadratic calibration equation from the centroid channel numbers of well-known standard γ-rays and then determining the energies of the unknown peaks from their centroids and this calibration curve. These energy calibration curves can be

prepared from either "internal" standards or "external" standards. Internal standards are counted simultaneously with the unknown source, and are contained in the same spectrum. External standards are counted under the same experimental conditions as the unknown but are contained in a separate spectrum. Internal standards generally give more accurate calibrations but have the disadvantage of obscuring some of the unknown peaks. Normally, one uses internal standards to establish the energies of several unknown peaks and subsequently uses these established energies in later spectra as secondary internal standards to calibrate weak and previously obscured peaks. In some experiments (e.g., on-line, pulsed-beam experiments), the use of internal standards is quite difficult, and one must rely on external standards. Sometimes side reaction products and contaminants (e.g., ^{22}Na) provide γ rays which can be utilized as internal standards in such experiments.

The proper selection and utilization of these standard calibration sources are very important factors in determining the accuracy of the energy calibration curve. The ideal selection would consist of a few standards, having only γ rays which closely surround the unknown peaks, that are of approximately the same intensity and which cover the entire interval of interest without obscuring any of the unknown γ rays. In reality this never happens, and one is forced to compromise the limited number of available standards and the need for good calibration points with the spectral distribution of his unknown. Usually, this requires the bootstrap method of calibrating a few unknown peaks and then employing these as secondary internal standards.

The γ-ray relative intensities are determined by using previously prepared detector efficiency curves. Since photopeak efficiencies of

Ge(Li) detectors are a function of many factors such as detector size, geometry, total active volume, etc., individual sets of efficiency curves must be tailor-made for each detector. Since the detector efficiency varies with the detector-source geometry, an efficiency curve must be prepared for the various possible geometries. Current calibrations include curves for front-entry geometry with the source at contact, 2 inches and 10 inches from the detectors. These efficiency curves were prepared using γ rays whose relative intensities were well-known. The data were then fitted to a third order polynomial of the form: log (efficiency) = $A + B \log E + C (\log E)^2 + D (\log E)^3$, where A, B, C and D are empirical constants and E is the energy in keV. A typical efficiency curve is shown in Figure 3-9. This curve is for a 10.4% Ge(Li) detector with a source-detector distance of 10 inches. A more complete discussion of the preparation of detector efficiency curves may be found in (Gie71).

These curves have been incorporated into MOIRAE E(I) and are available on cards for SAMPO input. One merely specifies the detector employed and the source distance, and the programs use the calculated energies and appropriate efficiency calibration to convert the net peak areas into relative intensities.

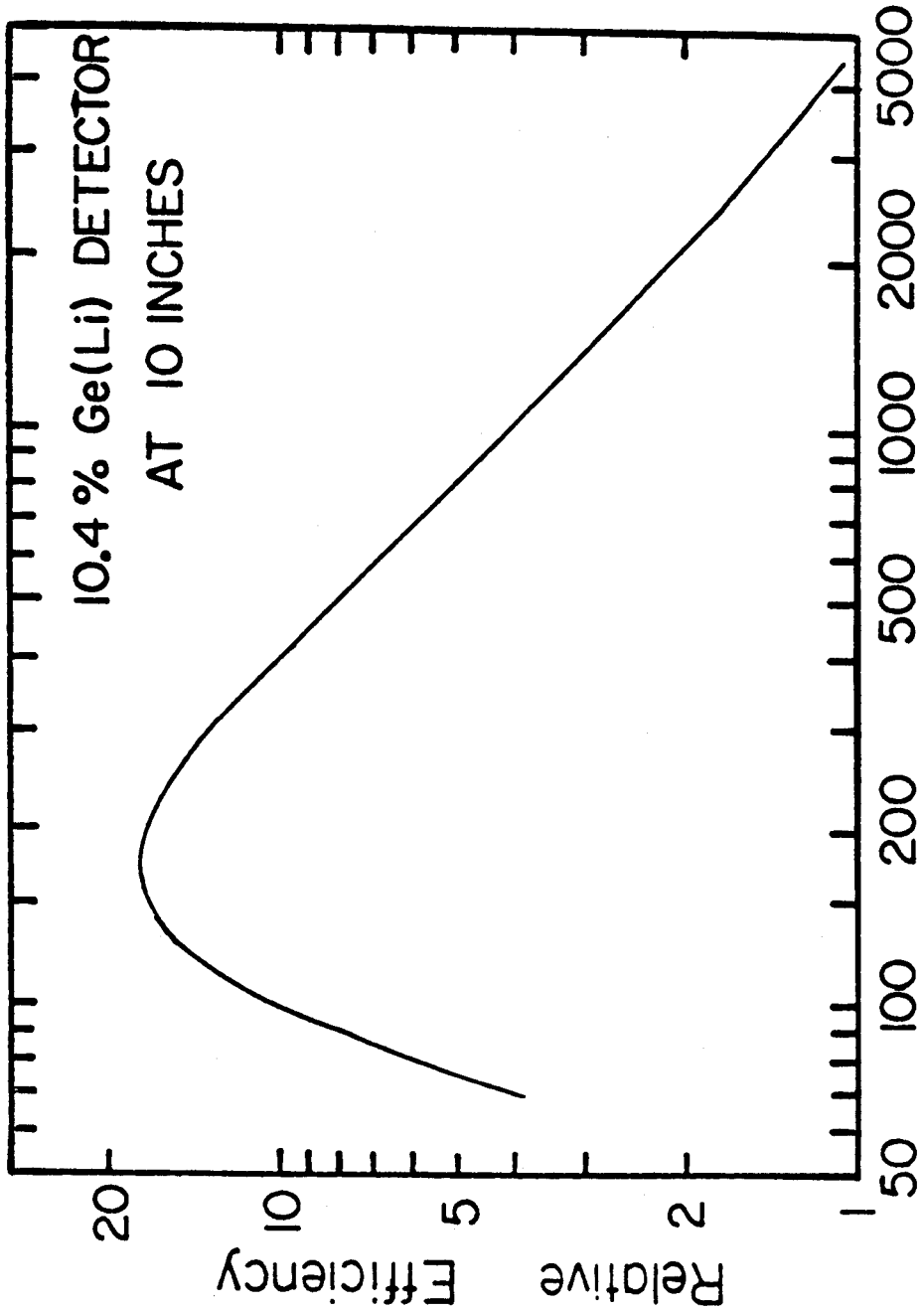

Figure 3-9. A typical detector efficiency curve for Ge(Li) detectors. This curve is for a 10.4% efficient Ge(Li) detector with a source-detector distance of 10 inches.

3.2 Double and Single Escape Peaks

Early studies performed with relatively small, inefficient Ge(Li) detectors made extensive use of single escape peaks (i.e., peaks differing from a full-energy photopeak by 511.01 keV) and double escape peaks (peaks having energies 1022.02 keV less than a full-energy photopeak). However, the development of larger, more efficient detectors has relegated this once useful, routine tool to more specialized applications. Only studies of highly energetic γ rays (>3000 keV) now utilize escape peaks for routine photopeak energy determination. The 511 keV-511 keV-γ triple coincidence experiment described in Section 3.6.2B is normally used to determine which peaks in a given spectrum are double escape peaks. Another technique for determining single and double escape peaks is their lack of Compton edges. However, this method is virtually useless in complex spectra. The use of escape peaks for the determination of full-energy photopeaks may be slightly inaccurate, since recent evidence has suggested that the energy differences need to be corrected by a "field increment effect" factor, based upon the detector-source geometry and the electric field in the detector produced by the diode bias voltage (Gun68). (The effect is most important for planar detectors, and is washed out in coaxial ones.) This factor is quite small (<0.1 keV) and was not considered in this study, especially since escape peaks were not relied on for precise energy determinations. In this study, single and double escape peaks were utilized to indicate or confirm the existence of highly energetic γ rays from the decay of ^{40}Sc and other short-lived species.

3.3 The PDP-9 Computer and Related Programs

In addition to providing an excellent facility for data acquisition, the Nuclear Chemistry group's PDP-9 computer has been extremely useful for various numerical calculations used in data analysis. The various programs are written in FORTRAN, stored on DECtape and run under a keyboard monitor system. Each program is called from a magnetic tape into core, as needed, via an appropriate teletype command. The majority of the present programs were written by R. Eppley of the Nuclear Chemistry group, now at LBL. More complete details of the PDP-9 operation and program descriptions can be found in references (Epp70a) and (Epp69).

The following are a few of the programs which were used in this study:

1) ARITH - This program allows the PDP-9 to be used as an electronic desk calculator, capable of performing simple numerical calculations.

2) INTEN - A program used for the calculation and renormalization of γ-ray intensities.

3) FERM 3 - This code calculates Fermi functions for use in preparing Fermi-Kurie plots of electron and positron spectra.

4) PROB - This very useful program is for the calculation of transition probabilities and half-lives of γ-ray transitions based on the single particle equations of Moszkowski.

5) PLYFIT - This is a general polynomial least-squares program.

6) ICC - This is a program which is used for the interpolation of the theoretical internal conversion coefficients from

published tables.

7) INTERP - A program similar to ICC, but which is based on the theory of splines and adapted from the program given by Hager and Seltzer (Hag68).

8) VC - This program calculates Clebsch-Gordon coefficients, using Racah's general equation.

9) TRIGA - A program which calculates the expected activity of samples submitted for irradiation with the MSU TRIGA reactor.

In addition to these programs, more complete data analysis routines of the MOIRAE variety are currently being developed for use on the PDP-9. When the present task of interfacing the PDP-9 and the Sigma-7 is complete, the convenience and versatility of using the PDP-9 for data acquisition and analysis will be greatly enhanced.

3.4 The Analysis of Beta Spectra

The data obtained from beta singles and beta-gamma coincidence experiments must be analyzed in order to extract the desired beta end-point energies and spectral shapes. The method used is that of preparing Fermi-Kurie plots from the data. Although somewhat complex, this is the standard technique used for the analysis of beta spectra.

Since this technique has had little previous use or documentation by the Nuclear Chemistry Group, I would like to discuss the available theory, calculation and codes for beta analysis in some detail, beginning with a general discussion of beta analysis taken from (Tab51).

3.4.1 Principles of Beta Analysis

3.4.1A Beta-Ray Spectra

Positrons or electrons may be ejected in the course of spontaneous decay of atomic nuclei. The kinetic energy of these particles may be measured to a precision of one percent or *better*, depending upon the detection device. The most widespread instrument for precise measurement of electron energies is the magnetic spectrometer, although scintillation devices and solid-state detectors are commonly used. If one measures the energies of a few electrons emitted in succession by nuclei of a β-radioactive material, he finds that the energies are spread at random over a wide range without apparent continuity. However, upon measuring a large number of such energies a regular pattern emerges, and one can draw a curve representing their statistical distribution in various energy intervals. This distribution is the beta-ray spectrum of the material and is the curve representing the raw data from a typical experiment.

The statistical distribution of electrons covers all energies from zero up to a maximum energy, E_o, characteristic of the decay and

representative of the total energy actually released by the nucleus in the course of its β-disintegration process. Whenever the electron is ejected with an energy $E < E_o$, the remainder of the energy is carried away by a neutrino of energy $E_o - E$. The observed statistical distribution of electron energies reflects the relative probability of the various possible ways in which the total energy, E_o, released by a nucleus can be shared between an electron and a neutrino. The theoretical analysis of a beta-ray spectrum attempts to determine the factors that govern this sharing of energy.

The first step in the analysis consists of evaluating the influence of the pertinent extranuclear factors, i.e., those factors which are only incidental to the process of the decay and do not depend upon the internal processes of the nucleus. When these factors are properly subtracted, the remaining features of the beta-ray spectrum should reflect the truly nuclear features of the disintegration phenomenon.

3.4.1B The Statistical Weight Factor

In general, all beta-ray spectra are characterized by their bell-shaped plots. The electrons may carry away almost all of the available energy or practically none of it, although the probability of either of these conditions is extremely low. The most likely event is that the electron and the neutrino will share the total energy in comparable amounts. From statistical mechanics it is known that, of all modes of motion of two or more particles with a fixed total energy, the great majority correspond to approximately an even sharing of energy among the particles. More specifically, the types of motions of the electron and of the neutrino, which have been ejected from a nucleus, can be classified on the basis of the components p_x, p_y and p_z, and q_x, q_y

and q_z of their linear momenta. Any particular subdivision of the available energy E_o, between the electron (E) and the neutrino (E_o-E) implies fixing the magnitude of the momenta of the two particles, namely, $p = \sqrt{p_x^2 + p_y^2 + p_z^2}$ and $q = \sqrt{q_x^2 + q_y^2 + q_z^2}$. The smaller the value of E, and, consequently, the value of p, the smaller is the range of possible values of p_x, p_y, and p_z. This means that the variety of modes of motion of the electron is an increasing function of E. However, if E is so large that E_o-E and q become too small, the possible modes of motion of the neutrino become limited. Thus, in order to maintain a large variety of combined motions for both particles, the total energy E_o should be shared comparably. This argument leads one to prove, through a quantum mechanical treatment, that the probability that the magnitude of the electron's momentum lies between p and $p + dp$ is proportional to the product

$$p^2q^2dp \tag{3-1}$$

This result is frequently expressed by the statement that the value of p^2q^2dp represents the statistical weight of a particular subdivision of energy.

3.4.1C Energy and Momentum Formulas

The momentum of an electron can be expressed in terms of the product of its mass, m, and the velocity of light, c, by means of the symbol

$$\eta = \frac{p}{mc} \tag{3-2}$$

Likewise, the energies E and E_o are expressed in terms of the product mc^2, by means of the symbols

$$\varepsilon = \frac{E}{mc^2}, \quad \varepsilon_o = \frac{E_o}{mc^2} \tag{3-3}$$

The energy, E, includes the rest energy mc^2, of the electron, as well as its kinetic energy. Thus, ε is related to η by the equation

$$\varepsilon = \sqrt{1 + \eta^2} \tag{3-4}$$

Since the neutrino has a negligible rest mass, the magnitude of its momentum, q, is proportional to its energy, $\varepsilon_o - \varepsilon$.

The expression (3-1) for the statistical weight of a particular energy subdivision may be rewritten as

$$\eta^2(\varepsilon_o - \varepsilon)^2 d\eta = \eta^2(\sqrt{1 + \eta_o^2} - \sqrt{1 + \eta^2})^2 d\eta \tag{3-5}$$

The *magnetic* techniques for measurements of electron energy lead to a direct determination of the momentum, rather than of the energy. The momentum is proportional to the product of the strength, B, of a magnetic field and of the radius of curvature, ρ, of the path that it forces the electron to follow:

$$B\rho = 1704.3\eta \text{ gauss cm} \tag{3-6}$$

Consequently, the experimental methods yield directly the statistical distribution of momenta, i.e., the number

$$N(\eta)\, d\eta \tag{3-7}$$

of electrons whose momenta lie between η and $\eta + d\eta$.

3.4.1 D The First Step of the Analysis

The significance of the concept of statistical weight is as follows: If all other conditions were discounted such that only the statistical weight could influence the sharing of energy between electron and neutrino, the number (3-7) should be proportional to (3-5), that is, the ratio of (3-7) to (3-5) *should* be a constant, independent of η (although this is not always true). Nevertheless, if one divides the observed distribution (3-7) by the statistical weight (3-5), he achieves a first step in the analysis of the experimental data. In this way, one eliminates the effect

of an extraneous factor that would otherwise obscure the details of the nuclear mechanism.

3.4.1E Maximum Beta Energy Determination

Inspection of the plot of $N(\eta)$ does not enable one to determine ε_o accurately, since the number of electrons observed near the maximum energy is very small. Therefore, in practice, one can use the following procedure.

Instead of dividing (3-7) by (3-5), one may divide it by $\eta^2 d\eta$ and then take the square root of the resulting ratio

$$\sqrt{N(\eta)d\eta/\eta^2 d\eta} = \sqrt{N/\eta^2} \qquad (3\text{-}8)$$

and plot it against ε (Kur36). If (3-7) were proportional to (3-5), the ratio (3-8) would be proportional to $\varepsilon_o - \varepsilon$, and its plot would be a straight line intercepting the ε-axis at ε_o. Although the resulting plots are not really expected to be straight lines, they are reasonably straight near the high-energy limit and serve well for the graphical determination of ε_o as the intercept.

3.4.1 F Effect of Electrostatic Forces

An electron that has been ejected by a nucleus finds itself subject to the electrostatic action of the nucleus, which is attractive or repulsive, depending on whether the electron is negative or positive. This electrostatic force remains appreciable until the electron gets sufficiently far away from the nucleus. The force affects the motion of the electrons to a different extent depending upon their energy. Therefore, it may modify the relative probability that an electron be ejected with one energy or another.

The qualitative effect of the electrostatic force is readily

understandable in the case of positron emission. If a positron were liberated with no kinetic energy at the edge of a nucleus, the repulsion exerted on it by the nuclear charge would speed it up to attain an eventual kinetic energy of the order of millions of electron volts. This circumstance might seem to indicate that positive beta rays necessarily leave a radioactive material with a high kinetic energy. However, they can also come out with a lower energy by "leaking" through the repulsive potential barrier that surrounds the nucleus, just as α particles do. The fact remains that the emission of low-energy positive electrons by nuclei meets unfavorable conditions.

The qualitative discussion of the effect of the electrostatic force upon the emission of negative electrons is not so simple. However, this effect is opposite to the effect on positrons. It may be carried out rather conveniently by treating the transit of the electron from the nucleus to the space outside the atom as a problem in electron optics, that is, according to a "wave picture." In this way one arrives at the rule for calculating the effect of the electrostatic force upon the beta-ray spectrum, both for positive and negative electrons.

An electron traveling away from a nucleus finds itself in a region where the electrostatic potential changes very rapidly from one point to the next. It is a fundamental phenomenon of atomic physics that the motion of an electron through a rapidly variable potential causes a substantial reflection of the electron wave-function, just as a rapid variation of the refraction index causes a substantial reflection of light. One can argue rather easily that, in the case of a negative electron, the reflection effect takes place within the limits of the K shell of

the atom. At larger distances from the nucleus the potential experiences only a small fractional change within a wavelength, and this is just the condition for the absence of reflection. Mathematically, this means that one can apply a WKB approximation in this latter region (Ros36). For the same reason, the reflected wave that returns to the nucleus interferes constructively with the wave that goes out from there in the opposite direction. This explains why the emission of negative electrons is enhanced by the electrostatic force. The effect of reflection is the more conspicuous, the larger the electrostatic potential with respect to the kinetic energy of the electron, i.e., the larger the atomic number and the smaller the electron energy. As the reflection takes place within the inner part of the atom, we may also assume in practice that the electrostatic force exerted by the nucleus follows the "$1/r^2$" law, i.e., that it is not greatly modified by the presence of the atomic electrons (Ros36).

The idea of treating the outward travel of the electron as an optical phenomenon also suggests that one applies a principle of optical reciprocity to the determination of the probability of electron emission. Accordingly, we argue that an electron released at the nucleus has the same chance of eventually leaving the atom with a certain energy as an electron entering the atom with the same energy has of eventually reaching the nucleus. In fact quantum mechanical calculation (Fer34) shows that, other conditions being equal, the probability of emission of a beta ray of given energy is proportional to the ratio

$$F = |\psi(\text{center})|^2 / |\psi(\text{out})|^2 \qquad (3\text{-}9)$$

where ψ is the wave function of an electron of that energy in the space containing the atom, ψ(center) is the value of that function at the

center of the atom, i.e., at the nucleus, and ψ(out) is the value outside the atom.

The ratio F may be calculated from a knowledge of the solution of the wave equation for an electron moving in a "$1/r^2$" field of force. This particular portion of the beta-ray problem appears thus to coincide with a standard problem of atomic physics. Therefore, the numerical calculation of F represents a contribution to a general problem of atomic physics.

The value of the ratio F depends primarily on two quantities:

(a) The electric charge of the nucleus, that is, its atomic number Z. The appropriate value of this number is the one pertaining to the end product of the β disintegration, i.e., to the nuclear charge after the emission of the electron.

(b) The energy, E, or the momentum, η, of the electron after it has left the atom.

3.4.1G The Second Step of the Analysis

From the discussion above, it follows that the statistical distribution of electron momenta, $N(\eta)$, should be proportional to the function $F(Z,\eta)$ alone, if the distribution were determined entirely by the effect of the electrostatic force. This is not the case, but one can apply here again the procedure used earlier to deal with the statistical weight factor: the effect of two incidental factors upon the beta-ray spectrum is removed if one divides the distribution $N(\eta)d\eta$ by the statistical weight factor (3-5) and by the electrostatic factor $F(Z,\eta)$, that is, if he plots the ratio

$$N(\eta)d\eta/[\eta^2(\varepsilon_0 - \varepsilon)^2 d\eta F(Z,\eta)] \qquad (3\text{-}10)$$

against ε.

Alternately, by analogy to (3-8), one may plot the ratio

$$\sqrt{N(\eta)/\eta^2 F(Z,\eta)} \qquad (3\text{-}11)$$

against ε. If the effects of statistical weight and of the electrostatic force are the only important factors, this plot should be a straight line, intercepting the ε-axis at ε_o. This is actually observed in a large number of beta spectra. One concludes from this result that, in a broad class of beta disintegrations, the truly nuclear effects do not influence the sharing of energy between the electron and the neutrino.

The plot of the function (3-11) against ε is usually called a Fermi plot or a Fermi-Kurie plot after the authors who suggested this method of analysis (Kur36).

3.4.1H Allowed and Forbidden Spectra

A particle may be ejected from a nucleus not straight outward but, so to speak, tangentially, that is, endowed with a certain angular momentum of orbital motion about the nucleus. Such a particle experiences at once the effect of a powerful centrifugal force that pushes it away from the nucleus. This force acts much like the electrostatic repulsion does upon positive beta particles.

As in the case of the electrostatic repulsion, the effect of the centrifugal force may be described as the effect of a potential barrier that surrounds the nucleus. This potential barrier can rise even more sharply than an electrostatic potential barrier and it may affect the outgoing neutrino as well as the electron.

The orbital angular momentum of an outgoing particle must be

a whole multiple of $\hbar$, according to quantum mechanics. If this angular momentum amounts to a few units of $\hbar$, the centrifugal potential barrier reaches such a high level at the edge of a nucleus that the outgoing particle must "leak through" it.

This circumstance has two effects. First, any particle that must come out with an orbital angular momentum other than zero is unlikely to take the minor share of the total energy available because this would involve a more difficult leakage through the barrier. Second, if the conditions are such that at least one of the particles must come out with some non-zero angular momentum, the process of disintegration must proceed slowly, at a pace set by the rate of leakage through the barrier. A kind of disintegration that proceeds under these conditions is said to be "forbidden".

A very special interest is attached to the case where the particles are ejected "straight out" from the nucleus, that is, without any angular momentum. This case is particularly easy to handle because no centrifugal effect need be considered. Moreover, this case may be expected to be a most frequent one in practice. In fact, whenever a process of nuclear disintegration may develop through alternate paths, it naturally has a high probability of following a path that does not require outgoing particles to leak through a potential barrier, other conditions being equal.

Most of the work on beta spectra has been devoted in the past to the study of "allowed" spectra that do not exhibit any effect of centrifugal forces. Fermi's original theory of beta emission dealt particularly with this case.

A few spectra that exhibit the effect of centrifugal forces have been analyzed successfully, beginning about 1949 (Lan49), (Wu49), and (Oso49). The theoretical analysis of such "forbidden" beta spectra has been the object of a paper by Konopinski and Uhlenbeck (Kon41) and is also discussed in Konopinski's review article (Kon43).

3.4.1I The $F(Z,\eta)$ Factor for Allowed Spectra

The motion of an electron in the space around a nucleus proceeds, in the main, according to the Schrödinger equation. This equation does not apply when the velocity of the electron approaches the velocity of light, but in this case the attraction of the nucleus becomes unimportant, and there is little need for a special study (except in the immediate proximity of the nucleus, as discussed below).

The solution of the Schrödinger equation for an electron moving under the electrostatic attraction or repulsion of a nucleus, without any angular momentum, leads to a well-known expression for F, namely, (Kur36)

$$F_n(Z,\eta) = y/|1 - \exp_{\mp}(y)| \qquad (3\text{-}12)$$

where the upper sign applies to negative and the lower to positive electrons, and

$$y = 4\pi^2 Ze^2/hv = 2\pi Z/137(v/c) = 2\pi\gamma/\beta = 2\pi Z\sqrt{1+\eta^2}/137\eta \qquad (3\text{-}13)$$

and

$$v = c\eta/\sqrt{1+\eta^2} = c\eta/\varepsilon = \beta c \qquad (3\text{-}14)$$

is the eventual velocity of the electron after escaping from the atom.

The relativistic effect is not quite unimportant because an electron always approaches the speed of light when it moves in the immediate proximity of the nucleus. Approach to the speed of light brings about an increase of the apparent mass of the electron, that

is, the momentum becomes a more rapidly increasing function of the kinetic energy than it is at lower speeds. In turn, the wavelength experiences a more rapid decrease. Consequently, the relativistic effect enhances the fractional change of the electrostatic potential over one electron wavelength, which is responsible for the reflection effect discussed previously. Therefore, this effect makes the value of $|\psi(\text{center})|^2$ and hence that of $F(Z,\eta)$ larger than they are expected to be on the basis of the nonrelativistic treatment.

Relativistic wave functions for the motion of an electron in a "$1/r^2$" field of force are known from the solution of the appropriate Dirac equation. The relativistic effect just discussed is so strong that the wave functions would become infinitely large right at the position of the nucleus, if the nucleus were actually a point charge as it is assumed to be in the calculation. Fermi suggested in his original work (Fer34) a practical way of estimating $F(Z,\eta)$, despite this difficulty. One should first calculate the wave function as if the nucleus were a point charge and then introduce into equation (3-9) in the place of $|\psi(\text{center})|^2$ the value of $|\psi|^2$ at the edge of the nucleus. The idea is that the electrostatic force no longer follows the "$1/r^2$" law within the nucleus and, therefore, ψ should no longer increase very much within the nucleus itself.

The value of $F(Z,\eta)$ calculated according to this procedure is

$$F(Z,\eta) = \left|\frac{\Gamma(3)}{\Gamma(3+2S)}\right|^2\left(\frac{4\pi mc\eta R}{h}\right)^{2S} e^{\pm\pi\delta} \times|\Gamma(1+S+i\delta)|^2\left(1+\frac{S}{2}\right) \qquad (3\text{-}15)$$

where R is the nuclear radius, the $\pm$ sign applies to negative or positive electrons and

$$S = \sqrt{1 - Z^2/137^2} - 1$$

$$\delta = Z\sqrt{1 + \eta^2}/137\eta = y/2\pi \qquad (3\text{-}16)$$

This value reduces to (3-12) if one sets $S = 0$, since $|\Gamma(1 + i\delta)|^2 = \pi\delta/|\sinh\pi\delta|$. Therefore, (3-15) can be written in the form

$$F(Z,\eta) = F_n(Z,\eta)\left(\frac{4\pi mc\eta R}{h}\right)^{2S} \times \left|\frac{\Gamma(3)\Gamma(1 + S + i\delta)}{\Gamma(3 + 2S)\Gamma(1 + i\delta)}\right|^2 \left(1 + \frac{S}{2}\right) \qquad (3\text{-}17)$$

This last formula shows clearly how the relativistic effect depends on the magnitude of S.

3.4.1J Screening Corrections

It is pointed out in section *F* that the presence of the atomic electrons does not modify the electrostatic *force* in the space *near* a nucleus where it matters for the determination of β spectra. Nevertheless, the attraction or repulsion that the atomic electrons exert farther away from the nucleus does modify to some extent the electrostatic *potential* near the nucleus. This modification of the potential is called the effect of "outer screening", because the external electrons of the atom screen off the outside space from the electrostatic force of the nucleus.

A negative electron of given total energy that penetrates near the nucleus through the outer screen of electrons does not have so high a kinetic energy as it would have in the absence of the screen. Conversely, a positive electron preserves more of its kinetic energy. Therefore, Rose pointed out (Ros36) that one can take into account the effect of outer screening by calculating the electrostatic effect as if the electron energy differed from its actual value by an amount equal to the potential energy, V_o, due to the outer screening.

The value of V_o is not defined very exactly, as the whole picture that the atomic electrons exert only an effect of outer screening represents only an approximation. The approximation is justifiable insofar as the effect on the β spectra is itself quite small.

A rather good estimate of V_o can be obtained from the comparison of the experimental binding energies of *K* electrons with the theoretical values for the hydrogen-like model. This estimate should be good at least for application to the case of electrons whose kinetic energy outside the atom does not greatly exceed the *K* electron binding energy. In the case of electrons of higher kinetic energy, the important electrostatic effect stems from a region closer in than the *K* shell, and one might use a somewhat higher value of V_o, especially for light elements.

Another estimate of V_o may be obtained more simply from the Thomas-Fermi distribution of electrons in the atom. The outer screening potential is a function of the distance from the nucleus. An average value pertaining to the interesting range of distances has been estimated (Ros36) to be about $30\ Z^{4/3}$ eV. The Thomas-Fermi value of V_o calculated for an electron right at the center of the atom is $48\ Z^{4/3}$ eV and sets an upper limit to the effective value of V_o.

The evaluation of the effect of outer screening according to the method suggested by Rose applies to the calculation of eigenfunctions normalized "per unit *energy*". Therefore, one should take the function $\eta\sqrt{1+\eta^2}F(Z,\eta)$ or the equivalent function $f(Z,\eta)\sqrt{1+\eta^2}/\eta$ and find out what fractional change it experiences if the β-ray energy is reduced by V_o in the case of negative electrons or increased by V_o in the case of positive ones.

This change turns out to amount to a few percent, at most,

except in the case of low energy positrons.

The outer screening has a much larger effect upon positive electrons than upon negative ones because it reduces the height and thickness of the potential barrier through which the positive beta rays have to leak.

An accurate calculation of the screening effect has been performed by J. R. Rietz (Rie50) for a number of values of the atomic number and of the electron energy. He calculated numerically the relativistic wave function of an electron moving through an atom whose normal complement of electrons follows the Thomas-Fermi distribution. Thereby, Rietz obtained an almost exact evaluation of the "Fermi function" that can be compared with the values uncorrected for screening or with the values corrected by less refined methods.

3.4.1K The Total Beta Emission Probability

The factors considered in the preceding sections do not influence only the subdivision of energy between electron and neutrino. They affect the total rate at which the beta disintegration proceeds. In other words, the absolute probability of beta emission is actually proportional to the statistical weight factor and to $F(Z,\eta)$, other conditions being equal.

Therefore, the total value of this product, covering all possible ways of subdividing the energy between the two particles, namely,

$$\int_0^{\sqrt{1+\eta_0^2}} \eta^2(\varepsilon_0 - \varepsilon)^2 F(Z,\eta)\,d\eta$$

$$= \phi(Z) \int_0^{\sqrt{1+\eta_0^2}} (\varepsilon_0 - \varepsilon)^2 f(Z,\eta)\,d\eta \qquad (3\text{-}18)$$

represents a determining factor of the disintegration rate, which is

incidental to the nuclear process itself.

The systematic evaluation of the integral (3-18) for all values of Z and η_0 involves a substantial amount of labor. Calculations of the integral (3-18) for the values of Z and η_0, which correspond to observed beta radioactivities have been made by S. Moszkowski and by E. Feenberg and G. Trigg (Fee50). In both cases a preliminary evaluation of the Fermi function was required. This evaluation was carried out by the authors by using approximate formulas to the desired precision.

3.4.2 Preparation of Fermi Plots

Fermi plots of the data obtained in this study were prepared both by the use of tabulated Fermi functions and corrections and by computer programs designed to calculate these functions. Although considerable effort was expended in the development of computer programs, the final analyses presented here were performed using tabulated functions (Tab51). The convenience, reliability, and number of corrections (e.g. screening) offered in various tables are difficult to beat, unless a large number of analyses need to be performed. Since the analysis involves the use of the Γ function of a complex argument, a function which cannot be readily evaluated, tabulated results from rather extensive calculations are most convenient for occasional use by the experimentalist.

The tables used for the analyses presented in this work were compiled by the National Bureau of Standards and are perhaps the most useful and comprehensive tabulation available (Tab51).

The main tables give the value of the so-called "Fermi Function":

$$f(Z,\eta) = \eta^{2+2S} e^{\pm\pi\delta} |\Gamma(1 + S + i\delta)|^2$$

where the $\pm$ sign applies to the spectra of negative and positive electrons,

respectively, and

η = momentum of the electron, after its ejection from the atom, in units of mc.

$S = \sqrt{1 - Z^2/137^2} - 1$

Z = atomic number

$\delta = Z\sqrt{1 + \eta^2}/137\eta$.

The tabulation covers all the values of Z that may be encountered in practice. The set of values of η are sufficient to enable the user to calculate the function at intermediate values readily by interpolation. The tabulation extends to η=7 ($\approx$3.5 MeV). Higher values of $f(Z,\eta)$ may be calculated to within approximately one percent by an empirical expression.

Key values of $|\Gamma(1 + S + i\delta)|^2$ were obtained by interpolating the table by W. Meissner (Mei39). In particular, the table used gives $\log_{10} |\Gamma(z)|$ for the triangular net

$$z = (2m+i2n\sqrt{3})/24$$

and

$$z = [(2m+1)+i(2n+1)\sqrt{3}]/24$$

with m = 6, 7, . . . , 17; n = 0, 1, . . . , 6, 7. Beyond the range of this table use was made of the following relation:

$$|\Gamma(a+ib)|^2=|\Gamma(a)|^2 \prod_{n=0}^{\infty}[1+b^2(n+a)^{-2}]^{-1}$$

The right-hand side may be expressed also in the following form, which is more suitable for computation:

$$\log|\Gamma(a+ib)|^2=2\log|\Gamma(a)| - \log\left(1+\frac{b^2}{a^2}\right)$$
$$b^2\frac{d^2}{da^2}\log\Gamma(a+1) + \frac{b^4}{12}\frac{d^4}{da^4}\log\Gamma(a+1) - \ldots$$

Values of $\Gamma(a)$, $(d^2/da^2)\log\Gamma(a+1)$, and $(d^4/da^4)\log\Gamma(a+1)$, etc., were obtained by interpolation in H. T. Davis (Dav35).

Key values of $f(Z,\eta)$ for Z = 10 to 100 and η = 0 to 7 were then obtained by adding the logarithms of the Γ function and of the factors $e^{\pm\pi\delta}$ and η^{2+2S}. These values were then differenced, and subtabulation, using Lagrangian interpolation formulas, was performed on IBM machines.

3.4.3 Program FERM 3

Program FERM 3 is a FORTRAN routine written by R. Eppley (Epp69), which runs on the PDP-9 computer. It was developed to calculate the values of Fermi functions at intermediate values not included in tabulations. However, the program is not for the interpolation of values, but, instead, actually calculates the Fermi function at each point, using a power series method. This program gives values in good agreement with those found in the tables and could easily be incorporated as a subroutine in a more complete code. The method of calculation is as follows:

The Fermi function can be written as (Tab51)

$$f(Z,\eta) = \eta^{2+2S} e^{\pm\pi\delta} |\Gamma(1+S+i\delta)|^2$$

where Z = atomic number

η = electron momentum

$S = \sqrt{1-\gamma^2} - 1$

$\gamma = Z/137.0$

$\delta = Z\sqrt{1+\eta^2}/137.0\ \eta$

The difficulty in the numerical computation is in evaluating the complex gamma function. It is of the form $|\Gamma(x+iy)|^2$ where $x = 1+S$ and $y = \delta$.

This expression is evaluated by the use of the expansion (Abr67)

$$\left|\frac{\Gamma(x+iy)}{\Gamma(x)}\right|^2 = \prod_{n=0}^{\infty} [1+y^2/(x+n)^2]^{-1}$$

Also,

$$\Gamma(x) = 1/\sum_{k=1}^{\infty} C_k x^k$$

where the coefficients C_1 through C_{26} are given in reference (Abr67). The required function is then constructed from the product of those two series.

$$|\Gamma(x+iy)|^2 = \left(\sum_{k=1}^{\infty} C_k x^k\right)\left(\prod_{n=0}^{\infty} [1+y^2/(x+n)^2]^{-1}\right)$$

The number of terms needed varies depending on the values of Z and η input.

3.4.4 Program FERMPLOT

Program FERMPLOT is a FORTRAN routine for the preparation of Fermi plots used in analysis of beta spectra. The program is a much modified version of a code originally written by G. Berzins for use with results from a magnetic spectrometer. The routine reads the data from the original punched deck, calculates the Fermi ordinate and energy for each point, makes a least-squares fit to the high energy portion, and finds the end-point channel number and its energy. It outputs on the line-printer the raw data, the calculated Fermi ordinate for each point, the Fermi ordinate converted to integral numbers (for use with the NDPLOT plotting routine), the interval used, the end-point channel and energy, the least-squared fit of the Fermi ordinates, and the least-squared fit in terms of integral numbers. Simultaneously, the integral Fermi ordinates and the integral least-squared fit of the Fermi ordinates are punched on cards for immediate plotting under NDPLOT. Resolving possible second and third end-points from the Fermi-Kurie plot is best performed by hand, although a routine is available which does this.

The following control cards, formats, and definitions are used with the program.

Card 1, (I5)

NCASES = The number of spectra for which calculations are to be performed

Card 2, (3I5, 8A8)

NCHAN = The number of channels in the spectrum to be read

MIN = The first channel number for which the calculations are to be performed .

MAX = The last channel number for which the calculations are to be performed

TITLE = The title of the spectrum

Card 3, (5F 10.6)

Z = Atomic number of the daughter

A = Number of nucleons in the daughter

B, C, D = Coefficients of the polynomial fit of energy to channel number

A FORTRAN listing of FERMPLOT may be found in Appendix A.

CHAPTER IV

THE DECAYS OF ^{53g}Fe AND ^{53m}Fe

4.1 Introduction

^{53}Fe, an 8.5-min nuclide decaying by both positron emission and electron capture, was first produced in 1937 by an (α,n) reaction on naturally occurring chromium (Rid37). However, the γ-ray activity associated with the decay of ^{53}Fe was not reported until 1953 (Nus53). Other than the work of Juliano, et al. in 1959 (Jul59), very little work has been performed to ascertain the levels in ^{53}Mn populated by the decay of ^{53}Fe. The bulk of the available knowledge concerning the levels in ^{53}Mn has been obtained through in-beam, reaction and scattering studies. For example, the levels have been investigated by means of the ^{52}Cr$(p,\gamma)^{53}$Mn reaction (Vui66,67), (McE68,70); the ^{56}Fe$(p,\alpha)^{53}$Mn reaction (Vej64); and the ^{52}Cr$(^3$He$,d)^{53}$Mn reaction (O'Br67).

The original impetus for undertaking this study was simply to elucidate the structure of ^{53}Mn by careful γ- and β-ray investigation of the levels populated in the ^{53}Fe decay. This approach was relatively untried, especially with Ge(Li) γ-ray detectors and would complement the existing direct excitation studies.

Knowledge of the ^{53}Mn level scheme is very important, not just for its own sake, but because it promises a good test of the validity of the simple shell model. de Shalit has pointed out that the N=28 closed shell is particularly stable, and therefore much less subject to configuration mixing than N=20 (deS63a). Thus, the ^{53}Mn nucleus with 28 neutrons and 25 protons provides an excellent example for study of the $(1f_{7/2})^{-3}$ proton configuration.

During the course of the investigation, a shorter-lived species was observed and subsequently attributed to an isomer in ^{53}Fe (Esk66). This isomer has a half-life of 2.5 min and an excitation energy of 3040.6 keV (Esk66,67), (Der68), (Bla71). It has been interpreted primarily through isomer preparation ratios (Esk67) and the reduced transition probability of the isomeric transition, apparently of $E4$ multipolarity, as having a spin and parity of $19/2^-$. This corresponds to the highest spin state that can result from the three-quasiparticle configuration, $[(\pi f_{7/2})^{-2}]_6+(\nu f_{7/2})^{-1}$. Careful examination of the γ rays de-exciting the $19/2^-$ isomeric level has resulted in direct observation of transitions of multipolarities $M5$ and $E6$. These transitions and their measured rates have profound implications for testing concepts of the shell model theory (see section 5.5.2). The discovery of a three-quasiparticle isomer in this region of the periodic table also prompted a rather extensive search for additional isomers in nearby isotopes having analogous configurations. In this respect, the $^{53g+m}$Fe investigation has been quite typical of most research projects, beginning with a simple concept, whose execution necessitates increasing complexity and engenders many new ideas and experiments.

4.2 Source Preparation

^{53m}Fe and ^{53g}Fe sources were prepared by the ^{55}Mn$(p,3n)^{53}$Fe reaction, a clean and relatively unexplored method of production, having a calculated Q-value of -23.9 MeV (Mye65). Proton beams having an energy of 34 MeV (the threshold for the production of ^{52}Fe) from the Michigan State University sector-focused cyclotron were used initially to bombard powdered manganese metal (99.94%) targets contained in thin aluminum packets. For the production of the ^{53g}Fe, 0.5-g targets typically were bombarded with a 2-μA beam of 34 MeV protons for 3 min. However, for production of the metastable isomer, ^{53m}Fe, a 2-μA beam of 40-MeV protons was utilized for 0.5-1.0 min per bombardment. Excitation functions for the ^{55}Mn$(p,3n)^{53m+g}$Fe reaction from (Esk67) are shown in Figure 4-1. The upper curve represents the 8.5-minute activity; the lower curve, the 2.5-minute isomer activity.

To expedite handling of the short-lived activities, the pneumatic rabbit system described in section 2.4 was used to transport targets from the beam to the counting area with a transit time of ≈2 sec. For experiments in which a chemical separation was not necessary, transfer of the powder to a plastic counting vial was accomplished merely by punching a hole in the aluminum packet while still attached to the rabbit (see Figure 2-20) and draining the radioactive material directly into the vial. Thus, the total elapsed time between the end of a bombardment and the beginning of counting was typically ≈ 10 sec for most experiments. In some early experiments and also in later ones which emphasized the ^{53g}Fe activity (8.5 min), a more leisurely transfer was made, such

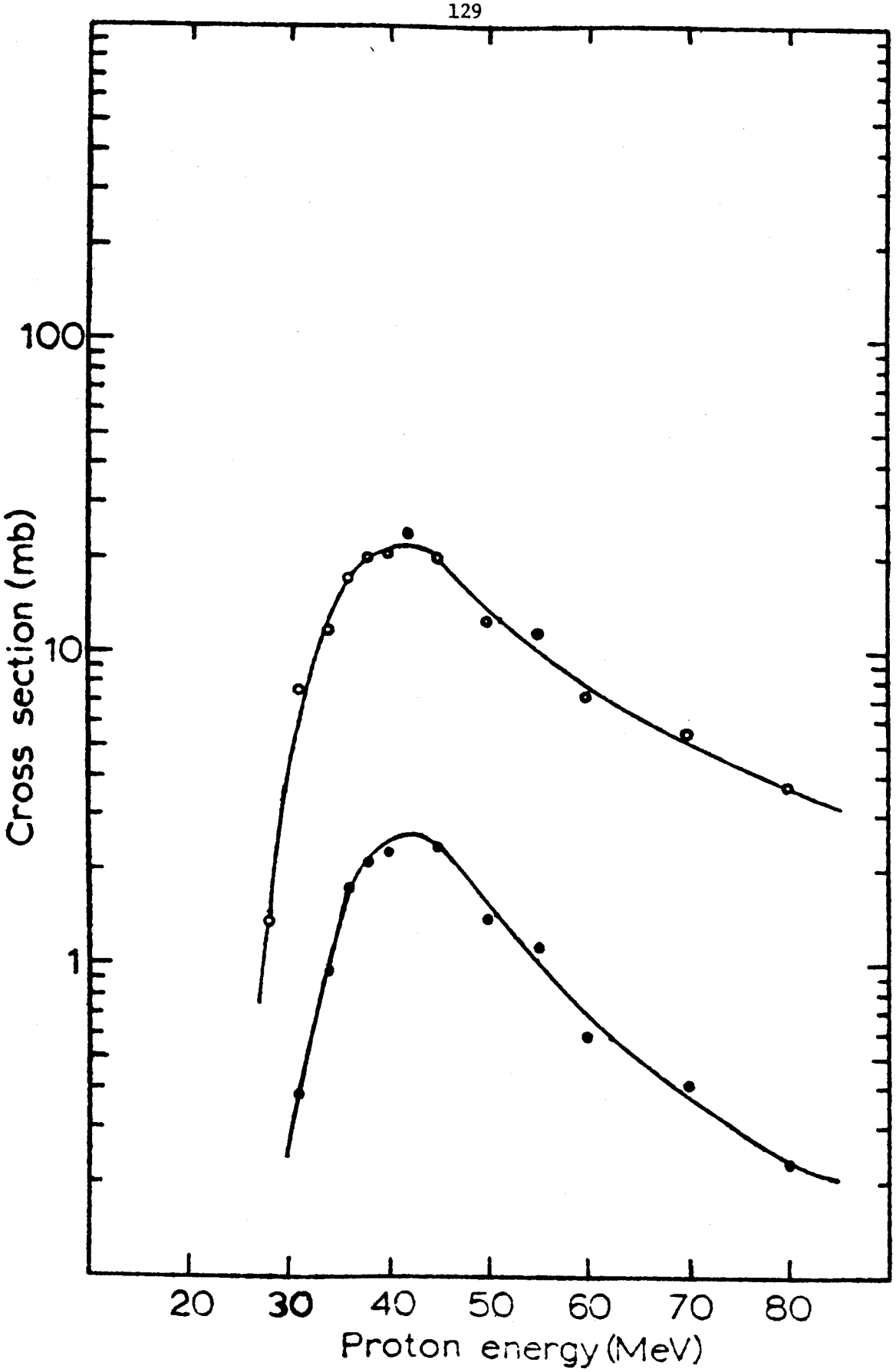

Figure 4-1. Excitation functions from (Esk67) for the $^{55}Mn(p,3n)$-$^{53m+g}Fe$ reaction. The upper curve represents the 8.5m-activity, and the lower one the 2.5m- isomer activity.

that the total time required was 3 min. In many experiments a simple but effective chemical separation was carried out after each bombardment in order to remove unwanted contaminants and insure that only the iron was being counted. This procedure is outlined in Section 2.8. For positron studies a small portion of the resulting aqueous solution containing the separated iron was dried carefully on a thin foil holder and then counted with appropriate detectors. Since most counting periods were for roughly 24 hours, multiple bombardments and separations were performed, material from each bombardment being counted 2 to 15 min depending on the experiment.

For on-line experiments, the target consisted of powdered manganese in a Duco cement or polystyrene binder mounted on a thin mylar foil. While this target was relatively crude and produced additional background γ-ray activity, the results obtained were meaningful and useful. Generally, this same target was used throughout each run.

4.3 γ-Ray Experimental Data

The primary original goal in undertaking the ^{53}Fe study was to search for new γ rays in ^{53}Mn. Earlier investigations using NaI(Tl) scintillation detectors had found only a single, strong γ ray at an energy of about 380 keV (Jul59). It was felt that a thorough study, using high resolution Ge(Li) detectors, could provide additional γ-ray information about this very interesting nucleus. In retrospect, although a couple of very weak γ rays were found to be present in the ^{53}Fe decay, the importance of the study was dominated by the confirmation of an isomer, ^{53m}Fe. The existence of this isomer and its associated γ rays has provoked considerable theoretical interest (Chapter V). During the course of this investigation many types of γ-ray experiments were performed.

4.3.1 γ-Ray Singles Spectra

The γ-ray energies and intensities from a radioactive species are best characterized by singles experiments. (However the relationships between these γ rays are not determined in such an experiment.) Although a wide variety of Ge(Li) detectors were used to obtain the $^{53m+g}$Fe spectra throughout this study, three were employed most often. Early studies utilized a 7-cm^3 active-volume, five-sided coaxial detector [≈0.5% efficient for the ^{60}Co 1332-keV γ ray, compared to a 3×3-in. NaI(Tl) detector at 25 cm], which had a resolution of 2.9 keV FWHM for the 1332-keV peak of ^{60}Co. Later work centered about a 2.5% efficient detector manufactured by Nuclear Diodes and having a resolution of ≈2.2 keV and a peak-to-Compton ratio of 16.5:1. More recent experiments have been performed with a 10.4% efficient Nuclear Diodes detector having

a resolution of 2.1 keV and a peak-to-Compton ratio of 36:1. The first detector was used with a room-temperature field effect transistor preamplifier, whereas, the 10.4 and 2.5% detectors utilized cooled FET preamplifiers. The remainder of the system consisted of linear amplifiers having near-Gaussian pulse shaping, pole-zero compensation and baseline restoration, and 4096 channel analyzers or analog-to-digital converters (ADC) interfaced to computers.

The energies of the γ rays were measured by counting the $^{53g+m}$Fe sources simultaneously with a number of well-known calibration sources. The γ-ray energy standards used for the $^{53m+g}$Fe investigation are given in Table 4-1. Using the oscilloscope computer code MOIRAE (see section 3.1.1), a background correction was made for each peak by fitting higher order equations (usually cubic) to channels above and below each peak and then subtracting. Having determined the centroids of the standard peaks, a quadratic calibration equation was prepared for comparison with the $^{53m+g}$Fe centroids. Once the stronger $^{53m+g}$Fe γ rays were established, these also were used as internal standards to verify the energies of weaker transitions present in the spectrum. Peak areas were converted to γ-ray intensities through curves previously determined in this laboratory for each detector. These curves were obtained using a set of standard γ-ray sources whose relative intensities had been measured carefully with a 3×3-in. NaI(Tl) detector.

Having performed more than 30 experiments with this nucleus, we have succeeded in identifying six γ rays resulting from the decay of ^{53m}Fe and at least three from the β^+/ε decay of ^{53g}Fe. A singles spectrum taken with the 2.5% detector is shown in Figure 4-2. (Two of the very weak γ rays in ^{53m}Fe are not shown in this spectrum, but

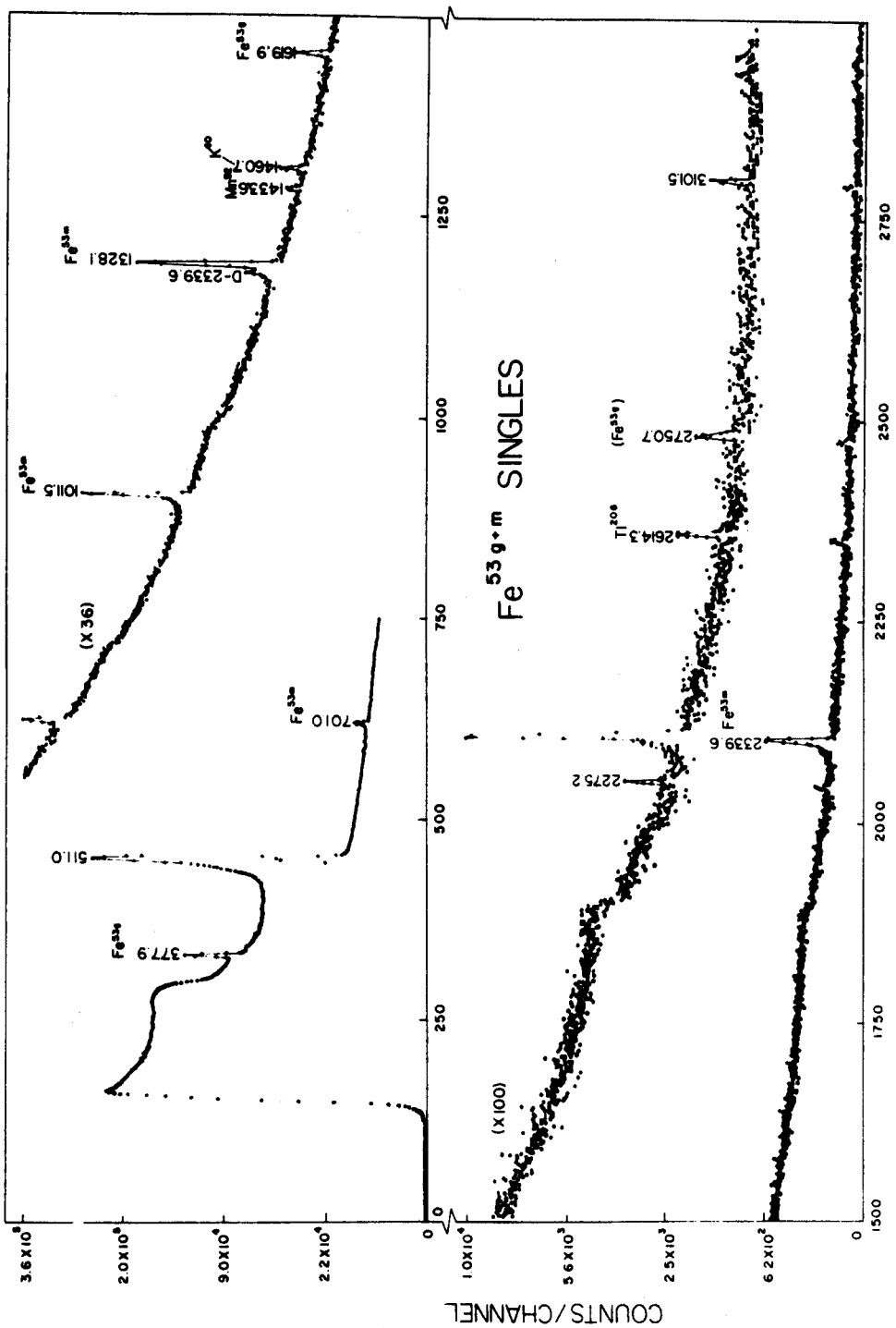

Figure 4-2. γ-Ray singles spectrum of $^{53m+g}$Fe taken with the 2.5% detector.

Table 4-1

γ-Ray Energy Standards Used in the $^{53m+g}$Fe Investigation

Nuclide	γ-Ray Energies (keV)	Reference
^{56}Co	846.79±0.03	(Mey70)
	1037.91±0.03	"
	1238.30±0.02	"
	1771.41±0.03	"
	2034.92±0.03	"
	2598.58±0.03	"
	3202.30±0.04	"
	3253.62±0.04	"
	3273.26±0.08	"
	3451.56±0.20	"
^{22}Na	1274.55±0.04	(Mur65), (Bla67), (Ram67), (Leg68)
^{60}Co	1173.226±0.040	(Mur65)
	1332.483±0.046	"
^{137}Cs	661.595±0.076	(Whi67)
^{141}Ce	145.43 ±0.02	(Bla67)
^{208}Tl(ThC")	583.14 ±0.02	(Mur65)
^{243}Cm	209.85 ±0.06	(Epp70a)
	228.28 ±0.08	"
	277.64 ±0.02	"

will be described in section 4.3.3). Many repeated bombardments and chemical separations were required to produce this spectrum, which represents some 17 hours of counting time. The ^{53g}Fe and ^{53m}Fe γ rays and their intensities are given in Tables 4-2 and 4-3, respectively.

4.3.2 γ-Ray Coincidence Spectra

In order to establish the relationships between the γ rays observed in the singles experiments and hence develop a decay scheme for $^{53g+m}$Fe, a number of standard γ-ray coincidence experiments were performed.

4.3.2A Anticoincidence Spectra

Even in a relatively simple decay scheme like the $^{53m+g}$Fe case, it is important to determine which transitions are ground-state transitions, particularly if these could be strongly ε fed. In order to obtain such information, we performed a number of anticoincidence experiments utilizing a 20-cm^3 Ge(Li) detector and an 8×8-in. NaI(Tl) split annulus. Briefly, this setup works as follows: The Ge(Li) detector is placed inside one end of the annulus tunnel and a 3×3-in. NaI(Tl) detector is inserted in the other end, with the source between them. The Ge(Li) detector is then operated in an anticoincidence mode (resolving time, $2\tau \simeq 200$ nsec) with either (optically isolated) half of the annulus or the 3×3-in. detector. A more complete description of this technique is given in Section 2.6.2. A 23 hour accumulation of $^{53m+g}$Fe taken in the above mode is shown in Figure 4-3. The only peak associated with these isotopes appearing in the spectrum is the 377.9-keV γ-ray. Thus, we see that this is most likely the only strong β^+/ε fed transition feeding the ground state of ^{53g}Fe or ^{53m}Fe. Extremely weak γ-rays, such as those from the 1619.9-keV transition, do not appear in the various

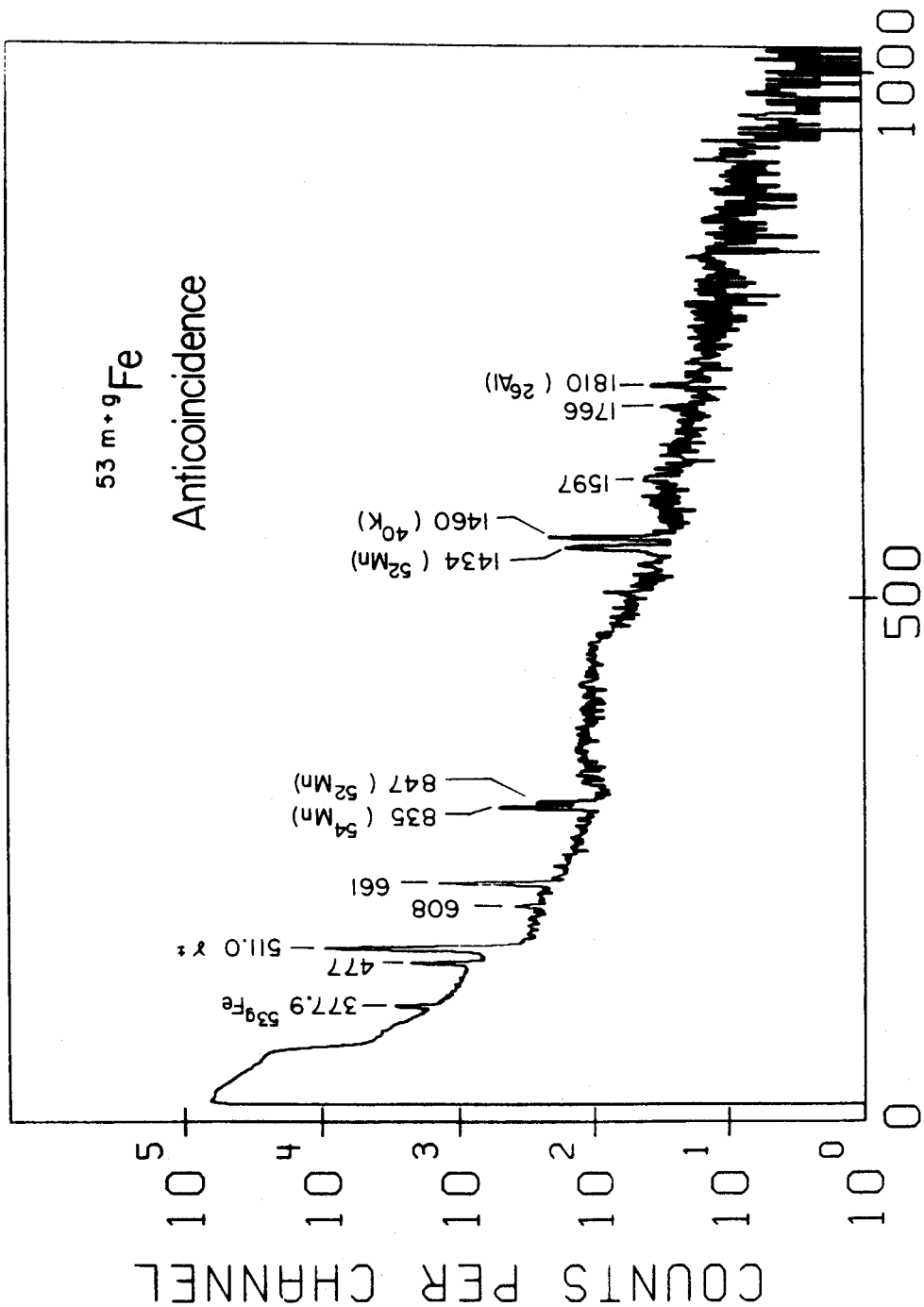

Figure 4-3. $^{53m+g}$Fe anticoincidence spectrum.

Table 4-2

^{53g}Fe γ Rays and Intensities

E_γ (keV)	Relative Intensity
377.9±0.1	≡100
(1288.0±0.1)[a]	<0.2
1619.9±0.1	1.2±0.2
(2750.7±0.1)[b]	0.7±0.1

[a]The 1288.0 level is fed very weakly by the β^+ decay of ^{53g}Fe. Its inclusion here is based upon results obtained in experiments having high statistics.

[b]This assignment is tentative.

Table 4-3

^{53m}Fe γ Rays and Intensities

E_γ (keV)	Relative Intensity
701.1±0.1	≡100
1011.5±0.1	86±9
1328.1±0.1	87±8
1712.6±0.3	1.3±0.1
2339.6±0.1	13±2
3040.6±0.5	0.06±0.01

coincidence spectra because of the poor statistics associated with these experiments.

4.3.2 B Any-Coincidence Spectra

By performing a coincidence experiment in which any observed γ ray is used as a gate for any other γ ray seen within the resolving time ($2\tau \simeq 100$ nsec), one may ascertain which transitions are in cascades. For our studies, the most effective of these experiments again utilized the 8×8-in. NaI(Tl) split annulus. A 7-cm^3 Ge(Li) detector was placed inside one end of the annulus and operated in coincidence mode with either half of the annulus. This technique is described in more detail in section 2.6.2. An 18-hr accumulation of $^{53m+g}$Fe taken in this configuration is shown in Figure 4-4. This spectrum clearly shows that the 701.1-, 1011.5-, 1328.1- and 2339.6-keV transitions are all in coincidence. The suppression of the 377.9-keV γ ray is not obvious just by looking at the spectrum. However, this spectrum was taken with sources prepared for optimum production of ^{53g}Fe (i.e. lower beam energy, longer bombardments, longer counting time per sample, etc.). The rather substantial 377.9-keV ^{53g}Fe peak appearing in the spectrum is a result of the very large g/m ratio and chance coincidence. Additional any-coincidence experiments, including those using only a 3×3-in. NaI(Tl) detector to gate a Ge(Li) detector, substantiated the above results.

4.3.2 C Spectra in Coincidence with the 377.9-keV γ Ray

Experiments were performed in an attempt to find γ rays which were in coincidence with the 377.9-keV transition in ^{53}Mn. The most effective experimental configuration used was a 7-cm^3 Ge(Li) detector placed in the 8×8-in. NaI(Tl) split annulus and operated in coincidence with either half of the annulus, both halves of which were gated on the 377.9-keV

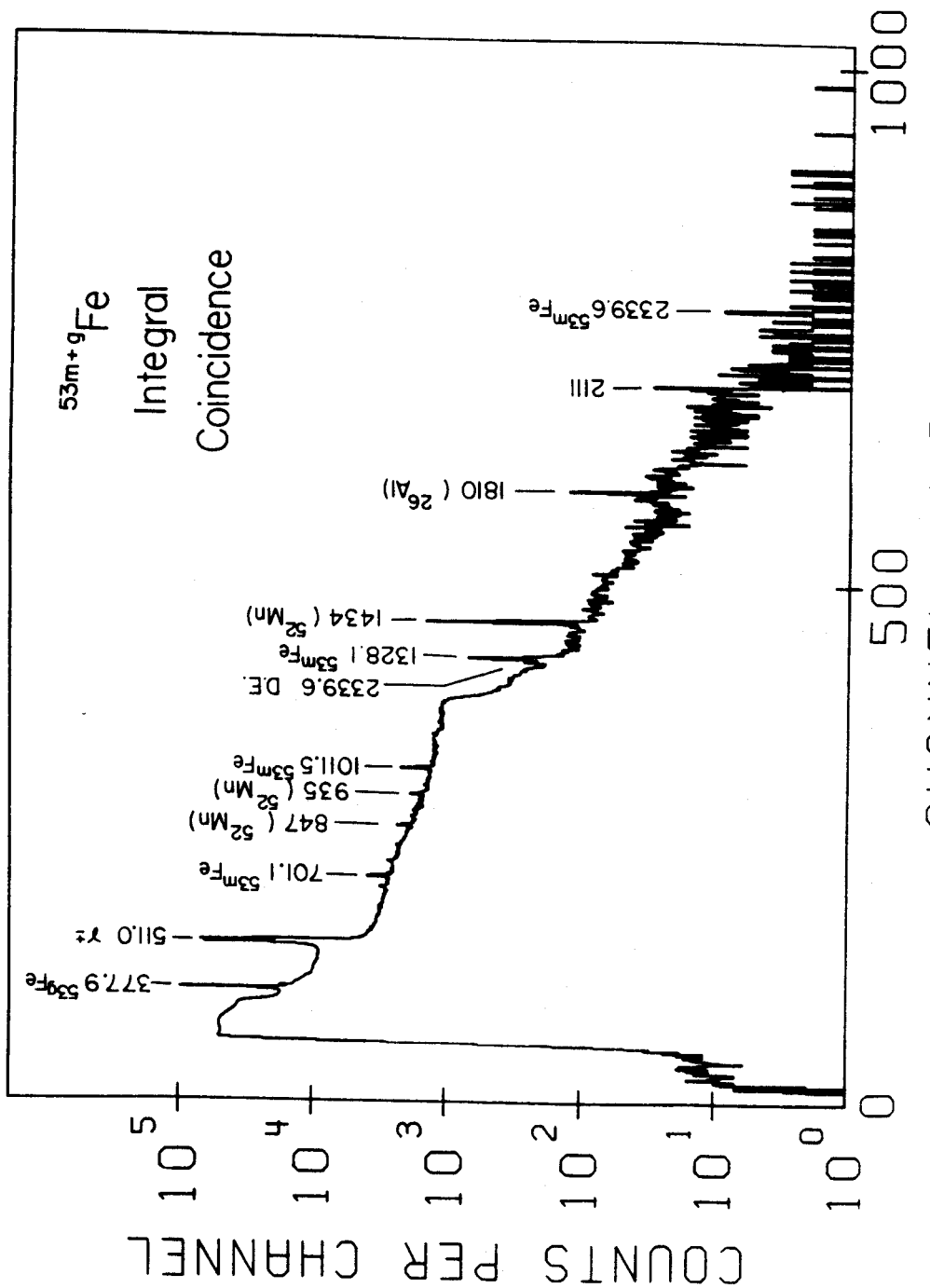
53m+g Fe
Integral
Coincidence
COUNTS PER CHANNEL
CHANNEL NUMBER
0
500
1000
10^0
10^1
10^2
10^3
10^4
10^5
377.9 53gFe
511.0 γ±
701.1 53mFe
847 (52Mn)
935 (52Mn)
1011.5 53mFe
2339.6 D.E.
1328.1 53mFe
1434 (52Mn)
1810 (26Al)
2111
2339.6 53mFe

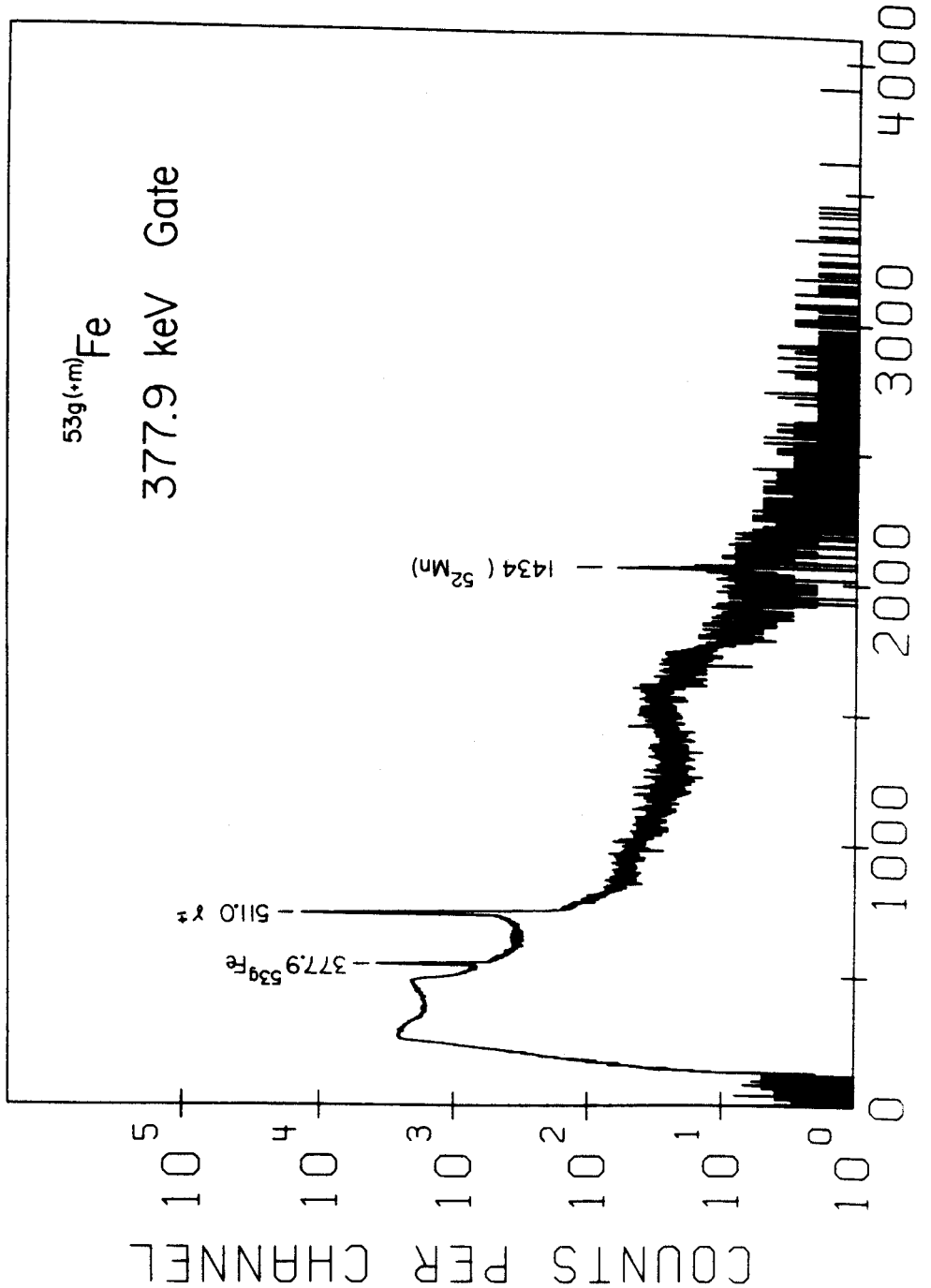

Figure 4-5. ^{53m,g}Fe coincidence spectrum with the gate on the 377.9-keV transition.

transition from ^{53g}Fe.

Again, a more complete description of this experiment may be found in Section 2.6.2. The results of such a gated experiment are shown in Figure 4-5. This spectrum represents a 12-hr accumulation of data, using the 7-cm^3 Ge(Li) detector in conjunction with the split annulus. Examination of the spectrum reveals that none of the assigned $^{53m+g}$Fe γ rays is in coincidence with the 377.9-keV transition in ^{53}Mn.

4.3.2D Two-Parameter Coincidence Experiments

Although the facilities for performing two-parameter "megachannel" type coincidence experiments are readily available in this laboratory, such an experiment was not deemed necessary for the $^{53m+g}$Fe study. However, Eskola has performed a two-parameter type experiment using a 4096-channel analyzer (Esk67). Although relatively simple, this experiment was sufficient to verify the ^{53m}Fe coincidence relations. These results are summarized in Table 4-4; a plus sign indicates an observed coincidence relation, and a minus sign, the lack of it.

4.3.2E 511 keV-511 keV-γ Coincidence (Pair) Spectra

The two halves of the 8×8-in. NaI(Tl) split annulus were used in conjunction with a 20-cm^3 Ge(Li) detector to determine the β^+ feeding to levels in ^{53}Mn and to identify possible double-escape peaks. Each half of the annulus was gated on the 511-keV $\gamma^{\pm}$ peak, and a triple coincidence (resolving time, $2\tau \simeq 100$ nsec) was required among these and the Ge(Li) detector. The relevant block diagram of the necessary electronics and details of the experiment may be found in Section 2.6.2. The spectrum resulting from this experiment is shown in Figure 4-6. As can be readily observed, only the 377.9-keV state in ^{53}Mn appears to

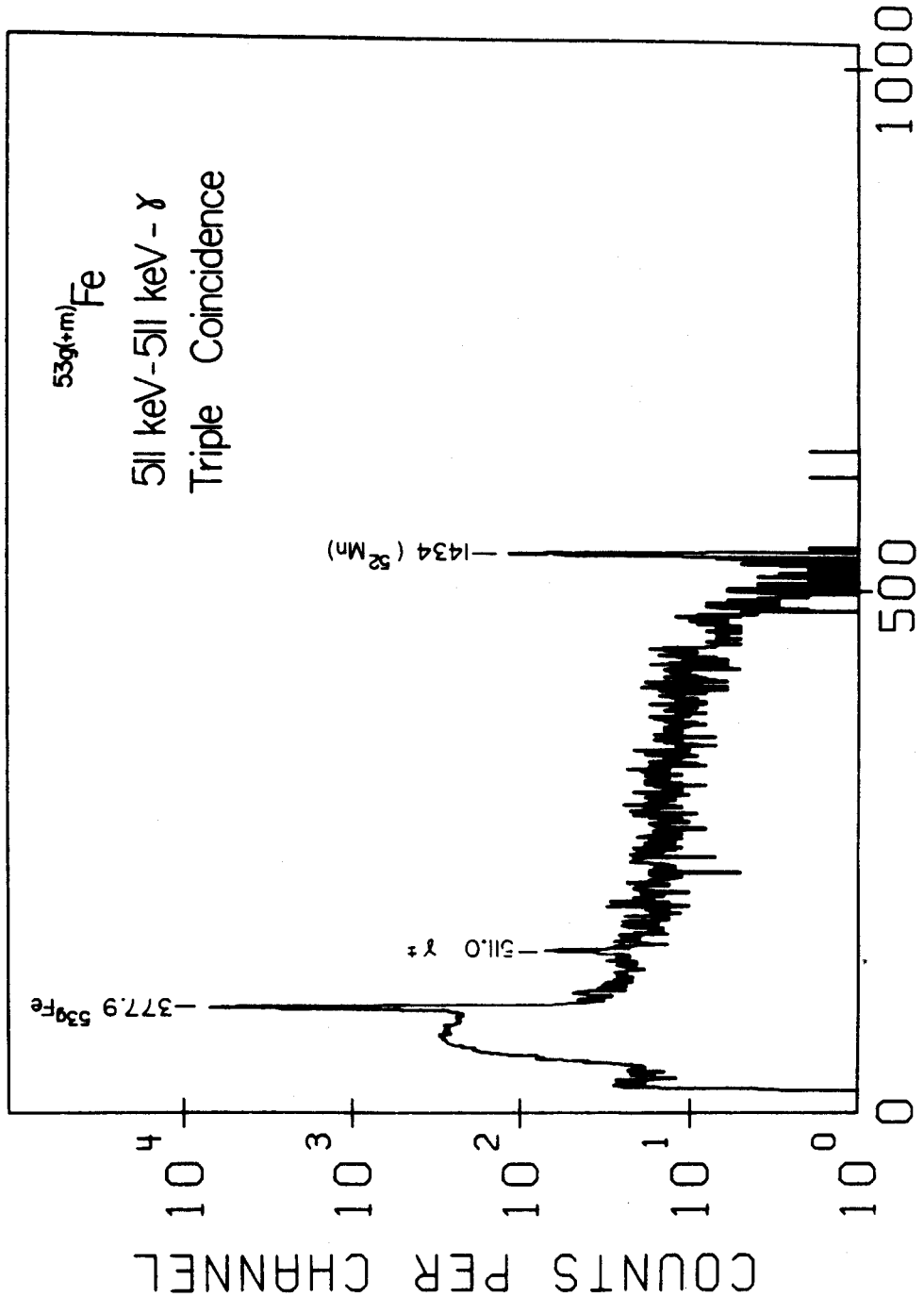

Figure 4-6. $^{53g(+m)}$Fe 511 keV-511 keV-γ triple coincidence spectrum.

Table 4-4

Coincidence Relations between γ Rays Observed in the Decay of ^{53m}Fe[a]

γ-Ray Energy (keV)	701.1	1011.5	1328.1	2339.6
701.1	-	+	+	+
1011.5	+	-	+	-
1328.1	+	+	-	-
2339.6	+	-	-	-

[a]From (Esk67).

be strongly β^+ fed. Extremely weak transitions like the 1619.9-keV γ ray do not appear in these spectra. The presence of these weakly fed states is verified by their appearance in long singles experiments using chemically separated sources, and by the lower energy β^+ end-point energies found in the Fermi plots of the ^{53g}Fe beta spectra. Based simply on the assumed log ft's for the β^+ decay to these weaker states, one finds that the predicted β^+ feeding is as follows: the β^+ feeding to the 1619.9-keV state is at best a factor of $\approx$12 less than that to the 377.9-keV state. However, the 1288.0-keV β^+ feeding should be less than the 377.9-keV intensity by a factor of $\approx 10^8$. One finds experimentally that the 1619.9-keV feeding is less than predicted, whereas the 1288.0-keV intensity appears enhanced, based on the observed γ-ray intensities from these levels. Note, however, that there exists the possibility of γ-feeding to these states from undetected, higher-lying levels. For most of these experiments, the upper limit of detectability for a γ ray in the 1200-to 1700-keV region was about 0.5% of the normal 377.9-keV γ-ray intensity.

4.3.3 High Multipolarity γ-Ray Transitions Following the Decay of ^{53m}Fe

The discovery of the high-energy, high-spin, three quasiparticle isomer in ^{53}Fe has provided an excellent opportunity for the direct observation of very high multipolarity γ-ray transitions. The existence of $M5$, $E6$, and higher multipolarities has never been substantiated by experimental fact except for their presence as small admixtures occasionally being invoked to explain small discrepencies in experiments such as angular correlations.

Having confirmed Eskola's gamma decay scheme for ^{53m}Fe, we initiated

a program to search for hitherto unobserved transitions of multipolarity $M5$ and $E6$. Source preparation was carried out as described in Section 4.2, with bombardment time, beam energy, and all other parameters adjusted to optimize the production of the metastable state. γ rays were detected with a 3.6% efficient true-coaxial Ge(Li) detector having a resolution of 2.0 keV. The remainder of this system consisted of an amplifier having high-rate baseline restoration and a 50-MHz analog-to-digital converter interfaced to a Sigma-7 computer. Graded lead absorbers having a combined thickness of $\sim$3 cm were used between the source and the detector to attenuate the lower-energy γ rays. Even so, counting rates as high as possible without appreciable deterioration of resolution were maintained throughout the experiments, with an average count rate of about 6700 counts/sec. This combination of isomer optimization, detector efficiency and resolution, and high-count-rate electronics was deemed absolutely necessary in order to obtain the number of events necessary for direct observation of the weak $E6$ and $M5$ transitions.

Various spectra were taken at different times and with different geometries and produced consistent results. Figure 4-7 shows the spectrum resulting from a 24-hr accumulation of data and front-end detector geometry. During this time a continuous cycle of bombarding and counting was maintained such that a fresh source was counted every 2 min. Definite peaks exist in this spectrum at the energies of 1712.6 and 3040.6 keV, where the $M5$ and $E6$ transitions are expected to occur. After careful energy and intensity analysis, these peaks were found to correspond to transitions having intensities of 1.3×10^{-2} and 6×10^{-4} as compared with the 701.-keV transition. Recent experiments using a large 10.5%-efficient Ge(Li) detector have shown that these peaks decay with the

2.5-min half-life of ^{53m}Fe and are the only peaks in the spectrum (other than the four well-known, intense ^{53m}Fe peaks) that decay with this half-life.

Having shown that these peaks are present, one is obligated to demonstrate that they are indeed true peaks and not merely the resultant sum peaks of two or more known constituents. Such sum peaks are known to occur in large-volume detectors under high-count-rate conditions. These can originate from two different physical conditions. First, if the source is sufficiently close to the detector so that the detector presents a large solid angle, summing of events in the same γ-ray cascade can occur. Second, if the source is strong, accidental summing of events from the same or different γ-ray cascades can occur. With our ^{53m}Fe experiments one needs to worry about both effects in turn.

This summing problem was examined both in light of the data themselves and also from additional experiments designed to elucidate the summing phenomenon. Considering the ^{53m}Fe data alone, we can formulate several interesting arguments. Examination of the established decay scheme (Figure 4-13) reveals that two of the most intense transitions, at 701.1 and 1328.1 keV, are in a cascade connected by the 1011.5-keV transition, the third most intense. If indeed cascade-type summing were to occur to an appreciable extent during an experiment such as that recorded in Figure 4-7, one would conclude that these two most intense transitions should give rise to a sum peak at 2029.2 keV. Examination of the spectrum, however, shows no evidence for a γ ray at this energy. Figure 4-8 shows a linear blowup of the 2029.2-keV region from the spectrum given in Figure 4-7. This absence was reproducible from experiment to experiment, with widely varying count rates and source-detector distances. One can estimate for this spectrum, for example, that the contributions

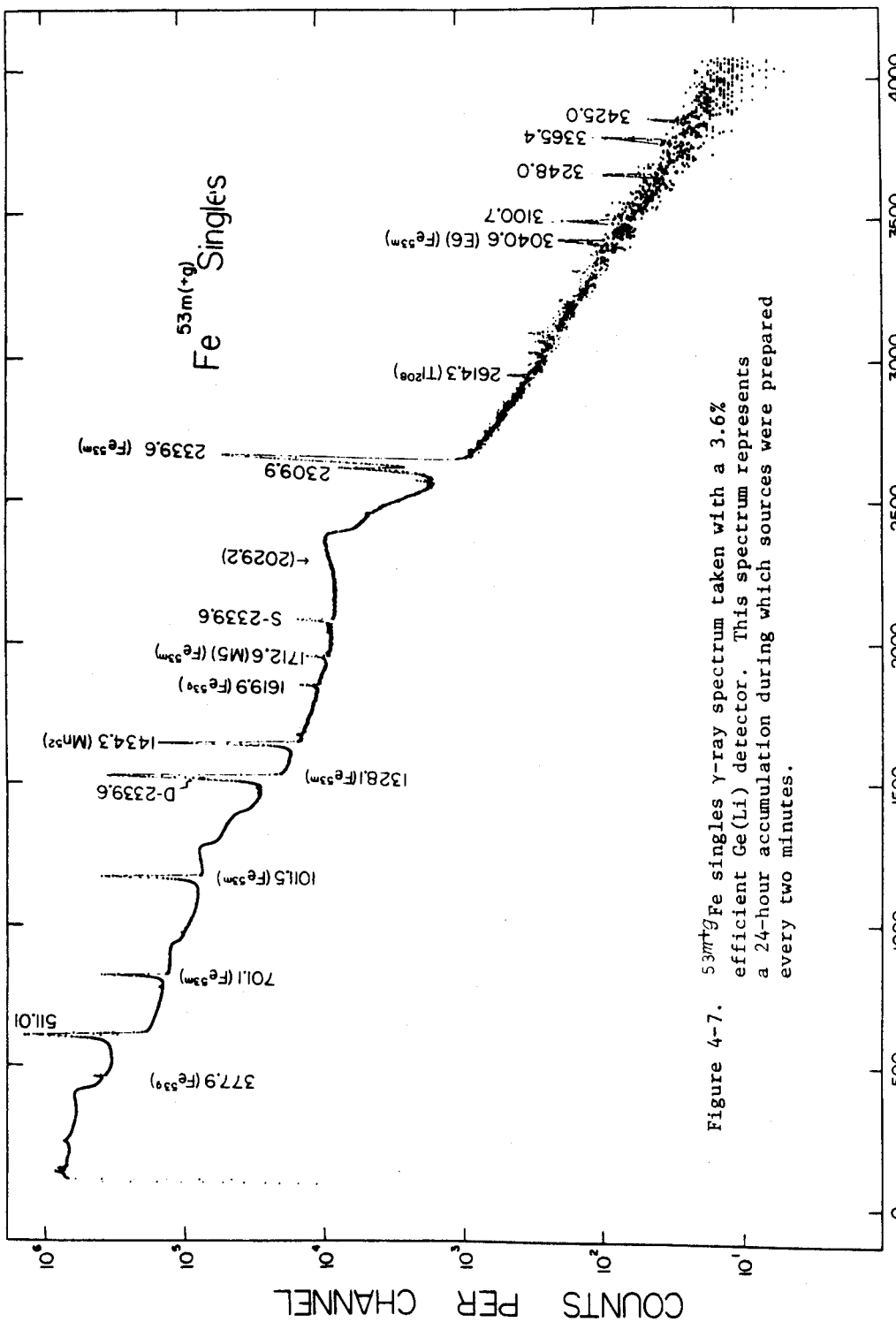

Figure 4-7. $^{53m+g}$Fe singles γ-ray spectrum taken with a 3.6% efficient Ge(Li) detector. This spectrum represents a 24-hour accumulation during which sources were prepared every two minutes.

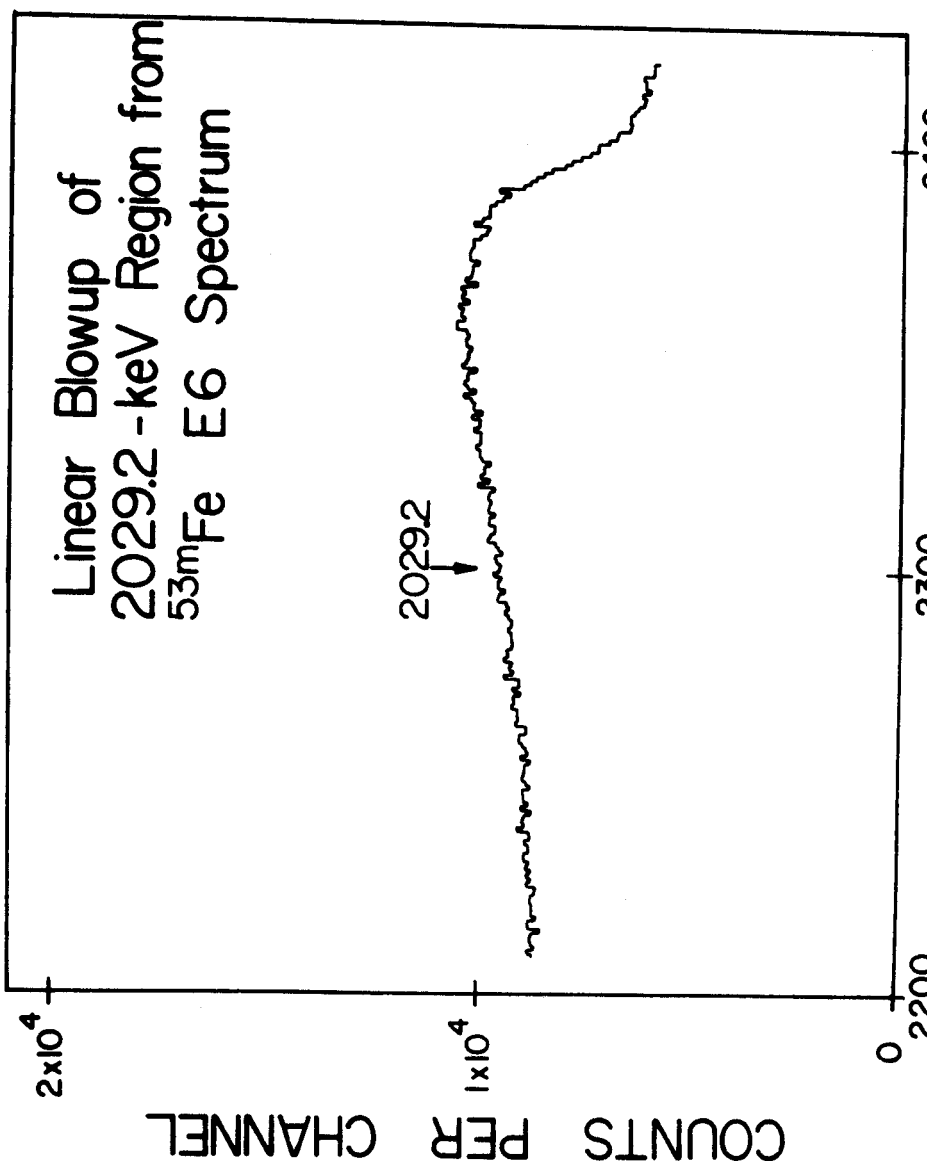

Figure 4-8. Linear blowup of the 2029.2-keV region from Figure 4-7, showing the absence of cascade-type summing.

of summing to the $M5$ and $E6$ peaks would be considerably less than 0.1% and 10%, respectively, and come almost entirely from chance coincidences. Also, although the 511.01-keV $\gamma^{\pm}$ peak was the most intense peak in the spectrum, no evidence was found for $\gamma^{\pm}$ summing to give a 1022-keV peak or of their summing with any of the stronger γ rays in the spectrum. This indicates that chance type summing was not a significant factor in these experiments except for a small (<10%) possible contribution to the weak $E6$ peak. A third consideration is the peak width. In general, sum peaks or peaks containing significant summing components tend to be wider than their true counterparts. However, here one finds the peaks corresponding to the $M5$ and $E6$ transitions to be of normal width, providing further evidence for the fact that they are true peaks. Finally, the $E6$ and $M5$ decay with the same half-life as the $E4$ isomeric transition, and one would expect to measure a different half-life if there were a substantial contribution from chance-coincidence summing.

To check the internal data, a series of experiments was performed in which ^{60}Co spectra were taken with various source-detector geometries at a constant count rate. The degree of summing to form a 2505.71-keV sum peak was observed as a function of geometry. Then, using the same count rates and geometries, an analogous set of ^{53m}Fe spectra was taken. The resulting intensity variations of the $M5$ and $E6$ peaks as a function of geometry were compared with the variations of the ^{60}Co spectra. This method corroborated the fact that the 1712.6- and 3040.6-keV peaks are not sum peaks but do indeed reflect true transitions in the ^{53}Fe nucleus.

4.3.4 On-Line γ-Ray Spectra

A number of pulsed, in-beam experiments have been carried out during

the $^{53m+g}$Fe investigation. In these experiments, the cyclotron beam was pulsed by *RF* modulation such that the beam was on for about 0.4 sec and off about 0.4 sec per cycle. The targets consisted of powdered manganese in a Duco cement or polystyrene binder on a thin mylar backing. These targets were placed in a precision goniometer where they were viewed by Ge(Li) detectors through a thin kapton window. A shielded beam dump was located about 8 feet beyond the target position. The principal detector employed in these experiments was a 2% efficient, trapezoidal Ge(Li) detector, having a resolution of about 3.4 keV FWHM. Data were taken on-line with the Sigma-7 computer, using routing. Five 4096-channel spectra were routed as follows: one spectrum was taken during the beam-on portion of each cycle, with four more being taken in 0.1 sec time intervals during the beam-off period. Results of these in-beam experiments served largely to verify the results of our earlier $^{53m+g}$Fe experiments. A typical in-beam spectrum is shown in Figure 4-9. Since the beam-on spectra were capable of seeing direct excitation decays (as opposed to decays resulting from the β^+/ε decay of ^{53g}Fe), they proved to be most interesting. Earlier investigations of the ^{53g}Fe decay using different reactions such as (α,xn) indicated a state of about 1290 keV (Jul59). Our previous studies of the $^{53m+g}$Fe decay using the ^{55}Mn$(p,3n)^{53}$Fe reaction did not indicate a level of this energy. However, our in-beam data clearly contain a γ-ray at 1288 keV. In addition, two of the *E*6 search spectra (containing very high numbers of counts and good statistics) show evidence for such a transition. Thus, the 1288-keV level in ^{53}Mn appears to be only very weakly fed by the β^+/ε decay of ^{53g}Fe -- although its existence in the decay has been verified. From this ^{55}Mn$(p,3n)$ work,

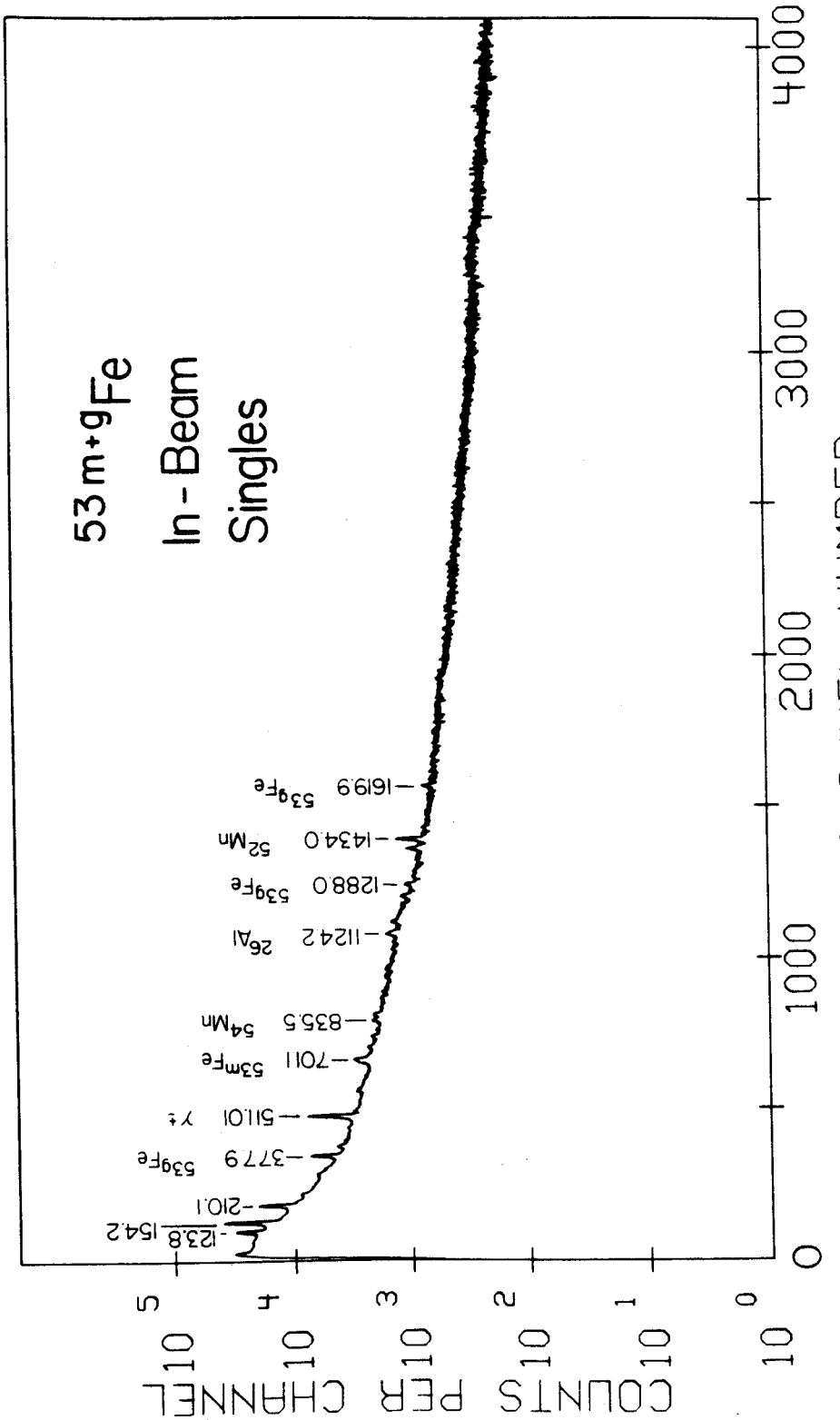

Figure 4-9. $^{53m+g}$Fe beam-on singles spectrum.

no γ ray was seen corresponding to the level of 1440 keV reported from earlier $^{53}Cr(p,n\gamma)^{53}Mn$ studies (McE68,70).

A comprehensive list of all γ rays observed in the $^{53m+g}Fe$ investigation is given in Appendix E.

4.4 β^+ Experimental Data

In addition to the γ-ray studies of ^{53g}Fe, an investigation of the β^+ spectrum associated with this nuclide also was carried out. This investigation included not only singles experiments, but also β^+-γ coincidence experiments in an effort to ascertain the β^+ end-point energies.

4.4.1 β^+ Singles Spectra

Although a number of devices were used in studying the β^+ decay of ^{53g}Fe, the most useful and convenient instrument was a Si(Li) surface-barrier detector. The detector utilized had an area of 200 mm^2 with a thickness of 1000μ. In order to reduce noise this detector was mounted in a dipstick cryostat immersed in a methanol-dry ice bath ($\approx$-77 C). The detector itself was covered by an evacuated Al can with a 0.10-mil Havar window for admission of the positrons. After performing a chemical separation on the target, a drop of the aqueous iron solution was carefully dried on a frame-mounted thin Havar backing and placed in an appropriate holder on the detector can. Each sample was counted for approximately 20 min, with a total counting time of 16-24 hr per run. The usual electronics were utilized, including a 1024-channel analyzer. An energy calibration for these spectra was obtained by using the conversion electrons of several well-known standards. Very thin sources of these standards were prepared by evaporation onto a thin aluminum backing mounted on a small ring holder. The standards used in this study, together with their conversion-electron energies, are listed in Table 4-5. Since most of these standards are relatively low in energy, one must necessarily extrapolate the energy calibration curve to higher energies -- a somewhat risky procedure,

Table 4-5

Electron Energy Standards Used in the ^{53g}Fe β^+ Studies

Source	Conversion-Electron Energy (keV)
^{137}Cs	624.15±0.08[a]
	655.88±0.10[a]
^{203}Hg	193.64±0.02[b]
	264.49±0.10[b]
^{207}Bi	481.61±0.06[c]
	554.37±0.10[c]
	975.57±0.06[c]
	1048.1 ±0.1

[a] (Mul52), (Lind53), (Gra60), (Led67)

[b] (Nij59), (Wol56), (Her64), (Led67)

[c] (Bra64), (Yav55), (Led67)

requiring cautious evaluation.

An ^{53g}Fe positron singles spectrum, obtained with the Si(Li) detector is shown in Figure 4-10. Even though the data are plotted on a log scale, the bell-shaped trend of the continuum is apparent. This spectrum represents an 18-hr accumulation of data, using chemically separated sources which were prepared every 15 min.

The conversion-electron peaks of the standards used with the above experiment were analyzed using the data analysis task MOIRAE. A first-order background fit was made to the peaks of these standards and their centroids determined. An energy calibration curve was then prepared by making a polynomial fit of energy to channel number, using a standard fitting routine. (The polynomial order was kept low, so that a more reliable high-energy extrapolation could be made.) Then, using the tables of NBS Applied Mathematic Series #13 (Tab51), the corrected Fermi ordinates were obtained and the Fermi plot obtained. Figure 4-11 shows a Fermi plot of an ^{53g}Fe singles positron spectrum. The end-point energies of the three resolved beta groups for ^{53g}Fe are given in Table 4-6.

4.4.2 β^+-γ Coincidence Spectra

4.4.2A β^+ Spectra in Coincidence with the 377.9-keV γ Ray

In order to elucidate the β^+ feeding to the levels in the ^{53}Mn nucleus, a number of β^+-γ coincidence experiments were performed. For these experiments a rather efficient 3×3-in. NaI(Tl) detector was used for the γ-ray gate, while the Si(Li) surface barrier detector described previously was used to observe the positrons in coincidence with these γ rays. The source detector geometrics were run at both 90° and 180°. If we assume that the highest end-point group observed at 2.8 MeV feeds

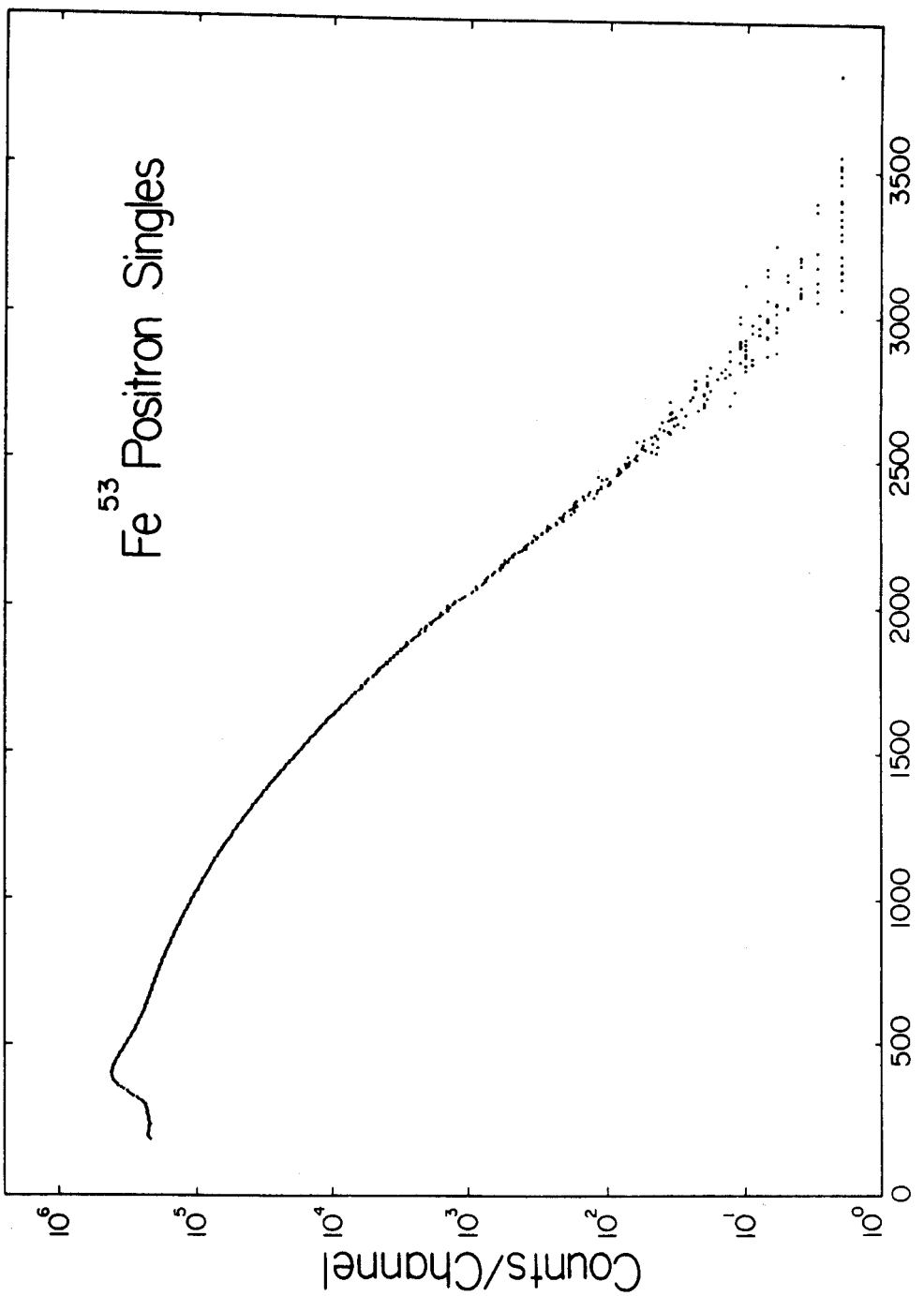

Figure 4-10. $^{53g}(^{4m})$Fe β^+ singles spectrum taken with a 200 mm^2 Si(Li) detector.

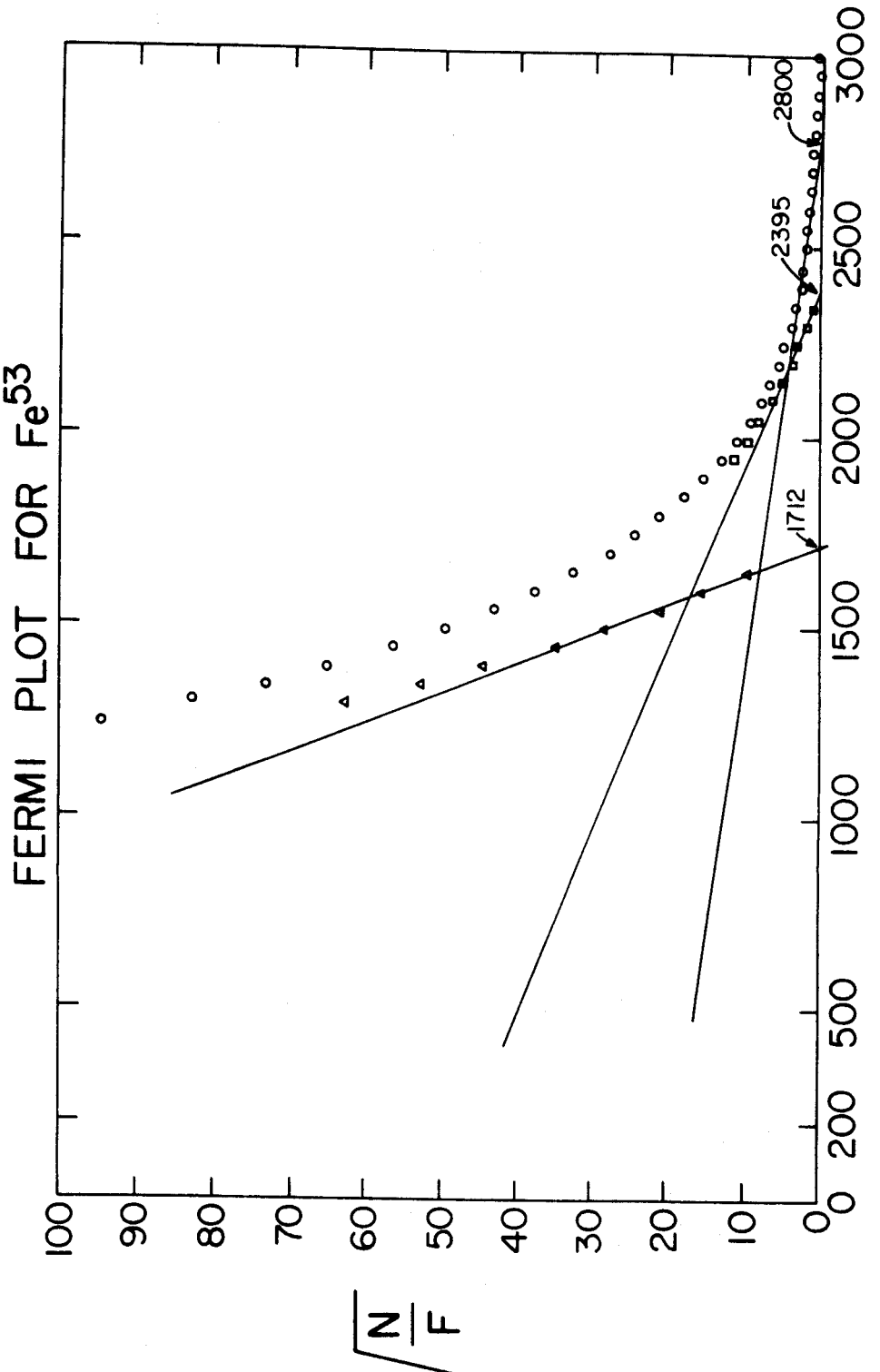

Figure 4-11. Fermi plot for the ^{53g}Fe β^+ singles spectrum shown in Figure 4-10.

Table 4-6

Resolved β^+ End-point Energies for ^{53g}Fe

Group Number	Energy, MeV	Relative Abundance (%)
1	2.80±0.10	56
2	2.40±0.10	41
3	1.71±0.35	≈1

the ground state of ^{53}Mn, then the 2.4-MeV group should correspond to feeding of the first excited state at 377.9 keV. When such experiments were performed, gating on this 377.9-keV γ-ray, the Fermi plots of the resultant beta spectra revealed a highest end-point group at 2.4-MeV -- 0.4 MeV less than the most energetic group in the ungated spectrum. Thus, these β^+-γ experiments confirm the earlier hypothesis that the 2.4 MeV group finds the 377.9-keV level in ^{53}Mn. A typical gated coincidence spectrum from above is shown in Figure 4-12.

4.4.2B β^+ Spectra in Coincidence with γ Rays above 511 keV

As a matter of interest, an experiment was performed to examine the positron spectrum in coincidence with γ rays above 511 keV. The experimental configuration used was the same as described above, except the NaI(Tl) γ-ray gate was opened and its lower limit set just above the 511-keV $\gamma^{\pm}$ peak. Since the β^+/ε decay to the ground and the first excited state of ^{53}Mn comprise over 98% of the available ^{53g}Fe decay, the experiment described above was only marginally feasible. Indeed, the results were not clear, but did hint in the appropriate direction. The positron spectrum indicated a weak end-point in the region of 2.2-2.4 MeV, with another strong end-point resolved at 1.2-1.4 MeV. This latter energy is in the region one would expect if feeding to the weak states of 1288.0 and 1619.9 keV were occurring. The higher energy group at 2.4-MeV is not explained but may well be due to chance coincidence. Thus, this experiment seems to confirm the fact that β^+ feeding is occurring to the 1288.0- and 1619.9-keV levels of ^{53}Mn.

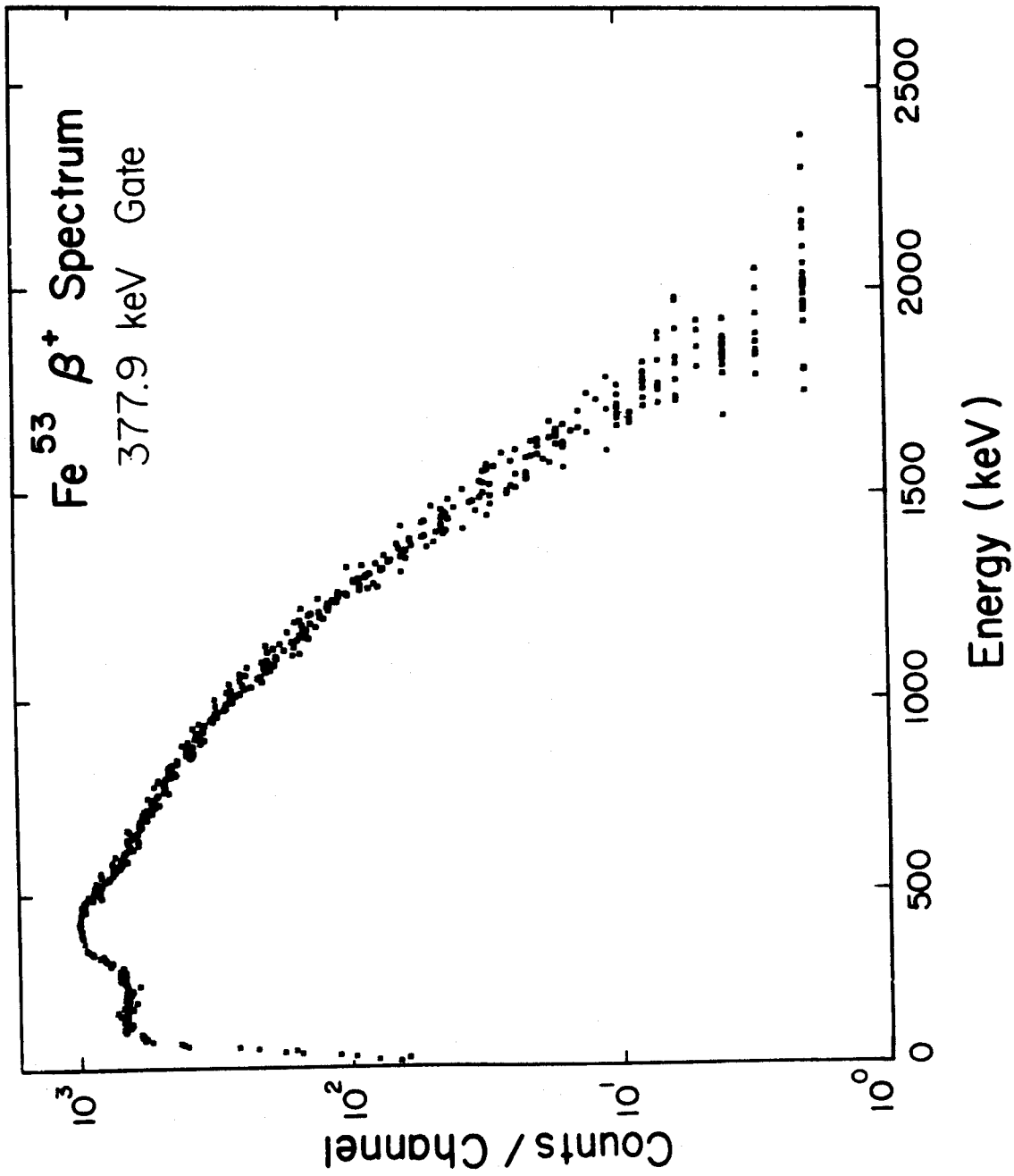

Figure 4-12. $^{53m+g}$Fe β^+ spectrum taken in coincidence with the 377.9-keV γ ray using a 200 mm^2 Si(Li) detector.

4.5 Proposed Decay Schemes

The information yielded by the β- and γ-ray experiments described above were fitted into consistent decay schemes for ^{53g}Fe and ^{53m}Fe. Both of these decay schemes are presented in Figure 4-13.

4.5.1 ^{53g}Fe Results

4.5.1A The ^{53}Mn Ground State

A large portion (≈57%) of the ^{53g}Fe decay proceeds directly to the ground state in ^{53}Mn. This long-lived state (2×10^6 y) has been shown experimentally to have a spin and parity of $7/2^-$ (Dob56). Positron feeding to this state with an end-point energy of 2.8 MeV has been demonstrated by both β^+ singles and β^+-γ coincidence experiments. The β^+ group feeding this level has an allowed shape and a log ft of 5.3.

4.5.1B The 377.9-keV Level

The first γ ray to be discovered in the ^{53}Fe decay was one reported at 370 keV by Nussbaum et al. in 1953 (Nus53). Previous investigations had characterized the ^{53}Fe decay only as positron emission with an end-point energy of approximately 2.6 MeV (Nel50). The present investigation has assigned an energy of 377.9±0.1 keV to the above level. This first excited level is by far the most highly β^+/ε fed of all the higher states, receiving ≈98% of the available decay to the excited states in ^{53}Mn. For many years this γ ray was the only one that could be assigned with certainty to the ^{53}Fe decay. β^+-γ coincidence experiments in this lab and elsewhere (Jul59) have shown that the 377.9-keV level is fed by a positron group having an end-point energy of about 2.4 MeV. This group appears to have an allowed shape and gives a log ft value of 5.1. A measurement of the spin for this level has been performed

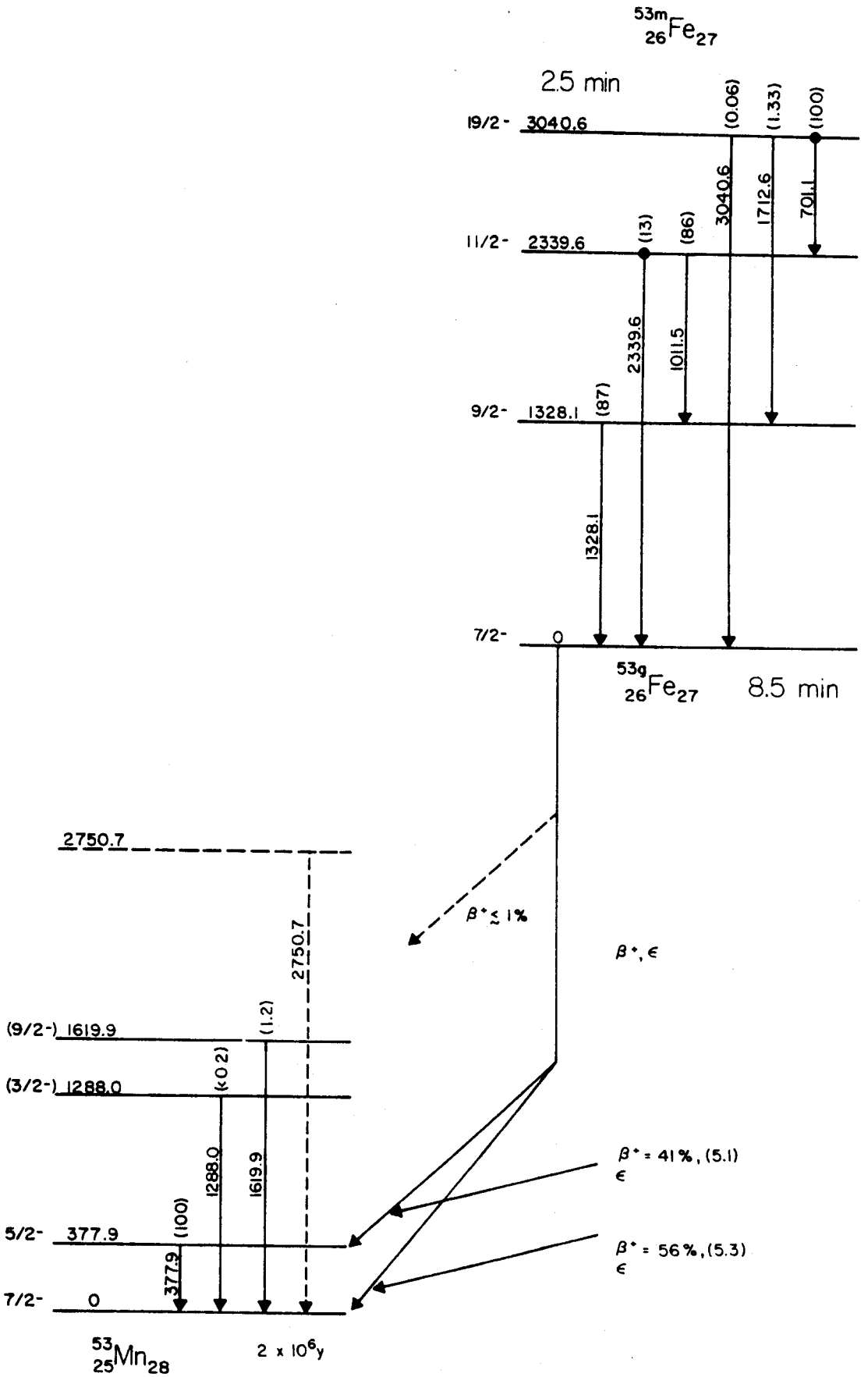

Figure 4-13. Proposed decay schemes for ^{53g}Fe and ^{53m}Fe.

and confirms the earlier assignment of $5/2^-$ (McE70), (Vui66), (Jul59). This finding is in agreement with other odd-mass nuclei in the $f_{7/2}$ region.

4.5.1C The 1288.0-keV Level

This investigation contains definite γ-ray evidence for β^+ feeding to higher levels in ^{53}Mn from the decay of ^{53} Fe. Heretofore, the only evidence for these levels has been obtained through reactions leading to excited ^{53}Mn states directly -- e.g., ^{52}Cr$(p,\gamma)^{53}$Mn.

The 1288.0-keV state appears to be populated only very weakly by the decay of ^{53g}Fe. Only experiments with very high statistics such as those from the *E*6 search revealed this level. This state also has been observed rather strongly in the in-beam data, where direct excitation is possible. Earlier workers using other reactions together with scattering experiments have reported a level near 1290 keV (Jul59), (McE70). The β^+ spectra analysis indicate group(s) near 1.2-1.4 MeV which may feed this level. A more positive statement about this feeding cannot be easily obtained, since resolution of the 3rd or 4th beta group in a Fermi plot is at best a tedious and somewhat inaccurate procedure. Also, the extremely weak nature of this γ ray does not permit a reliable β^+-γ coincidence experiment to be performed. Theoretically, the second excited state should be $3/2^-$, which would also be consistent with other odd-mass nuclides in this region (Jul59). Recent γ-ray angular distribution measurements by McEllistrem et al. (McE70) have experimentally verified the 3/2 spin assignment. This assignment would require that the positron group populating the 1288.0-keV state to be second forbidden with a log *ft* of approximately 13, and hence a negligibly low relative abundance.

Although our experiments show the 1288.0-keV state to be populated very weakly, the abundance is greater than that expected for a log ft of 13. Nevertheless, in view of systematics and the work of McEllistrem et al. an assignment of $3/2^-$ to this level does not seem unreasonable.

4.5.1D The 1619.9-keV Level

The population of this level by the ^{53g}Fe decay is relatively weak. However, we should recall that there is only about 1% of the total decay populating the higher levels in ^{53}Mn. In this perspective the state is relatively strong, supported by the fact that it was seen in every significant singles spectrum. β^+ experiments described earlier indicate possible feeding to a level of this energy. Half-life measurements show that this level follows the same half-life as ^{53g}Fe. Comparison with other scattering transition data confirms the existence of a level of about 1620 keV. The assignment of spin 9/2 to this level has been confirmed by γ-ray angular distribution measurements (McE70).

4.5.1E The 2750.7-keV Level

Possible evidence for a level at 2750.7 keV has been found during this investigation. A transition of the above energy has been observed in several spectra using chemically separated targets. Half-life measurements have shown that this γ ray follows the ^{53g}Fe half-life. This assignment is supported by reports of a level near 2700 keV in several ^{52}Cr(p,γ) experiments (Ste66), (Vui66). No spin assignment was made to this level, although it must be $5/2^-$, $7/2^-$, or $9/2^-$.

4.5.1F Other Possible Levels

Since 99% of the β^+/ε decay of ^{53g}Fe goes either to ground or to the first excited state, the task of determining high-lying levels in

^{53}Mn by the present approach is quite difficult. Distinguishing possible transitions from contaminants, background and statistical fluctuations also becomes increasingly difficult. Several γ rays seen in this investigation remain unidentified even after elimination of contaminants, side reactions, background, etc. All of these are quite weak and none can be placed in the decay schemes with confidence. Nevertheless, a couple of examples will be presented here for completeness. There exists one such γ ray at about 1730 keV which persists after chemical separation and follows approximately the ^{53g}Fe half-life. No level of this energy in ^{53}Mn has been reported. Another γ ray at about 3274 keV has been observed in the chemically separated targets and seems to follow a half-life similar to that of ^{53g}Fe. From the energetics involved we conclude that it is not fed from the ^{53g}Fe ground state. Additional lower-energy γ rays were observed but could not be assigned.

4.5.2 ^{53m}Fe Results

4.5.2A The ^{53}Fe Ground State

This ground state has a well-established spin of $7/2^-$ and a measured half life of 8.51 minutes (Ebr65). It is fed by all identified higher states, with the largest contribution (87%) from the first excited state.

4.5.2B The 3040.6-keV Metastable State

The γ-rays associated with the metastable state at 3040.6 keV were first identified by their shorter half-life. During excitation function studies, the concurrent appearance of these γ rays with the known ^{53g}Fe γ rays led to the belief that they comprised a metastable state in ^{53}Fe. Indeed, decay curve studies by Eskola have shown that there

is a parent-daughter relationship between the shorter 2.5-min activity and the 8.5-min ground state of ^{53}Fe (Esk67). Comparison of the excitation energy and half-life with single particle estimates (Mos65) indicate that spin values of the metastable and the ground state differ by at least five units. Since the ground state spin is $7/2^-$ this means the spin of the metastable state must be at least 17/2. If the metastable state is interpreted as a three-particle state, one obtains a spin value of 19/2 (Esk67). Gamma-feeding to every established level in ^{53}Fe from ^{53m}Fe has been demonstrated in this investigation.

4.5.2C The 2339.6-keV Level

This level was placed on the basis of γ-ray sums and verified by coincidence relations. The spin and parity were assigned on the basis of comparison with the Weisskopf single-particle estimate (Ann70). Recent experiments by Sawa and Bergström (Ann70) have verified the $11/2^-$ spin and parity assignment of this level. γ-rays were observed from this level which correspond to deexcitation to the ground and first excited states.

4.5.2D The 1328.1-keV Level

Based on the present experimental evidence, assignment of the first excited state in ^{53}Fe can be made at either 1328.1 keV or 1011.5 keV. However, shell model calculations indicate that the 1328.1-keV assignment is correct (see Section 5.3).

The assignment of $9/2^-$ to this lowest excited level is based upon the observed gamma branching ratio for the two γ rays de-exciting the $11/2^-$ level. Assuming that these 1011.5- and 2339.6-keV transitions

have multipolarities of $M1$ and $E2$ respectively, an estimate derived from the transition probability of a single proton (Mos65) yields a branching ratio which is consistent with the observed ratio -- with due regard to the generally observed retardation of $M1$ transitions with respect to the single particle estimate. The assignment of $9/2^-$ for the spin and parity has also been substantiated by experimental work (Ann70).

4.6 Discussion

In retrospect, the $^{53m+g}$Fe investigation has been very rewarding, and certainly turned out to be far more productive than we initially bargained for. The original task of elucidating the levels in ^{53}Mn populated by the β^+/ε decay of ^{53}Fe was accomplished, using both β^+- and γ-ray spectroscopy. However, the salient feature of the investigation was the discovery of several new transitions which were consequently attributed to a high-spin, three-particle isomer in ^{53}Fe. Careful γ-ray studies of this isomer revealed the existence of high multipolarity gamma rays corresponding to $M5$ and $E6$ transitions, which were heretofore unobserved.

Both ^{53}Fe and ^{53}Mn have interesting structures for shell model studies. ^{53}Fe contains two proton holes and one neutron hole outside the Z=28, N=28 doubly closed shell. The ^{53}Mn nucleus has a closed N=28 neutron shell, and three proton holes outside the Z=28 closed shell. The structure of the isomer, ^{53m}Fe, is also of considerable interest. The discussion of the ramifications of these structures and γ-ray transition rates with regard to the shell model has been deferred to the next Chapter (V).

CHAPTER V

SHELL MODEL CALCULATIONS FOR ^{53}Fe AND ^{53}Mn

5.1 Introduction

Our degree of understanding of the nucleus and its processes is measured not only by our ability to make detailed empirical observations but also by our capacity to explain and predict these phenomena from first principles. Therefore, in order to achieve a fuller insight into the nuclear realm the nuclear spectroscopist must not confine himself only to the experimental details, but rather explain and elaborate upon his discoveries through the use or formulation of an appropriate model. Indeed, without some employment of theoretical explanations, the experimentalist becomes merely a nuclear bookkeeper.

In this spirit of "understanding as well as measuring," I would like to use one such nuclear model in this chapter to describe the data presented in Chapter IV. While the complexity of the nuclear force and its lack of understanding have prevented the formulation of a universal nuclear model, many of the properties of nuclei have been explained by a few semi-phenomenological models. Among these, the shell model has been quite successful in many regions, and is the one which I would like to apply here.

5.2 The Shell Model

5.2.1 General Description

Motivated by the appearance of the so-called "magic nucleon numbers" (Z or N equal to 2, 8, 20, 28, 50, 82 and 126) where large discontinuities in nuclear binding energy occurred, M. Goeppert-Mayer (Goe49) and Haxel, Jensen, and Suess (Hax49) independently constructed a nuclear model similar to the atomic electron shell structure. In this model, each nucleon is assumed to be moving independently in an average potential due to all of the remaining nucleons. The potential was chosen to be intermediate between that of an isotropic harmonic oscillator and a square well. In order to generate the nuclear orbital spacings to give shell closure at the "magic numbers" a strong spin-orbit coupling term had to be added to the Hamiltonian. This had the effect of splitting each harmonic oscillator level into two levels, $j = \ell + 1/2$ and $j = \ell - 1/2$, which were $(2j + 1)$-fold degenerate. The $j = \ell + 1/2$ levels were found to lie lower in energy than the $j = \ell - 1/2$ levels. This fact gave energy level spacings that were consistent with the "magic numbers." The filling of levels inside a shell must be in accord with the Pauli principle for protons and neutrons separately. In the ground state, the nucleons are paired so that the nuclear properties are determined by the last unpaired nucleon. This prediction has been found accurate for odd mass nuclei having one nucleon just outside a closed shell. The model has failed to predict correctly several properties such as spin and magnetic moments, for nuclei that have several nucleons (or holes) outside a closed shell, i.e. nuclei with only partially filled shells. This is due partly to the fact that the

model cannot predict the order of the level filling because of the strengths of the spin-orbit coupling and residual interactions, which cannot be determined accurately. Another example is the failure of the simple shell model to predict the $E2$ transition rates and electric quadrupole moments in certain nuclei. These are almost invariably larger than the single particle estimates, often by several orders of magnitude. One model which has been used in attempting to account for these effects is the Intermediate Coupling Shell Model. The first attempts to extend the range of validity of shell model calculations consisted of the removal of the requirement that the particles move independently by including two-particle interactions. This was first done for particles in a single configuration, i.e. that giving the lowest energy. This restriction was later removed and "configuration mixing" was introduced. This corresponds to using a wave function which is a linear combination of wave functions for single particle states having nearly degenerate energies and the same total angular momentum. A principal difficulty in using this method is the complexity of the calculations when more than two or three particles are present outside a closed shell. Other modifications of the calculations including residual interactions have been made, but will not be included in this brief description.

5.2.2 Formulation of the Problem

In this section, a general outline of the solution of the shell model problem will be presented. This section, as well as much of the calculation, was taken from notes and material provided by Dr. B. H. Wildenthal of the MSU Cyclotron Laboratory and P. W. M. Glaudemans (Gla70). While quite general, this description pertains largely to

the Oak Ridge Shell Model Codes.

One begins with the basic postulates of the shell model, and in particular makes the assumptions that the single-particle orbits, $\rho(j_i)^{\pi}$, exist and have a given energy spectrum. In order to do the problem, one must divide these orbits into three distinct groups:

1. The "core", i.e. the "closed shells" or the "inactive particles".
2. The "active" orbits.
3. The "empty" orbits.

The core orbits are completely filled with as many nucleons as the Pauli Principle allows, and then dismissed from further orbit calculations. For a nucleus with A nucleons, C nucleons are used to fill the core orbits, and N are left to be distributed over the active orbits in all or some of the distributions allowed by the Pauli Principle. The choice of these "active" orbits also defines the "core" and "empty" groups.

A particular number distribution of active particles:

$$(\rho_{i+1})^{n1}\ (\rho_{i+2})^{n2}\ .\ .\ .\ .\ .\ .\ .\ .\ .\ (\rho_{i+a})^{n_a}$$

where $n_1 + n_2 + \ldots + n_a = N$ is called a *configuration*. The occupation numbers $n_1, n_2, \ldots . n_a$ can be individually limited either by the Pauli Principle alone or choice. The totality of allowed sets of $(n_1, n_2 \ldots . n_a)$, presupposing a choice of $(\rho_{i+1}, \ldots . \rho_{i+a})$, constitute the "allowable" or "model" configurations, and usually are sufficient to define the model vector space S. The rigorously good quantum numbers of S are N, π, J, and if one uses isospin, T. A basis vector of the space S is then expressed as:

$$NJT^{\pi}\psi_K = [\{(\rho_{i+1}^{n_1})_{j_1 t_1 x_1} (\rho_{i+2}^{n_2})_{j_2 t_2 x_2}\}_{J_{12} T_{12} X_{12}} \cdots (\rho_{i+a}^{n_a})_{j_a t_a x_a}]_{JT\pi} \quad (5\text{-}1)$$

This is an antisymmetric, orthonornal, N-particle ($(\sum_i n_i = N)$ state of total angular momentum J^i and total i-spin T, with "K" labeling different possible orthonormal vectors for a given N, J, T, π. The x_i are additional quantum numbers as needed to provide a unique specification of the single-shell n_i-particle wave functions $(\rho_i^{n_i})j_i t_i$. The parity of ψ is determined simply by the number of particles in odd-parity orbits.

From this point, attention will be focused on a subspace of S defined by the set of quantum numbers N, J, T, π = s. This subspace is spanned by $\mathcal{D}$ vectors ${}^s\psi_K$. Therefore, the wave functions will be expressed as:

$$^s\psi = \sum_{K=1}^{\mathcal{D}} a_K \, {}^s\psi_K \quad (5\text{-}2)$$

The "dimension" $\mathcal{D}$ of the subspace s is a strong function of the number of orbits in S as well as $j(\rho_i)$, J, and T. The wave functions Ψ are eigenfunctions of the shell model Hamiltonian H, and $\mathcal{D}$ orthonormal Ψ's can be obtained from the diagonalization of the matrix $\langle\psi_i|H|\psi_K\rangle$. These eigenfunctions are ordered according to the magnitude of their associated eigenvalues and labeled by θ, the order number, with θ = 1 corresponding to the lowest energy state of that NJTπ(S) and so on. The shell model eigenvalue problem can now be written as:

$$H^{s\theta}\,\Psi = {}^{s\theta}E^{s\theta}\,\Psi \quad (5\text{-}3)$$

or

$$H|NJT\pi\theta\rangle = {}^{NJT\pi\theta}E|NJT\pi\theta\rangle \quad (5\text{-}4)$$

H consists of one-body terms (i.e. the interactions of particles in active orbits with the core), and two-body terms (i.e. the interactions of particles in active orbits with each other).

$$H^{s\theta}\ \psi = H \sum_{K=1}^{\mathcal{D}} {}^{s\theta}a_K\, {}^{s\theta}\psi_K = {}^{s\theta}E \sum_{K=1}^{\mathcal{D}} {}^{s\theta}a\, {}^{s\theta}\psi_K \tag{5-5}$$

or

$$H|s> = \sum_{K=1}^{\mathcal{D}} {}^{s}a_K\, H|{}^{s}K> = \sum_{K=1}^{\mathcal{D}} {}^{s}a_K|{}^{s}K>\ {}^{s}E \tag{5-6}$$

multiplying by $<{}^{s}K'|$ gives:

$$\sum_{K=1}^{\mathcal{D}} {}^{s}a_K <{}^{s}K'\ |H|\ {}^{s}K> = \sum_{K=1}^{\mathcal{D}} {}^{s}a_K\ {}^{s}E\delta_{KK'} \tag{5-7}$$

This can be rewritten as:

$$\sum_{K=1}^{\mathcal{D}} {}^{s}a_K\, {}^{s}H_{K'K} = {}^{s}a_{K'}\, {}^{s}E \tag{5-8}$$

where $K' = 1 \ldots\ldots \mathcal{D}$

These equations form a matrix equation:

$$ {}^{s}\begin{pmatrix} H_{11} & H_{12} & \cdots & H_{1\mathcal{D}} \\ H_{21} & & & \\ \cdot & & & \\ \cdot & & & \\ \cdot & & & \\ \cdot & & & \\ H_{\mathcal{D}1} & & & H_{\mathcal{D}\mathcal{D}} \end{pmatrix} {}^{s}\begin{pmatrix} a_1 \\ a_2 \\ \cdot \\ \cdot \\ \cdot \\ \cdot \\ a_{\mathcal{D}} \end{pmatrix} = {}^{s}E \begin{pmatrix} a_1 \\ a_2 \\ \cdot \\ \cdot \\ \cdot \\ \cdot \\ a_{\mathcal{D}} \end{pmatrix} \tag{5-9}$$

For the above matrix equation, there exists $\mathcal{D}$ solutions $({}^{s\theta}E, {}^{s\theta\rightarrow}a)$.

Thus, the shell model problem has been reduced to:

1) Evaluation of the multiparticle matrix elements:

$$<{}^{S}\psi_{K}|H|{}^{S}\psi_{K'}>.$$

2) Diagonalization of the resulting matrix.

The first problem is by far the more difficult. In order to evaluate the $H_{KK'}$, one must employ the "Fundamental Theorem" of the shell model:

If H has only zero-, one-, and two-body forces, then *any* multiparticle matrix element $<\psi_K|H|\psi_{K'}>$ can be written as a linear sum of one- and two-particle matrix elements,

$$<\rho_\alpha|H|\rho_{\alpha'}> \text{ and } <(\rho_\alpha\rho_\beta)_{JT}|H|(\rho_{\alpha'}\rho_{\beta'})_{JT}>.$$

This can be restated as:

$$<{}^{S}\psi_{K'}|H|{}^{S}\psi_{K}> = {}^{S}H_{K'K} = \sum_{m=1}^{M} {}^{S}C_{K'Km}\,\chi_m \qquad (5\text{-}10)$$

where the χ_m are the one- and two-body matrix elements.

The singular importance of the "Fundamental Theorem" is that, whereas there exists a semi-infinite number of multiparticle matrix elements $<{}^{S}\psi_{K'}|H|{}^{S}\psi_{K}>$, there is a relatively small, well-defined number of two-body matrix elements, for any given choice of ρ_{i+1}, ρ_{i+2}, ... ρ_{i+a}. From these two-body matrix elements, any multiparticle matrix element in S can be calculated. Thus, the first step of the shell model problem is separated into:

1) Finding the coefficients ${}^{S}C_{K'Km}$ which relate the two-body matrix elements and the single-particle matrix elements to the multiparticle matrix elements. This is a very difficult algebraic problem, but one which is explicitly defined. The C's are fixed for a given assumption for the model space S. The basic function of the

shell model code is to determine these C coefficients.

2) Finding the shell model Hamiltonian, that is the one- and two-body matrix elements. This is not a mathematical problem, but one which is empirically determined from "nature".

Some attention will now be given to part two. If one now considers equation (5-6):

$$H|s> = \sum_{K=1}^{\mathcal{D}} H|{}^{s}K > {}^{s}a_{K} = {}^{s}E\ s>$$

Now, multiplying from the left by:

$$<s| = \sum_{K'=1}^{\mathcal{D}} {}^{s}a_{K'} <{}^{s}K'| \ .$$

This yields:

$$<s|H|s> = {}^{s}E <s|s> = \sum_{K,K'=1}^{\mathcal{D}} {}^{s}a_{K'} <{}^{s}K'|H|{}^{s}K> {}^{s}a_{K} \qquad (5\text{-}11)$$

or rewritten in another form:

$$= \sum_{K,K'=1}^{\mathcal{D}} <s|{}^{s}K'> <{}^{s}K'|H|{}^{s}K> <{}^{s}K|s> \qquad (5\text{-}12)$$

Thus, the multiparticle matrix elements, $<{}^{s}K'|H|{}^{s}K>$ are related to the eigenvalues ${}^{s}E$.

However, the two-body matrix elements and the single-particle matrix elements, the parameters of H, are related to the multiparticle matrix elements by the geometrical coefficients ${}^{s}C_{K'Km}$. Inserting this substitution, one obtains:

$$\sum_{K,K'=1}^{\mathcal{D}} {}^{s}a_{K'} {}^{s}a_{K} \left(\sum_{m=1}^{M} {}^{s}C_{K'Km} \chi_{m} \right) = \sum_{m=1}^{M} {}^{s}F_{m} \chi_{m} = {}^{s}E \qquad (5\text{-}13)$$

where ${}^{s}F_{m} = \sum_{K',K=1}^{\mathcal{D}} {}^{s}a_{K'} {}^{s}a_{K} {}^{s}C_{K'Km}$ and χ_{m} are the two-body matrix elements and single-particle matrix elements.

It should be emphasized that the set of two-body matrix elements and single-particle matrix elements is *fixed* for a given shell model, i.e. all eigenvalues in S are derived from them. This allows the shell model problem to be self-contained, or in a sense, self-consistent. The use of the single-particle and two-body matrix elements provides the most general specification possible of the shell model potential. One should also note that:

1) The eigenvalues of the multiparticle states are related to parameters of the Hamiltonian through geometrical coefficients and eigenvector amplitudes.

2) These eigenvalues of multiparticle states presumably correspond to energies of experimentally observable nuclear levels.

One can now require that the two-body matrix elements and the single particle matrix elements be such as to yield a least-squares fit between the calculated ${}^{s}E$ and the presumed experimental counterpart values, ${}^{s}\varepsilon$.

If one knows L experimental energy levels ${}^{s}\varepsilon$, then for each one he can construct an equation:

$$\sum_{m=1}^{M} {}^{s}F_{m} \, {}^{s}\chi_{m} = {}^{s}E \xrightarrow{\text{approach}} {}^{s}\varepsilon \qquad (5\text{-}14)$$

S = NJTθ running over L values.

If one can then manage $L >> M$, he can perhaps determine the χ_m meaningfully. First, some initial choice must be made for H (= Ho), determined by χ°_{m}, m = 1,M. One then calculates ${}^{s}E^{\circ}$, ${}^{s}a^{\circ}{}_{k}$, ${}^{s}F^{\circ}{}_{m}$. Using these, L identities are set up:

$$\sum_{m=1}^{M} {}^{s}F^{\circ}{}_{m} \, \chi^{\circ}{}_{m} = {}^{s}E^{\circ} \qquad (5\text{-}15)$$

Now, one substitutes in these expressions ${}^{s}\varepsilon$ for the ${}^{s}E^{o}$ and treating the χ_m's as unknowns, least-squares solves for a new set. Suppose that a new set of ${}^{s}\psi$, ${}^{s}E$ has been obtained. After inspection of ${}^{s}E$ *vs.* ${}^{s}\varepsilon$, it is appropriate to calculate expectation values of other operators besides H. There are only a very few operators (moments) which have expectation values that are functions of one ${}^{s}\psi$. Most of the physically measurable observables connect one ${}^{s}\psi$ to another ${}^{s'}\psi$.

If one wishes to evaluate some such operator:

$$<{}^{f}\psi|O_\rho|{}^{i}\psi> \tag{5-16}$$

$$\text{where } {}^{f}_{\psi} = \sum_{j=1}^{f_D} {}^{f}a_j|f_j>$$

$$\text{and} \quad i_\psi = \sum_{\ell=1}^{i_D} {}^{i}a_\ell|{}^{i}_{\ell}>$$

The first step is the construction of the matrix $<O\rho>$:

$$<O_\rho> = \begin{pmatrix} <f_1|O_\rho|i_1><f_1|O_\rho|i_2> \ \ldots \ <f_1|O_\rho|i_{i_D}> \\ <f_2|O_\rho|i_1><f_2|O_\rho|i_2> \ \ldots \ <f_2|O_\rho|i_{i_D}> \\ \cdot \\ \cdot \\ \cdot \\ <f_{f_D}|O_\rho|i_1><f_{f_D}|O_\rho|i_2><f_{f_D}|O_\rho|i_{i_D}> \end{pmatrix} \tag{5-17}$$

where the matrix elements $<f_j|O_\rho|i_\ell>$ connect different basis vectors

$^{k}\psi$ (or $|K\rangle$) of the model space S. O_ρ can be either one-body or two-body. Most observables correspond to one-body operators — e.g. spectroscopic factors for single nucleon transfer, $E2$ strengths, inelastic scattering strengths, etc. These observables can all be represented either by a bare or weighted creation operator or a creation-annihilation pair. In either case, $\langle f_j|$ can differ at most one particle from $|i_\ell\rangle$. In addition, angular momentum and isospin must be conserved from state "i" through O_ρ^{JT} to state "f". Considering the expression:

$$\langle f_j| = [(\rho_1)^{n1}_{J_1\alpha_1} (\rho_2)^{n_2}_{J_2\alpha_2} \cdots (\rho_a)^{n_a}_{J_a\alpha_a}] \; f(NJT) \qquad (5\text{-}18)$$

and

$$|i_\ell\rangle \; [(\rho_1)^{n_1'}_{J_1'\alpha_1'} (\rho_2)^{n_2'}_{J_2'\alpha_2'} \cdots (\rho_a)^{n_a'}_{J_a'\alpha_a'}] \; i(N'J'T') \qquad (5\text{-}19)$$

where $N_{(f)} = N_{(i)}$ or $N_{(i)} + 1$ and $\Delta(JJ'\Delta J(O\rho))$

$(a^+a) \quad (a^+) \qquad \Delta(TT'\Delta T(O\rho))$

For $O_\rho \alpha a^+$ $\quad n_K = n_K'$ except for one case, where $n_K = n_K' + 1$. In addition, all non-K J's and T's must satisfy $\delta(J_K, J_K')$ etc.

For $O_\rho \alpha a^+a$ $\quad$ One particle can change orbit (including returning to the same) and so all $n_K = n_K'$ except for two, which must correlate: $n_K = n_K' + 1$; $n_K = n_K' - 1$.

The matrix elements of these operators are constructed with the aid of the coefficients of fractional parentage libraries in a manner analogous to the construction of the $\langle\psi_K|H|\psi_{K'}\rangle$ in terms of the two-body

matrix elements times geometrical coefficients.

After construction of the matrix $<O\rho>$, it is multiplied by the amplitude of the eigenvectors:

$$<^{f}\psi|O\rho|^{i}\psi> = (^{f}a_1, ^{f}a_2, \ldots ^{f}af_D) \begin{pmatrix} O\rho \end{pmatrix} \begin{pmatrix} i_{a_1} \\ i_{a_2} \\ \cdot \\ \cdot \\ i_{ai_D} \end{pmatrix} \qquad (5\text{-}20)$$

With the shell model code, these procedures are accomplished in two steps, First, the operator matrices are constructed and stored. Second, the eigenvector amplitudes, saved from a previous eigenvalue-eigenvector calculation, are combined with the matrices to obtain the observable values.

In addition to the above general description of the shell model code, I have found that detailed "how-to-do-it" input instructions for the code to be very helpful in understanding the shell model problem, as well as providing the format for running the program.

Because of the length and the "secondary relevancy" of these input instructions and comments, I have deferred their discussion to Appendix B. However, anyone who desires a more complete grasp of the problem, or wishes to perform such a calculation will find this section very valuable.

5.3 ^{53}Fe Calculations

5.3.1 Predicted Level Scheme

The Oak Ridge Shell Model Codes were used first to calculate the energy level spacings for ^{53}Fe. A proton-neutron formalism was chosen, instead of the isospin formalism, and the levels calculated in a pure $f_{7/2}$ approximation. Eigenstates of the mass 53 system were calculated assuming 7 active neutrons, 6 active protons, and the proton-neutron interactions of Vervier. (Ver67). Table 5-1 contains this useful list of interactions from Vervier. All three interactions were tried with our code, and found to give very good results. These results are summarized in Table 5-2. Note that agreement with experiment is quite satisfactory in all three cases. Also, the large spin-gap which gives rise to the isomeric character of the 19/2- level is predicted in all cases. Vervier points out in his paper (Ver67) that the persistence of this isomeric prediction with varying effective interactions is due to the following facts: (1) the 7^+ state lies very low in the spectrum of the $(\pi f_{7/2})(\nu f_{7/2})$ interaction, much lower than the 6^+, 5^+, 4^+ and 3^+ levels (for the three cases of Table 5-1), indicating a strong attraction between the $1f_{7/2}$ proton and neutron when their spins are as much aligned as possible. (2) The 6^+ and 4^+ states of the $(\pi f_{7/2})^{-2}$ configuration are quite close together, indicating that the proton-neutron interaction "dominates" the proton-proton interaction and pushes the $19/2^-$ level, where the maximum spin alignment occurs, below the $17/2^-$, $15/2^-$, and $13/2^-$ states of the $(\pi f_{7/2})^{-2}(\nu f_{7/2})^{-1}$ configuration. The occurrence of similar spin gaps and their corresponding isomeric levels has been explained

Table 5-1

Effective Proton-Neutron Interactions in the $(\pi f_{7/2})^{-1}(\nu f_{7/2})^{-1}$ Configuration

Spin	Interaction		
	(1)	(2)	(3)
0^+	0	0	0
1^+	1.035	0.610	0.618
2^+	1.509	1.510	1.590
3^+	2.248	1.960	1.518
4^+	2.998	2.750	2.844
5^+	1.958	2.250	2.220
6^+	3.400	3.190	3.191
7^+	0.617	0.530	0.526

Interaction (1) has been adapted from the work of McCullen, et al. (McC64). The two others are based on more recent experimental data; (2) was deduced by Ball (BalJB) from a least-squares fit of the experimental spectra of ^{42}Sc and ^{48}Sc; (3) differs from (2) mainly in the assignment of the 3^+ level based on recent (^{3}He,p) results (Zur66).

Table 5-2

Predicted Levels and Spins for ^{53}Fe from

Shell Model Calculations Using the Interaction from Vervier.

Interaction (1)		Interaction (2)		Interaction (3)		Experimental	
Energy(MeV)	Spin	Energy	Spin	Energy	Spin	Energy	Spin
0.00	7/2	0.00	7/2	0.00	7/2	0.00	7/2
1.68	9/2	1.64	9/2	1.66	9/2	1.33	9/2
2.44	11/2	2.50	11/2	2.46	11/2	2.34	11/2
3.25	7/2	3.47	19/2	3.47	19/2	3.04	19/2
3.41	3/2	3.64	5/2	3.50	5/2		
3.64	19/2	3.66	15/2	3.60	7/2		
3.71	15/2	3.68	13/2	3.64	13/2		
3.85	13/2	3.70	7/2	3.72	3/2		

previously by essentially the same arguments in ^{211}Po, ^{212}Po (Aue64) and ^{93}Mo (Aue64a).

5.3.2 Comparison with Other Model Calculations and with Experimental Results.

A schematic comparison of the results of various calculations with the experimental results obtained in this study is presented in Figure 5-1.

The first level scheme is from the work of McCullen, et al. (McC64). The wave functions used in this calculation were constructed from a ^{40}Ca core plus (Z-20) protons and (N-20) neutrons in the $1f_{7/2}$ shell. The $1f_{7/2}$ nucleon-nucleon interaction was determined from the observed levels of ^{42}Sc, assuming that they could be interpreted as due to the configuration $(1f_{7/2})^2$. Using the method of Talmi, the interaction was treated exactly — within the framework of the pure configuration assumption. As shown in Figure 5-1, this model produces a level scheme which is in good agreement with our results from gamma decay. The energies, spins, and parities are in accord with those assigned to the experimental scheme.

The second level scheme shown is from Vervier (Ver67). These calculations are similar to those of McCullen, et al., in that both assume the energy levels of ^{53}Fe arise from the $(\pi f_{7/2})^{-2}(\nu f_{7/2})^{-1}$ configuration. The effective proton-proton interaction in the $(\pi f_{7/2})^{-2}$ configuration was taken from the experimental spectrum of ^{54}Fe. Several effective proton-neutron interactions in the $(\pi f_{7/2})^{-1}$ $(\nu f_{7/2})^{-1}$ configuration were used (see Table 5-1). The level scheme shown was obtained using interaction (3), although all the effective interactions gave

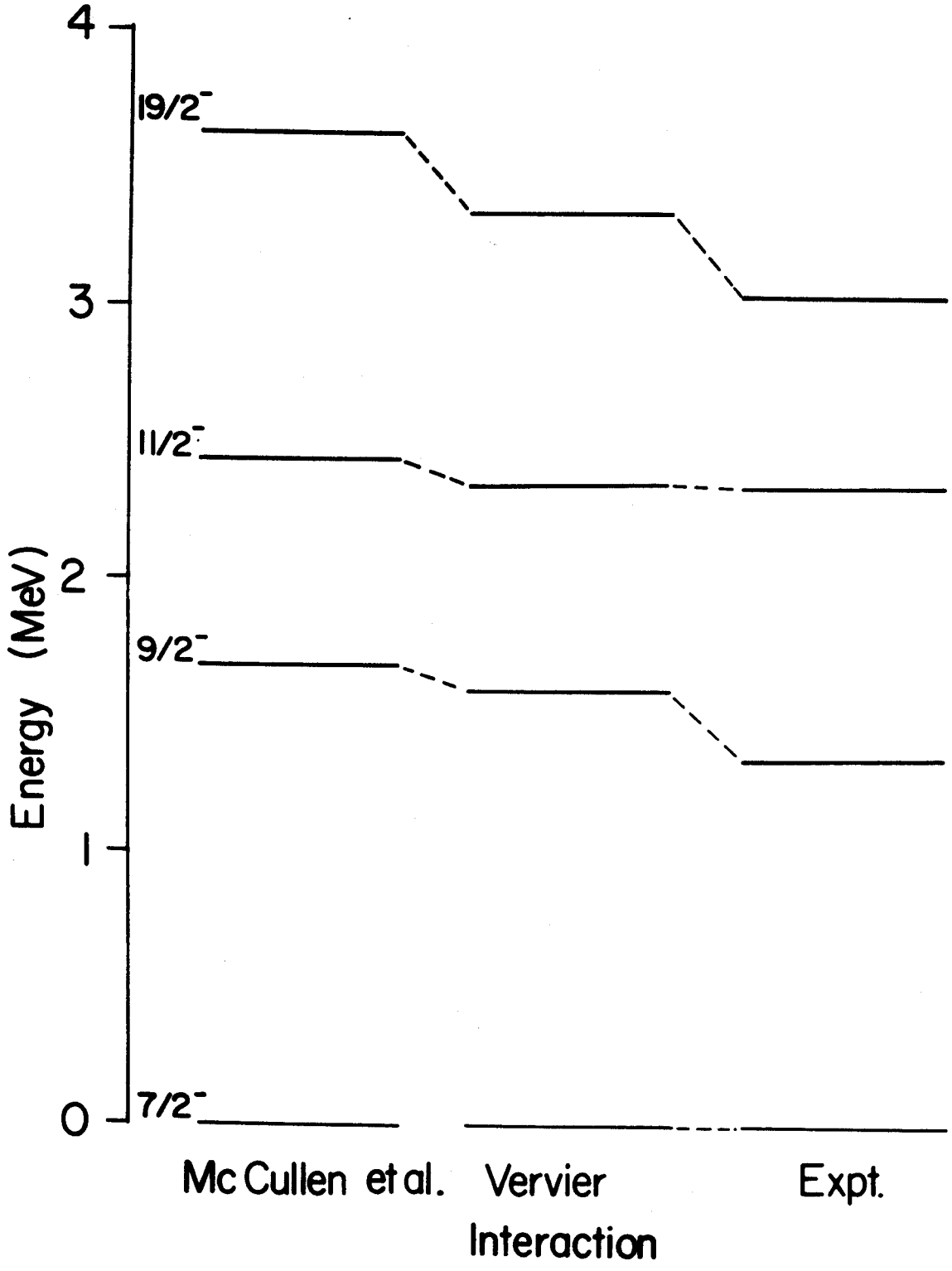

Figure 5-1. Schematic comparison of ^{53}Fe level schemes predicted by two calculations versus the experimental results obtained in this study.

practically the same results. The isomeric nature of the $19/2^-$ level is predicted in all cases, thus demonstrating that the existence of the isomer does not depend strongly on the details of the effective interactions.

Since our calculations using the Oak Ridge Shell Model Codes, utilized the interactions of Vervier, the resultant level scheme is practically the same as that reported by Vervier. Hence, our scheme is not included in Figure 5-1, but may be thought of as being the "Vervier Interaction". However, the results of our calculations are listed in Table 5-2.

5.4 ^{53}Mn Calculations

5.4.1 Predicted Level Scheme

Calculation of the energy level scheme for ^{53}Mn was accomplished using the Oak Ridge Shell Model Codes as described above. The calculations were performed assuming five active protons, in a pure $f_{7/2}$ approximation.

The results of these ^{53}Mn calculations, together with our experimentally determined levels, are given in Table 5-3.

5.4.2 Comparison with Other Model Calculations and with Experimental Results.

The levels of ^{53}Mn have been calculated by several workers. For comparison, a few of these level schemes are presented in Figure 5-2, alongside our experimentally determined level structure.

The results shown in the first theoretical decay scheme are those of Talmi (Lip58). These calculations are based on a closed core, with only the outer nucleons contributing to the level scheme. When there exist more than one nucleon in definite orbits outside this closed core, there are many levels obtained by the various modes of coupling of the angular momenta of the extra nucleons. Since the energy in the central field is the same for all these nucleons, one must consider their mutual interaction in order to remove the degeneracy and split the levels. Talmi's approach has been to start with the shell model and using jj-coupling wave functions predict the energies. He did not make any specific assumption for either the interaction or the radial functions. He assumed only that the effective interaction was a

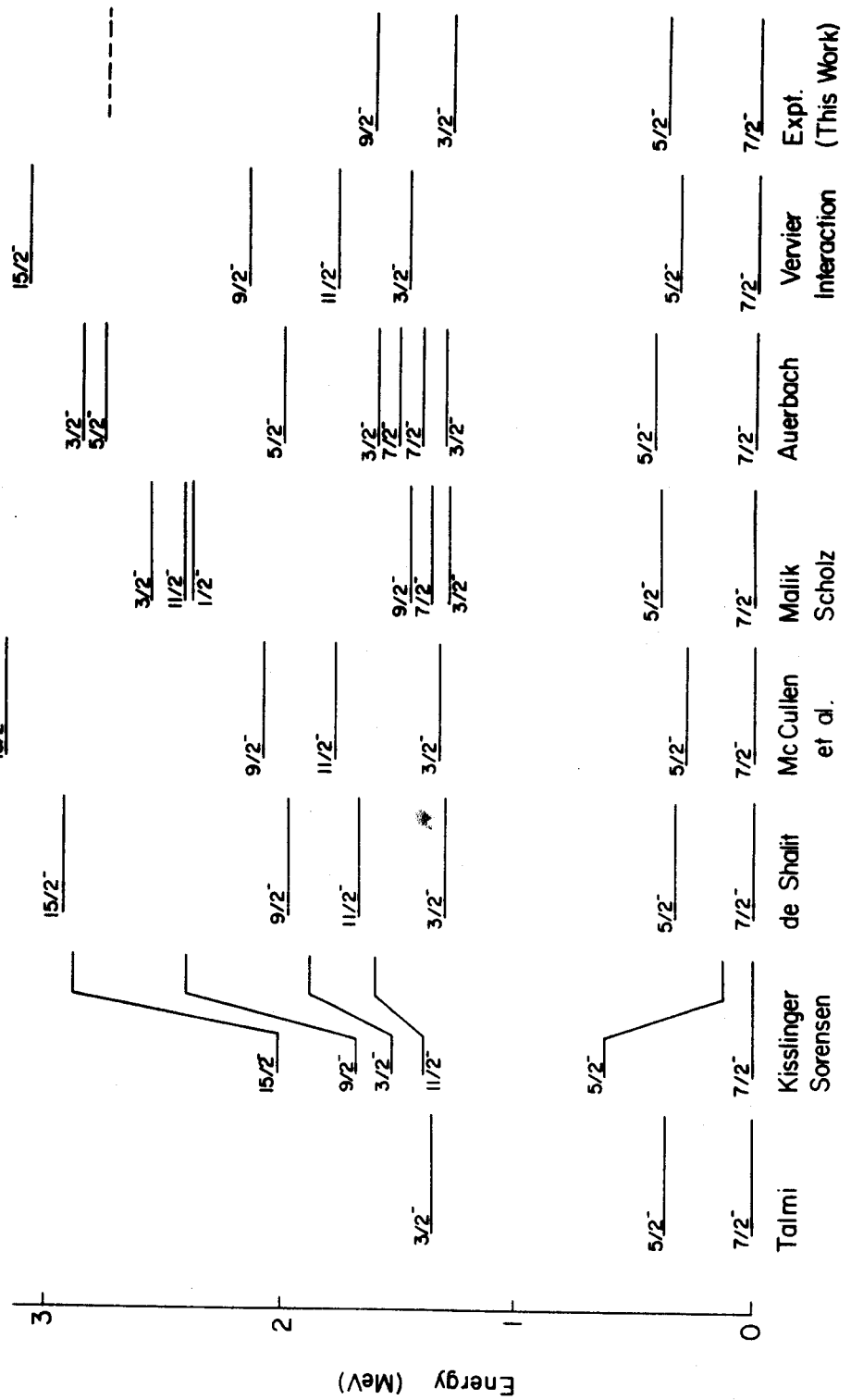

Figure 5-2. Schematic comparison of ^{53}Mn level schemes predicted by various calculations versus the experimental results obtained in this study.

Table 5-3

Predicted Levels and Spins for ^{53}Mn from Shell Model Calculations Using an Interaction from Vervier

Calculated		Experimental	
Energy (MeV)	Spin	Energy	Spin
0.00	7/2	0.00	7/2
0.32	5/2	0.38	5/2
1.47	3/2	1.29	3/2
1.78	11/2	1.62	9/2
2.15	9/2	2.75	( )
3.08	15/2		

two-body force. The results of his calculations for the first two excited states of ^{53}Mn are in excellent agreement with the experimental facts.

The second level scheme shows the results of Kisslinger and Sorensen (Kis60). Their model combines features of the unified nuclear model and the independent-particle model, with a two-body residual interaction. The residual action used consists of two parts — a pairing force and a long-range part. Calculations were performed for various values of the two strength parameters, using single-particle levels taken from experiments. Agreement with experimental results for ^{53}Mn was rather poor, although qualitatively correct. Prediction of the $11/2^-$ level being depressed under the $3/2^-$ level is not in agreement with other work. Also, the higher lying excited states are predicted to be somewhat too high in energy.

The third level scheme is that from deShalit (deS63). This rather detailed shell model calculation gives levels that are in good agreement with the experimental results. The separation of the higher states appears to be slightly too large.

The fourth level scheme is from the work of McCullen et al. (McC64). The methods of this calculation have already been described (Section 5.3.2). The first excited state is predicted a bit low, while the upper levels are slightly higher and more separated than in deShalit's work. Nevertheless, qualitatively, the level scheme is in agreement with experiment.

The fifth level scheme is that predicted by Malik and Scholz (Mal66). Their levels are calculated using a strong-coupling symmetric-rotator model including the Coriolis coupling between bands. The

single-particle energy levels and wave functions in the deformed well were computed for a spin-orbit strength consistent with the observed splitting in ^{41}Ca. The band-head energies were calculated from the appropriate summation over the occupied single-particle energy levels. The moment of inertia was taken from the excitation energy of the first excited 2^+ state of neighboring even-even nuclei assuming a rotational character for the state. The matrix elements of the Coriolis coupling were computed from the single-particle wave functions. The final excitation spectra were obtained by diagonalizing the Coriolis coupling term with the rotational wave function based on the ten available particle or core excited states in the $1f$-$2p$ shell. Energy levels and wave functions were calculated as a function of the deformation parameter, β. The results for ^{53}Mn are shown in Figure 5-3. The scheme agrees well with the experimental results, although the higher levels are a little low. Spin assignments to higher levels are also not in the same order as those of previous calculations shown.

The sixth theoretical level scheme presented is that of Auerbach (Aue67). Instead of the pure configuration description, he has employed a configuration mixing approach. A ^{48}Ca nucleus was assumed to be an inert core with the extra n-protons outside this core forming $f_{7/2}^{n}$ and $f_{7/2}^{n-1}$ configurations. The calculation was performed by the method of effective interactions. The results of this calculation for ^{53}Mn agree very well with those from the experiment.

The last calculation shown, labeled "Vervier Interaction", is our calculation using the Oak Ridge Shell Model Codes and the same proton-neutron effective interaction as used by Vervier. These levels

are in good agreement with the experimental results, although quantitatively they are not quite as close as some of the other calculations shown. In general, all of the calculations shown are in agreement with the lower-lying levels of ^{53}Mn as determined in our experimental work.

5.5 Calculation of ^{53}Fe Transition Probabilities

5.5.1 Methods of Calculation

5.5.1A Moszkowski Single Particle Estimates

Although the single particle estimates are rather crude and are not expected to yield accurate results, they do provide a good starting point for interpretation of ones results. Only a brief description of the derivation of the estimates will be provided here, since these details have been treated previously (Epp70a) (Mos65).

The total power radiated by a pure multipole over all angles is given by

$$P(\ell,m) = \frac{c}{8\pi k^2} \left|a(\ell,m)\right|^2 \qquad (5\text{-}21)$$

where P is the total power radiated and the a's are the multipole coefficients.

The transition probability may be written in quantum mechanical terms as

$$T = \frac{1}{\tau} = \frac{P}{\hbar\omega} \qquad (5\text{-}22)$$

where T is the transition probability and τ is the mean lifetime of the state.

Expressions can now be written for the electric and magnetic transition probabilities:

$$T_E(\ell,m) = \frac{2\pi c}{\hbar\omega[(2\ell+1)!!]^2} \left(\frac{\ell+1}{\ell}\right) k^{2\ell+2} \left|Q_{\ell m} + Q'_{\ell m}\right|^2 \qquad (5\text{-}23)$$

$$T_M(\ell,m) = \frac{2\pi c}{\hbar\omega[(2\ell+1)!!]^2} \left(\frac{\ell+1}{\ell}\right) k^{2\ell+2} \left|M_{\ell m} + M'_{\ell m}\right|^2 \qquad (5\text{-}24)$$

These equations still contain the classical expressions for charge and current densities, which must now be transformed to their quantum mechanical equivalents. Performing these transformation, one obtains:

$$Q_{\ell m} = e\langle f|r^{\ell}Y^{*}_{\ell m}|i\rangle \tag{5-25}$$

$$Q'_{\ell m} = \frac{iek\hbar}{2(\ell+1)M}\langle f|\mu_n \vec{\sigma}\times\vec{r}\cdot\vec{\nabla}(r^{\ell}Y^{*}_{\ell m}) + 2r^{\ell}Y^{*}_{\ell m}\frac{\vec{r}\cdot\vec{p}}{h}|i\rangle \tag{5-26}$$

$$M_{\ell m} = \frac{e\hbar}{(\ell+1)M}\langle f|\vec{\nabla}(r^{\ell}Y^{*}_{\ell m}\cdot\vec{L})|i\rangle \tag{5-27}$$

$$M'_{\ell m} = \frac{1}{2}\mu_n\frac{e\hbar}{M}\langle f|\vec{\sigma}\cdot\vec{\nabla}(r^{\ell}Y^{*}_{\ell m})|i\rangle \tag{5-28}$$

At this point, the calculation of the transition probabilities cannot proceed without having explicit forms for the wave functions involved. Thus, we must invoke some particular nuclear model in order to provide the wave functions, and consequently, the radial matrix elements.

The single-particle model assumes that the structure of the excited nuclear state is determined entirely by the last, unpaired nucleon in the nucleus, either a proton or a neutron. The nuclear properties are therefore established by the properties of this last unpaired nucleon. γ transitions from excited nuclear states are then defined as changes in the state of the odd nucleon under the influence of a spherically symmetric potential created by the remainder of the nucleons in the nucleus.

Calculation of the single-particle transition probability is usually carried out assuming that the odd particle is a proton, although neutron transitions can be treated by a slight modification of the

expressions.

If we consider the transitions of a proton in a central, velocity-independent well, equations (5-23) and (5-24) now can be written as:

$$T_{i\to f}^{(EL)} = \frac{2(\ell+1)}{\ell[(2\ell+1)!!]^2}\,\omega\left(\frac{e^2}{\hbar c}\right)\left(\frac{\omega a}{c}\right)^{2\ell}\cdot\left(\int_0^\infty R_f\left(\frac{r}{a}\right)^{\ell} R_i r^2 dr\right)^2 S(j_i,\ell,j_f) \qquad (5\text{-}29)$$

and

$$T_{i\to f}^{(ML)} = \frac{2(\ell+1)}{\ell[(2\ell+1)!!]}^{2\omega}\,\frac{e^2}{\hbar c}\left(\frac{\omega a}{c}\right)^{2\ell}\left(\frac{\hbar}{mca}\right)^2\cdot\left(\mu_p\ell - \frac{\ell}{\ell+1}\right)^2\left(\int_0^\infty R_f\left(\frac{r}{a}\right)^{\ell-1} R_i r^2 dr\right)^2\cdot$$

$$S(j_i,\ell,j_f) \qquad (5\text{-}30)$$

where

ℓ = the angular momentum carried away by the emitted quantum.

R_i, R_f = Radial wave functions of the initial and final states, respectively

$\omega = (E_i - E_f)/\hbar$

c = velocity of light

a = nuclear radius

μ_p = proton magnetic moment

S = statistical factor

The radial integrals can be evaluated explicitly if one makes a few assumptions concerning the nuclear wavefunctions. A very simple view of the nuclear wavefunctions is provided by the assumption that the radial wavefunctions, R, for both the initial and final states are constant throughout the interior of the nucleus (for r<a) and vanish outside (for r>a) (Bla52), (Wei51).

On the basis of this constant density model, the radial integrals

may be rewritten as:

$$\int_0^\infty R_f \left(\frac{r}{a}\right)^\ell R_i \, r^2 dr = \frac{3}{(\ell+3)} \tag{5-31}$$

A more detailed calculation of radial integrals, using the radial wavefunctions of a single proton in a spherical square well was found to give practically the same results as the simple assumption above, except for *M*1 transitions (Mos53). In order to obtain more accurate results it would be necessary to take into account the diffuseness of the nuclear potential (Blo60).

Using the constant density model estimate, the γ-decay transition probability for a single proton, equations (5-29) and (5-30), can be written in the following form:

$$T_{sp}^{(EL)} = \frac{4.4(\ell+1)}{\ell[(2\ell+1)!!]^2} \left(\frac{3}{\ell+3}\right)^2 \left(\frac{\hbar\omega}{197 \text{ MeV}}\right)^{2\ell+1} \times$$

$$(a \text{ in } 10^{-13} \text{ cm})^{2\ell} \, S(j_i,\ell,j_f) \times 10^{21} \text{sec}^{-1} \tag{5-32}$$

and

$$T_{sp}^{(ML)} = \frac{0.19 \ (\ell+1)}{\ell[(2\ell+1)!!]^2} \left(\frac{3}{\ell+2}\right)^2 \left(\mu_p \ell - \frac{\ell}{\ell+1}\right)^2 \times$$

$$\left(\frac{\hbar\omega}{197 \text{ MeV}}\right)^{2\ell+1} (a \text{ in } 10^{-13} \text{cm})^{2\ell-2} \times$$

$$S(j_i,\ell,j_f) \times 10^{21} \text{sec}^{-1} \tag{5-33}$$

A few of these estimates are listed in Table 5-4. These expressions include the assumptions that $a = 1.2 \times 10^{-13} A^{1/3}$ and $\mu p = 2.79$.

The statistical factor, S, contains the angular dependence of

Table 5-4

Single-Particle Estimates for the Transition Probability of a Single Proton.

Multipolarity		T_{sp} in sec^{-1}
*E*1	=	$1.0\times10^{14} \cdot A^{2/3} \cdot E_\gamma^3$ S
*E*2	=	$7.4\times10^{7} \cdot A^{4/3} \cdot E_\gamma^5$ S
*E*3	=	$3.4\times10^{1} \cdot A^{2} \cdot E_\gamma^7$ S
*E*4	=	$1.1\times10^{-5} \cdot A^{8/3} \cdot E_\gamma^9$ S
*E*5	=	$2.5\times10^{-12} \cdot A^{10/3} \cdot E_\gamma^{11}$ S
*M*1	=	$2.9\times10^{13} \cdot A^{0} \cdot E_\gamma^3$ S
*M*2	=	$8.4\times10^{7} \cdot A^{2/3} \cdot E_\gamma^5$ S
*M*3	=	$8.7\times10^{1} \cdot A^{4/3} \cdot E_\gamma^7$ S
*M*4	=	$4.8\times10^{-5} \cdot A^{2} \cdot E_\gamma^9$ S
*M*5	=	$1.7\times10^{-11} \cdot A^{8/3} \cdot E_\gamma^{11}$ S

($a = 1.2\times10^{-13} A^{1/3}$ cm., $\mu_p = 2.79$, E_γ in MeV)

the transition probability, and can be defined as:

$$S(j_i,\ell,j_f) = 4\pi(2j_i+1)^{-1} \sum_{m_i} \sum_{m_f} \sum_{M} \left| \int_{4\pi} \Theta^{m_f *}_{\ell_f j_f} Y^*_{\ell m} \Theta^{m_i}_{\ell_i j_j} \, d\Omega \right|^2 \tag{5-34}$$

A simple expression for S can be deduced from the above

$$S(j_i,\ell,j_f) = (2j_f+1)[C(j_i,j_f\ell,\tfrac{1}{2} - \tfrac{1}{2}\ 0)]^2 \tag{5-35}$$

where C is a Clebsch-Gordon coefficient (Edm57, Ros57).

For the special case where $|j_i-j_f| = \ell$, the expression for S becomes relatively simple:

$$S(j_i,\ell,j_f) = \frac{[(j-(1/2)]!}{(2j_i)!!} \times \frac{(2\ell+1)!!}{\ell!} \times \frac{(2j_f)!!}{[(j_f-(1/2)]!} \tag{5-36}$$

In particular,

$$S(\ell+1/2,\ \ell,1/2) = 1 \tag{5-37}$$

Viewed strictly from a single particle picture, magnetic transition probabilities in odd-neutron nuclei are expected to be slightly smaller than the corresponding magnetic transition probabilities in odd proton nuclei (Mos65), by the factor

$$\left| \frac{\mu_N}{\mu_p - (\ell+1)^{-1}} \right|^2 \tag{5-38}$$

The equations from Table 5-4 were incorporated into a PDP-9 computer program, PROB, written by Dr. R. Eppley. This program calculates transition probabilities and half-lives of γ-ray transitions based on the single particle equations by Moszkowski. The input information consists of the type of transition (neutron or proton), the transition energy, and the value of the statistical factor. The output contains

the transition probability and half-life for the transitions $E1$ through $E5$ and $M1$ through $M5$. This program may be found on the library DECtape and is run under the keyboard monitor system.

5.5.1B Shell Model Methods

Present day shell model calculations are capable of going far beyond the simple estimates outlined in Section A. Multiparticle configurations as well as configuration mixing can be treated. While somewhat complex, the formalism for reducing these expressions containing many-particle matrix elements to single particle matrix elements exists and is well-defined (Gla70). This essentially reduces the problem to the evaluation of single particle matrix elements. In this section, I would like to outline the calculation of these single particle matrix elements, which are the basis of the shell model transition probability formalism. In some ways, this amounts to a partial restatement of Section A, but is more complete and provides a good insight into the calculation.

We wish to evaluate the following matrix elements for electric transitions:

$$\langle \rho_f | | | S^L \mathbb{1}^\circ | | | \lambda_i \rangle \quad \text{and} \quad \langle \rho_f | | | V^L \tau^1 | | | \lambda_i \rangle \tag{5-39}$$

where S^L and V^L are defined by

$$S^L_m(el) = \sum_{i=1}^{A} \frac{e_p(i)+e_n(i)}{2} r_i^L Y^L_m(\hat{r}) \qquad V^L_m(el) = \sum_{i=1}^{A} \frac{e_p(i)-e_n(i)}{2} r_i^L Y^L_m(\hat{r}_i) \tag{5-40}$$

The wave functions $|\rho\rangle$ can be separated into a radial, spin, and isospin part

$$|\rho\rangle \equiv |R_{n,\ell}\rangle |\ell j m\rangle |tt_Z\rangle \tag{5-41}$$

The same can be done for $|\lambda>$. We can now rewrite the expressions for the matrix elements in (5-39)

$$<\rho_f||S^L \mathcal{M}^\circ||\lambda_i> = (\frac{e_p+e_n}{2})<R_{\ell f}||r^L||R_{\ell i}><\ell_f j_f||Y^L(\hat{r})||\ell_i j_i><t||\mathcal{M}||t>$$

and

$$<\rho_f||V^L\tau^1||\lambda_i> = (\frac{e_p - e_n}{2})<R_{\ell f}||r^L||R_{\ell i}><\ell_f j_f||Y^L(\hat{r})||\ell_i j_i><t||\tau^1||t>$$

(5-42)

We now consider each part of (5-42).

1. $$<R_{\ell f}||r^L||R_{\ell i}> = \int_0^\infty R^*_{n_f \ell_f}(\hat{r})\, r^L\, R_{n_i \ell_i}(\hat{r})\, dr \equiv <r^L> \qquad (5\text{-}43)$$

2. $$<\ell_f j_f||Y^L(\hat{r})||\ell_i j_i> = <\ell_\rho \underset{j_f}{\triangle}^{\frac{1}{2}} ||Y^L(\hat{r})||^{\ell_i} \underset{j_i}{\triangle}^{\frac{1}{2}} > \equiv M \qquad (5\text{-}44)$$

Since $Y^L(\hat{r})$ does not operate on spin we have:

$$M = (-1)^{\ell_f+1/2+j_i+L}\sqrt{(2j_f+1)(2j_i+1)}\begin{Bmatrix}\ell_f & \ell & L\\ j_i & j_f & \frac{1}{2}\end{Bmatrix}<\ell_f||Y^L(\hat{r})||\ell_i> \qquad (5\text{-}45)$$

The last part of 5-45) can be evaluated using equation 17.14 of deShalit and Talmi (Des63b).

$$<\ell_f||Y^L(\hat{r})||\ell_i> = (-1)^{\ell_f}\sqrt{\frac{(2L+1)\ (2\ell_f+1)\ (2\ell_i+1)}{4\pi}}\begin{pmatrix}\ell_f & L & \ell_i\\ 0 & 0 & 0\end{pmatrix} \qquad (5\text{-}46)$$

This vanishes for $\ell_f + L + \ell_i$ = odd.

Therefore, the resultant expression is:

$$<\ell_f j_f||Y^L(\hat{r})||\ell_i j_i> = (-1)^{2\ell_f+\frac{1}{2}+j_i+L}\sqrt{\frac{(2j_f+1)(2j_i+1)(2\ell_f+1)(2L+1)(2\ell_i+1)}{4\pi}}$$

$$\times \begin{Bmatrix}\ell_f & \ell_i & L\\ j_i & j_f & \frac{1}{2}\end{Bmatrix}\begin{pmatrix}\ell_f & L & \ell_i\\ 0 & 0 & 0\end{pmatrix} \qquad (5\text{-}47)$$

3. The last part of (5-42) can be calculated directly with the Wigner-Eckart theorem

$$\text{Since } 1 = \langle \tilde{tt} || \mathbb{1} || \tilde{tt} \rangle = \overbrace{\frac{\langle tt00|tt\rangle}{\sqrt{(2t+1)}}}^{+1} \langle t || \mathbb{1} || t \rangle$$

$$\text{we get } \langle t || \mathbb{1} || t \rangle = \sqrt{2t+1} \tag{5-48}$$

Likewise, one can prove from

$$t_z = \langle \tilde{tt} | t_z | \tilde{tt} \rangle$$

that

$$\langle t || t^{\ell} || t' \rangle = \sqrt{\tau(\tau+1)(2\tau+1)}\ \delta_{tt'} \tag{5-49}$$

for $t = 1/2$ we get using $\vec{\tau} = 2\vec{t}$

$$\begin{aligned} \langle 1/2 || \mathbb{1}^{\circ} || 1/2 \rangle &= \sqrt{2} \\ \langle 1/2 || \tau^{1} || 1/2 \rangle &= \sqrt{6} \end{aligned} \tag{5-50}$$

The final expressions for the single-particle matrix element for an electric transition can now be written as:

$$\langle \ell_f j_f t || S^L(el) \cdot \mathbb{1}^{\circ} || \ell_i j_i \rangle = \left[\frac{e_p + e_n}{2} \right] \left[(-1)^{\frac{1}{2}+j_i+L} \sqrt{\frac{(2j_f+1)(2j_i+1)(2L+1)(2\ell_i+1)}{4\pi}} \right.$$

$$\left. \times \begin{Bmatrix} \ell_f \ell_i L \\ j_i j_f \frac{1}{2} \end{Bmatrix} \begin{pmatrix} \ell_f L \ell_i \\ 0\ 0\ 0 \end{pmatrix} \right] \sqrt{2}\ \langle r^L \rangle \tag{5-51}$$

$$\langle \ell_f j_f t || V^L(el)\tau^\ell || \ell_i j_i t\rangle = \left[\frac{e_p - e_n}{2}\right]\left[(-1)^{\frac{1}{2}+j_i+L}\sqrt{\frac{(2j_f+1)(2j_i+1)(2L+1)(2\ell_i+1)}{4\pi}}\right.$$

$$\left.\times \begin{Bmatrix} \ell_f \ell_i L \\ j_i j_f \frac{1}{2} \end{Bmatrix} \begin{pmatrix} \ell_f L \ell_i \\ 0\ 0\ 0 \end{pmatrix}\right] \sqrt{6}\ \langle r^L\rangle \qquad (5\text{-}52)$$

The curly brackets indicate a 6-j symbol and the parentheses a 3-j symbol.

The corresponding calculation of single particle matrix elements for magnetic transitions is more complex and somewhat more difficult.

The reduced transition probability for a magnetic transition, B(L) contains many-particle matrix elements

$$B(L) = \frac{1}{(2J_i+1)(2T_f+1)} \underbrace{\left[\sum_{\tilde{j}_i \tilde{j}_f} \frac{\langle J_i \tilde{J}_i L \tilde{L} | J_f \tilde{J}_f\rangle}{\sqrt{2J_f+1}}\right]^2}_{=1}$$

$$\times \left[\langle T_i \tilde{T}_i 00 | T_f \tilde{T}_f\rangle \langle J_f T_f ||| S^L \mathbb{1}^\circ ||| J_i T_i\rangle + \right.$$

$$\left. -\langle T_i \tilde{T}_i 10 | T_f \tilde{T}_f\rangle \langle J_f T_f ||| V^L \tau^1 ||| J_i T_i\rangle \right]^2 =$$

$$= \frac{1}{(2J_i+1)(2T_f+1)} \left[\langle J_f T_f ||| S^L \mathbb{1}^\circ ||| J_i T_i\rangle \delta_{T_i T_f} + \right.$$

$$\left. \langle T_i \tilde{T}_i 10 | T_f \tilde{T}_f\rangle \langle J_f T_f ||| V^L \tau^1 ||| J_i T_i\rangle \right]^2 \qquad (5\text{-}53)$$

It can however, be expressed in terms of one-particle matrix elements.

$$\langle \rho || S^L \mathbb{1}^\circ || \lambda\rangle \qquad (5\text{-}54)$$

$$\langle \rho || V^L \tau^1 || \lambda\rangle \qquad (5\text{-}55)$$

where S^L and V^L are given by

$$S^L_m(\text{magn.}) = \sum_{i=1}^{A} \left[\text{grad } r_i^L Y^L_m(\hat{r}_i)\right] \cdot \left[\frac{g_p^{(\ell)}(i) + g_n^{(\ell)}(i)}{2} \frac{2\vec{\ell}_{-i}}{L+1} + \frac{g_p^{(s)}(i) + g_n^{(s)}(i)}{2} \vec{s}_i\right] \frac{e\hbar}{2M_p c} \tag{5-56}$$

$$V^L_m(\text{magn.}) = \sum_{i=1}^{A} \left[\text{grad } r_i^L Y^L_m(r_i)\right] \cdot \left[\frac{g_p^{(\ell)}(i) - g_n^{(\ell)}(i)}{2} \frac{2\vec{\ell}_i}{L+1} + \frac{g_p^{(s)}(i) - g_n^{(s)}(i)}{2} \vec{s}_i\right] \frac{e\hbar}{2M_p c} \tag{5-57}$$

Again separating the wave functions $|\rho>$ in space and isospin parts we have

$$<\rho||S^L \mathbb{1}^\circ||\lambda> = <\ell_f j_f||S^L \mathbb{1}^\circ||\ell_i j_i><t||\mathbb{1}^\circ||t> \tag{5-58}$$

and

$$<\rho||V^L \tau^1||\lambda> = <\ell_f j_f||V^L||\ell_i j_i><t||\tau^1||t> \tag{5-59}$$

The matrix elements of the isospin part were calculated above, see (5-50). For the space part, we may use the values of

$$<\ell_f j_f|[\text{grad}]r^L Y^L(\hat{r})|\cdot\vec{\ell}||\ell_i j_i> \tag{5-60}$$

and

$$<\ell_f j_f|[\text{grad}]r^L Y^L(\hat{r})|\cdot\vec{s}||\ell_i j_i> \tag{5-61}$$

Using the expression (17.19) from deShalit (deS63b), one can perform a calculation for a magnetic dipole ($M1$) transition. For the orbital

angular momentum part we obtain:

$$\langle \ell_f j_f | \mathrm{grad}[rY^1(\hat{r})]\cdot\vec{\ell} || \ell_i j_i \rangle = \frac{3}{4\pi} \langle \ell_f j_f || \vec{\ell} || \ell_i j_i \rangle \qquad (5\text{-}62)$$

This can be rewritten as:

$$\langle \ell_f j_f || \vec{\ell} || \ell_i j_i \rangle = \langle \ell_f \underset{j_f}{\triangle^{\frac{1}{2}}} || \vec{\ell} || \ell_i \underset{j_i}{\triangle^{\frac{1}{2}}} \rangle =$$

$$(-1)^{\ell_f+1/2+j_i+1} \sqrt{(2j_i+1)(2j_f+1)} \begin{Bmatrix} \ell_f & \ell_i & 1 \\ j_i & j_f & 1/2 \end{Bmatrix} \langle \ell_f || \vec{\ell} || \ell_i \rangle \qquad (5\text{-}63)$$

Applying the Wigner-Eckart theorem we have:

$$\langle \ell_f || \vec{\ell} || \ell_i \rangle = \sqrt{\ell_i(\ell_i+1)(2\ell_i+1)}\ \delta_{\ell_i \ell_f} \qquad (5\text{-}64)$$

Substituting (5-64) into (5-63) and (5-63) into (5-62) we get:

$$\langle \ell_f j_f || \mathrm{grad}[rY^1(\hat{r})\cdot]\vec{\ell} || \ell_i j_i \rangle =$$

$$\sqrt{\frac{3}{4\pi}}\ (-1)^{\ell_f+j_i+3/2} \sqrt{(2j_i+1)(2j_f+1)}\ \sqrt{\ell_i(\ell_i+1)(2\ell_i+1)}$$

$$\begin{Bmatrix} \ell_f & \ell_i & 1 \\ j_i & j_f & 1/2 \end{Bmatrix} \times \delta_{\ell_i \ell_f} \qquad (5\text{-}65)$$

Likewise, a similar expression can be derived for the intrinsic spin part:

$$\langle \ell_f j_f || \text{grad}[r Y^1(\hat{r})]\cdot\vec{s} || \ell_i j_i \rangle =$$

$$\sqrt{\frac{3}{4}}\,(-1)^{\ell_f+j_f+3/2}\,\sqrt{(2j_f+1)(2j_i+1)}\,\sqrt{\frac{3}{2}}\,\begin{Bmatrix} 1/2 & 1/2 & 1 \\ j_i & j_f & \ell_f \end{Bmatrix}\delta_{\ell_i\ell_f} \qquad (5\text{-}66)$$

Final expressions for the magnetic dipole transitions may be written as:

For the isoscalar term:

$$\langle \ell_f j_f t || S^1(M1)\mathcal{M}^0 || \ell_i j_i t \rangle = \sqrt{\frac{3}{4\pi}}\,\sqrt{(2j_i+1)(2j_f+1)}\,(-1)^{\ell_f}\delta_{\ell_i\ell_f}\times$$

$$\left[(-1)^{j_i+3/2}\left(\frac{g_p^{(\ell)}+g_n^{(\ell)}}{2}\right)\sqrt{\ell_i(\ell_i+1)(2\ell_i+1)}\,\begin{Bmatrix} \ell_f & \ell_i & 1 \\ j_i & j_f & 1/2 \end{Bmatrix} + \right.$$

$$\left.(-1)^{j_f+3/2}\left(\frac{g_p^{(s)}+g_n^{(s)}}{2}\right)\sqrt{\frac{3}{2}}\,\begin{Bmatrix} 1/2 & 1/2 & 1 \\ j_i & j_f & \ell_f \end{Bmatrix}\right]\sqrt{2}\,\frac{e\hbar}{2M_pc} \qquad (5\text{-}67)$$

For the isovector term:

$$\langle \ell_f j_f t || V^1(M1)\tau^1 || \ell_i j_i t \rangle = \sqrt{\frac{3}{4\pi}}\,\sqrt{(2j_i+1)(2j_f+1)}\,(-1)^{\ell_f}\delta_{\ell_i\ell_f}\times$$

$$\left[(-1)^{j_i+3/2}\left(\frac{g_p^{(\ell)}-g_n^{(\ell)}}{2}\right)\sqrt{\ell_i(\ell_i+1)(2\ell_i+1)}\,\begin{Bmatrix} \ell_f & \ell_i & 1 \\ j_i & j_f & 1/2 \end{Bmatrix} + \right.$$

$$\left.(-1)^{j_f+3/2}\left(\frac{g_p^{(s)}-g_n^{(s)}}{2}\right)\sqrt{\frac{3}{2}}\,\begin{Bmatrix} 1/2 & 1/2 & 1 \\ j_i & j_f & \ell_f \end{Bmatrix}\right]\sqrt{6}\,\frac{e\hbar}{2M_pc} \qquad (5\text{-}68)$$

Note that both matrix elements vanish unless

$$|j_i - j_f| \leq 1 \quad \text{and} \quad \ell_i = \ell_f \qquad (5\text{-}69)$$

Note that the conditions given by (5-69) are the selection rules for *M*1 transitions.

The above discussion was included here to give the reader some feeling for the techniques involved in performing these calculations. The *M*1 probability calculation outlined above is relatively simple compared to higher order magnetic transitions. The ^{53m}Fe problem contained only one such transition, but it was an *M*5!

Before continuing it is appropriate to discuss the matter of units. Calculation of the reduced transition probability, $B(L,\pi)$, yields so-called "natural" units of $[e^2fm^{2L}]$ and $[\mu_o^2 fm^{2L-2}]$ for electric and magnetic transitions, respectively. One may wish to go from these to partial half-lives, or vice versa, in order to compare with experiment. The following formulas and conversions are quite useful in accomplishing the change of units.

The partial width of a gamma transition (with angular momentum L, energy E_γ, and parity π) from an initial level with spin j_i to a final level with j_f is given by the expression (Pre62)

$$\Gamma_{L,\pi} = \frac{8\pi(L+1)}{L[(2L+1)!!]^2}\left(\frac{E_\gamma}{\hbar c}\right)^{2L+1} B(L,\pi) \qquad (5\text{-}70)$$

where $B(L,\pi)$ is the reduced transition probability, in units of (e^2fm^{2L}) or $(\mu_o^2 fm^{2L-2})$.

Convenient units for plugging into this equation are:

$\hbar c = 1.973 \times 10^{-11}$ MeV cm

$e^2 = 1.440$ MeV fm

$\mu_o^2 = 0.1589$ MeV fm^3

The lifetime of the initial state may be calculated by:

$$\Gamma \cdot \tau = \hbar = 0.6582 \times 10^{-15} \text{ eV sec} \qquad (5\text{-}71)$$

and the half-life obtained with

$$T_{1/2} = 0.693\ \tau \qquad (5\text{-}72)$$

The above equations allow the results of our calculations to be expressed in various units.

5.5.2 Results

5.5.2A Single Particle Estimate

The values of the single particle estimate were obtained using program PROB — which utilizes the formulas listed in Table 5-4. Such a formula was not available for the *E*6 transition, and it was calculated using formula (5-32). The statistical factor, S, was obtained by use of expression (5-36).

The results of these Moszkowski single particle estimates for the relevant ^{53m}Fe transitions together with the experimental data are given in Table 5-5.

5.5.2B Shell Model Results

The reduced transition probabilities, B(L,π), and consequently the partial half-lives also were calculated using the Oak Ridge Shell Model Codes. These shell model estimates for the relevant *E*6, *M*5, and *E*4 decays were calculated in an $f_{7/2}$ approximation. Eigenstates of the mass 53 system were calculated assuming 7 active neutrons, 6 active protons and the $f_{7/2}$ interaction of Vervier. The $19/2^-$ state is purely $(\nu f_{7/2})^7_{J=7/2}(\pi f_{7/2})^6_{J=6}$, whereas the $11/2^-$ and $7/2^-$ states are

Table 5-5

Comparison of Experimental Results with Moszkowski Single Particle Values for Partial Half-life.

E (keV)	Multipolarity	Photon Intensity	Expt.[a]	Calc.	Retardation Expt./Calc.
701.1±0.1	E4	100	1.57×10^{2}	2.06×10^{1}	7.6
1011.5±0.1	M1	86±5	...	...	...
1328.1±0.1	M1	87±4	...	...	...
1712.6±0.3	M5	1.3±0.1	1.17×10^{4}	2.76×10^{3}	4.2
2339.6±0.1	E2	13±2	...	...	...
3040.6±0.5	E6	0.06±.01	2.6×10^{5}	6.17×10^{4}	4.3

[a] The 701.1-keV transition was corrected for conversion using a value of $\alpha_k = 0.003$, which we obtained by a linear extrapolation from the tables of R.S.Hager and E.C.Seltzer, Nucl. Data., Sec. A4, 1(1968). The conversion coefficients for the other transitions were small enough to be negligible.

mixtures of the J=4 and 2; and J=2 and 0 proton couplings, respectively. For the electric transitions, effective charges of $e_p = 1.5$ and $e_n = 0.5$ were assumed, together with a harmonic oscillator radial dependence. Free nucleon g-factors and harmonic oscillator radial dependence were assumed for the *M*5 calculation.

Table 5-6 contains the results of these calculations, both in terms of the photon partial half-lives and in terms of the reduced transition probability.

The experimental values also are shown in the same units for easy comparison. In addition a retardation factor for the half-lives is given.

5.5.3 Discussion

The Moszkowski single particle estimates, summarized in Table 5-5, are in remarkably good agreement with the experimental results. Moszkowski himself states that these theoretical values are "crude" and "not expected to represent accurately transitions in actual nuclei". (Mos65). However, in this case, a single-particle description appears to be an adequate approximation. It is rather surprising that the decay of the three-particle isomeric state to various levels of different couplings can be described so well by a single particle model.

The results of the shell model calculations of partial half-lives are presented in Table 5-6. The agreement with experimental values is not as good as in the case of the Moszkowski estimates. In addition, the formalism for calculating higher order magnetic transitions, such as the *M*5 has not been checked completely. Therefore, the calculated value for the *M*5 transition may be in error. The results for the

Table 5-6

Comparison of Experimental Results with Shell Model Values for Partial Half-life.

E_γ (keV)	Multi-polarity	Photon Intensity	Partial Photon $t_{1/2}$ (sec.) Expt.	Calc.	Retardation expt./calc.	B(L, π) Expt.	Calc.
701.1±0.1	E4	≡100	1.57×10^{2}	1.28×10^{1}	12.3	$6.37\times10^{2}\ e^{2}fm^{8}$	$7.8\times10^{3}\ e^{2}fm^{8}$
1011.5±0.1	M1	86±5	---	---	---	---	---
1328.1±0.1	M1	87±4	---	---	---	---	---
1712.6±0.3	M5	1.3±0.1	1.17×10^{4}	1.06×10^{2}	110	$5.08\times10^{1}\ \mu_N^2 fm^{8}$	$7.2\times10^{7}\ \mu_N^2 fm^{8}$
2339.6±0.1	E2	13±2	---	---	---	---	$(4.59\times10^{3}\ e^{2}fm^{10})$
3040.6±0.5	E6	0.06±.01	2.60×10^{5}	1.15×10^{4}	22.6	$2.74\times10^{5}\ e^{2}fm^{12}$	$6.2\times10^{6}\ e^{2}fm^{8}$

*E*4 and *E*6 are more reliable, and indicate that the experimental values are retarded by factors of 12 and 22, respectively. The method of calculation was described earlier and will not be detailed here. The apparent difference between the calculated and measured values could be attributed to the following:

1) The effective charges of the proton and neutron may be smaller than expected in this case. This is a reasonable possibility, and is sufficient to account for most of the observed differences.

2) Configuration mixing may be taking place in the $7/2^-$ and $11/2^-$ states, with contributions from a $(p_{3/2})^2$ configuration. Transitions from the pure $f_{7/2}$, $19/2^-$ state to these configuration-mixed states are sufficient to explain the differences between the experimental values and those we calculated.

This last possibility is quite intriguing, since it offers a way to demonstrate the concept of configuration mixing. The three-particle isomeric state is, of course, a pure $f_{7/2}$ configuration. On the other hand, it is quite possible that the other states are configuration mixed — most likely with a $(p_{3/2})^2$ component. This rather unusual situation provides a rare opportunity to check the configuration-mixing theory directly. We are now preparing to carry out a series of shell model calculations in which we will determine the transition probability of decays going to such configuration-mixed states. If these calculations reproduce the observed values, a significant step in demonstrating the concept of configuration mixing will have been made.

CHAPTER VI

THE DECAY OF ^{40}Sc

6.1 Introduction

The γ-ray spectrum associated with the decay of ^{40}Sc was first studied by Glass and Richardson in 1955 (Gla55). ^{40}Sc was produced by the ^{40}Ca$(p,n)^{40}$Sc reaction using 20-MeV protons on a natural calcium foil. Only one γ ray, of energy 3.75±0.04 MeV, was attributed to the decay of ^{40}Sc.

Since this first investigation, many studies have been performed in order to determine the levels in ^{40}Ca populated by ^{40}Sc. The fact that ^{40}Sc is a doubly-closed shell nucleus (N=20, Z=20), has motivated much of the interest in this isotope. The bulk of the available information on the levels in ^{40}Ca has been obtained through scattering experiments (Bra56), (End67), (Ers66), (Gra65), (Spr65). Although some earlier γ-ray work has been performed on the ^{40}Sc decay (And66), Arm68), (Kas68), the rather short half-life of this isotope and the high energy of its γ rays have hindered precise γ-ray investigations of the levels in ^{40}Ca populated by its disintegration. However, with the advent of improved "slow"-pulsing techniques for the MSU Cyclotron and good on-line detection systems, it has now been possible to study the γ decay of ^{40}Sc with a relatively high degree of accuracy.

6.2 Target Preparation

For these on-line, pulsed-beam experiments, several kinds of targets were tried in attempts to reduce the background of unwanted γ rays. Early targets consisted of slurries of $CaCO_3$ (both natural and isotopically enriched) prepared in polystyrene or Duco cement binders on thin mylar foils. Later experiments utilized natural calcium metal targets. However, good results were not obtained until a 2-mg/cm^2, 99.973% isotopically-enriched ^{40}Ca foil, prepared at the Oak Ridge National Laboratory, became available from Dr. C. R. Gruhn. Originally the target was mounted in an Argon atmosphere and since has been maintained in a target storage chamber which is evacuated to a vacuum of the order of 5×10^{-6}mm by an absorption pumping system. Transfer of the target to various experimental setups was accomplished by a vacuum-transfer lock assembly designed by K. Thompson (Tho69) and C. Maggiore (Mag70) (see section 2.3.3). Thus, the target has not been exposed to air.

The amounts of contamination in the target due to oxidation and condensation of pump oil were obtained from elastic scattering data by T. Kuo (Kuo70). It was found that the thickness of oxygen was about 0.019±0.002 mg/cm^2; carbon, 0.0026±0.003 mg/cm^2; and hydrogen, 0.0017±0.0002 mg/cm^2. A small amount of fluorine was also observed but not measured. The isotopic and spectrographic analysis supplied by ORNL is listed in Table 6-1.

The ^{40}Sc activity was produced by the ^{40}Ca$(p,n)^{40}$Sc reaction, using a 24-MeV proton beam from the MSU cyclotron. Typically, the

Table 6-1

Isotopic and Spectrographic Analysis* of ^{40}Ca Target Used in This Study

Isotopic Analysis		Spectrographic Analysis			
^{40}Ca	99.973%	Ag	<0.02%	Mo	<0.05%
^{42}Ca	0.008	Al	<0.05	Na	0.01
^{43}Ca	0.001	B	<0.01	Ni	<0.05
^{44}Ca	0.018	Ba	<0.02	Pb	<0.05
^{46}Ca	<0.001	Co	<0.05	Pt	<0.05
^{48}Ca	0.001	Cr	<0.05	Rb	<0.02
		Cu	<0.05	Si	<0.05
		Fe	<0.02	Sn	<0.05
		K	<0.01	Sr	0.02
		Li	<0.01	Ti	<0.02
		Mg	<0.05	V	<0.02
		Mn	<0.02	Zr	<0.1

*Supplied by Oak Ridge National Laboratory.

foil was bombarded with a 10-nA beam for ≈0.4 sec per pulsed interval.

For an experiment utilizing the helium-jet thermalizer, an evaporated, self-supporting foil (≈1 mg/cm^2) of natural calcium was prepared. The recoils were produced by a 200-nA beam of 24-MeV protons over a period of 15 hours. Severe deterioration of the foil was noted at the end of the thermalizer experiment, with almost complete oxidation of the foil having taken place.

6.3 γ-Ray Spectra

The most valuable experiments performed in this investigation utilized pulsed-beam, routing techniques accomplished with the aid of the routing timer module described in section 2.2.1A. Although various Ge(Li) detectors were used throughout the study, the best results were obtained with a 2.5% detector, having a resolution of 2.2 keV and a peak-to-Compton ratio of 16.5:1. The activations were carried out in the vacuum-transfer chamber, with the target plane inclined 45° to the beam. The detector viewed the target through a 1/2-mil Kapton window at 90° to the beam. The target-to-detector distance was about two inches.

The resulting γ-ray pulses were amplified and then sorted in a 50-MHz, 13 bit analog-to-digital converter (ADC) connected on line to the Laboratory's XDS Sigma 7 computer. Usually, one 4096-channel spectrum containing the beam-on data and four successive 4096-channel spectra from the beam-off period were routed into the computer under program HYDRA. Four beam-off routed spectra from this study are shown in Figure 6-1. These resulted from a 32-hour accumulation of data in the slow-pulsing mode. In this particular experiment, a beam-on time of 0.40 sec and a beam-off period of 0.60 sec per pulse were used. The beam-off period was divided into four equal counting intervals of 0.15 sec each. No inhibition period was used between the end of a beam burst and the beginning of the first routed spectrum. Consequently, the first spectrum shown in Figure 6-1 shows the "washed-out" effect resulting from some beam-on spillover. Based on the half-lives of the transitions and comparison with scattering data, at least seven γ rays were found to belong to the decay of ^{40}Sc. The energies and

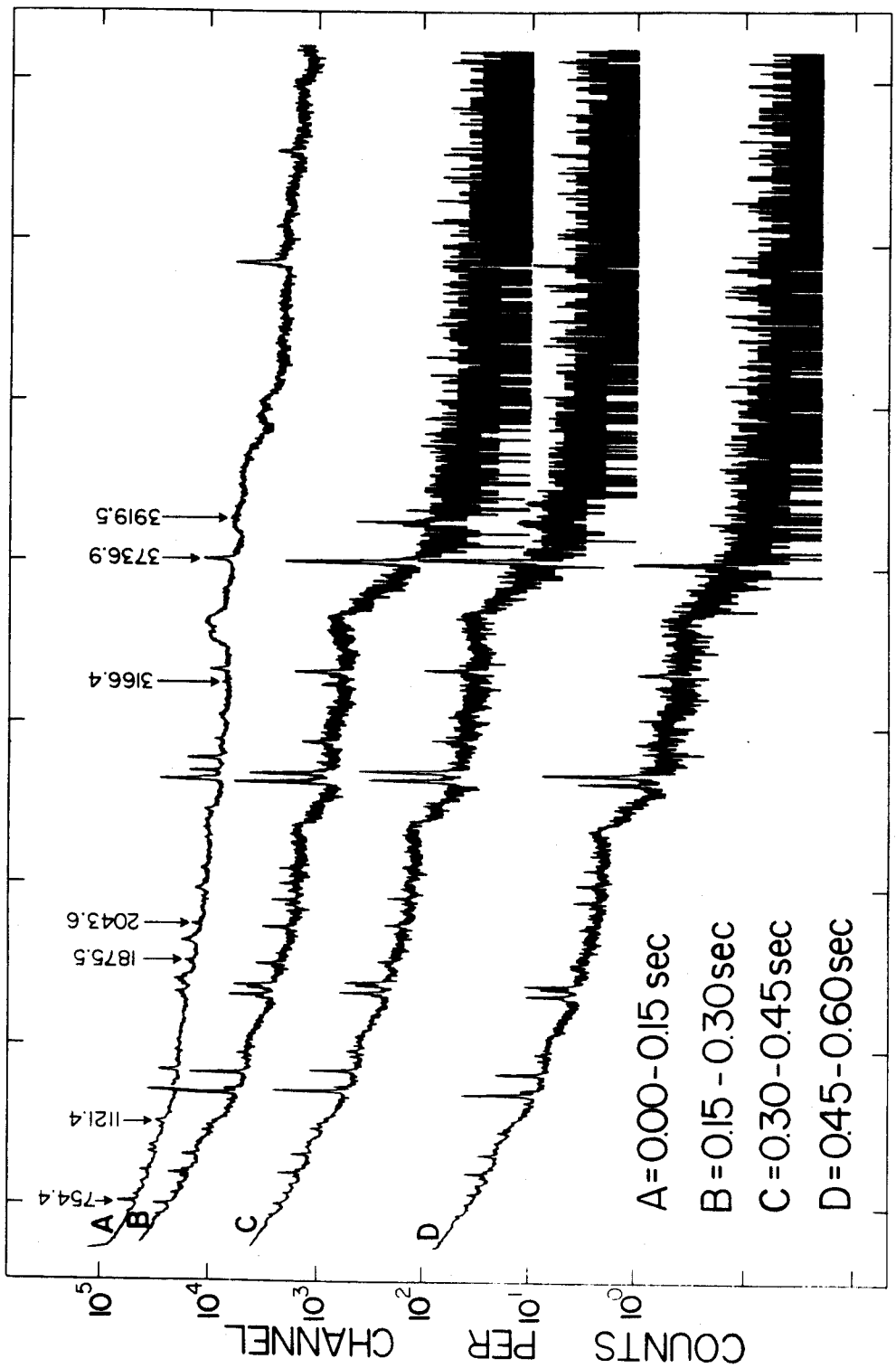

Figure 6-1. Beam-off, routed γ-ray spectra from the decay of ^{40}Sc.

intensities of these γ rays are given in Table 6-2.

The relatively thin natural calcium target and its rapid deterioration in impure helium severely limited the ^{40}Sc thermalizer experiment. Because of the success with pulsed-beam techniques, no further thermalizer runs were performed in the ^{40}Sc study.

Table 6-2

γ-Ray Energies and Intensities from the Decay of ^{40}Sc

Energy (keV)	Relative Intensity
754.4±0.2	48±3
1121.4±0.6	13±2
1875.5±0.5	25±2
2043.6±0.3	27±3
3166.4±0.6	14±2
3736.9±0.7	≡100
3919.5±1.0	10±2

6.4 Proposed Decay Scheme

The seven γ rays attributed to the decay of ^{40}Sc were fitted into a consistent decay scheme, as shown in Figure 6-2. The transition intensities, level energies and β^+-feeding information were obtained from this study. The ^{40}Sc half-life was taken from the work of Armini, et al. (Arm68). The number of γ transitions observed in this study and their placement in the decay scheme coincides with previous results (And66), (Arm68), (Kas68). However, the energy assignments of the observed γ rays are different from earlier work by as much as 8 keV, leading to somewhat different energy assignments for the level spacings. The measured intensities are generally in agreement with previous experiments. The results of this study are listed along with those from previous investigations in Table 6-3.

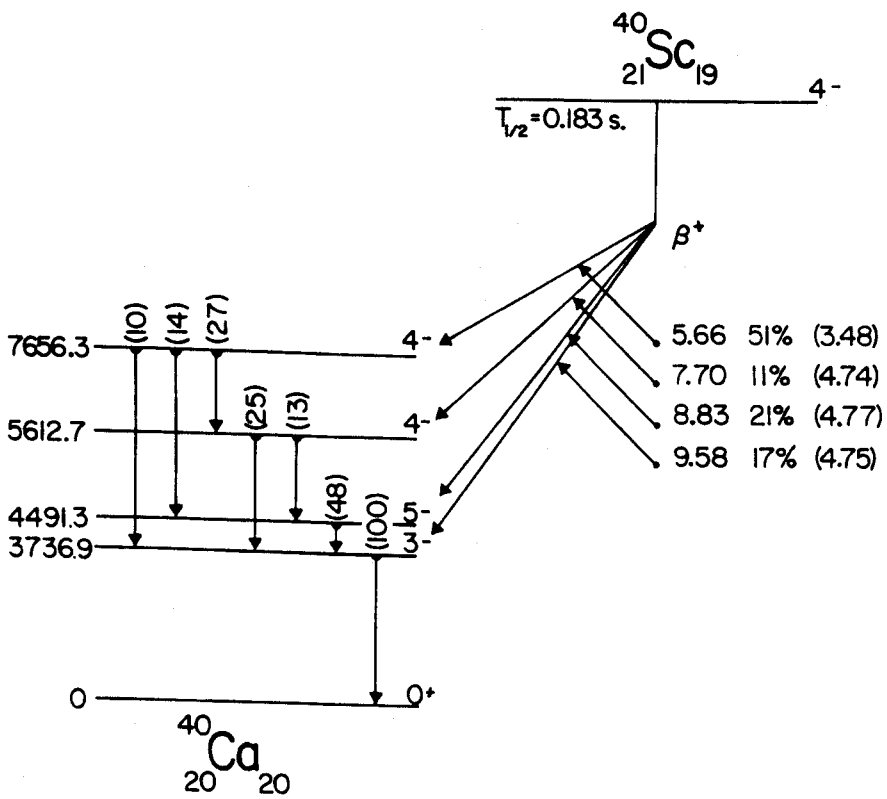

Figure 6-2. Proposed decay scheme for ^{40}Sc.

Table 6-3

^{40}Sc γ-Ray Energies and Intensities from This Investigation Compared with the Results from Previous Work

Anderson et al.[a]		Armini et al.[b]		Kashy&Snelgrove[c]	Present Work	
E(γ), MeV	Intensity(%)	E(γ), keV	Intensity(%)	E(γ), keV	E(γ), keV	Intensity(%)
0.73 ±.01	41.0±6.0	755.0±2.5	46±2	754.6±0.4	754.4±0.2	48±3
1.11 ±.03	7.0±2.0	1125.2±2.5	12±2	1121.7±0.7	1121.4±0.6	13±2
1.83 ±.02	24.3±2.0	1880.2±2.5	23±3	1877.0±0.5	1875.5±0.5	25±2
2.02 ±.02	22.0±2.0	2048.7±2.2	24±3	2044.9±0.5	2043.6±0.3	27±3
3.19 ±.04	13.4±2.0	3171.1±2.1	13±2	3167.0±0.4	3166.4±0.6	14±2
3.730±.004	100.0	3741.7±2.1	100±1	3736.9±0.3	3736.9±0.7	100
3.916±.007	17.6±2.5	3927.3±2.1	11±1	3921.7±0.5	3919.5±1.0	10±2

[a] (And66)

[b] (Arm68)

[c] (Kas68)

6.5 Discussion

Although this investigation did not reveal additional γ rays associated with the decay of ^{40}Sc, it did provide a basis for narrowing down the exact energies and intensities of these transitions. For example, the excitation energy of the first T=1 analog state of ^{40}Ca has been reported recently in the range of 7669.1 keV (Arm68) to 7658.9 keV (Kas68). Our measurements indicate that the lower value is the true one. Likewise, other level assignments in ^{40}Ca decay scheme were assigned more positively as a result of this study.

Many types of model calculations have been performed in attempts to describe the ^{40}Ca nucleus. One of the more successful of these is the rather extensive intermediate-coupling shell-model calculation performed by Kunz (Kun66). The results of this calculation are compared with current experimental values in Table 6-4. The agreement is reasonably good, although the predicted 4^- level at 6.5 MeV is presumably the observed 5612.7-keV level. A spin and parity of 4^- have been reported for this level (Gra66).

Table 6-4

Comparison of the Experimental Results of ^{40}Sc with Intermediate-Coupling Shell-Model Calculations[a]

I^{π}	^{40}Ca Energy Level		β Decay			
			log ft		Branching Ratio	
	Expt. (keV)	Theory (MeV)	Expt.	Theory	Expt.	Theory
4^-	7656.3	$7.62(4^-)$	3.48±0.15	3.27	51±1	52
		$6.9\ \ 3^-)$		4.49		6
4^-	5612.7	$6.58(4^-)$	4.74±0.12	4.44	11±1	10
5^-	4491.3	$4.13(5^-)$	4.77±0.10	4.59	21±1	21
3^-	3736.9	$3.80(3^-)$	4.75±0.08	5.14	17±1	8

[a] (Kun66)

CHAPTER VII

THE DECAY OF ^{53m}Co

7.1 Introduction

The discovery of a high-spin, three-quasiparticle metastable state in the ^{53}Fe nucleus has prompted the search for analogous states in nuclei having similar configurations. One of the most promising cases for comparison with the ^{53}Fe structure is the nucleus ^{53}Co. However, until quite recently, no evidence was available to support the existence of this nuclide or its possible metastable state. Since the structure of ^{53}Co differs from ^{53}Fe only in that it has a pair of neutron holes and a single proton hole outside the N=28, Z=28 doubly-closed shell instead of a pair of proton holes and a single neutron hole, one would expect the level schemes of the two nuclei to be very similar. An early search by Eskola for the ^{53}Co metastable state yielded negative results for possible states with half-lives greater than 15 sec (Esk67). However, one would expect a relatively short half-life for ^{53m}Co since the $19/2^-$ state can decay via a super-allowed β^+ transition to the isobaric analogue state in ^{53m}Fe. Therefore, a search was initiated to look for γ rays that could be attributed to the decay of ^{53m}Co. This effort utilized various pulsed-beam and helium-jet thermalizer techniques developed for examining short-lived species.

7.2 Target Preparation

All of our attempts to produce ^{53m}Co were made using the ^{54}Fe $(p,2n)^{53}$Co reaction induced by 30-40-MeV protons from the MSU cyclotron. Early pulsed-beam experiments were performed with isotopically separated ^{54}Fe in the form of Fe_2O_3. The oxide was mixed in a polystyrene binder and mounted on 1/4-mil mylar backings in target frames. Later in-beam and thermalizer runs utilized a 1.02 mg/cm^2, 97.4% enriched self-supporting ^{54}Fe foil. The major isotopic contaminant in this foil was ^{56}Fe which was present in the amount of 2.21 atomic percent. The Q-value for the ^{54}Fe$(p,2n)^{53}$Co reaction was calculated to be -22.8 MeV. The threshold for the next higher reaction, i.e., $(p,3n)$ was also calculated and found to be -39.2 MeV (Mye65). In a separate study of possible proton radioactivity from ^{53m}Co, Cerny et al. report an excitation function for producing ^{53m}Co by the ^{54}Fe$(p,2n)$ reaction (Cer70). This graph is reproduced in Figure 7-1. All of our experiments were carried out at proton energies of 30 to 40 MeV -- coinciding well with the peak region reported in the excitation function shown in Figure 7-1.

Typical beam currents for pulsed-beam experiments were 0.5-10.0 nA depending upon the target and detector used. The helium-jet thermalizer runs utilized a beam current of $\approx$1 μA on the 1 mg/cm^2 foil to produce reasonable count rates from the transported recoils.

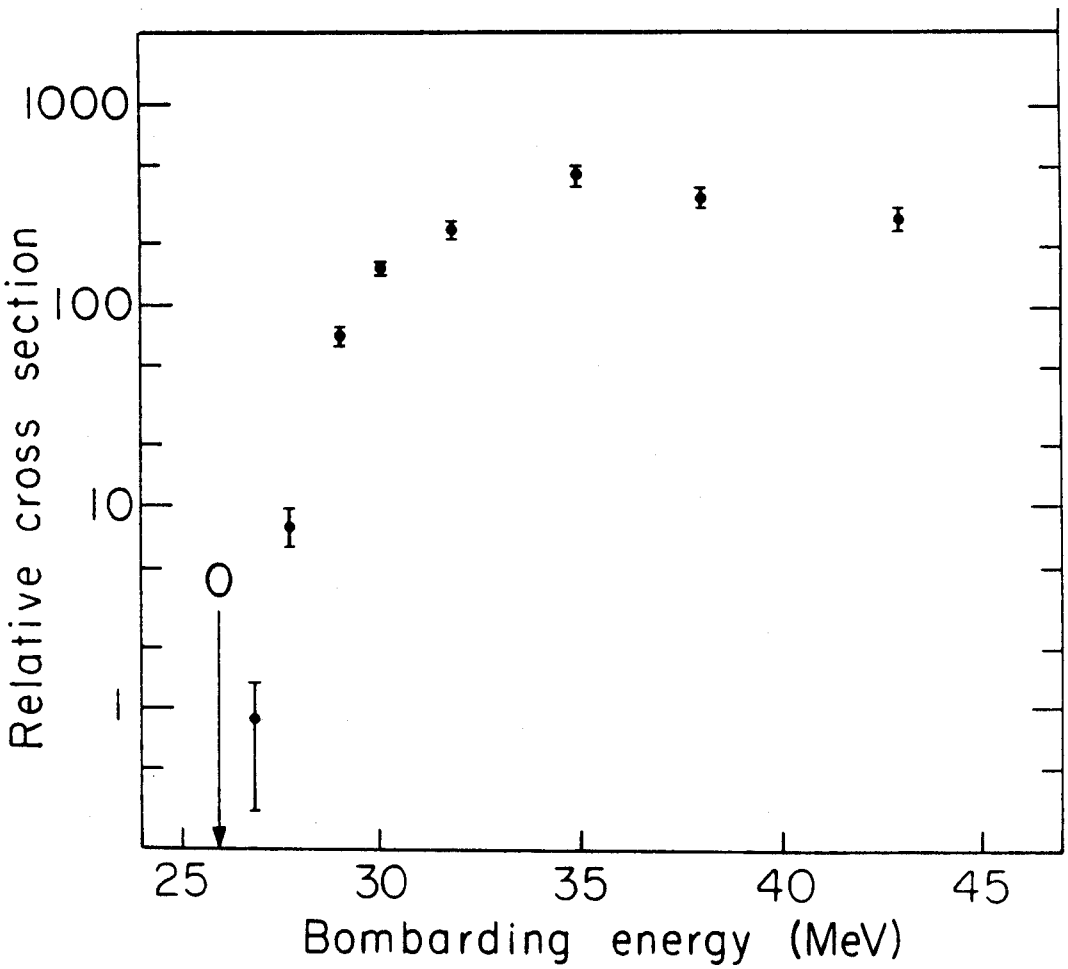

Figure 7-1. Excitation function for the $^{54}Fe(p,2n)^{53m}Co$ reaction reported by Cerny, et al. (Cer70).

7.3 Experimental Results

7.3.1 Proton Decay

Before proceeding with a description of the γ-ray spectra obtained in this study, I would like to review briefly the results reported by Cerny et al. regarding the possible proton decay of ^{53m}Co (Jac70), (Cer70).

In the course of searching for beta-delayed protons from ^{53}Ni produced by the ^{40}Ca(^{16}O,3n) reaction, Jackson et al. observed a 1.53±0.04-MeV proton activity with a 245±20-msec half-life which subsequently was attributed to the proton radioactivity of ^{53m}Co (Jac70). However, this experiment could not rule out the possibility that the isomer decayed by beta-delayed proton emission. Later experiments utilizing proton-induced reactions on ^{54}Fe produced a proton activity with a threshold of 26.3±0.4 MeV which was assigned to ^{53m}Co (Cer70). The direct proton radioactivity of the isomer was established by failure to detect positron-proton coincidences in the decay. The values for the proton energy and half-life were found to be 1.57±0.03 MeV and 242±15 msec, respectively. The observed half-life implies that the dominant mode of decay is by positron emission to ^{53m}Fe, with the proton emission constituting only a weak branch in the decay of ^{53m}Co. The partial half-life for the Fermi component of the super-allowed β^+-decay was calculated to be 0.35 sec (Fre66). Inclusion of the Gamow-Teller matrix element (assuming pure $(f_{7/2})^{-3}$ configurations), yields a predicted half-life of 0.2 sec (deS63b) -- in agreement with the observed value.

7.3.2 γ-Ray Spectra

The primary objective of this investigation was to search for a γ-ray branch in the decay of ^{53m}Co. Two techniques were employed in

this effort. First, pulsed-beam, routing methods were used to look for short-lived species and to assign relative half-lives to those observed. Second, a helium-jet thermalizer system was utilized to obtain good statistics in a low-background counting area in order to detect very weak, short-lived γ rays.

Since Eskola's work placed an upper limit of 15 sec on the half-life of ^{53m}Co, our early pulsed-beam experiments were aimed at quite short half-lives -- with routing intervals of 0.5-0.10 sec (Esk67). The subsequent report of a ^{53m}Co proton activity attributed a half-life of 0.242±0.015 sec to the isomer (Cer70). Consequently, routing intervals of ≈0.17 sec each were used to optimize the possibility of detecting and verifying γ-ray half-lives similar to that reported for ^{53m}Co. The most effective of the pulsed-beam experiments utilized the separated isotope ^{54}Fe foil described above and a 2.5%-efficient Ge(Li) detector. A representative set of beam-off, routed spectra from this study are shown in Figure 7-2. These four spectra contain the data obtained in four consecutive 0.17-sec intervals following a beam-on period of 0.45 sec per cycle -- no inhibition period was used. The total accumulation time for this experiment was 3.0 hr. Most of the peaks in Figure 7-2 have been labeled with their approximate energies. Some known contaminants and side-products also have been labeled. During this phase of the ^{53m}Co search, ten separate pulsed-beam experiments were carried out over a period of several months -- some of which contained better statistics and more peaks than those shown. However, based on the energies and approximate half-lives observed, no γ ray could be assigned positively to the decay of ^{53m}Co.

The ^{54}Fe foil again was utilized in the helium-jet thermalizer system. The foil was bombarded with 30-35-MeV protons and the resulting

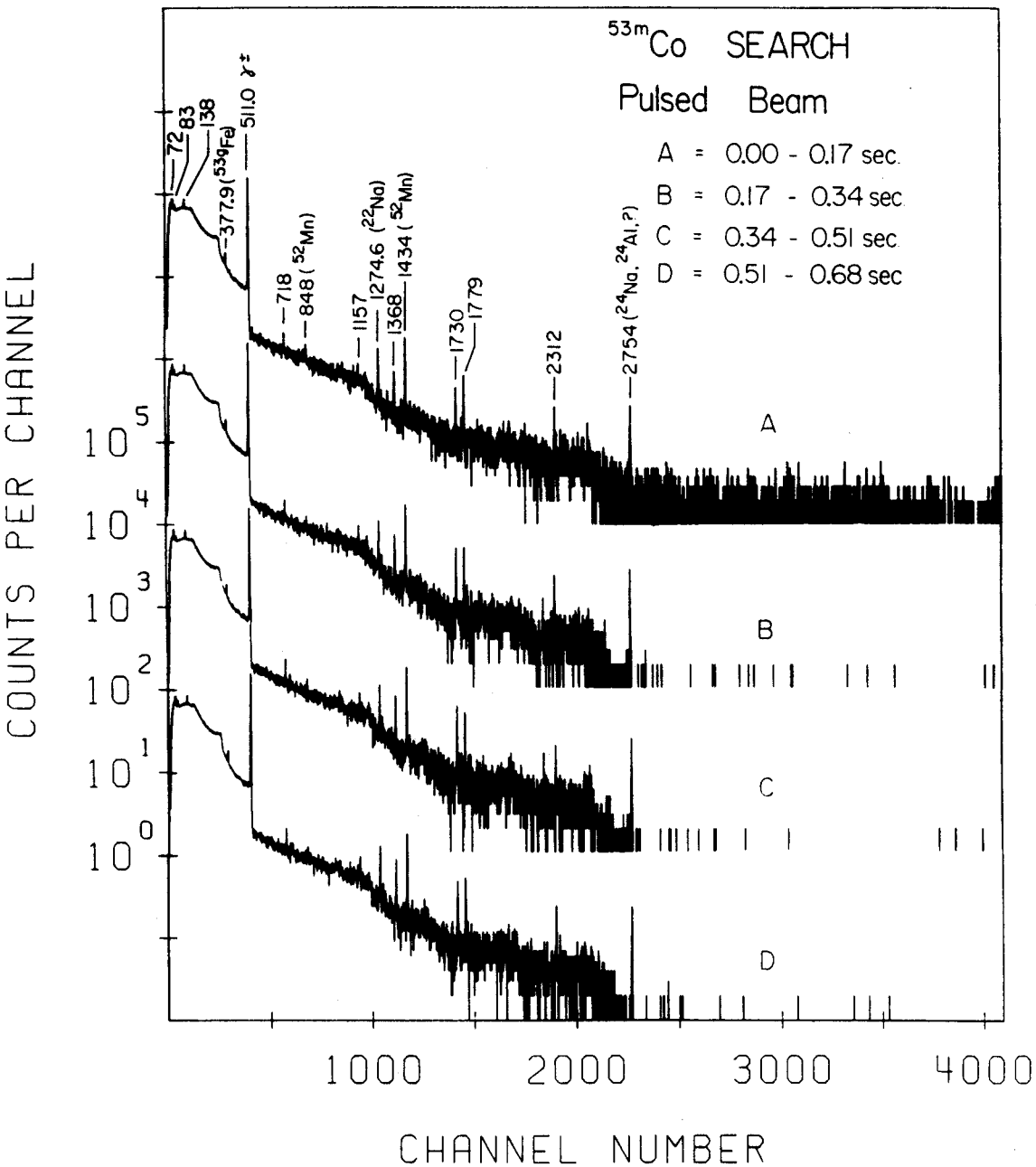

Figure 7-2. Four routed beam-off spectra from the ^{53m}Co search using the "slow-pulsing" technique.

recoils were thermalized in helium and piped up to a fixed collector on the roof of the cyclotron vault. Under these relatively low background conditions, a 10.4% Ge(Li) detector was used to observe the γ rays associated with the recoils. Since the mechanism for moving the collecting surface was not operational when these spectra were taken, some peaks due to the buildup of long-lived species were present. An example of such a spectrum is shown in Figure 7-3. This spectrum represents a total accumulation time of 11.5 hr. Note the greatly improved statistics as compared with the pulsed-beam runs. Although significant amounts of $^{53m+g}$Fe are present in this spectrum, one cannot conclude merely from the observation of $^{53m+g}$Fe gamma rays that he has produced its $^{53m+g}$Co analogue since the threshold for the ^{54}Fe$(p,pn)^{m+g}$Fe reaction (13.6 MeV) is lower than the threshold for the ^{54}Fe$(p,2n)^{53}$Co reaction (22.8 MeV). The situation also is hampered by the fact that the thermalizer beam entrance window is constructed of thin Havar -- containing natural iron and thus contributing recoil contamination. Although the ^{53m}Co thermalizer spectra contain several unidentified γ rays, it has not been possible to attribute them definitely to the decay of ^{53m}Co or establish any sort of decay scheme.

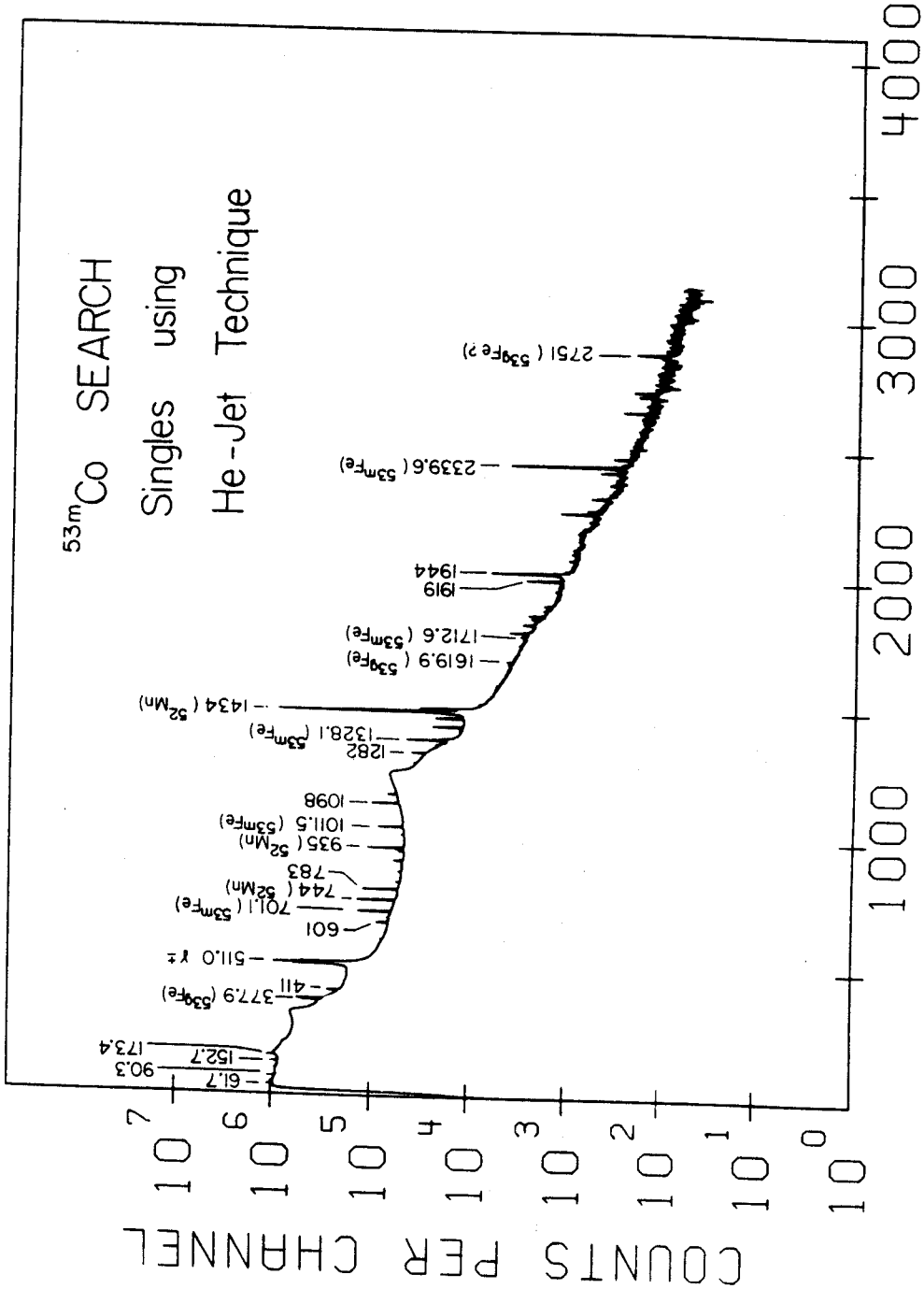

Figure 7-3. γ-ray singles spectrum from the ^{53m}Co search using the helium-jet thermalizer technique.

7.4 Discussion

The facts currently known about the modes of decay of ^{53m}Co are illustrated in Figure 7-4. The values for the half-life and proton decay are from the work of Cerny et al. (Cer70). The calculated ground state and predicted levels which could be populated by a γ-decay branch also are indicated.

If one assumes that the structure of ^{53m}Co is exactly analogous to the ^{53m}Fe case including a 2.5-m γ-decay half-life, and further assumes that .242 sec is the correct overall half-life, then a γ/β^+ branching ratio of only about 1:500 would be expected for the ^{53m}Co decay. If these conditions prevailed, the discovery of a γ-decay branch in ^{53m}Co by the present techniques would be most unlikely, since the lower limit of detection for the β^+/γ ratio is about 1:10 using these methods. However, any enhancement of the γ decay de-exciting the isomeric level would bring the γ-ray portion of the branching ratio closer to the limits of detection. For example, if the $15/2^-$ level were to occur below the $19/2^-$ level in ^{53m}Co, the $E2$ γ ray de-exciting the isomeric level would compete very favorably with β^+ decay. Thus, one cannot rule out the possibility of observing a γ-decay branch in the ^{53m}Co decay.

One somewhat anomalous feature was noted in several pulsed-beam experiments. Although over 99% of the ^{53m}Co is presumed to β^+ decay to ^{53m}Fe, several cases were found in which no significant amount of ^{53m}Fe activity was recorded. These were all cases in which the target, beam energy, beam alignment, etc. were chosen carefully to optimize the production of ^{53m}Co. On the other hand, all experiments revealed relatively large amounts of ^{53g}Fe and ^{52}Fe. Since ^{53m}Fe was not present in the

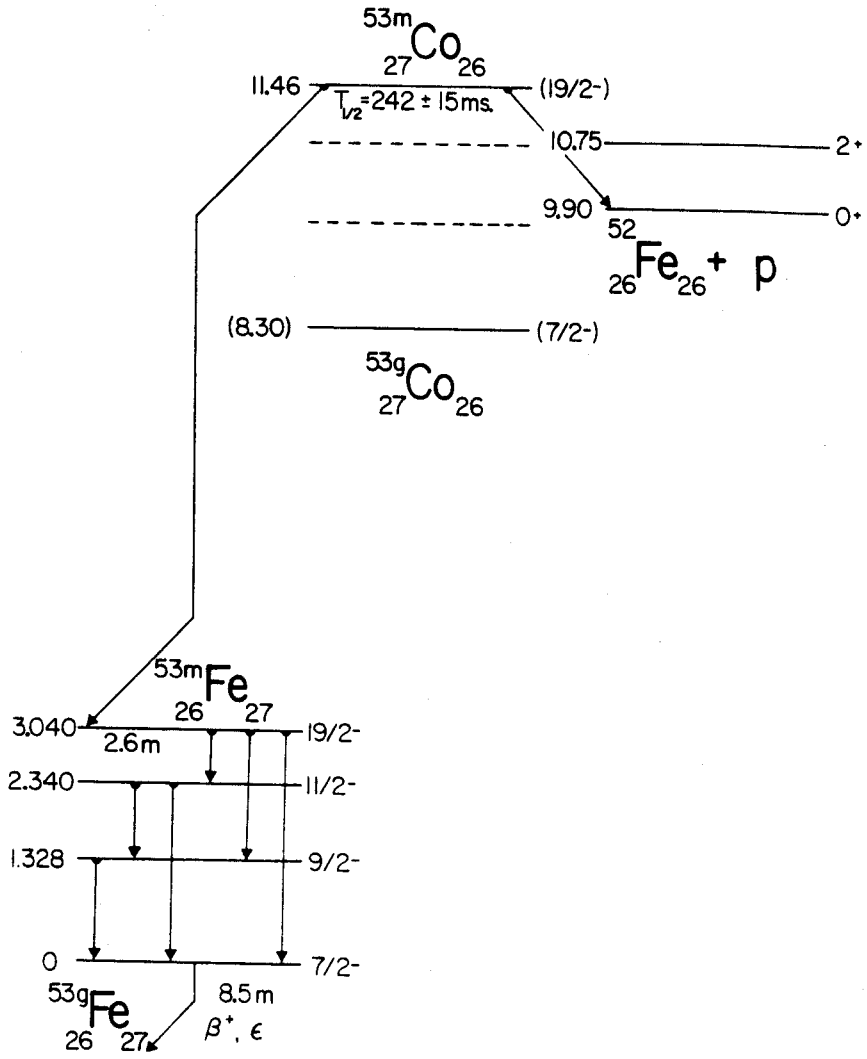

Figure7-4. Proposed decay scheme for ^{53m}Co showing the known modes of decay for the isomer.

expected amounts, it would appear as if either ^{53m}Co was not being produced in large amounts, or other decay modes were dominant.

Although this study could not provide positive assignment of γ rays to a γ-decay branch in ^{53m}Co, it did provide a number of unidentified possibilities. For the benefit of those who also may wish to investigate the ^{53m}Co structure, I have provided a comprehensive listing of all the γ rays observed in this investigation in Appendix C.

CHAPTER VIII

THE SEARCH FOR 3-PARTICLE ISOMERIC STATES IN ^{43}Ti AND ^{43}Sc

8.1 Introduction

High-spin, three-particle metastable states analogous to that discovered in ^{53}Fe also may exist in ^{43}Ti and ^{43}Sc. ^{43}Ti is of course the particle conjugate of the ^{53}Fe nucleus, and ^{43}Sc is the particle conjugate of ^{53}Co. The large decay energy of ^{43}Ti and the possibility of the decay of its $19/2^-$ state by a super-allowed β^+ transition to the $19/2^-$ state of ^{43}Sc implies that the half-life of the state is shorter than 1 sec. On the other hand, the $19/2^-$ state of ^{43}Sc should be similar to the ^{53}Fe case. Preliminary experiments were performed on both ^{43}Ti and ^{43}Sc, but were limited to γ-ray activities with half-lives greater than 15 sec (Esk67). This study was undertaken in an attempt to establish possible γ-ray activities associated with the decay of ^{43}Ti or ^{43}Sc.

8.2 Target Preparation

Because of the availability of target material, most of the experiments in this search have utilized the $^{45}Sc(p,3n)^{43}Ti$ reaction using 35-MeV protons from the MSU cyclotron. Since scandium is monoisotopic, the preparation of a suitable target was quite straightforward. Small pellets of purified scandium metal from A.D.MacKay, Inc., were hydraulically pressed into disks approximately 1 cm in diameter and 1 mm thick. Each disk was suspended in a target frame by thin mylar strips and used in the standard irradiation chambers. Typical beam currents were 0.5 - 10.0 nA for most on-line experiments. The above reaction affords both the possibility of observing γ rays from the de-excitation of ^{43m}Ti directly or from the de-excitation resulting after a super-allowed β^+ transition to the analogous level in ^{43m}Sc. Since the cross section for the $^{45}Sc(p,2np)^{43}Sc$ reaction is expected to be quite significant, one would also anticipate the formation of ^{43m}Sc directly by this route.

Another type of experiment was performed in which a helium-jet thermalizer was employed to look for ^{43m}Sc. The target for this experiment was a thin ($\simeq$0.5 mg/cm^2) layer of isotopically separated ^{44}Ca evaporated onto a tantalum backing (the target was mounted with the tantalum side facing the beam -- thus allowing the tantalum produced recoils to be trapped in the calcium, while the calcium produced recoils left the target and were thermalized.). A beam of 24-MeV protons was used to produce the ^{43}Sc by the $^{44}Ca(p,2n)^{43}Sc$ reaction. A beam current of $\simeq$1 μA was utilized to produce the recoils. After being thermalized in helium, the recoils were transported through a polyethylene capillary to a collector and counting facility on the roof of the cyclotron vault. Due to the transit

time in the capillary, this method was limited to detecting activities with half-lives greater than a few tens of msec.

8.3 γ-Ray Spectra

Most of the experiments performed in this study made use of the "slow-pulsing" technique to look for half-lives in the 10-1000 msec range. In these experiments, the cyclotron was pulsed by *RF* modulation, such that the activity was produced by beam bursts of about 1-2 sec duration and then counted in 4 successive, routed, beam-off spectra of about 100-600 msec each. A spectrum of the beam-on period also was obtained. A typical set of beam-off spectra from this type of experiment is shown in Figure 8-1. Peaks which have been reported as belonging to ^{43}Sc are labeled where appropriate.

Since beam pulsing in the μsec range was unavailable, an attempt was made to examine possible transitions in the nsec range -- thus bracketing the μsec region. This was achieved by routing γ spectra in the time intervals between the microscopic structure of the cyclotron beam. This period is about 50-60 nsec, depending on the beam energy. The spectra shown in Figure 8-2 are from such an experiment. Spectrum A is the beam-on data, representing the 19.8 nsec per pulse during which the beam was on target. (This period is dependent on the phase width.) Spectra B through E are the 4-8.5-nsec beam-off intervals following each *RF* bunch. These spectra contain many more peaks than found with the "slow-pulsing" technique, but are very useful in establishing lower limits for possible half-lives. A few representative scandium lines have been labeled for reference in Figure 8-2.

The helium-jet thermalizer experiment utilizing the ^{44}Ca target did not reveal significant amounts of known scandium γ rays. Because of the successful acquisition of data with pulsed-beam techniques, additional

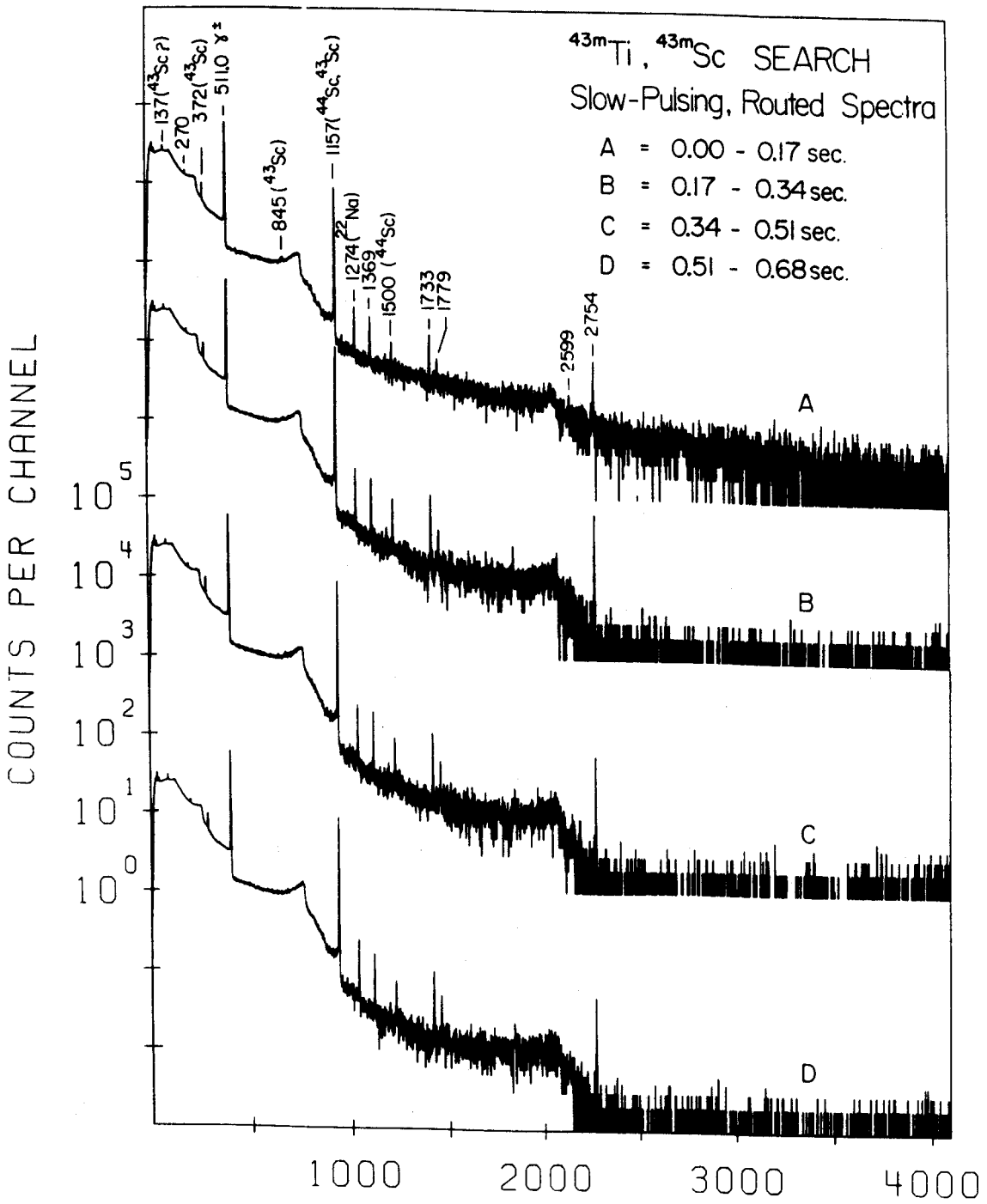

Figure 8-1. Four beam-off routed spectra from the ^{43m}Ti, ^{43m}Sc search using the "slow-pulsing" technique.

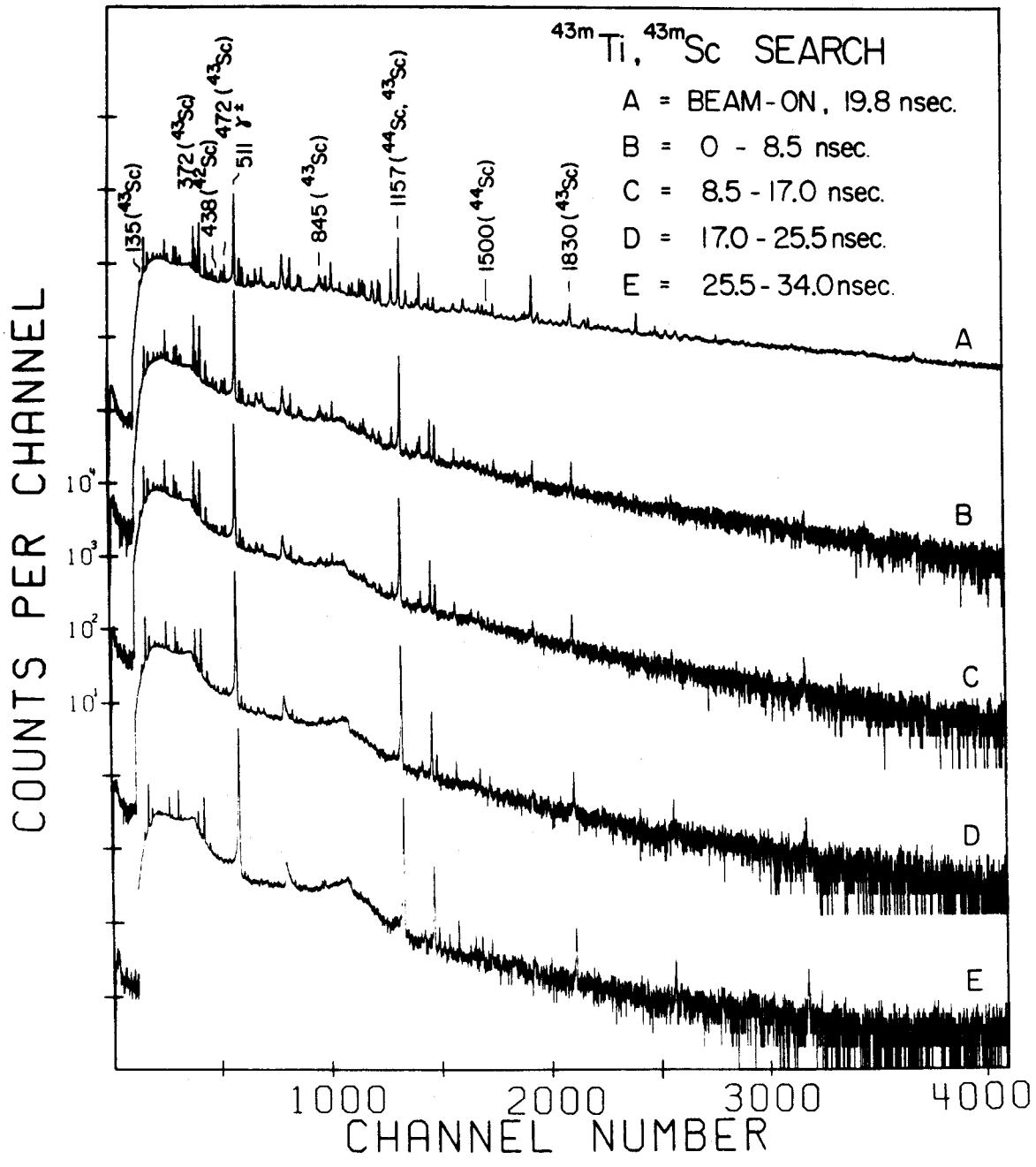

Figure 8-2. Routed spectra from the ^{43m}Ti, ^{43m}Sc search utilizing the microscopic structure of the cyclotron beam for timing.

thermalizer experiments were discontinued.

All of the methods described above utilized large high-resolution Ge(Li) detectors having efficiencies of 2.5-10.4% compared with a 3×3-in. NaI crystal at 25 cm.

The isomeric level in ^{43}Sc has been tentatively identified by other workers. Iordahescu reported the existence of two short-lived species in this region when performing a survey of α particles of 17.2-20.0 MeV on a number of thick natural targets (Ior68). With a potassium target, a γ activity with an energy of 154 keV and a half-life of 456 μsec was reported. With a calcium target, a γ ray with an energy of 163 keV and a half-life of 450 μsec was found. More recently Sawa and Bergström have reported a γ-decay scheme for ^{43m}Sc (Ann70). This level scheme is shown in Figure 8-3. The isomeric transition they report is an *E*2 with an energy of 136 keV and a half-life of 0.5 μsec. It appears that the $15/2^-$ state has crossed below the $19/2^-$ level, resulting in a much shorter half-life than one would expect from comparison with the ^{53m}Fe conjugate configuration.

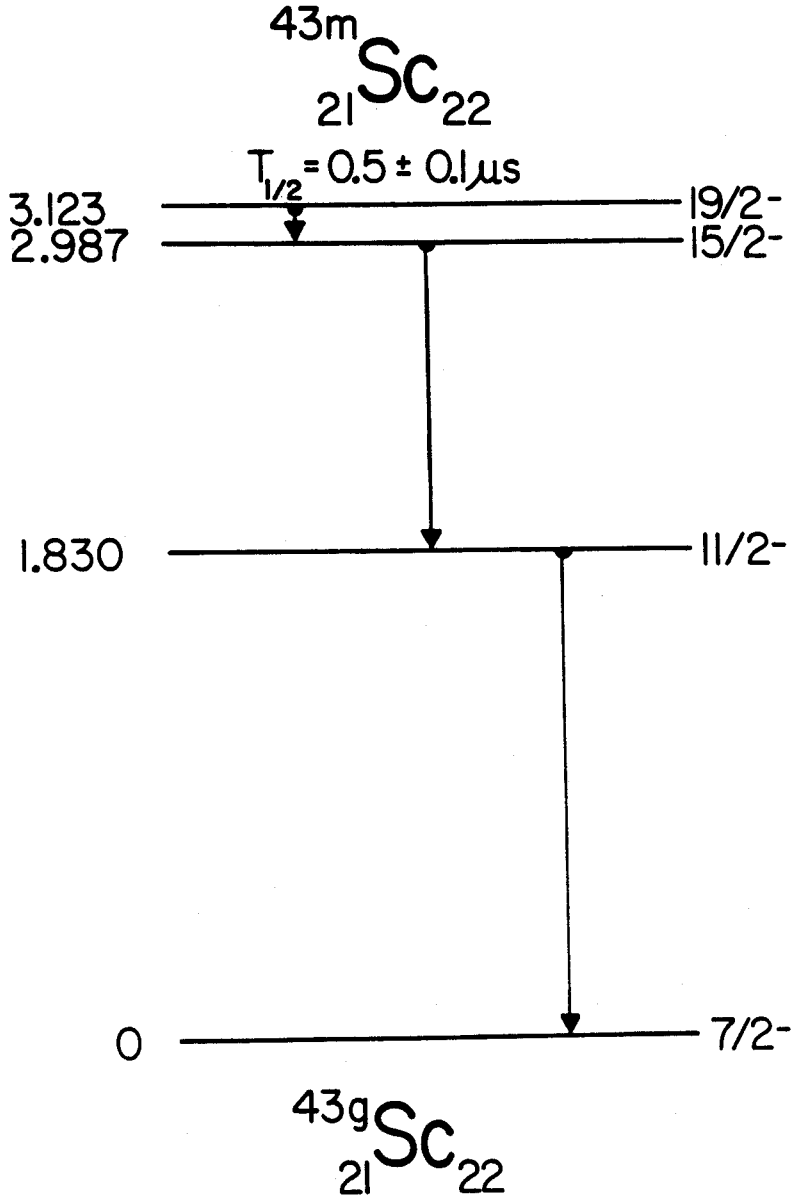

Figure 8-3. Proposed decay scheme for ^{43m}Sc reported by Sawa and Bergström (Ann70).

8.4 Discussion

In our present study, we have observed all the γ rays reported by Sawa and Bergström, including the 136-keV transition. However, the assignment of these γ rays to a decay scheme for ^{43m}Sc has not been attempted, since a number of problems exist which are difficult to reconcile with our data. If the isomeric transition decays with a half-life of about 0.5 μsec, then one would expect the γ rays in the resultant cascade to follow a similar half-life. However, our pulsed-beam measurements indicate a much longer (>2 sec) half-life for the 1157-keV (15/2 $\rightarrow$ 11/2) transition. Indeed, the assignment of this γ ray to the ^{43m}Sc decay scheme is ambiguous, since the reactions used to produce ^{43}Sc also make ^{44}Sc, the decay of which contains a strong γ ray at almost the same energy (1156 keV). Using our method of bracketing the μsec half-life range, we have found several γ rays which fall into the correct lifetime range. However, because of the lack of energy sums and crossovers, it is not obvious that one can construct a completely unambiguous decay scheme for ^{43m}Sc. The rather extensive study of the low-lying states in ^{43}Sc by Ball, et al. provides a few states which could belong to the isomer decay cascade. Nevertheless, the positive assignment of γ rays and the establishment of a decay scheme for ^{43m}Sc is extremely tedious based on the currently available data. The relatively large number of side products from unwanted reactions and contaminants, coupled with the rather weak γ-rays expected from de-excitation of possible isomeric states makes the detection and assignment of these unknown γ rays very difficult. By comparison with the ^{53m}Co - ^{53m}Fe case, one would expect any possible γ-decay branch in ^{43m}Ti to be quite weak with the dominant mode of decay being the super-allowed β^+ decay to ^{43m}Sc.

Although no definite decay schemes for ^{43m}Ti and ^{43m}Sc could be established as a result of this study, several unidentified γ rays were observed which might be associated with the decay of the isomers. At the present time there is no definite evidence to support the existence of ^{43m}Ti. A comprehensive table of all γ rays observed in the ^{43m}Ti, ^{43m}Sc search is given in Appendix D.

IX. SUMMARY AND CONCLUSIONS

Viewed in retrospect the rather diverse series of studies which constitute this thesis presents many interesting facets -- both from an experimental and a theoretical standpoint. Although they do not contain a "wealth" of information in the sense of establishing dozens of new levels, each segment of the study provides some insight into the nuclear problem.

The establishment of new levels in ^{53}Mn populated by the β^+ decay of ^{53}Fe provides not only additional knowledge of these states, but allows further testing of the simple shell model. deShalit has pointed out that the N=28 closed shell is particularly stable and therefore much less subject to configuration mixing than N=20 (deS63a). Thus, the ^{53}Mn nucleus with 28 neutrons and 25 protons provides an excellent example for the study of the $(1f_{7/2})^{-3}$ proton configuration.

Likewise, the elucidation of a metastable state in ^{53}Fe has provoked considerable interest -- both experimental and theoretical. Experimentally, the direct observation of γ-ray transitions having multipolarities of $E6$ and $M5$, the highest ever observed, was most exciting. Since the metastable state has a spin of 19/2, the highest that can result from the three-quasiparticle configuration $[(\pi f_{7/2})^{-2}]_{6+}(\nu f_{7/2})^{-1}$, its character is expected to be almost pure $f_{7/2}$. Therefore, transitions from this state and their measured rates have profound implications for testing concepts of the shell model theory. For example, since decays from this relatively pure state lead to states which may be highly configuration mixed, a rare opportunity is provided for direct testing of the concept of configuration mixing. Results obtained from this study also have suggested that perhaps the proton and neutron effective charges

are smaller than expected in this region.

Switching to the ^{40}Ca double-closed shell region, a comprehensive study was made to determine the levels populated by the decay of ^{40}Sc. Although no new levels were established as a result of this effort, significant improvement was realized in the exact energy of the ^{40}Ca levels. Experimentally, this study was used to develop and utilize on-line,pulsed-beam techniques for studying short-lived species. Since both the levels in ^{40}Ca and the β^+ decay to them are well characterized, a good opportunity exists to backtrack and describe the ^{40}Sc structure and wavefunction in some detail.

The unexpected discovery of an isomeric state in ^{53}Fe turned the course of this investigation toward a search for similar states in nuclei having analogous configurations. ^{53}Co and the particle conjugates ^{43}Ti and ^{43}Sc were chosen as the most likely candidates for having similar three-particle isomeric states. A comprehensive search for γ-ray activity from possible metastable states in these nuclei was carried out using various experimental techniques developed for short-lived species. After an exhaustive search, very little evidence was found to support the existence of such states. However, since other modes of decay have been demonstrated for at least one of these (Cer70), their existence is not ruled out. There is some evidence that in ^{43}Sc the level structure has shifted so that the half-life is very short with an $E2$ transition de-exciting the metastable level (Ann70). Although the goal of revealing isomeric states in these nuclei was not achieved, this facet of the investigation should not be deemed as unworthwhile. Having eliminated this avenue of inquiry narrows down the choice of approaches to the problem. Also, the results found here may be quite useful in criticizing or confirming other data.

In addition to the nuclei actually investigated, this study has suggested several other species which would be natural extensions of this work. The nucleus ^{39}Sc is not known, although it is quite interesting from both a theoretical and an experimental viewpoint. The use of on-line, pulsed-beam techniques should be very helpful in establishing its existence and possibly a level scheme. Another very interesting case is ^{51}Fe which also is not known. Knowledge of this structure would be very helpful for comparison with the ^{53}Fe data. A survey of other nuclei in this region to search for additional metastable states would be relatively simple and is certainly worth considering. Extension of on-line, pulsed-beam techniques to short-lived species in other regions of interest presents many possibilities for meaningful research.

Although the data presented in this thesis do not by themselves provide an answer to fundamental questions in the nuclear problem, it is hoped that they constitute a small, but significant addition to the total body of knowledge regarding nuclear structure.

BIBLIOGRAPHY

BIBLIOGRAPHY

A

(Abr67) M. Abramowitz and I. Stegun, Handbook of Mathematical Functions, National Bureau of Standards, Applied Mathematics Series 55 (1967).

(And66) W. C. Anderson, L. T. Dillman and J. J. Kraushaar, Nucl. Phys. 77, 401 (1966).

(Ann70) Z. P. Sawa and I. Bergström, Annual Report, Research Institute for Physics, 10405 Stockholm, Sweden (1970).

(Arm68) A. J. Armini, J. W. Sunier and J. R. Richardson, Phys. Rev. 165, 1194 (1968).

(Arn64) S. E. Arnell and S. Sterner, Ark. Fys. 26, 423 (1964).

(Aub66) R. L. Auble, W. C. McHarris and W. H. Kelly, Nucl. Phys. A91, 225 (1966).

(Aub67) R. L. Auble, D. B. Beery, G. Berzins, L. M. Beyer, R. C. Etherton, W. H. Kelly and Wm. C. McHarris, Nucl. Instr. and Methods 51, 61 (1967).

(Aue64) N. Auerbach and I. Talmi, Phys. Lett. 9, 153 (1964).

(Aue64a) N. Auerbach and I. Talmi, Phys. Lett. 10, 297 (1964).

(Aue67) N. Auerbach, Phys. Lett. B24, 260 (1967).

B

(Bal70) G. C. Ball, J. S. Forster, F. Ingebretsen and C. F. Monahan, Can. J. Phys. 48, 2735 (1970).

(BalJB) J. B. Ball, Phys. Rev. to be published.

(Bay71) D. L. Bayer, Michigan State University Cyclotron Laboratory Report, MSUCL-35 (1971).

(Bee69) D. B. Beery, Ph.D. Thesis, Michigan State University, Cyclotron Laboratory (1969).

(Ben68) W. Benenson, R. deForest, W. P. Johnson and E. Kashy, Nucl. Instr. and Methods 64, 40 (1968).

(Bla52) J. M. Blatt and V. F. Weisskopf, Theoretical Nuclear Physics, John Wiley and Sons, New York (1952).

(Bla67) W. W. Black and R. L. Heath, Nucl. Phys. A90, 650 (1967).

(Bla71) J. N. Black, Wm. C. McHarris and W. H. Kelly, Phys. Rev. Lett. 26, 451 (1971).

(Blo60) J. Blomquist and S. Wahlborn, Ark. Fys. 16, 545 (1960).

(Blo61) H. G. Blosser, Communication and Electronics, (January, 1961).

(Blo66) H. G. Blosser and A. I. Galonsky, IEEE Trans. on Nuclear Science NS-13, No. 4, 466 (1966).

(Bra56) C. M. Braams, Phys. Rev. 101, 1764 (1956).

(Bra64) F. P. Brady, N. F. Peek and R. A. Warner, Nucl. Phys. 66, 365 (1964).

C

(Cer70) J. Cerny, J. Esterl, R. Gough and R. Sextro, UCRL-19973, Preprint (1970).

D

(Dav35) H. T. Davis, Tables of the Higher Mathematical Functions V.II, Principia Press Inc., Bloomington, Indiana (1935).

(Der68) I. Dernedde, Z. Phys. 216, 103 (1968).

(deS63a) A. deShalit, Selected Topics in Nuclear Theory, ed. by F. Janouch, I.A.E.A., Vienna (1963).

(deS63b) A. deShalit and I. Talmi, Nuclear Shell Theory, Academic Press (1963).

(Dob56) W. Dobrowolski, R. V. Jones and C. D. Jeffries, Phys. Rev. 104, 1378 (1956).

(Doe70) R. E. Doebler, Ph.D. Thesis, Michigan State University (1970).

E

(Ebr65) T. G. Ebrey and P. R. Gray, Nucl. Phys. 61, 479 (1965).

(Edm52) A. R. Edmonds and B. H. Flowers, Proc. Roy. Soc. A214, 515 (1952).

(Edm57) A. R. Edmonds, Angular Momentum in Quantum Mechanics, Princeton University Press (1957).

(End67) P. M. Endt and C. Van Der Leun, Nucl. Phys. A105, 1 (1967).

(Epp69) R. E. Eppley, Michigan State University Nuclear Chemistry Annual Report COO-1779-13, 141 (1969).

(Epp70) R. E. Eppley, W. C. McHarris and W. H. Kelly, Phys. Rev. 2, 1077 (1970).

(Epp70a) R. E. Eppley, Ph.D. Thesis, Michigan State University, Department of Chemistry (1970).

(Ers66) J. R. Erskine, Phys. Rev. 149, 854 (1966).

(Esk66) K. Eskola, Phys. Lett. 23, 471 (1966).

(Esk67) K. Eskola, Ann. Acad. Sci. Fenn. AVI 261, 45 (1967).

(EVENT) A program written for the MSU Cyclotron Laboratory Sigma-7 computer by D. Bayer, D. B. Beery and G. C. Giesler.

F

(Fee50) E. Feenberg and G. Trigg, Rev. Mod. Phys. 22, 399 (1950).

(Fer34) E. Fermi, Z. Physik 88, 161 (1934).

(Flo52) B. H. Flowers, Proc. Roy. Soc. A212, 248 (1952).

(Fre66) J. Freeman, J. Jenkin, G. Murray and W. Burchum, Phys. Rev. Lett. 16, 959 (1966).

(Fre69) J. B. French, E. C. Halbert, J. B. McGreory and S. S. M. Wong, Advances in Nuclear Physics V.3, ed. by M. Baranger and E. Vogt, Plenum Press Inc., New York (1969).

G

(Gei)65) J. S. Geiger, R. L. Graham, I. Bergström and F. Brown, Nucl. Phys. 68, 352 (1965).

(Gie71) G. C. Giesler, Ph.D. Thesis, Michigan State University, Department of Chemistry (1971).

(Gin65) J. N. Ginocchio, Nucl. Phys. 63, 449 (1965).

(Gla55) N. W. Glass and J. R. Richardson, Phys. Rev. 98, 1251 (1955).

(Gla70) P. W. M. Glaudemans, "Applications of the Nuclear Shell Model", Nuclear Physics Seminar, Groningen (1970) Lecture notes compiled by J. E. Koops and A. S. K. Buisman.

(Goe49) M. Goeppert Mayer, Phys. Rev. 75, 1766 (1949).

(Gor68) M. M. Gordon, R. E. Berg and H. G. Blosser, Nucl. Instr. and Methods 58, 327 (1968).

(Gra60) R. L. Graham, G. T. Ewan and J. S. Geiger, Nucl. Instr. and Methods 9, 245 (1960).

(Gra65) W. S. Gray, R. A. Kenetick and J. J. Kraushaar, Nucl. Phys. 67, 542 (1965).

(Gra66) M. A. Grace and A. R. Poletti, Nucl. Phys. 78, 273 (1966).

(Gun68) R. Gunnick, R. A. Meyer, J. B. Niday and R. P. Anderson, Nucl. Instr. and Methods 65, 26 (1968).

H

(Hag68) R. S. Hager and E. C. Seltzer, Nucl. Data 4A, 1 (1968).

(Hax49) O. Haxel, J. H. D. Jensen and H. E. Suess, Phys. Rev. 75, 1766 1949).

(Her64) C. J. Herrlander and R. L. Graham, Nucl. Phys. 58, 544 (1964).

(Ior68) A. Iordachescu, Rev. Roum. Phys. 13, 911 (1968).

(Jac70) K. Jackson, C. Cardinal, H. Evans, N. Jelley and J. Cerny, UCRL-19963, Preprint (1970).

(Jud63) B. R. Judd, Operator Techniques in Atomic Spectroscopy, McGraw-Hill, New York (1963).

(Jul59) J. O. Juliano, C. W. Kocher, T. D. Nainen and A. C. G. Mitchell, Phys. Rev. 113, 602 (1959).

K

(Kas68) E. Kashy and J. L. Snelgrove, Phys. Rev. 172, 1124 (1968).

(Kis60) L. S. Kisslinger and R. A. Sorensen, Mat. Fys. Medd. Dan. Vid. Selsk. 32, No. 9 (1960).

(Kon41) E. J. Konopinski and G. E. Uhlenbeck, Phys. Rev. 60, 308 (1941).

(Kon43) E. J. Konopinski, Rev. Mod. Phys. 15, 209 (1943).

(Kop69) J. Kopf, Ph.D. Thesis, Michigan State University, Department of Physics (1969).

(Kos69) K. L. Kosanke and J. Black, in Michigan State University Nuclear Chemistry Annual Report COO-1779-13, 153 (1969).

(Kos70) K. L. Kosanke, in Michigan State University Nuclear Chemistry Annual Report COO-1779-44, 247 (1970).

(Kos71) K. L. Kosanke, Michigan State University, Department of Chemistry, private communication.

(Kun66) P. D. Kunz, Nucl. Phys. 77, 425 (1966).

(Kuo70) T. Y. Kuo, Ph.D. Thesis, Michigan State University, Department of Physics (1970).

(Kur36) F. N. D. Kurie, J. R. Richardson and P. C. Paxton, Phys. Rev. 49, 368 (1936).

L

(Lan49) L. M. Langer and H. C. Price, Jr., Phys. Rev. 76, 641 (1949).

(Led67) C. M. Lederer, J. M. Hollander and I. Perlman, Table of Isotopes, 6th Ed., Wiley (1967).

(Leg68) J. Legrand, J. P. Boulanger and J. P. Brethon, Nucl. Phys. A107, 177 (1968).

(Lin53) G. Lindstrom, K. Siegbahn and A. H. Wapstra, Proc. Phys. Soc. (London) 66B, 54 (1953).

(Lip58) I. Talmi, in Proceedings of the Rehovoth Conference on Nuclear Structure, ed. H. J. Lipkin, North-Holland Publishing Co., Amsterdam (1958).

M

(Mac63) R. D. MacFarlane and R. D. Griffioen, Nucl. Instr. and Methods 24, 461 (1963).

(Mac67) G. H. Mackenzie, E. Kashy, M. M. Gordon and H. G. Blosser, IEEE Trans. on Nuclear Science NS-14 No. 3, 450 (1967).

(Mac69) R. D. MacFarlane, R. A. Gouch, N. S. Oakey and D. F. Torgerson, ORO-3820-2 (1969); Nucl. Instr. and Methods 73, 285 (1969).

(Mac71) R. D. MacFarlane, Private communication.

(Mag70) C. Maggiore, Ph.D. Thesis, Michigan State University, Department of Physics (1970).

(Mal66) F. B. Malik and W. Scholz, Phys. Rev. 150, 919 (1966).

(May55) M. G. Mayer and J. H. D. Jensen, Elementary Theory of Nuclear Shell Structure, John Wiley and Sons, New York (1955).

(McC64) J. D. McCullen, B. F. Bayman and L. Zamick, Phys. Rev. 134, B515 (1964).

(McC64a) J. D. McCullen, B. F. Bayman and L. Zamick, Technical Report NYO-9891, Palmer Physical Laboratory, Princeton University, Princeton, New Jersey (1964).

(McE68) M. T. McEllistrem, K. W. Jones and D. M. Sheppard, Bull. Am. Phys. Soc. 13, 1426 (1968).

(McE70) M. T. McEllistrem, K. W. Jones and D. M. Sheppard, Phys. Rev. 1, 1413 (1970).

(Mei39) W. Meissner, Deutsche Mathematik 4, 537 (1939).

(Mey70) R. A. Meyer and D. Camp, Private communication, Lawrence Radiation Laboratory, Livermore, California (1970).

(Mos53) S. A. Moszkowski, Phys. Rev. 89, 474 (1953).

(Mos65) S. A. Moszkowski, The Theory of Multipole Radiation, in Alpha-, Beta-, and Gamma-Ray Spectroscopy, ed. by K. Siegbahn, North-Holland Publishing Co., Amsterdam (1965).

(Mul52) D. E. Muller, H. C. Hoyt, D. J. Klein and J. W. M. DuMond, Phys. Rev. 88, 775 (1952).

(Mur65) G. Murray, R. L. Graham and J. S. Geiger, Nucl. Phys. 63, 353 (1965).

(Mye65) W. D. Myers and W. J. Swiatecki, University of California Lawrence Radiation Laboratory Report UCRL-11980 (1965).

N

(Nel50) M. E. Nelson and M. L. Pool, Phys. Rev. 77, 682 (1950).

(Nie60) J. M. Nielson, National Academy of Sciences - National Research Council Nuclear Science Series, NAS-NS 3017 (1960).

(Nij59) G. J. Nijgh, A. H. Wapstra, L. Th. M. Ornstein, N. Salomons-Grobben, J. R. Huizenga and O. Almen, Nucl. Phys. 9, 528 (1959).

(Nus53) R. H. Nussbaum, van Lieshout and A.H. Wapstra, Phys. Rev. 92, 207 (1953).

O

(O'Br67) J. O'Brien, W. E. Corenbusch, T. A. Belote and J. Rapaport, Nucl. Phys. A104, 609 (1967).

(Oso49) J. S. Osoba, Phys. Rev. 76, 345 (1949).

P

(Pre62) M. A. Preston, Physics of the Nucleus, Addison-Wesley, Reading, Mass. (1962).

R

(Ram67) A. V. Ramayya, J. H. Hamilton, S. M. Brahmavar and J. J. Pinajian, Phys. Lett. 24B, 49 (1967).

(Rid37) L. N. Ridenour and W. J. Henderson, Phys. Rev. 52, 889 (1937).

(Rie50) J. R. Rietz, Phys. Rev. 77, 10 (1950).

(Ros36) M. E. Rose, Phys. Rev. 49, 727 (1936).

(Ros57) M. E. Rose, Elementary Theory of Angular Momentum, Wiley, New York (1957).

(Rou69) J. T. Routti and S. G. Prussin, Nucl. Instr. and Methods 72, 125 (1969); J. T. Routti UCRL-19452.

S

(Sne67) J. L. Snelgrove and E. Kashy, Nucl. Instr. and Methods 52, 153 (1967).

(Spr65) A. Springer and B. G. Harvey, Phys. Lett. 14, 116 (1965).

(Ste66) S. Sterner, L. Jonsson and S. E. Arnell, Ark. Fys. 31, 567 (1966).

T

(Tab51) "Tables for the Analysis of Beta Spectra", National Bureau of Standards, Applied Mathematics Series, No. 13 (1951).

(Tho68) K. M. Thompson and C. R. Gruhn, Bull. Am. Phys. Soc. 13, 701 (1968).

(Tho69) K. M. Thompson, Ph.D. Thesis, Michigan State University, Department of Physics (1969).

V

(Vej64) E. Veje, C. Droste, O. Hansen, and S. Holm, Nucl. Phys. 57, 451 (1964).

(Ver67) J. Vervier, Nucl. Phys. A103, 222 (1967).

(Vui66) P. H. Vuister, Nucl. Phys. 83, 593 (1966).

(Vui67) P. H. Vuister, Nucl. Phys. A91, 521 (1967).

W

(Wei51) V. F. Weisskopf, Phys. Rev. 83, 1073 (1951).

(Whi67) D. H. White and D. J. Groves, Nucl. Phys. A91, 453 (1967).

(Wol56) J. L. Wolfson, Can. J. Phys. 34, 256 (1956).

(Wu49) C. S. Wu and L. Feldman, Phys. Rev. 76, 696 (1949).

Y

(Yav55) A. I. Yavin and F. H. Schmidt, Phys. Rev. 100, 171 (1955).

Z

(Zur66) R. W. Zürmuhle, C. M. Fou, and L. W. Swenson, Nucl. Phys. 80, 259 (1966).

APPENDICES

```
FORTRAN
      1          C      PROGRAM FERMPLOT
      2                 INTEGER YY
      3                 REAL*8 TITLE
      4                 DOUBLE PRECISION X,Y,GAMMA
      5                 DIMENSION YY(1024),TITLE(8),RES(1024),RRES(1024),IR(1024)
      6                 DIMENSION EN(30),CH(30),SRES(1024),ISR(1024),IRC(1024),IRRC(1024)
      7                 COMMON/N1/GAMMA,X,Y
      8                 COMMON/N2/AVED,RES,ALPHA,BETA,GANNA,DELTA,A1,A0,B,C,D,MIN,NA,NB,
      9                1LEV,NOD,CH,EN
     10                 CALL KILL (3)
     11                 READ 102,NCASES
     12                 DO 25 NCASE=1,NCASES
     13                 READ 102,NCHAN,MIN,MAX,(TITLE(I),I=1,8)
     14                 READ 101,Z,A,B,C,D
     15                 DO 195 I = 1,NCHAN
     16           195   YY(I) = 0
     17                 CALL CREAD (YY,NCHAN,NRUN,NERR)
     18                 PRINT 200,YY
     19           200   FORMAT (10I10)
     20                 IF (NERR.EQ.0) GO TO 20
     21                 PRINT 131,NERR
     22                 GO TO 25
     23            20   CONTINUE
     24                 NB =MAX
     25                 NA=MIN
     26                 PRINT 109,(TITLE(I),I=1,8)
     27                 AZ=Z/137.04
     28                 V = 1.13*AZ*AZ/(Z*(Z**0.333))
     29                 GAMNO=SQRTF(1-AZ*AZ)
     30                 R = 0.5/(137.04*(A**0.333))
     31                 DO 115 I=MIN,MAX
     32                 W=B+C*I+D*I*I
```

```
      WW=W+V
      P=SQRTF(WW*WW-1)
      VNU=-AZ*WW/P
      X=GAMN0
      Y=VNU
      CALL GAMMASQ
      GAM1=GAMMA
      X=2*GAMN0+1
      Y=0
      CALL GAMMASQ
      GAM2=GAMMA
      F0 =2*(1+GAMN0)/(2*P*R)**(2*(1-GAMN0))*EXPF(3.1416*VNU)*GAM1/GAM2
      FUM =F0*SQRTF((WW*WW-1)/(W*W-1))*WW/W
  115 RES(I)=SQRTF(YY(I)/(FUM*P*W))
      PRINT 119,(RES(I),I=MIN,MAX)
      DO 5 I = 0,1023
      IR(I) = 0.0
    5 CONTINUE
      DO 1 I = MIN,MAX
      RRES(I)=RES(I)*(10.**4.0)
      IR(I) = RRES(I)
    1 CONTINUE
      PRINT 90
   90 FORMAT ('0'/10X,' FERMIPLOT ORDINATE IN INTEGRAL NOS')
      PRINT 19,(IR(I),I = MIN,MAX)
   19 FORMAT (10I8)
      NCHAA = MAX
      CALL CPUNCH (IR,NCHAA,NRUN)
      PRINT 118,NA,NB
      CALL LEASQRE
      PRINT 91
   91 FORMAT ('0'/10X,' LEASQRE FERMIPLOT ORDINATE')
      DO 130 I=1,LEV
  130 PRINT 129, CH(I),EN(I)
```

```
      PRINT 9
      PRINT 119,(RES(I),I=MIN,MAX)
      DO 6 I = 0,1023
      ISR(I) = 0.0
    6 CONTINUE
      DO 2 I = MIN,MAX
      SRES(I) = RES(I)*(10.**4.0)
      ISR(I) = SRES(I)
    2 CONTINUE
      CALL CPUNCH (ISR,NCHAA,NRUN)
      PRINT 92
   92 FORMAT('0'/10X,'LEASQRE INTEGRAL FERMIPLOT ORDINATE')
      PRINT 19,(ISR(I),I = MIN,MAX)
   25 CONTINUE
    9 FORMAT (1HO)
  101 FORMAT(5F10.6)
  102 FORMAT (3I5,8A8)
  109 FORMAT (1H1,15X,8A8)
  110 FORMAT (F6.0,9F7.0)
  118 FORMAT (1H0,' CHANNELS',I10,' THRU',I10,10X,'ENDPOINTS CHANNEL
     1ENERGY')
  119 FORMAT (10F8.4)
  129 FORMAT (F63.2,F8.2)
  131 FORMAT(1X,'NERR= 'I4)
      END
      SUBROUTINE GAMMASQ
      DOUBLE PRECISION X,Y,GAMMA,PROD,G,AX,AY
      COMMON/N1/GAMMA,X,Y
      ZET =2*.57721566
      G=(X*X+Y*Y)*DEXP(ZET*X)
      N=1
   14 AX=X/N
      AY=Y/N
      PROD =((1+AX)*(1+AX)+AY*AY)/DEXP(2*AX)
```

```
10              IF (PROD -.999995)15,15,16
11          15  G=G*PROD
12              N=N+1
13              GO TO 14
14           16 IF (1.000005 - PROD) 15,15,17
15          17  G=G*PROD
16              GAMMA =1./G
17              END
1               SUBROUTINE LEASQRE
2               DIMENSION RES(1024),CALC(1024)
3               COMMON/N2/AVED,RES,ALPHA,BETA,GANNA,DELTA,A1,A0,B,C,D,MIN,NA,NB,
4              1LEV,NOD,CH,EN
5               LEV=0
6           745 ALPHA=0
7               BETA=0
8               GANNA=0
9               DELTA=0
10              SUMD=0
11              DO 750 J=NA,NB
12              ALPHA=ALPHA+RES(J)
13              BETA=BETA+J
14              GANNA=GANNA+J*RES(J)
15          750 DELTA=DELTA+J*J
16              NOD =NB-NA+1
17              A1=(GANNA-ALPHA*BETA/NOD)/(DELTA-BETA*BETA/NOD)
18              A0=(ALPHA-A1*BETA)/NOD
19              DO 755 J=NA,NB
20              CALC(J)=A0+A1*J
21              DIF=CALC(J)-RES(J)
22          755 SUMD=SUMD+DIF*DIF
23              AVED=SQRTF(SUMD/NOD)
24              CALL CHECKER
25              IF (NA-MIN-10) 760,745,745
26          760 END
```

```
1                SUBROUTINE CHECKER
2                DIMENSION CALC(1024),RES(1024),CH(30),EN(30)
3                COMMON/N2/AVED,RES,ALPHA,BETA,GANNA,DELTA,A1,A0,B,C,D,MIN,NA,NB,
4               1LEV,N0D,CH,EN
5           200  IF (NA-MIN-6) 206,206,208
6           208  NC=NA-6
7                DEV=0
8                DO 201 J=NC,NA
9                CALC(J)=A0+A1*J
10               DIF =CALC(J)-RES(J)
11          201  DEV=DIF*DIF+DEV
12               DEV=SQRTF(DEV/(NA-NC+1))
13               IF (DEV-AVED) 205,205,206
14          205  NA=NA-1
15               N0D=N0D+1
16               J=NA
17               ALPHA=ALPHA+RES(J)
18               BETA=BETA+J
19               GANNA=GANNA+J*RES(J)
20               DELTA=DELTA+J*J
21               A1=(GANNA-ALPHA*BETA/N0D)/(DELTA-BETA*BETA/N0D)
22               A0=(ALPHA-A1*BETA)/N0D
23               GO TO 200
24          206  LEV=LEV+1
25               CH(LEV)=-A0/A1
26               EN( LEV)=B+C*CH(LEV)+D*CH(LEV)*CH(LEV)
27               DO 210 K=MIN,NA
28          210  RES(K)=RES(K)-A0-A1*K
29               NB=NA-1
30               NA=NB-10
31               END
```

APPENDIX B

Input Instructions for the Oak Ridge Shell Model Codes

The following comments and format instructions pertain to the use of the Oak Ridge Shell Model Codes as adapted for the XDS Sigma 7 computer at the Michigan State University Cyclotron Laboratory. These instructions were provided by Dr. B. H. Wildenthal. I have included them here both because of their benefit in helping one understand the shell model calculations and because of their practical value to others planning to perform such calculations.

The basic input cards for the codes are distinguished by index numbers in columns 1-3. The different logical sections of the input are referred to by these index numbers, as well as by "description-of-function" names. Punch columns are indicated by bracketed superscript numbers.

→ $0^{(3)}$ This is the Title card for a job.

→ $1^{(3)}$ $\text{NSHELS}^{(10)}$ $0100^{(59)}$

NSHELS is the number of active orbits in a calculation, e.g., if one uses the $1d_{5/2}$, $2s_{1/2}$, and $1d_{3/2}$ orbits in a calculation, NSHELS = 3.

→ $2^{(3)}$ $\text{ID}^{(10)}$ $2j^{(20)}$ $\pm1^{(30)}$ $1^{(40)}$

(Etc.)

There must be NSHELS 2-cards. ID is a 2-character nmemonic for a shell, e.g. D5 for $1d_{5/2}$. 2j is 2-times the angular momentum of a particle in orbit ID. Enter +1 for an even-parity orbit, -1 for an odd-parity orbit. The order in which the 2-cards appear defines the shell

index order number, ISHEL, by which the program treats the various shells. These shells will henceforth be referenced as shell #1, shell #2, etc. This ordering of shells is sometimes important, because the available coefficient of fractional parentage tables are not always symmetric in particle coupling. The j = 5/2 shell should generally be shell #1.

→ $12^{(3)}$ $2j(ISHEL)^{(6)}$ $ISHEL^{(10)}$ $n_i^{(15)}$ $2J_i^{(20)}$ $2T_i^{(25)}$...etc.

(Etc.)

$12^{(3)}$ $-1^{(10)}$ terminates section

There must be a block (≥1) of 12-cards for each 2-card, occurring in the same order as the 2-cards. Each individual 12-card describes a "single-shell wave function", that is, a proper antisymmetric combination of n_i particles (each of angular momentum j) in shell ISHEL, coupled to total angular momentum, J_i, total i-spin T_i, etc. as needed to completely specify a unique state. The multi-shell, multiparticle, wave functions will be constructed by using the single-shell wave functions (SSWF) from the input as building blocks. Unless one specifically intends to truncate the model space by omitting 12-cards, he should take care to use a complete set. These are available as library decks. If some single-shell combinations are missing, the program assumes that one wishes to truncate, and hence will proceed. On the other hand, it is inefficient to include many 12-cards which will not be used, e.g. if one has only 4 active particles, it is unnecessary to include j = 5/2 12-cards with $n_i > 4$.

→ $125^{(3)}$ $N^{(2)}$

This card informs the program that you wish to construct a state (or states) with N active particles.

→ $13^{(3)}$ $n^{(20)}_{(ISHEL=1)}$ $n^{(30)}_{(ISHEL=2)}$ ····· $n^{(10)}_{(ISHEL=NSHELS)}$

(Etc.)

$13^{(3)}$ $0^{(20)}$ $0^{(30)}$ etc. terminates

The 13-cards list the configurations (particle partitions over the NSHELS active orbits) that one wishes to include in (or by which he wishes to define) the space S. The limit on $n_{(ISHEL)}$ can either be Pauli-imposed or limited more strictly by the user. The 13-cards must be ordered so that the multiple-digit numbers $n_1n_2\ldots n_{NSHELS}$ increase in magnitude: (so-called "odometer" ordering) i.e., the first 13-cards should call for as many particles as possible in the last shell, as many as possible of the remainder in the next to last shell, etc. The individual cards of a given 13-card block must all have the same parity, that is, all cards must either have an even number of particles in odd-parity orbits (and hence have even parity) or all must have an odd number in odd-parity orbits (and hence have odd parity). The parity of an N-particle state is thus defined implicitly. Different parity states of the same number of active particles require two separate 125-13-card sets.

→ $14^{(3)}$ $2J^{(20)}$ $2T^{(30)}$

(Etc.)

One then stacks as many 14-cards after the 13-cards as there are J-T combinations to be calculated for this number N of active particles.

→ $125^{(3)}$ $N'^{(20)}$ loops back into a new 125-13-14 sequence.

→ $14^{(3)}$ $(-1)^{(20)}$ terminates

After a 125-13-14 set, one can either loop back to a new set

of 125-13-14 cards or terminate this section of the program input.

After passing from the 125-13-14 section, the program proceeds to construct the multiparticle, multishell basis vectors for the states of NJT^{π} as requested. This process uses a combination of the information inputted by the 12-cards and via the 125-13 cards.

Up to this point, all applications or versions of the shell model codes have identical input. Now, however, one must consider the operator, and depending on the form of the operator, there are different inputs. The eigenvalue-eigenvector problem will be treated first.

→ $21^{(3)}$ $N2bme^{(20)}$ $NSHELS^{(30)}$

This card announces the number of two-body matrix elements (N2bme) which will follow and inputs a redundant (but very necessary) value of NSHELS. The number of two-body matrix elements is usually the maximum that can be constructed in the model space S, although in some cases, a subset of cards can be omitted.

→ $28^{(3)}$ $ISHEL(a)^{(15)}$ $ISHEL(b)^{(20)}$ $ISHEL(c)^{(25)}$ $ISHEL(d)^{(30)}$ $2J^{(35)}$ $2T^{(40)}$ $2bme^{(65)}$

There must be N2bme of these 28-cards. The ISHEL indices denote which set of orbits are used for this 2bme, $\langle(\rho_a\rho_b)_{JT}|H|(\rho_c\rho_d)_{JT}\rangle_{asym}$ and J and T are the spin and i-spin of the coupled pairs. The value of the matrix element is entered as "2bme". The cards must be ordered such that the multiple-digit numbers ISHEL(a) ISHEL(b) ISHEL(c) ISHEL(d) 2J 2T occur in increasing magnitude.

→ $32^{(3)}$ $NSHELS^{(10)}$ PFIL $(SHELL\#1)^{(15)}$ $SSMEFILE^{(20)}$ PFIL $(SHELL\#2)^{(25)}$ $SSMEFILE^{(30)}$ PFIL $SHELL\#3)^{(35)}$ $SSMEFILE^{(40)}$ etc.

Card 32 informs the program where the NSHELS different coefficients of fractional parentage tables that will be needed to do the problem

are located. These are stored either on tape or disk and are all under one file number (SSMEFILE). Recent use has been with SSMEFILE = 8, but this is arbitrary. The SSMEFILE is multiple-filed. The PFIL (K) are the Pfil numbers needed to reach the desired SSME blocks (for shell K) from the start of the whole file, (i.e., the file is rewound after each "read"). The sequence of files is noted in the file name or on the tape label. The present order is 5/2, 1/2, 3/2, 7/2 max.T, 5/2 max.T. If shell #1 is 3/2, then PFIL (shell #1) = 2, etc.

→ $33^{(3)}$

Present instructions call for including this card, but leaving it blank.

→ $34^{(3)}$

There should be NSHELS 34-cards, which should be left blank.

→ $51^{(3)}$ $1^{(10)}$ SPE(1)$^{(20)}$ SPE(2)$^{(30)}$ SPE(3)$^{(40)}$ etc.

and/or

→ 52

These cards are for the input of one (use 52 if one) or more sets of single particle energies.

For example: 1 = $(1d_{5/2})$ SPE(1) = -4.15

2 = $(2s_{1/2})$ SPE(2) = -3.28

3 = $(1d_{3/2})$ SPE(3) = +0.93

→ $999^{(3)}$ End of input

Present files are used as follows:

8 - SSME

9 - Intermediate storage of H-matrix elements.

14 - Eigenvector output

15 - Storage of basis vector list

If the SMIT-tape option is used, File 14 will receive G-coefficients prior to eigenvectors.

Other Operators: All versions of the shell model code generate a list of N, J. T cases. This ordered list is always part of the output, such that in calling for the construction of operator matrices connecting different states in the list, one makes use of the order-number of the state concerned, i.e. he calls for a matrix connecting the "5th" state and the "9th" state.

For Single Nucleon S-factor:

Follow the "14" – "-1" card one needs to have:

→ $21^{(3)}$ $\text{ISHEL}^{(10)}$

The 21-card indicates in which orbit a nucleon is to be created. The program treats one j-transfer at a time.

→ $1^{(3)}$

→ $32^{(3)}$ $\text{NSHELS}^{(10)}$ $\text{PFIL(ISHEL)}^{(5+10\times\text{ISHEL})}$ $\text{SSMEFILE}^{(10+10\times\text{ISHEL})}$

This is just like the Hamiltonian operator version, except that the numbers for the specific orbit in question are to be listed.

→ $33^{(3)}$ blank card

→ $0^{(3)}$ blank card

→ $40^{(3)}$ $\text{N(left;final)}^{(10)}$ $\text{N(right;initial)}^{(20)}$

$\text{NCASES}(\ell)^{(30)}$ $\text{NCASES(r)}^{(40)}$ $\text{NSKIP}(\ell)^{(50)}$ $\text{NSKIP(r)}^{(60)}$

$\pi\text{L}^{(70)}$ $\pi\text{R}^{(80)}$

ETC.

$40^{(3)}$ $(-1)^{(10)}$ terminates

The N (left and right) refer to the numbers of active particles in the left and right-hand (final and initial) states. The NCASES refer to the number of states in a left-hand or right-hand block.

For example, for a given state one might want to connect to several final states, or vice versa, or both. The NSKIP refer to how many states in the NJT list must be skipped in order to arrive at the desired state, left or right. The position after a 40-card is the sum of NCASES and NSKIP -- valid for "left" and "right" independently of each other. The various 40-cards are cumulative. The π's (± 1) are the parities of the states.

APPENDIX C

Energies of γ Rays Observed in the ^{53m}Co Search[1]

(keV)

52.5 L	396.1 B	835.3 NA	1125.3 B	1712.8 L
61.7 NA	411.7 NA	843.9 B	1130.2 NA	1727.1 L
72.0 L	415.0 B	846.4 L	1157.0 L	1731.5 L
83.5 L	440.0 B	852.3 B	1238.7 L	1757.4 L
90.3 L	447.8 B	866.6 B	1246.8 L	1779.6 L
99.1 L	454.1 B	870.1 NA	1249.6 B	1791.2 NA
122.3 NA	477.6 NA	888.5 NA	1275.0 L	1807.0 B
129.9 L	511.0 L	909.8 B	1280.6 B	1810.4 NA
138.4 L	539.6 NA	922.4 NA	1312.8 NA	1820.0 NA
147.2 L	583.0 B	931.1 L	1317.7 NA	1829.4 NA
153.2 L	595.6 B	934.9 L	1328.2 L	1880.6 NA
159.7 L	601.0 NA	954.5 B	1334.9 NA	1919.6 L
168.9 B	645.7 B	961.5 NA	1362.7 NA	1944.8 L
173.5 L	661.8 L	984.0 B	1368.4 L	1954.0 NA
183.6 NA	681.8 B	990.0 NA	1377.8 L	1992.9 NA
196.6 B	693.7 B	1009.7 B	1407.9 L	2140.0 NA
203.3 B	701.1 L	1011.5 L	1433.7 L	2167.8 NA
217.4 B	717.7 L	1019.7 NA	1441.4 B	2177.8 NA
241.6 B	730.2 B	1026.0 NA	1461.0 L	2209.8 B
276.5 B	741.3 B	1039.5 L	1530.6 NA	2220.6 B
320.5 L	754.1 B	1074.6 B	1607.9 NA	2243.5 NA
356.2 B	783.9 B	1096.7 B	1619.9 L	2274.6 NA
368.3 B	811.3 L	1112.1 B	1633.6 B	2313.5 L
377.9 L	832.8 B	1116.0 L	1679.3 NA	2318.9 NA

APPENDIX C - Continued

2339.7 L

2369.4 NA

2540.2 NA

2597.9 L

2603.5 NA

2614.1 L

2750.7 L

3054.6 NA

3098.9 L

3375.6 B

3404.0 B

3414.4 NA

3447.1 B

4079.2 B

4214.6 B

4242.2 B

[1]Each γ-ray energy is accompanied by a symbol denoting its approximate half-life based on the experiments performed in this study. The meanings of these are as follows:

S = short, $t_{1/2}$ <0.1 sec

M = medium, 10.0 sec >$t_{1/2}$ > 0.1 sec

L = long, $t_{1/2}$ >10.0 sec

NA = not available, i.e., the experiment in which the γ ray was seen did not include time discrimination.

B = beam on, i.e., this γ ray was observed only during beam-on intervals. The reader is cautioned not to interpret the beam-on designation as implying a short half-life. In most experiments the beam-on counting period was at least four times as long as each individual beam-off routed spectrum.

APPENDIX D

Energies of γ Rays Observed in the ^{43m}Ti and ^{43m}Sc Searches[2]

(keV)

50.9 M	280.5 S	511.0 L	812.2 L	1014.0 B
63.9 M	292.0 S	530.5 S	816.7 B	1022.3 B
72.8 L	296.0 S	542.7 S	827.3 NA	1038.5 B
84.1 L	303.6 NA	566.1 S	830.4 B	1050.8 B
91.2 L	321.5 L	571.5 S	836.8 L	1056.8 L
107.7 L	335.7 L	593.2 L	841.9 B	1069.9 B
115.6 NA	347.9 B	607.8 B	844.8 L	1074.0 B
127.2 L	349.2 S	610.8 NA	846.4 L	1083.1 B
135.4 L	356.3 S	618.1 L	850.3 S	1116.6 L
139.1 L	363.6 S	628.7 S	857.6 S	1125.6 B
142.5 M	373.2 L	657.6 NA	869.6 S	1146.2 NA
151.0 L	395.8 S	663.0 NA	872.3 NA	1157.9 L
153.9 L	398.4 B	667.8 B	878.9 B	1174.5 L
166.7 L	403.6 L	671.1 NA	884.4 L	1183.3 B
178.5 L	414.9 S	683.8 NA	890.4 S	1186.0 S
189.2 S	424.2 L	696.5 B	911.5 S	1209.8 B
196.0 S	431.3 B	699.4 B	926.5 S	1212.2 B
205.5 S	438.5 B	723.2 B	932.1 L	1228.8 B
219.8 S	456.2 NA	727.0 B	936.1 L	1236.1 B
221.6 L	461.0 L	745.6 L	960.0 B	1239.3 L
234.0 S	472.2 B	758.4 L	975.0 S	1246.5 L
245.9 S	478.6 L	761.4 B	984.6 L	1259.7 NA
270.5 L	482.7 B	769.2 B	990.4 B	1263.5 NA
274.3 L	500.9 B	772.3 S	1002.3 S	1275.6 L

Appendix D - Continued

1285.6	(M)	1611.5 B	1934.1 NA	3194.8 NA
1291.9	B	1642.7 B	1944.6 NA	3254.3 NA
1296.8	L	1651.9 B	1980.3 B	3271.2 NA
1313.2	L	1657.7 NA	2034.0 NA	3538.7 NA
1317.3	L	1662.1 B	2093.8 B	4156.2 B
1325.3	B	1668.5 L	2101.9 NA	
1327.5	B	1676.3 B	2168.0 NA	
1333.6	L	1700.1 B	2178.9 B	
1337.4	B	1729.8 L	2208.7 B	
1362.6	NA	1733.9 L	2222.6 B	
1369.8	L	1758.4 L	2241.7 L	
1372.3	L	1765.7 L	2245.8 L	
1378.3	L	1771.8 L	2247.2 B	
1409.3	L	1780.7 L	2313.2 L	
1413.6	NA	1791.7 NA	2316.3 NA	
1435.7	L	1803.0 B	2396.9 NA	
1461.7	L	1807.8 B	2599.9 L	
1468.6	B	1828.6 B	2615.0 L	
1484.6	B	1861.9 NA	2657.0 L	
1493.4	NA	1875.1 NA	2741.6 B	
1500.1	L	1879.4 NA	2744.2 NA	
1525.0	L	1883.3 NA	2753.2 L	
1560.6	B	1887.4 B	2756.3 L	
1575.8	NA	1902.3 B	3001.2 B	
1591.6	L	1919.9 L	3124.5 NA	

Appendix D - Continued

[2]Each γ-ray energy is accompanied by a symbol denoting its approximate half-life based on the experiments performed in this study. The meanings of these are as follows:

S = short, $t_{1/2}$ <0.1 sec.

M = medium, 10.0 sec > $t_{1/2}$ >0.1 sec.

L = long, $t_{1/2}$ >10.0 sec.

NA = not available, i.e., the experiment in which the γ ray was seen did not include time discrimination.

B = beam on, i.e., this γ ray was observed only during beam-on intervals. The reader is cautioned not to interpret the beam-on designation as implying a short half-life. In most experiments the beam-on counting period was at least four times as long as each individual beam-off routed spectrum.

APPENDIX E

Energies of γ Rays Observed in the $^{53m+g}$Fe Investigation

(keV)

74.1	751.1	1288.0	1826.7	3100.7
85.6	777.2	1310.8	1971.5	3122.1
123.8	788.7	1315.4	2018.3	3160.1
154.2	817.8	1318.8	2083.9	3248.0
184.9	834.5	1328.1	2102.3	3274.5
210.1	842.9	1367.7	2111.8	3282.9
224.6	846.8	1398.4	2166.7	3365.4
249.2	853.6	1407.0	2242.1	3425.0
319.1	896.1	1434.3	2273.5	3487.1
377.9	906.0	1461.8	2308.5	3783.1
415.4	935.9	1505.3	2316.5	4015.3
438.0	962.4	1538.6	2330.0	4153.3
457.4	983.8	1589.4	2339.6	4184.9
469.0	1011.5	1597.6	2613.2	4291.9
477.0	1039.3	1619.9	2685.6	
497.4	1077.5	1712.6	2722.1	
511.0	1095.8	1730.6	2746.5	
608.0	1124.3	1757.5	2750.7	
660.9	1169.5	1763.7	2756.4	
669.7	1217.8	1777.8	2754.6	
701.1	1230.5	1790.4	2852.4	
715.7	1247.5	1798.7	2944.6	
744.1	1274.3	1810.3	3040.6	